

THIS WEEK

EDITORIALS

PRIZES While some biologists celebrate, others grumble **p.402**

WORLD VIEW China has not learned the lessons of Fukushima **p.403**

NECTAR Electric flowers help to attract pollinating insects **p.405**



Gold on hold

The move towards providing full open access to research papers was undermined last week, but should prevail in the long term.

A US announcement on open access was eagerly awaited. But when it came last week, the new policy was a blow for anyone who wants fully paid-for, immediate access to the results of publicly funded research.

The US Office of Science and Technology Policy has asked federal agencies to prepare plans to ensure that all articles and data produced from research that they fund are made publicly accessible within 12 months of publication (see page 414). That delayed-access approach would have looked progressive five years ago, when the US National Institutes of Health was first putting into practice its mandate that (at least) the authors' final versions of papers must be freely available within a maximum of a year of publishing — a 'green' open-access approach, with which this publication has consistently complied. But in 2013, it looks as if a combination of financial constraints and a lack of firm resolve at the top of the US government is blocking movement towards the policy that ultimately benefits science the most: 'gold' open access, in which the published article is immediately freely available, paid for by a processing charge rather than by readers' subscriptions.

The US decision adds risk to a bolder approach taken by the United Kingdom. A policy set by Research Councils UK, an umbrella body for seven national funding agencies, has committed the research councils to using some 1% of their government-provided funds to pay for a proportion of the research that they fund to be 'gold'. This policy, set to come into effect from 1 April this year, acknowledges that publishers add value to the published versions of research, and that this value should be paid for explicitly. A gold approach is the only one that seems likely to do justice to the promise of digital science (see *Nature* **481**, 409; 2012), in which online papers are linked seamlessly to data sets, software and analysis tools, and in which papers are published under a liberal licence that enables their easy re-use for applications such as text-mining. (That vision is also expressed in the Fair Access to Science and Technology Research (FASTR) bill that was introduced to the US Congress two weeks ago — but with the caveat of a six-month delay on open access after publication and without the assurance that publishers will be able to recoup their costs.)

The United Kingdom seems isolated in proactively pursuing its golden goal, to the nation's disadvantage. Both the United States and the European Commission will allow researchers to pay for their work to be made free immediately, but neither requires it. If major international funders are happy to keep full papers behind paywalls for a year or more, the United Kingdom's libraries will find it difficult to reduce their subscription budget. For a time, Britain will be paying extra for its vision of gold open access.

The length of this transition period is one of the concerns for UK libraries and researchers scrambling to adjust to the policy before it comes in. A report released last week by the House of Lords said that this confusion was "unacceptable", although the report committee was

mollified by reassurance that Research Councils UK would transition to the gold policy slowly over five years, and would review it in 2014. The Higher Education Funding Council for England, another UK group that supports universities through taxpayer-funded grants,

"Some researchers are keen to pay for their work to be made open immediately."

says only that it wants research to be open access, without expressing a preference for green or gold.

UK science minister David Willetts is coming under pressure to justify the country's preference for immediate open access. At a meeting this week at the Royal Society in London, he argued correctly that only

gold unambiguously achieves the objective of open access for taxpayer-funded research when it is published — an objective surely worth paying a transitional price for.

The US position acknowledges the reality that the country's funding bodies have bigger short-term priorities. And despite the White House's stated green-access policy, much work from federal agencies such as the National Institutes of Health and the National Science Foundation is even now published through the gold open-access route — some researchers are keen to pay for their work to be made open immediately even when they are not compelled to do so. As for *Nature*, we view the US position as a signal that in the longer term, for highly selective journals, fully funded gold open access is a scientific necessity. ■

Starvation diet

A severe approach to slashing US spending bodes ill for the research enterprise.

Unless a miraculous truce descends on a deeply polarized Congress before the end of this week, the US government will be forced to cram US\$85 billion in across-the-board spending cuts into the seven months that remain of the fiscal year. Science agencies will not be spared. The \$30.7-billion National Institutes of Health (NIH) will lose \$1.6 billion; the National Science Foundation (NSF), more than \$370 million; the Department of Energy's Office of Science, \$260 million; and NASA's science budget, almost \$270 million.

The cuts, known as 'sequestration', are already having an impact, as agencies pare back or cling to their grant dollars, anticipating the worst (see *Nature* **494**, 158–159; 2013). In biomedical labs, postdocs are not being hired and equipment repairs are being put off. At the

NSF, few, if any, new grants are being awarded.

Conservatives pooch-pooch the public alarm that the White House raised this week in a last-ditch effort to persuade Congress to avert the cuts. What programme of the oversized US government, they ask, cannot find 5% in excess fat to trim? Unfortunately, science agencies have very little. At the NIH, for instance, funding rates for grant applicants are already at historic lows: the agency spends roughly 85% of its budget in the extramural community, yet the chance of winning a competitive grant has fallen from about one in three 10 years ago to around one in six today. At the NSF, the odds are only slightly better, at just over one in five.

The risk is that these numbers will begin to look generous as the sequester takes effect. On 25 February, NIH director Francis Collins predicted that “hundreds and hundreds” of new grants, and grants competing for renewal, will not be awarded if the sequester takes effect. Furthermore, the agency has been holding back money from the instalments it owes on multi-year grants that were awarded in previous years; at any point in time, these constitute the bulk of its extramural spending and they will need to be cut to reach the \$1.6-billion mark. Such instalments have been funded at 90% so far this year; under the sequester, awardees will never see the full 100%.

The outlook is no merrier at other science agencies. NSF director Subra Suresh wrote to Senator Barbara Mikulski (Democrat, Maryland) this month that he will be obliged to reduce his portfolio by nearly 1,000 grants and to terminate \$35 million in contracts for work already in progress on major facilities for environmental and oceanographic research. At the Department of Energy, cuts to the basic science mission will be “severe”, director Steven Chu wrote to Mikulski this month, affecting an estimated 25,000 researchers and

operations-support staff at the ten national labs and compelling a reduction in both the size and the number of the department's grants.

Opponents of the sequester worry not only about its effects, but also that the public is likely to notice them only gradually. For instance, the tens of thousands of government employees who are expected to be lost from agencies such as the Food and Drug Administration require 30 days' notice, pushing noticeable effects into

“Researchers will leave the country, or they will leave science.”

April. The loss 2,000 disease trackers supported by the Centers for Disease Control and Prevention might not become apparent until the next time *Salmonella* poisons peanut butter. By the time the public outcry becomes sufficient to cause Congress to enact a remedy for the sequester, significant

damage is likely to have been inflicted on science and on public health, not to mention the vast reaches encompassed by the rest of the government.

But for research, what is most deeply troubling about the looming cuts is not the absolute dollars lost or the immediate damage done, painful as that will be. It is what they both signify and portend, as the work of a profoundly divided government that shows no sign of being able to deliver, in anything like the foreseeable future, the stable, predictable funding that excellent science requires. Without that stability and predictability, not only will the United States' lead in science and innovation continue to erode in the face of international competition, but, in an age of unparalleled scientific opportunity, the next generation of would-be researchers will begin, understandably, to vote with their feet. They will leave the country, or they will leave science. Either way, the United States and its people will lose. ■

Prize drawback

The narrow distribution of awards aimed at the broad arena of the ‘life sciences’ raises concerns.

Recipients of the newly established Breakthrough Prize in Life Sciences were said to have been ‘floored’, not just by the award, but also by the sum of money involved. At US\$3 million per laureate, the prize dwarfs the Nobel Prize in Physiology or Medicine — which in 2012 totalled 8 million Swedish Krona, or \$1.2 million — especially given that that is often shared between two or three individuals. The objective of the Breakthrough Prize, according to its website, is “to recognize excellence in research aimed at curing intractable diseases and extending human life”; however, the web page also says that the prizes are given for “accomplishments in life sciences broadly defined”.

By the first criterion, the list of laureates is fair enough. The 11 recipients, all scientists in the front rank, work in the biomedical sciences, and the word ‘cancer’ appears in the citations for seven of them. The second criterion is more problematic. Any reading of the life sciences as ‘broadly defined’ must extend beyond (valuable and necessary) research into cures for diseases that mainly affect people in wealthy nations. There is no mention in any of the awards of malaria, schistosomiasis, cholera or malnutrition.

Taking an even broader view, the narrow scope of the prizes awarded excludes any discipline that considers the attributes of living organisms in general. Genetics gets a look in (knowledge of genetics illuminates disease states) but there is little recognition of developmental biology or neurobiology, and nothing at all on evolution, ecology, parasitology, demography, biomechanics, microbiology, environmental science, zoology, botany, conservation biology, systematics, taxonomy, palaeontology, geobiology or even astrobiology.

The apparent blind spot of the prize-givers towards these fields has been criticized in the wake of the awards, often by people in those very fields. But there is more to this than an academic turf war and sour grapes. In recent decades, the life sciences have split into two camps that can be summarized as the biology of cells and the biology of organisms. Perhaps because of their closeness to medicine, cell biologists have assumed the ascendant, and attract most funding. This has led to a perception — at least among those who study whole organisms — that cell biologists regard their own discipline not only as important (which it is) but as the only kind of biology that matters (which it is not).

Solutions to many of the world's problems will demand intensive research in many disciplines that are too-often excluded from even broad definitions of the life sciences. Efforts to mitigate the effects of climate change will require a detailed inventory of the world's species (biodiversity, zoology, botany, taxonomy, microbiology, marine biology and so on) and their interactions with one another (ecology) and the environment.

Research into many of these areas is undertaken in museums. At the time the Breakthrough Prize was announced, the Field Museum of Natural History in Chicago, Illinois, was facing tough decisions over a major shortfall in income. It is in the process of disbanding its separate research departments, reducing both the museum's capacity for research into biodiversity and its high quality of educational outreach — crucial in a nation in which the very idea of evolution is perpetually under threat.

Further cuts will be necessary; the museum announced in December that it will have to slash \$3 million from its research budgets (see *Nature* <http://doi.org/j6q>; 2012): an amount, coincidentally, that is equivalent to just one Breakthrough Prize, given to just one researcher in life sciences as defined by the Breakthrough Prize Foundation. It is

a laudable aim to work for ways to prolong lives, even those that are already long and luxurious.

To work for a world that can harbour billions of human beings in tolerable comfort is also worthy of recognition. ■

➤ **NATURE.COM**
To comment online,
click on Editorials at:
go.nature.com/xhunq



Nuclear safety lies in greater transparency

With ambitious expansion plans, China must work to create a robust and reliable nuclear regulatory system, says Qiang Wang.

China has restarted its aggressive nuclear-power programme after a 19-month suspension in the wake of the Fukushima accident in Japan. Almost half of the atomic reactors under construction worldwide are in China, and the country wants to triple its nuclear-power capacity in just 4 years — from 12.5 gigawatts in 2011 to 40 gigawatts in 2015 — a feat unlikely to be achieved anywhere else in the world.

As we approach the second anniversary of the Fukushima disaster, it is pertinent to ask whether China has learned any lessons from its great rival, Japan. Will the 28 reactors it is constructing be well run and properly regulated? Will they be safe? It is far from clear that they will.

China's nuclear expansion relies on generation III reactors, such as the Westinghouse AP1000 and the Areva European Pressurized Reactor (EPR). The industry promises that these models are safer because they put greater reliance on 'inherent' safety measures — for example, they do not require active pumps to maintain safe operation — but we must take these assurances on trust. Of greater concern, perhaps, is whether the Chinese business and construction system, in which corruption, shoddy work and cost-cutting often flourish, will sacrifice safety for speed.

What China needs to avoid is a repeat of the situation in 1998, when its home-made CNP-300 reactor at Qinshan had to be rebuilt because of defects in the welding of the steel vessel that contained the reactor.

Areva says that an EPR nuclear reactor can be built in China for about US\$4 billion — 40% less than it costs in Europe — and in about 46 months, compared with 71 months in Europe. This is the same reactor that faced massive cost overruns and delays when attempted in Finland and France.

To date, the AP1000 reactors in the Zhejiang and Shandong provinces are the only commercial units worldwide. Of the four EPR units under construction worldwide, two are being built in China's Guangdong province. China seems to be the nuclear industry's living laboratory for generation-III reactor designs and construction.

This means that China should have the world's most rigorous regulatory system. However, the nation's industry rules and guidelines are a decade out of date, and the country has no coherent legal system to govern the use of nuclear energy. Furthermore, China has taken no effective action to reform and strengthen its nuclear regulations or its regulatory bodies in the wake of Fukushima. Regulatory failures in Japan turned the accident at Fukushima into a crisis. China's system is just as bad, if not worse.

Just like Japan's, China's ability to monitor and ensure nuclear safety is undermined by a cosy relationship between state-owned nuclear regulators and state-owned operators, as well as by a revolving door that allows staff to move frequently

between government and industry. The nation's nuclear governance is fragmented and split between multiple agencies. Worse, the regulators are lower in the political pecking order than are the operators.

China's two main regulatory agencies, the National Nuclear Safety Administration and the National Energy Administration, are several steps removed from the ruling State Council. Yet the major nuclear utility companies — the China National Nuclear Corporation, the China Guangdong Nuclear Power Group and the State Nuclear Power Technology Corporation — report directly to the State Council. Thus, it is the operators, not the regulators, who will have the ear of those in power in the event of an emergency.

Had there been greater transparency and public participation in Japan's nuclear industry, then the closed community of the 'nuclear village' that dictated the nation's nuclear development would not have

formed, and the Fukushima accident would perhaps have been averted. It is unclear how China avoids the conflict of interest that brought down Japan's nuclear policy-making.

At present, China's nuclear policy-making relies too heavily on closed expert panels. And because most of the nuclear institutes in China are subsidiaries of nuclear utilities, the majority of the experts involved in evaluating proposals to build new reactors are affiliated with nuclear operations.

Like Japan, China does not yet foster transparency and public participation in its nuclear issues. The public is invited to comment on environmental-impact assessments of planned projects, but is given just ten days to do so, making thorough and independent evaluation of nuclear safety virtually impossible.

China needs nuclear energy to meet its energy demands and carbon-reduction targets. But it needs to do more to reform and strengthen its nuclear-safety system to match its expansion. It must aim for greater transparency and public involvement and set up independent nuclear institutes, giving them long-term financing to carry out independent nuclear research, especially on nuclear-safety software. But most urgently, China needs to set up a comprehensive legal framework to govern nuclear energy and give responsibility for reactor safety to an independent, credible and authoritative regulatory body. As dozens of nuclear construction sites across China whirl into action again, one thing is sure: the nation has its work cut out to gain the trust of its people and of the world. ■

Qiang Wang is director of the Western Research Center for Energy and Eco-Environmental Policy at the Xinjiang Institute of Ecology and Geography of the Chinese Academy of Sciences in Urumqi. The views expressed are his own.
e-mail: wang_q@ms.xjb.ac.cn

CHINA'S
NUCLEAR
POLICY-MAKING
RELIES
TOO HEAVILY ON
CLOSED
EXPERT PANELS.

➔ **NATURE.COM**
Discuss this article
online at:
go.nature.com/ofi6fe

RESEARCH HIGHLIGHTS

Selections from the
scientific literature

METABOLISM

Insulin's daily rhythm

The increased risk of type 2 diabetes and obesity seen in people who keep unusual hours may be tied to daily, or circadian, rhythms relating to the blood-glucose-regulating hormone insulin.

Carl Hirschie Johnson and his group at Vanderbilt University in Nashville, Tennessee, showed that mice are less responsive to insulin during the day — when they rest. The researchers disrupted the day–night cycles of mice by exposing them to continuous light or by knocking out a gene that is associated with the circadian clock. When fed a high-fat diet, the disrupted mice became fatter than non-disrupted animals.

The authors suggest that the human internal clock could be targeted to modify metabolic diseases.

Curr. Biol. <http://dx.doi.org/10.1016/j.cub.2013.01.048> (2013)

MEDICINE

Stem cells guide Alzheimer's drugs

Neural cells grown from stem cells of patients with Alzheimer's disease could be used to evaluate drugs for subsets of patients.

Teams led by Haruhisa Inoue of Kyoto University, and Nobuhisa Iwata of Nagasaki University, both in Japan, generated induced pluripotent stem (iPS) cells from patients with inherited and non-inherited forms of the disease. Neurons derived from these cells were treated with the omega-3 fatty acid docosahexaenoic acid — which has previously failed in some clinical trials for Alzheimer's

disease. The compound partially increased the survival time of neurons from a patient with an inherited form of the disease but had no effect on the survival of neurons from patients with non-inherited disease. Responses to cellular stress as well as accumulation of the protein amyloid- β , which is associated with the disease, also varied between neurons derived from different patients.

The authors suggest that patient-specific iPS cells could help researchers to explain

variable clinical results and guide drug development.

Cell Stem Cell <http://dx.doi.org/10.1016/j.stem.2013.01.009> (2013)

BIOGEOCHEMISTRY

Carbon cycles Down Under

Despite emissions from wildfires, changes in land use and extreme variability in carbon uptake from the biosphere, Australian

colleagues have made similar, but slightly heavier aerogels, from graphene oxide sheets. Their aerogel is extremely elastic, bouncing back when compressed, so may be useful in absorbing energy and dampening vibrations for a variety of machinery. Although similarly light carbon aerogels have been made before, they have relied on template scaffolds that were later etched away, a technique that limits the size of the final structure.

Adv. Mater. <http://dx.doi.org/10.1002/adma.201204576>; <http://dx.doi.org/10.1002/adma.201204530> (2013)



NANOMATERIALS

Solid carbon, springy and light

Two projects have produced elastic, ultra-light carbon foams without using a template.

Chao Gao and his colleagues at Zhejiang University in Hangzhou, China, freeze-dried solutions of carbon nanotubes and large sheets of graphene oxide, and then chemically removed oxygen to leave a conductive, elastic, solid foam (pictured with long-stemmed grass) with a density lower than that of air. These aerogels can absorb up to 900 times their own weight in oil — better than commercial absorbents.

Zongbin Zhao and Jieshan Qiu, at Dalian University of Technology in China and their

ecosystems absorbed enough carbon to offset nearly a third of its fossil-fuel emissions between 1990 and 2011.

Vanessa Haverd of the Commonwealth Scientific and Industrial Research Organisation in Canberra and her colleagues combined a regional biogeochemical model with emissions data extracted from databases and the literature to produce a comprehensive carbon budget. Contributing to the offset, rising carbon dioxide

CHAO GAO

levels and climate change increased carbon uptake by around 80 million tonnes per year, whereas fire and land-use change boosted carbon emissions by an average of 44 million tonnes per year. In addition, Australia exported 1.5 times more carbon in fossil fuels than it consumed over the two decades, and 2.5 times more from 2009 to 2010. *Biogeosciences* 10, 851–869 (2013)

MICROBIOLOGY

Healthier prehistoric plaque

When humans turned to agriculture, and later to modern starch- and sugar-filled diets, the microbes colonizing their teeth changed drastically.

Alan Cooper at the University of Adelaide, Australia, and his colleagues sequenced microbial DNA from the calcified dental plaque (pictured) of 34 mesolithic to medieval human skeletons. The oral microbial populations of individuals who lived in early farming communities were much less diverse than those of hunter-gatherers, and harboured more bacteria linked to diseases such as gingivitis.

Contemporary microbial populations are, in turn, less diverse than those of earlier communities and are dominated by bacteria linked to diseases such as those that cause cavities. The authors believe that the recent shift probably occurred during the Industrial Revolution, when processed sugar and flour became widely available.

Nature Genet. <http://dx.doi.org/10.1038/ng.2536> (2013)

ECOLOGY

Flower power guides bees

Along with colour and scent, electrical fields on flowers can guide bees' search for pollen and nectar.

Flowers often have a negative charge, whereas insects such as bumblebees (*Bombus terrestris*) tend to build up a positive charge as they fly. Daniel Robert and his colleagues at the University of Bristol, UK, placed electrodes in stems of petunias (*Petunia integrifolia*) and found that visits from bumblebees changed the flowers' electrical potential for a short time. The bees



could sense such electrical cues and use them to recognize and remember which flowers provided them with a reward. Coating the flowers with coloured, charged particles (pictured) showed that the floral electrical fields were strongest at the outer edges of petals.

Electrical signals could be a particularly versatile way for plants and pollinators to communicate, the authors say. *Science* <http://dx.doi.org/10.1126/science.1230883> (2013)

For a longer story on this research, see go.nature.com/nvjbl

HOLOGRAPHY

Liquid crystal movies

Holographic technology can produce three-dimensional images that can be seen without special eyewear and without causing visual fatigue, but the images are usually static.

COMMUNITY CHOICE

The most viewed papers in science

NEUROSCIENCE

Lonely teen rats choose drugs

HIGHLY READ
on www.cell.com/neuron in February

Socially isolated adolescent rats acquire amphetamine- and alcohol-associated memories faster — and in the case of amphetamine are slower to extinguish, or 'unlearn', them — than rats kept in groups.

Hitoshi Morikawa and his colleagues at the University of Texas at Austin found that isolated rats formed a preference for drug-associated stimuli after only one exposure, whereas rats housed in groups required repeated exposures. The researchers also showed that social isolation boosted signalling by certain neurons in a part of the brain that links behaviours with rewards. This boost was not reversed by returning the rats to a social environment.

Such effects may help to explain how pre-adult experiences can increase vulnerability to addiction, the authors suggest.

Neuron 77, 335–345 (2013)

Takeo Sasaki and his colleagues at Tokyo University of Science used liquid crystals made from organic compounds to produce a dynamic hologram. An electrical field applied to the liquid-crystal mixture alters how this medium bends, or refracts, the direction of incoming light. The researchers sent coupled laser beams through the crystal mixture to generate a holographic image.

Although small and monochromatic, the hologram exhibited more than seven times the light amplification of previous attempts, and refreshed every 8 milliseconds — fast enough to produce a smooth holographic movie. Such a technique could be used for three-dimensional displays. *Appl. Phys. Lett.* 102, 063306 (2013)

than 3,200 kilometres down eastern North America to overwinter in Mexico. The insects navigate by internal clocks that are calibrated by sunlight. But what halts the journey south? The answer is the cold.

Steven Reppert and Patrick Guerra of the University of Massachusetts Medical School in Worcester caught butterflies at the beginning of the autumn migration and kept them in the chilly temperatures that they would experience at sites in the mountains of central Mexico. When released after 24 days in the cold, the butterflies flew off northward, the direction they would normally take in spring. Simulating changes in day length did not have this effect.

Worryingly, if climate change obscures the cold signal, butterflies may keep flying south and not know when to return.

Curr. Biol. <http://dx.doi.org/10.1016/j.cub.2013.01.052> (2013)

NATURE.COM

For the latest research published by Nature visit:
www.nature.com/latestresearch

ANIMAL BEHAVIOUR

How monarchs know where to go

Migrating butterflies may use temperature to choose their flight direction.

Each autumn, monarch butterflies (*Danaus plexippus*) migrate more



SEVEN DAYS

The news in brief

RESEARCH

Coronavirus cases

A total of 13 cases of the novel coronavirus have been confirmed globally. Seven of the patients have died, with the latest death being in Saudi Arabia, the World Health Organization said on 21 February. At least three cases have occurred in a family living in England, with two of them arising through human-to-human transmission, the European Centre for Disease Prevention and Control in Stockholm said on 19 February. One of the UK cases has died and another is seriously ill, but the third shows only mild symptoms, suggesting that other mild cases of infection could be escaping detection.

NASA programme

NASA has created a department to develop the pioneering technologies needed for current and future space missions, it announced on 21 February. The Space Technology Mission Directorate will collaborate with academia and industry — including defence companies — to pursue space exploration while boosting US economic

NUMBER CRUNCH

74.8%

The percentage of gross national expenditure on research and development spent by South Korean businesses in 2010, the latest year for which data are available. The nation continues to have higher business investment in research than China, Asia's research powerhouse.



YNA/EPA/CORBIS

Crackdown on illegal fishing launched

INTERPOL, the world's largest police organization, launched an initiative to tackle illegal fishing (pictured) at a conference in Lyons, France, on 26 February. Project Scale will establish national environmental task forces to ensure cross-border collaboration on fishing crime, conduct operations to enforce

national legislation, and develop case studies on fisheries-crime hotspots in regions such as West Africa. The initiative's fisheries-crime working group meets for the first time this week to assess what resources vulnerable member countries will need to combat illegal fishing effectively. See go.nature.com/5cl8zs for more.

competitiveness. "A robust technology-development programme is vital to reaching new heights in space and sending American astronauts to new destinations like an asteroid and Mars," said NASA administrator Charles Bolden.

Asteroid hunter

The first satellite designed to search for and keep track of asteroids and space debris was launched into orbit on 25 February. The Canadian Space Agency's Near-Earth Object Surveillance Satellite will circle the globe every 100 minutes, scanning space to pick out asteroids that may one day pose a threat to Earth. It would not have provided advance warning of the meteor that exploded over Russia earlier this month, however,

because it will focus on detecting and tracking much larger asteroids and comets, says the agency. See go.nature.com/5ec274 for more.

POLICY

Risky research

The US National Institutes of Health finalized a framework on 21 February for funding research that will ultimately allow the agency to support studies on mammalian-transmissible H5N1 avian influenza. A moratorium on the research was in place for more than a year until it was lifted in January. Also on 21 February, the US Office of Science and Technology Policy published a draft policy guiding scientists and institutions on how to monitor dual-use

research — research that could potentially be manipulated to do harm. The policy is open for public comment for 60 days. See go.nature.com/ephnei for more.

AIDS relief review

Control of the United States' 10-year programme to tackle HIV/AIDS in developing countries should be handed over to the nations in which it operates, says an advisory report released on 20 February. The President's Emergency Plan for AIDS Relief spent more than US\$38 million between 2004 and 2011, saving and improving millions of lives, finds the report from the US Institute of Medicine in Washington DC. The United States should now take a step back, providing less direct

BILL YOUNGBLOOD/CALTECH support and more technical assistance. See go.nature.com/8kwzwo for more.

Irish science

The Irish government announced on 25 February that €300 million (US\$393 million) will be used to set up seven centres to promote collaboration between industry and researchers in areas including photonics and marine renewable energy. "This is the largest single research announcement to date in Ireland in terms of people and projects," says Mark Ferguson, director-general of Science Foundation Ireland, which will distribute the state funding. See go.nature.com/crfzv7 for more.

US open access

Research by any federal agency that spends more than US\$100 million on research and development will be made free to the public one year after publication, the US government announced on 22 February. The mandate expands a policy that until now has applied only to biomedical science. See pages 401 and 414 for more.

PEOPLE

President swap

Jean-Lou Chameau (pictured) is to leave his post as president of the California Institute of Technology (Caltech) in



Pasadena to head the King Abdullah University of Science and Technology (KAUST) in Thuwal, Saudi Arabia, KAUST confirmed on 19 February. Chameau, a French engineer, has helped to raise nearly US\$1 billion for Caltech since arriving at the university in 2006. At KAUST, he will replace Choon Fong Shih, an engineer who has overseen the university since it opened in 2009. See go.nature.com/kr6zvp for more.

Nobel physicist dies

Robert Richardson, a physicist who was awarded a Nobel prize in 1996 for his work on superfluidity, has died aged 75. Richardson worked at Cornell University in Ithaca, New York; in 1971, he showed that helium-3 can flow with no friction at temperatures very close to absolute zero. The discovery led to major advances in the understanding of quantum effects in fields such as materials science and astrophysics.

BUSINESS

Drug approval

The US Food and Drug Administration approved a new drug, Kadcyla (ado-trastuzumab emtansine), to treat some advanced breast cancers, on 22 February. The drug, developed by Genentech in San Francisco, California, is an 'antibody-drug conjugate' that links the blockbuster antibody therapy Herceptin (trastuzumab) to a chemotherapy treatment. The technique aims to reduce side effects and boost efficacy by using the antibody to deliver the treatment directly to cancer cells.

AWARDS

Biology prizes

Eleven biologists received the inaugural Breakthrough Prize in Life Sciences for their work in cancer, genomics, stem cells and neurobiology on 20 February. The prizes, worth US\$3 million each, are sponsored by entrepreneurs including Russian social-media mogul Yuri Milner, and aim to raise the profile of biomedical research. In future, five prizes will be awarded annually. Last year, Milner awarded the first \$3-million Fundamental Physics Prizes for theoretical physicists. See page 402 and go.nature.com/rxb34b for more.

COMING UP

3–14 MARCH

The Conference of the Parties to the Convention on International Trade in Endangered Species of Wild Fauna and Flora meets for the 16th time, in Bangkok. See page 411 for more. go.nature.com/z6jyep

4–8 MARCH

The Global Challenges, Global Collaboration conference on the role of science in tackling international issues is held in Brussels, organized by the Irish presidency of the European Council. go.nature.com/5youky

FUNDING

Charitable giving

Stanford University in California became the first institution to raise more than US\$1 billion in charitable contributions in a year, according to the Council for Aid to Education, a non-profit organization in New York city. Fund-raising by US colleges and universities totalled \$31 billion in 2012, up 2.3% on 2011.

FACILITIES

Nuclear leaks

The US Department of Energy has identified six leaking nuclear-waste storage tanks at the Hanford Site in Washington, a cold-war facility plagued with contamination problems. On 22 February, a week after the department confirmed a leak in one tank, Washington governor Jay Inslee (Democrat) announced that another 5 had been found among the site's 177 tanks.

➔ NATURE.COM

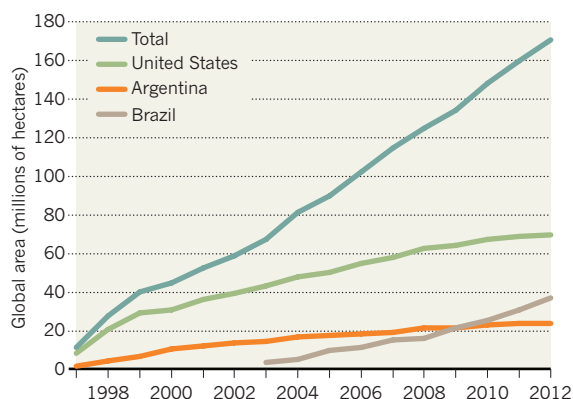
For daily news updates see: www.nature.com/news

TREND WATCH

The United States planted 69.5 million hectares of genetically modified (GM) crops in 2012, just 0.7% more than the year before. But Brazil — the second-largest GM adopter after the United States — planted 21% more than in 2011 to reach 36.6 million hectares. It is leading a surge that saw developing and emerging countries overtake industrialized nations (the United States, Canada, Australia and Europe) in total hectares planted last year, according to figures released on 20 February.

BRAZIL'S GM-CROP SURGE

Planting of genetically modified (GM) crops grew by 6% in 2012 compared with 2011, reaching 170 million hectares worldwide.



NEWS IN FOCUS

PUBLIC HEALTH The shaky science of cholesterol guidelines **p.410**

CONSERVATION DNA from elephant dung pinpoints ivory poachers **p.411**

REGENERATIVE MEDICINE Induced stem cells make clinical debut **p.413**

NOMENCLATURE 'Ome sick or 'ome run? Biology's suffix du jour **p.416**

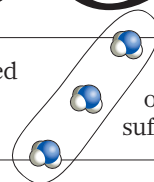


PHOTO SHOT



Ernest Moniz looks set to be the next leader of the US Department of Energy.

POLICY

Physicist tipped for US energy post

Ernest Moniz considers natural gas a bridge to clean energy.

BY JEFF TOLLEFSON

As the administration of US President Barack Obama prepares for a renewed push towards cleaner energy and reduced greenhouse-gas emissions, the White House appears to have chosen another physicist to head the effort. The leading candidate to replace departing energy secretary Steven

Chu is Ernest Moniz, director of the Energy Initiative at the Massachusetts Institute of Technology (MIT) in Cambridge. He would bring to the office a pragmatic support for nuclear power and natural gas, along with a candid desire to, in his own words, “innovate like hell” on basic energy technologies. Colleagues at MIT are waiting for a confirmation of the appointment, which could come as early

as this week. “Ernie is a real people person, and he took us to a whole new level in terms of both size and visibility,” says Howard Herzog, a participant in the Energy Initiative who works on carbon capture and sequestration technologies at MIT.

Both Chu and Moniz are respected physicists with a passion for energy, but the resemblance ends there. Chu came to Washington as a policy outsider — and sometimes struggled with relationships on Capitol Hill (see *Nature* **462**, 978–983; 2009). But Moniz is primed for the post: he served as an associate director in the White House Office of Science and Technology Policy under president Bill Clinton before becoming undersecretary of energy in 1997. In that role, he worked on science and energy issues as well as nuclear weapons and nonproliferation programmes. For the past four years, he has served on the President’s Council of Advisors on Science and Technology (PCAST).

Equipped with a disarming smile and a trademark over-the-ears hairstyle, Moniz can address science, engineering and public policy in plain English, on the fly and under a spotlight. “Ernie is really a big-picture guy,” says Rosina Bierbaum, a fellow PCAST member and an environmental-policy expert at the University of Michigan in Ann Arbor. “He can talk the details of science far better than most of us, but he never ever gets lost in the weeds.”

Colleagues say that Moniz would probably aim to build on the work of Chu, who sought to overhaul the Department of Energy’s research and development programme. Chu’s initiatives include the Advanced Projects Research Agency—Energy, which funds risky, high-impact research, and five innovation hubs intended to promote interdisciplinary research on topics such as energy-efficient buildings and batteries.

Moniz took a similar interdisciplinary approach to energy research when he returned to MIT from Washington DC in 2001. His first major project was *The Future of Nuclear Power*, a 2003 report that declared that nuclear energy is an “important option” for producing low-carbon power, and that explored the science, engineering, economics and policy needed ▶

“He can talk the details of science far better than most of us, but he never ever gets lost in the weeds.”

► to expand it. After launching the Energy Initiative in 2006, Moniz and his MIT colleagues produced a series of reports on topics including geothermal energy, the electric grid, coal and the nuclear fuel cycle.

Most prominent, and controversial, was a 2011 report on natural gas. It highlighted the possibility that hydraulic-fracturing technologies could expand US gas production, displacing dirtier-burning coal in electricity generation and thus reducing US greenhouse-gas emissions. Moniz's enthusiasm for natural gas worries some environmentalists, who

are concerned about the air and water pollution resulting from its extraction. But gas has indeed helped to reduce emissions: in 2011, US greenhouse-gas emissions were nearly 8% below those in the peak year of 2007.

Talking to *Nature* last July, Moniz laid out his energy-policy goals for the current decade: reduce demand; substitute gas for coal; and innovate to reduce the cost of low-carbon technologies for areas such as nuclear power, renewable energy and capturing and sequestering carbon dioxide from fossil-fuel combustion. Moniz noted how basic research on

hydraulic fracturing, funded by the Department of Energy and dating back to the 1980s, is now paying off. "If you came out with a policy to reduce coal use by a third, all hell would break loose politically. But the market did it by itself, and you don't hear anybody complaining," he said. "To me, the lesson from that is the importance of innovation to reduce the costs of the zero-carbon options."

The key, he said, is to put in place a long-term plan to reduce greenhouse-gas emissions once gas has replaced coal. "Gas is a bridge, but it has to be a bridge to somewhere," he said. ■

HEALTH

Cholesterol limits lose their lustre

Revised guidelines for heart health are set to move away from target-based approach.

BY HEIDI LEDFORD

Soon after Joseph Francis learned that his levels of 'bad' LDL cholesterol sat at twice the norm, he discovered the shortcomings of cholesterol-lowering drugs — and of the clinical advice guiding their use. Francis, the director of clinical analysis and reporting at the Veterans Health Administration (VA) in Washington DC, started taking Lipitor (atorvastatin), a cholesterol-lowering statin and the best-selling drug in pharmaceutical history. His LDL plummeted, but still hovered just above a target mandated by clinical guidelines. Adding other medications had no effect, and upping the dose of Lipitor made his muscles hurt — a rare side effect of statins, which can cause muscle breakdown.

So Francis pulled back to moderate Lipitor doses and decided that he could live with his high cholesterol. Later, he learned that other patients were being aggressively treated by doctors chasing stringent LDL targets. But Francis found the science behind the target guidelines to be surprisingly ambiguous. "You couldn't necessarily say lowering LDL further was going to benefit the patient," he says.

The standard advice may soon change. For the first time in more than a decade, the US National Heart, Lung and Blood Institute is revising the clinical guidelines that shaped Francis's treatment (see 'How low can you go?'). Expected to be released later this year, the fourth set of guidelines, called ATP IV, has been drawn up by an expert panel of 15 cardiologists appointed by the institute. The guidelines will set the tone for clinical practice in the United States and beyond, and will profoundly

influence pharmaceutical markets. They will also reflect the growing debate over cholesterol targets, which have never been directly tested in clinical trials.

"We can't just assume that modifying the risk factor is modifying risk," says Harlan Krumholz, a cardiologist at Yale University in New Haven, Connecticut. "We've been burned so many times in the past decade by that assumption."

Since 2002, when ATP III called on doctors to push LDL levels below set targets, the concept of low cholesterol has become synonymous with heart health. Patients brag about their cholesterol scores, physicians joke about adding statins to drinking water, and some hospitals reward doctors when patients hit cholesterol targets.

In 2011, US doctors wrote nearly 250 million prescriptions for cholesterol-lowering drugs, creating a US\$18.5-billion market, according to IMS Health, a health-care technology and information company based in Danbury, Connecticut. "The drug industry in particular is very much in favour of target-based measures," says Joseph Drozda, a cardiologist and director of outcomes research at Mercy Health in Chesterfield, Missouri. "It drives the use of products."

ATP III reflected a growing consensus among physicians that sharply lowering cholesterol would lessen the likelihood of heart attacks and strokes, says Richard Cooper, an epidemiologist at the Loyola University of Chicago Stritch School of Medicine in Illinois, who served on the committee that compiled the guidelines. The committee drew heavily on

clinical data, but also took extrapolations from basic research and post hoc analyses of clinical trials. LDL targets were set to be "less than" specific values to send a message, Cooper says. "We didn't want to explicitly say 'the lower the better' because there wasn't evidence for that," he says. "But everybody had the strong feeling that was the correct answer."

By contrast, the ATP IV committee has pledged to hew strictly to the science and to focus on data from randomized clinical trials, says committee chairman Neil Stone, a cardiologist at Northwestern University School of Medicine in Chicago. If so, Krumholz argues, LDL targets will be cast aside because they have never been explicitly tested. Clinical trials have shown repeatedly that statins reduce the risk of heart attack and stroke, but lowering LDL with other medications does not work as well. The benefits of statins may reflect their other effects on the body, including fighting inflammation, another risk factor for heart disease.

Krumholz's scepticism is rooted in experience. In 2008 and 2010, the Action to Control Cardiovascular Risk in Diabetes (ACCORD) clinical trial challenged dogma when it

"We can't just assume that modifying the risk factor is modifying risk."

HOW LOW CAN YOU GO?

US guidelines set by the Adult Treatment Panel (ATP) have gradually lowered acceptable levels for LDL 'bad' cholesterol, while shifting focus to prevention in patients at risk of a heart attack.

Name	Year	LDL target for people with the highest risk of heart attack (mg dL ⁻¹)
ATP I	1988	≤130
ATP II	1993	<130
ATP III	2002	<100
ATP III (update)	2004	<70

► **NATURE.COM**
For more on heart health, see *Nature's* Outlook:
go.nature.com/rbift4

reported that lowering blood pressure or blood sugar to prespecified targets did not reduce the risk of heart attack or stroke. In the case of blood sugar, the risks were worsened. The trial demonstrated the folly of assuming that risk factors must have a causal role in disease, says Robert Vogel, a cardiologist at the University of Colorado, Denver. "Short people have a higher risk of heart disease," he says. "But wearing high heels does not lower your risk."

Jay Cohn, a cardiologist at the University of Minnesota Medical School in Minneapolis, also worries that the focus on LDL levels offers up the wrong patients for statin therapy. Most of those who have a heart attack do not have high LDL, he notes. Cohn advocates treating patients with statins based on the state of health of their arteries, as revealed by noninvasive tests such as ultrasound. "If your arteries and heart are healthy, I don't care what your LDL or blood pressure is," he says.

Not all cardiologists want to abolish LDL targets. Indeed, Seth Martin, a fellow in cardiology at Johns Hopkins University School of Medicine in Baltimore, Maryland, believes that ATP IV should reduce LDL targets further. The simplicity of targets has helped to deliver an important public-health message, he says, and motivated many patients to get the statin therapy that he believes they need. "Just to throw that out the window doesn't seem like the ideal scenario."

Whatever the decision, the pharmaceutical industry will be watching closely, says Donny Wong, an analyst at Decision Resources, a market-research company based in Watertown, Massachusetts. Although most statins are off patent, the big pharmaceutical companies are racing to bring the next LDL-lowering drug to market. In particular, millions of dollars have been poured into drugs that inhibit a protein called PCSK9, an enzyme involved in cholesterol synthesis. This approach lowers LDL but has not yet been shown to reduce heart attacks or strokes.

Francis expects the new guidelines to relax the targets. He and his colleagues decided last autumn to change the VA's own clinical standards, so that they no longer rely solely on an LDL target but instead encourage doctors to prescribe a moderate dose of statin when otherwise healthy patients have high LDL cholesterol. The ATP IV guidelines will take a similar approach, he speculates, noting that the VA consulted several outside experts who are also serving on the ATP committee.

Despite an increasingly vegetarian diet, Francis's cholesterol has not budged. "Sometimes I want to call my physician and say, 'Don't worry about that target,'" he says. "It's going to be changing very soon." ■



BRUCE DAVIDSON/NATUREPL.COM

Guards in Garumba National Park, Democratic Republic of Congo, are working to stamp out poaching.

CONSERVATION

Tusk tracking will tackle illegal trade

Forensic testing of seized ivory could track down poachers.

BY DANIEL CRESSEY

International treaties meant to protect elephants are not working. Researchers estimate that tens of thousands of African elephants are now being killed by poachers each year, from a total wild population of around 400,000.

"It doesn't take much math to show we have a serious, urgent problem," says Samuel Wasser, director of the Center for Conservation Biology at the University of Washington in Seattle.

The only way to catch the people who are slaughtering the elephants is to redouble efforts to track illegal ivory back to its source. That is the stark message that Wasser and others will deliver to policy-makers in Bangkok next week, at the triennial conference of the parties to the Convention on International Trade in Endangered Species of Wild Fauna and Flora (CITES; see 'Candidates for protection').

Nearly 39,000 kilograms of illegal ivory were traded worldwide in 2011, more than at any other time in the 16-year history of the Elephant Trade Information System (ETIS), which tracks the ivory trade for CITES. Another CITES programme, Monitoring the Illegal Killing of Elephants, will report at the

meeting that between 3.5% and 11.7% of the total African elephant population was killed by poachers in 2011 — the worst year for illegal killing since the programme began collecting data in 2002.

Those on the ground in Africa predict that, once the data are all in, the figures for 2012 will be even worse. The trade is being driven by the high prices that ivory now commands: about US\$1,600 per kilogram in the Far East, according to the Born Free Foundation, a wildlife charity based in Horsham, UK. But many fear that attempts to stem the demand now — although crucial — may come too late.

"We're really at a tipping point, I think," says George Wittemyer, an ecologist at Colorado State University in Fort Collins, who studies elephants in the Samburu National Reserve in Kenya. "We're seeing declines in the species as a whole and we're seeing poaching spread into what were once untouchable safe havens."

Poachers in Samburu are also switching focus from males to older females and killing entire social groups, says Wittemyer.

Scientists argue that an international drive to trace seized ivory back to its origins is urgently needed, so that authorities can curb poaching before elephant populations collapse. ►



Next week, parties to the Convention on International Trade in Endangered Species of Wild Fauna and Flora (CITES) will discuss dozens of measures to protect animals and plants. Here are a few to watch for.

● Rhinos

White rhinos (*Ceratotherium simum*; pictured) and black rhinos (*Diceros bicornis*) are both being targeted by poachers; parties to CITES are set to discuss an expansion of DNA work to track down killing sites. Kenya has also

TREATY TALKING POINTS

Candidates for protection

proposed that trade in white-rhino hunting trophies from South Africa and Swaziland should be blocked for at least six years.

● Polar bears

The United States has proposed that the polar bear (*Ursus maritimus*) be moved from Appendix II of CITES, which covers animals not in danger of extinction but needing trade protection, to Appendix I, for species threatened with extinction. But the CITES secretariat has recommended that the

proposal be rejected, saying that projections of polar-bear population decline vary widely.

● Sharks

Many sharks could be added to Appendix II, although in most cases protection will be delayed by 18 months to give affected countries some breathing room. The CITES secretariat is backing protection for oceanic whitetip sharks (*Carcharhinus longimanus*), porbeagles (*Lamna nasus*) and various species of hammerhead shark. **D.C.**

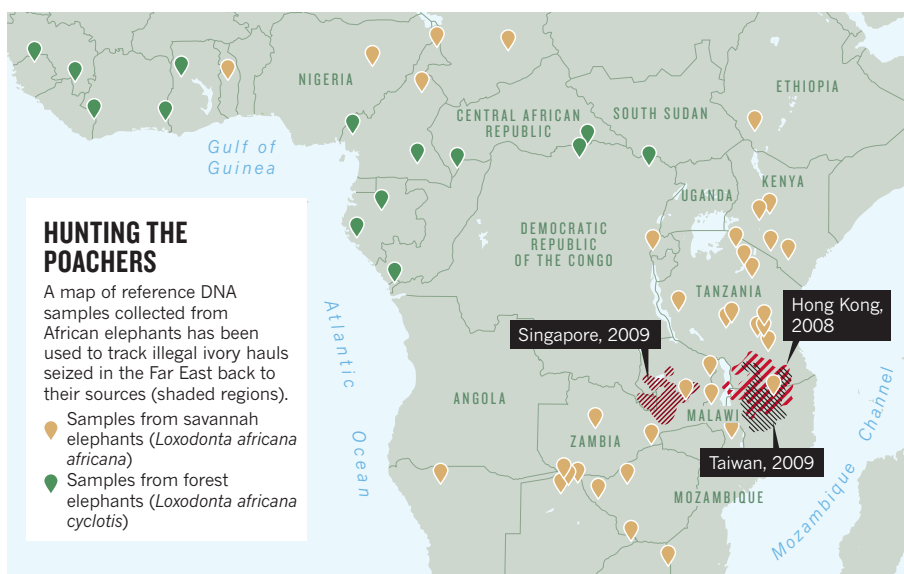
► There are few reliable estimates of regional elephant numbers, and counting corpses is inaccurate because many are likely to be lost in the vast forests and savannahs of Africa.

A team led by Wasser has developed a map of DNA samples collected across Africa¹ — often from elephant dung — which it uses to pinpoint the probable origins of seized ivory samples (see ‘Hunting the poachers’). Wasser has shown that illegal ivory shipments do not often originate from the countries in which the animals were poached.

He wants CITES to increase forensic scrutiny of the huge stockpiles of ivory in many African nations. He also wants the treaty to change so that authorities must test every item in all large ivory seizures, which can weigh many tonnes. This would give a more detailed picture of where poaching is occurring, and could be used to step up enforcement in regions where killing is rife.

Hitting these areas could have a big impact, says Wasser. “There are probably not as many of these poaching hotspots as people might think.”

Others are also working on tracking. Alfred Roca, a geneticist at the University of Illinois at Urbana-Champaign — whose work demonstrated that African elephants are actually likely to be two separate species² — has used mitochondrial DNA to trace ivory hauls³. He says that his technique could complement Wasser’s work. Male elephants tend to leave their herds at reproductive age, whereas females stay in the same social group, so mitochondrial DNA — which is passed through the female



line — could be used to help to triangulate the origins of the ivory, says Roca.

“It’s very important to source these large-scale ivory seizures. It should be mandated through CITES that there is forensic examination of the shipments so the source can be determined,” says Tom Milliken, the elephant expert at wildlife-trade monitoring group TRAFFIC, which is headquartered in Cambridge, UK. Milliken will be presenting the ETIS data at the Bangkok meeting.

He adds that it may be time for CITES to consider sanctions against countries

— including Thailand — that have failed to tackle the ivory trade within their borders. Such restrictions could block all trade in wild-animal and plant products from a nation. “We have reached a moment when the threat of sanctions is certainly warranted,” says Milliken. ■

1. Wasser, S. K. et al. *Proc. Natl Acad. Sci. USA* **101**, 14847–14852 (2004).
2. Roca, A. L., Georgiadis, N., Pecon-Slattery, J. & O’Brien, S. J. *Science* **293**, 1473–1477 (2001).
3. Ishida, Y., Georgiadis, N. J., Hondo, T. & Roca, A. L. *Evol. Appl.* **6**, 253–265 (2013).

SOURCE: S. WASSER


**MORE
ONLINE**

TOP STORY



Beach sands reveal long-lost continent under Indian Ocean
go.nature.com/qepipt

MORE NEWS

- Syrian crisis resembles fall of Akkadians 4,000 years ago go.nature.com/avtxxi
- Artificial peptide sneaks drugs past the immune system go.nature.com/vbhrpp
- Newt transcriptome resets date for regenerative abilities go.nature.com/73sfqa

PODCAST



Video games as brain-trainers; the neurological basis of birdsong; and the five 'omes that really matter
go.nature.com/mzu7it

REGENERATIVE MEDICINE

Stem cells cruise to clinic

Japanese study of induced pluripotent stem cells aims to demonstrate safety in humans.

BY DAVID CYRANOSKI IN TOKYO

In the seven years since their discovery, induced pluripotent stem (iPS) cells have transformed basic research and won a Nobel prize. Now, a Japanese study is about to test the medical potential of these cells for the first time. Made by reprogramming adult cells into an embryo-like state that can form any cell type in the body, the cells will be transplanted into patients who have a debilitating eye disease.

Masayo Takahashi, an ophthalmologist at the RIKEN Center for Developmental Biology in Kobe, Japan, plans to submit her application for the study to the Japanese health ministry next month, and could be recruiting patients as early as September. Stem-cell researchers around the world hope that if the trial goes forward, it will allay some of the safety concerns over medical use of the cells. And the Japanese government hopes that its efforts to speed iPS cells to the clinic by generously funding such work will be vindicated (see *Nature* 493, 465; 2013).

"The entire field is very dependent on this group and the Japanese regulatory agencies to ensure that preclinical evidence for safety and efficacy is very strong," says Martin Pera, a stem-cell expert at the University of Melbourne in Australia.

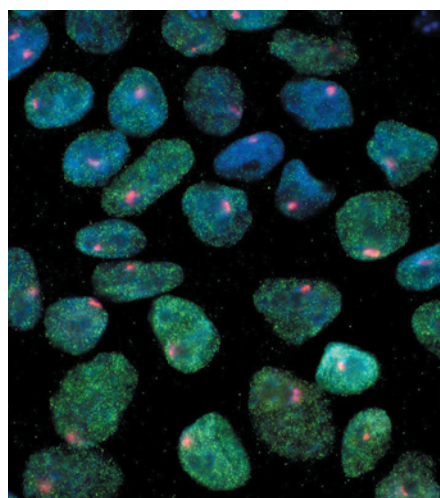
Takahashi, who has been studying the potential of iPS cells to rebuild diseased tissue for more than a decade, hopes to treat around six people who have severe age-related macular degeneration, a common cause of blindness that affects at least 1% of people aged over 50. The form of the disease that Takahashi will treat occurs when blood vessels invade the retina, destroying the retinal pigment epithelium that supports the light-sensitive photoreceptors. This form can be treated with drugs that block the growth of new blood vessels, but these often have to be injected repeatedly into the eye.

Takahashi will take a peppercorn-size skin sample from the upper arm and add proteins that reprogram the cells into iPS cells. Other factors will transform the iPS cells into retinal cells. Then a small sheet of cells will be placed under the damaged area of the retina, where, if things go well, the cells will grow and repair the pigment epithelium.

The researchers hope to see the transplants slow or halt the disease, but their main goal is to show that the cells are safe. One concern is that the reprogrammed cells will trigger an immune reaction — as has been seen in mice (T. Zhao *et al. Nature* 474, 212–215; 2011). But that concern has faded after a recent study suggested

that iPS cells did not provoke an immune reaction after all (see R. Araki *et al. Nature* 494, 100–104; 2013 and *Nature* 493, 145; 2013). "Immune compatibility seems to be as expected, so I am not so concerned about that issue," says stem-cell expert George Daley of Harvard Medical School in Boston, Massachusetts.

A bigger worry is that the reprogrammed



Induced pluripotent stem cells could soon be used in human trials in Japan.

cells might multiply uncontrollably and form tumours instead of healthy tissue. But Pera and Daley are reassured by the pre-clinical data that Takahashi has presented at conferences. Takahashi says that these results, submitted for publication, show that her iPS cells do not form tumours in mice and are safe in non-human primates.

Pera adds that the procedure to treat macular degeneration requires just a few stem cells, reducing the chances that a tumour will form. Also, any tumours would be relatively easy to remove because the eye is more accessible than some organs.

Daley does worry that the treatment, even if it proves harmless, might not be effective. The cells might not engraft properly, for example, or might not integrate with the patients' own tissue. "I think we will require many years of experience to learn more about how cells integrate," he says. Pera raises another concern: that the identity of the cells might not be stable, and that over time they would no longer function as retinal epithelium.

According to Robert Lanza, chief scientific officer at biotechnology firm Advanced Cell Technology (ACT) in Santa Monica, California,

iPS-cell studies like Takahashi's could be premature. "I cannot imagine any regulatory agency permitting such a trial without years of extensive pre-clinical testing," he says. ACT is racing to start a less-ambitious clinical trial of iPS cells for use in other diseases. Its study would inject healthy patients with platelets derived from iPS cells and from embryonic stem cells to see if they act like normal platelets, which could open the way to a treatment for blood-clotting disorders. Because platelets lack a nucleus, there is no risk of forming tumours, explains Lanza. He will meet with the US Food and Drug Administration later this month, and hopes to get approval to start the trial this year.

Lanza says that using iPS cells that contain a nucleus in human trials is "a far greater challenge" than his approach. But Takahashi's team is prepared, counters Pera. They are "among the pioneers in this field," he says, adding that they are "well placed to undertake these studies".

Takahashi is carrying out a 'clinical study' which, in Japan's somewhat confusing system, is less tightly regulated than a clinical trial and cannot by itself lead to approval for clinical use of a treatment. The data, if positive, might attract investors or help Takahashi to get approval for a formal clinical trial — required if the cells are ever to be used to treat patients in the clinic.

The study was approved by institutional review boards at both the Center for Developmental Biology and the Institute of Biomedical Research and Innovation in Kobe, where the surgical procedures will be carried out. Now, approval depends on a health-ministry

"The entire field is very dependent on this group and the Japanese regulatory agencies."

committee of 18 physicians, lawyers, administrators and scientists, including three stem-cell specialists. If Takahashi wins approval by September as expected,

it will take another eight months to grow the sheets of cells required for the transplants.

In Japan, future iPS-cell therapies may have an easier path to the clinic as the government continues its drive to capitalize on the technology, which was first developed there. A revised drug law, expected to be put before the Japanese parliament by late June, would fast-track therapies that seem to be effective in phase II or phase III trials. But the success of that drive, and the prospects for patients with macular degeneration, depend in part on Takahashi and her pioneering patients. ■

US science to be open to all

Government mandates that taxpayer-funded research be freely available within 12 months.

BY RICHARD VAN NOORDEN

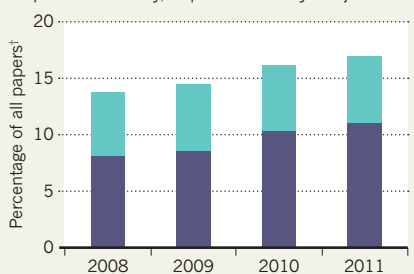
The rumours have been buzzing around Capitol Hill since before last year's election, and last week, supporters of open-access publication in the United States got most of what they wanted. The White House declared that government-funded research would be made free for all to read, rather than kept behind paywalls. However, those hoping that the government would require papers to be free from the time of publication were disappointed.

In a 22 February memo, John Holdren, director of the White House's Office of Science and Technology Policy (OSTP), gave federal agencies until 22 August to produce plans for making the data and papers from the research they fund more accessible to the public. The move, he says, would "accelerate scientific breakthroughs and innovation" and boost economic growth. Agencies should aim to make research papers free by 12 months after publication — a concession to

INTO THE OPEN

Publishers are making an increasing proportion of papers free to the public on their websites.

■ Immediately open access
■ Open after a delay, or published in hybrid journals*



*Hybrid journals: subscription journals that publish some articles open access. †All papers indexed in Elsevier's Scopus database.

publishers, who say that a year's delay is needed to maintain their revenue from subscriptions.

The policy applies to an estimated 19 federal agencies, which each spend more than

US\$100 million on research and development. It would roughly double the number of articles made publicly available each year to about 180,000, according to the Scholarly Publishing and Academic Resources Coalition, an open-access advocacy group in Washington DC, which called the memo a "landmark". Until now, only the US National Institutes of Health (NIH) has required its research to be publicly available after 12 months.

The latest move is a response to the 2011 reauthorization of the 2007 America COMPETES Act, which included billions of dollars for science, and also charged the OSTP with improving public access to research (see 'Into the open'). Another spur came in May 2012, when thousands petitioned the White House to require free access to journal articles arising from US taxpayer-funded research. Agencies such as the National Science Foundation and the Department of Energy have been laying the groundwork with publishers for the

SOURCE: M. LAIKSO & B.-C. BJÖRK BMC MED. 10, 124 (2012)

past 18 months, notes Fred Dylla, executive director of the American Institute of Physics, a publisher based in College Park, Maryland.

It will probably be a year or two before any policies are implemented, says Catherine Woteki, chief scientist at the US Department of Agriculture. Agencies might model their plans on the NIH approach, in which a government-funded repository, PubMed Central, is used to house the free research. "There's no sense in reinventing the wheel," says Woteki.

But Dylla suggests that the full text of papers could reside on publishers' websites, with agencies just providing links. The memo specifically encourages public-private collaborations, asks agencies not to duplicate existing mechanisms and requests that resources be found from existing budgets. These are hints, Dylla says, that the OSTP does not want to extend the PubMed Central approach. Some publishers resent that repository, which they see as deflecting attention from their own web pages.

The embargo time before papers are free could vary by discipline and journal, although agencies will have to justify any departure from the 12-month standard. In Europe, embargo times permitted in prospective public-access policies vary from 6 to 24 months. And just a week before the White House announcement, a bipartisan bill was introduced into Congress that would mandate a 6-month embargo for all.

But Michael Eisen, a biologist and open-access advocate at the University of California, Berkeley, says that he is disappointed. "They had an opportunity to do something dramatically important, and instead they recycled a 5-year-old policy and went to great lengths to say that embargoes are critical for maintaining the publishing industry," Eisen says. He would rather that research be made free immediately.

That is the approach being taken in the United Kingdom, where science minister David Willetts has championed a move to a system in which work is immediately free to read. The UK funding agencies plan to finance this 'gold' open-access route by diverting some 1% of the national research budget, and requiring that authors or their institutions use it to pay publishers up-front to make work public. That policy will start to take effect from 1 April, but will ramp up slowly over five years: only 45% of research will be immediately free to read this year.

The United Kingdom had hoped to jolt other governments into following its lead. "We maintain our belief that the gold route is the best means of promoting openness and collaboration," says Willetts. But so far, researchers in the United States and the rest of Europe are not obliged to use science funds to make their work free immediately. ■ [SEE EDITORIAL P.401](#)

BIOLOGY

Circular RNAs throw genetics for a loop

RNA 'sponges' mop up sequences that curb gene expression.

BY HEIDI LEDFORD

Behold the latest curio in the cabinet of RNA oddities: naturally occurring circular RNA molecules that influence gene expression.

At least some of the loops, described in two papers published this week by *Nature*^{1,2}, act as molecular 'sponges', binding to and blocking tiny gene modulators called microRNAs. But the researchers suspect that the circular RNAs have many other functions. The molecules comprise "a hidden, parallel universe" of unexplored RNAs, says Nikolaus Rajewsky, the lead author of one of the studies and a systems biologist at the Max Delbrück Center for Molecular Medicine in Berlin.

The discovery is yet another reminder that RNA is much more than a mundane messenger between DNA and the proteins it encodes. The past two decades have seen the discovery of a host of nonconformist RNAs. Some were unexpectedly short or surprisingly long, and some flouted orthodoxy by blocking other RNA strands from being translated into protein. But almost all were linear. The few accounts of circular RNAs in plants and animals were generally dismissed as genetic accidents or experimental artefacts, says Erik Sontheimer, a molecular biologist at Northwestern University in Evanston, Illinois.

Instead, the predominance of linear RNAs may have been the artefact. Typical RNA-sequencing methods isolate only those molecules with characteristic molecular 'tails'. With their ends joined together, round RNAs lack those tails, so have generally been overlooked.

But advances in sequencing have allowed biologists to accumulate large data sets of RNA sequences, including some from RNA without tails. Last year, Julia Salzman, a molecular biologist at Stanford University School of Medicine in California, and her colleagues sent the first missive from the circular universe. They reported finding a plethora of circular human RNAs while searching for RNA molecules that conventional methods might have missed³. And when Rajewsky and his colleagues mined databases for circular RNA molecules, they found thousands in nematode worms, mice and humans.

"It's yet another terrific example of an important RNA that has flown under the

radar," says Sontheimer. "You just wonder when these surprises are going to stop."

Rajewsky and his colleagues, and a second, independent team² led by Thomas Hansen and Jørgen Kjems of Aarhus University in Denmark, focused on a circular behemoth, some 1,500 nucleotides around, that is expressed in the brains of mice and humans. They found that it contains about 70 binding sites for a microRNA called miR-7. MicroRNAs are short fragments of RNA that can block gene expression by binding to and preventing the translation of messenger RNAs. MiR-7 targets have been linked to cancer and Parkinson's disease.

Hansen's team found that expression of the circular RNA blocked the blockers. The activity of miR-7 was suppressed, and the expression of miR-7's target genes increased, presumably because the RNA circle was capturing and inactivating miR-7. Rajewsky's team showed that expressing the circular RNA or deleting miR-7 in zebrafish altered their brain development.

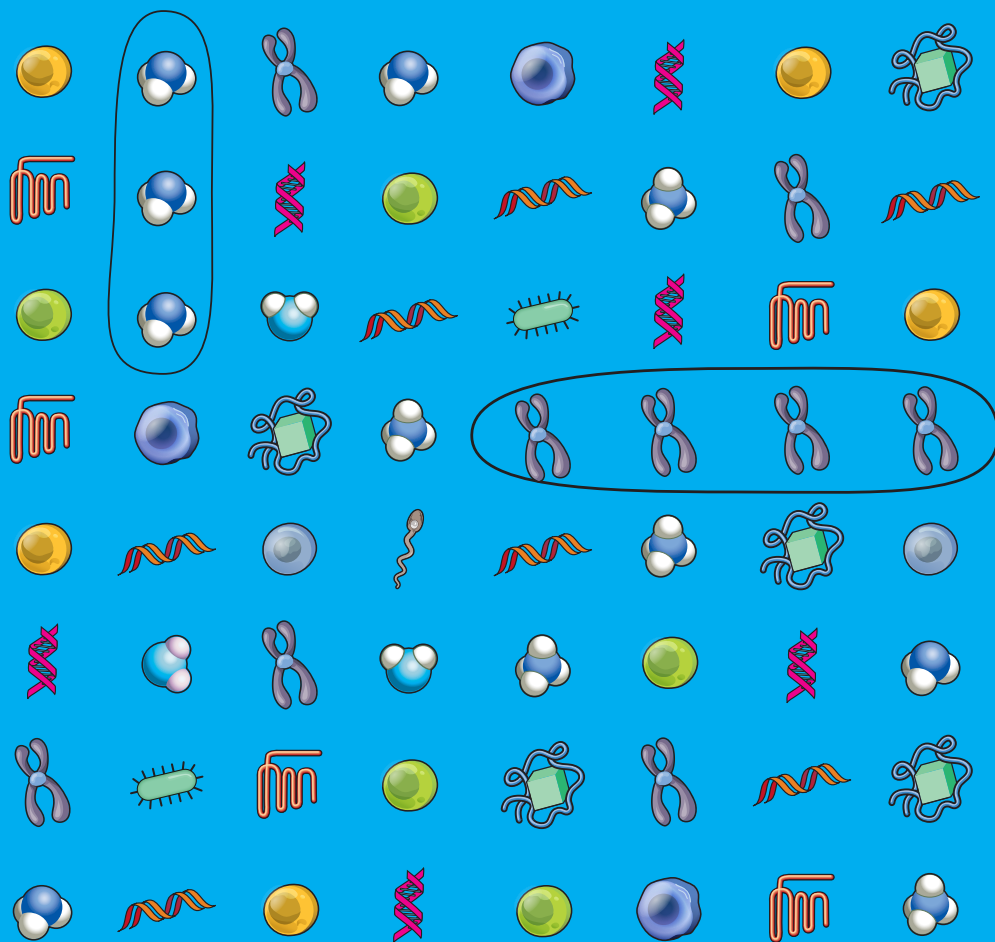
Circular RNAs could also be sponges for microRNA from outside the cell, notes Rajewsky. Some have possible binding sites for viral microRNAs, which can subvert immune responses. Rajewsky hypothesizes that circular RNA could even interact with RNA-binding proteins. Salzman agrees. "They are so abundant, there are probably a multitude of functional roles," she says.

So what other shapes might RNAs take? "I can't think of another form we might have missed," laughs Phillip Sharp, a molecular biologist at the Massachusetts Institute of Technology in Cambridge. "But you know somebody will find one." ■

1. Memczak, S. *et al.* *Nature* <http://dx.doi.org/10.1038/nature11928> (2013).
2. Hansen, T. B. *et al.* *Nature* <http://dx.doi.org/10.1038/nature11993> (2013).
3. Salzman, J., Gawad, C., Wang, P. L., Lacayo, N. & Brown, P. O. *PLoS ONE* **7**, e30733 (2012).

CORRECTION

The News story 'Dark-matter hunt gets deep' (*Nature* **494**, 291–292; 2013) wrongly gave the amount of usable xenon at PandaX as 25 kg instead of 120 kg.



THE 'OMES PUZZLE

Where once there was the genome,
now there are thousands of 'omes.

Nature goes in search of the
ones that matter.

BY MONYA BAKER

Omics bashing is in fashion. In the past year, *The New York Times* and *The Wall Street Journal* have run pieces poking fun at the proliferation of scientific words ending in -ome, which now number in the thousands. One scientist has created a bad-omics generator, which randomly adds the suffix to a list of biological terms and generates eerily plausible titles for scientific papers (example: 'Sequencing the bacteriostaticome reveals insights into evolution and the environment'). Jonathan Eisen, a microbiologist at the University of California, Davis, regularly announces awards for unnecessary additions to the scientific vocabulary on his blog (recent winner: CircadiOmics, for genes involved in daily circadian rhythms).

Botanist Hans Winkler had no idea what he was starting back in 1920, when he proposed the term 'genome' to refer to a set of chromosomes. Other 'omes existed even then, such as biome (collection of living things) and rhizome (system of roots), many of them based on the Greek suffix '-ome' — meaning, roughly, 'having the nature of'. But it was the glamorization of 'genome' by megabuck initiatives such as the Human Genome Project that really set the trend in motion, says Alexa McCray, a linguist and medical informatician at Harvard Medical School in Boston, Massachusetts. "By virtue of that suffix, you are saying that you are part of a brand new exciting science."

Researchers also recognize the marketing potential of an inspirational syllable, says Eisen. "People are saying that it's its own field and that it deserves its own funding agency," he says. But although some 'omes raise an eyebrow — museomics (sequencing projects on archived samples) and the tongue-in-cheek ciliomics (study of the wriggling hairlike projections on some cells) — scientists insist that at least some 'omes serve a good purpose. "Most of them will not make sense and some will make sense, so a balance should be in place," says Eugene Kolker, chief data officer at Seattle Children's Hospital in Washington, and founding editor of the journal *Omics*. "If we just laugh about different new terms, that's not good."

Ideally, branding an area as an 'ome helps to encourage big ideas, define research questions and inspire analytical approaches to tackle them (see 'Hot or not'). "I think -ome is a very important suffix. It's the clarion call of genomics," says Mark Gerstein, a computational biologist at Yale University in New Haven, Connecticut. "It's the idea of everything, it's the thing we find inspiring." Here, *Nature* takes a look at five up-and-coming 'omes that represent new vistas in science.

INCIDENTALOME

Several years before high-throughput sequencing made personal genomes a reality, Isaac Kohane, who studies medical informatics at Boston Children's Hospital, coined the term 'incidentalome' as a warning. The sheer quantity of available genetics information, he predicted in a 2006 article¹, would one day pose a challenge to medicine.

The term stems from 'incidentaloma', radiologists' slang for an asymptomatic tumour that shows up when doctors scan a patient for other complaints. The incidentalome describes the equivalent in human genome analyses: genetic information that no one was looking for. A search for the genetic cause of hearing loss in a child, for example, could turn up hints of future heart problems or a heightened risk of cancer. But who should be told what, and when? In an era in which more and more human genomes are being sequenced, the US National Human Genome Research Institute in Bethesda, Maryland, calls the question of what to tell individuals about their own DNA "one of the knottiest ethical issues facing genomics researchers".

A study last year² revealed the extent of the dilemma. It polled 16 genetic specialists about mutations implicated in 99 common genetic conditions that might show up in large-scale sequencing, whether or not a doctor was looking for them. For some 21 conditions or genes, including well-known sequence variants associated with certain cancers and a heart irregularity, all 16 specialists recommended informing adult patients. But only ten would do the same for Huntington's disease — an untreatable, fatal condition — and there was relatively little consensus on more obscure mutations, or what to tell parents when the variant showed up in a child's sequence.

The biggest problem with the incidentalome is that no one knows what most sequence variants — and there are more than 3 million in every human genome — mean for health. Wendy Chung, a clinical geneticist at Columbia University in New York, is developing

ways to help research participants and patients to choose which genetic results they want to learn. She is also measuring the behavioural and psychosocial impacts of the information. "If you ask people what they want to know about their DNA sequences, everyone initially either says everything, or nothing," says Chung. "When people are thoughtful, there are shades of grey."

As clinical sequencing gains popularity, the definition and scale of the incidentalome is blurring. Geneticists should expect these hard-to-handle results, says Holly Tabor, a bioethicist at Seattle Children's Hospital. "It's somewhat misleading to say that there are incidental results from a genome study. You know that they will be there."

**"BY VIRTUE OF
THAT SUFFIX,
YOU ARE SAYING
THAT YOU ARE
PART OF A BRAND
NEW EXCITING
SCIENCE."**

PHENOME

Human genomes are now easy to come by. What's missing are phenomes: thorough, exact descriptions of a person's every physical and behavioural characteristic. Researchers most want to know about the portion of the human phenome related to disease: facial abnormalities, limb deformities, whether and how people were diagnosed with

depression. And they want those descriptions in a form that computers can read — the better to see how such phenotypic traits might relate to genomes. "I do not know of another word or phrase with which we can say this better," says Peter Robinson, a computational biologist at the Charity University Hospital in Berlin, who is working to standardize such physical descriptions.

Phenome projects are already under way for mice, rats, yeast, zebrafish and the plant *Arabidopsis thaliana*. In the most systematic efforts, scientists knock out genes one by one, then carefully put organisms through a battery of measurements and physical tests to find out how genes shape physical form, metabolism and behaviour. Such comprehensive data cannot be had for human genes, but some clinical researchers hope to pull together a partial resource by carefully collecting patient data.

Even for 'Mendelian' diseases, known to be caused by a single mutated gene, matching up disease and gene is challenging. Of more than 6,000 rare, heritable disorders, fewer than half have been pinned to a genetic cause. One of the hardest parts is finding enough patients with such conditions, which may occur in fewer than one person in one million. "We could probably solve the majority of Mendelian disorders with an unknown cause if we had access to enough well-phenotyped cases," says Michael Bamshad, a geneticist at the University of Washington in Seattle.

But how to compile those cases? Many research and disease communities already have their own long-standing informatics tools and vocabularies to describe fine phenotypic details of various disorders. The challenge lies in getting these resources to work together. If one clinician enters 'stomach ache' and another 'gastroenteritis', patients with very similar symptoms may not get grouped together, explains Richard Cotton, a geneticist at the University of Melbourne in Australia.

In November last year, Cotton was among the scores of interested parties who came together in San Francisco, California, for a meeting called 'Getting ready for the Human Phenome Project'. The major aim of the meeting was to make the exchange of phenotypic data easier. A consortium that focuses on rare diseases, called Orphanet, is leading efforts to get clinicians and

➔ NATURE.COM

To hear more debate on 'omics, listen to the podcast at: go.nature.com/dd4ibo

scientists to agree on 1,000–2,000 standard terms — such as ‘short stature’, which may also be categorized as ‘decreased body height’, ‘height less than 3rd percentile’ and ‘small stature’. “If you agree on the terms, no matter what form you have, we can all be talking about apples and apples and apples,” says Ada Hamosh, a clinical geneticist at Johns Hopkins University School of Medicine in Baltimore, Maryland.

Other researchers are trying to unlock the often idiosyncratic information in electronic medical records so that computer algorithms can comb them and classify common phenotypes automatically. “The data are ugly and sparse, and the magic — the science — is turning that dross into gold,” says Kohane.

INTERACTOME

Biology’s central dogma is essentially a parts list. DNA codes for RNA, which codes for protein. That may give you three basic ‘omes (genome, transcriptome and proteome), but life happens only because these parts work together. A neuron fires and a cell divides or dies because molecules interact. The interactome describes all of those molecular interactions. And in terms of complexity, it is a king of the ‘omes. Just considering one-on-one interactions for 20,000 or so proteins generates 200 million possibilities.

That scope is not daunting to researchers such as Marc Vidal. Before he retires, the 50-year-old systems biologist at the Dana-Farber Cancer Institute in Boston hopes to see a first, rough draft of all the interactions that the genome encodes. Actually, he would be happy with a subset, a catalogue of all the proteins that come together in pairs. “That’s what we’ve been doing for the past 20 years, and we’re almost there now,” he says.

By ‘almost there’ Vidal means that his and a few other labs have observed 10–15% of human protein–protein interactions, based on studies of cells genetically engineered to generate a signal when a pair of proteins comes together. Other researchers have been pursuing the same goal by plucking proteins from crushed cells and seeing which others come along for the ride, scouring the literature and making computational predictions based on protein shapes and the behaviour of related molecules.

It has helped that, more than a decade after the first large-scale interactome study³, researchers are finally starting

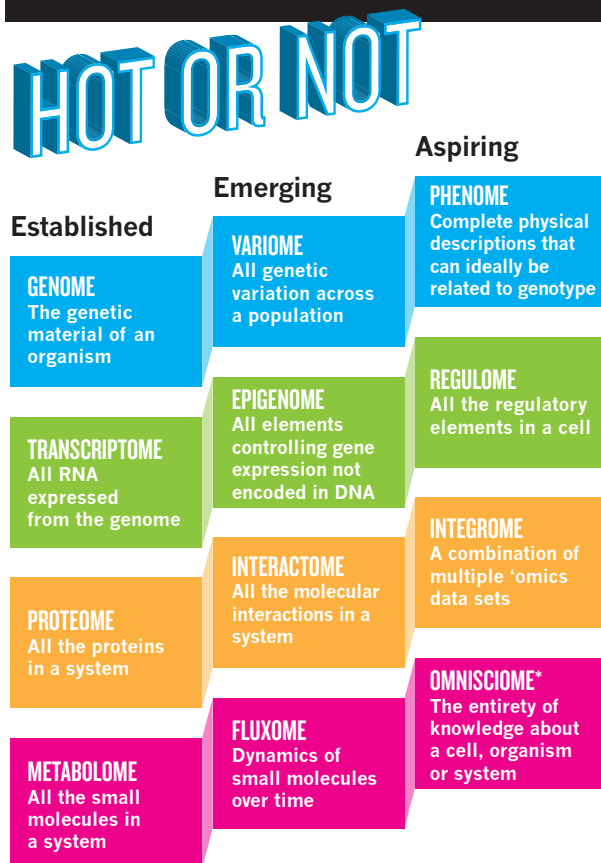
to get a handle on which observed interactions are real and which are artefacts. Making that distinction requires hunting for the same interaction using multiple techniques⁴. But lists do not need to be complete to be useful — and biologists are already beginning to consult the interactome.

Haiyuan Yu, a systems biologist at Cornell University in Ithaca, New York, tested about 18 million potential protein pairs and combed established databases for interactions, eventually identifying 20,614 interactions between 7,401 human proteins. For around one-fifth of these interactions, the team also got a good sense of what parts of these proteins made contact⁵. Yu and his colleagues showed that disease-causing mutations are more likely to be at these points of contact than elsewhere in the proteins. For example, the blood disorder Wiskott–Aldrich syndrome is caused by mutations in a protein called WASP — but only by mutations located in an area that interacts with a second protein called VASP. Patterns that make no sense in terms of genes, says Yu, can become clear when considered in terms of interactions.

Vidal believes that increasingly sophisticated information can be layered into the interactome. First will come fleshed-out basic networks: lists of proteins and their binding partners, ideally annotated by cell types. Next will come descriptive data, such as how long interactions last, the conditions necessary for them and the parts of proteins that make contact.

Vidal imagines a day when clinicians diagnosing a patient will consider not only their genome, but the consequences of all their sequence variants on the interactome — not to mention the influences of the interactome on the phenome. Genomes, after all, are generally static, says Trey Ideker, a systems biologist at the University of California, San Diego. “The sequence is not perturbed by drugs, tissues or other conditions. Interactomes are.”

“I’M MORE
EXCITED ABOUT
THIS TECHNOLOGY
THAN I’VE BEEN
ABOUT ANYTHING
IN A LONG, LONG
TIME.”



*Nature’s proposed addition to the scientific nomenclature.

TOXOME

Thomas Hartung wants to learn all the ways a small molecule can hurt you. To do so, he has organized the Human Toxome Project, funded with US\$6 million over five years from the US National Institutes of Health, plus extra support from the Environmental Protection Agency and the Food and Drug Administration. The -ome suffix, Hartung says, suited the scale of his goal: a description of the entire set of cellular processes responsible for toxicity. “The toxome is very similar to the Human Genome Project because it establishes a point of reference,” says Hartung, a toxicologist at Johns Hopkins Bloomberg School of Public Health in Baltimore.

Toxicity testing in animal studies costs millions of dollars for every compound that enters human trials, yet animal tests sometimes fail to predict toxicity in humans. More than one in six drugs are pulled for safety problems that are discovered during human

trials. Hartung says that the toxome could help to lay out a series of straightforward cell-based assays that could replace animal tests — and perhaps improve on them. Knowing which toxicity-related processes a compound triggers could also help scientists to tweak promising new drugs or industrial molecules into less-harmful versions.

To start with, Hartung wants to expose cells to toxic chemicals and then monitor their metabolomes (the set of all small molecules in the cell) and their transcriptomes. He hopes to piece together the details of pathways in human cells that disrupt hormone signals, poison liver cells, break the heart's rhythm or otherwise endanger people's health. The total number of pathways, Hartung believes, will be perhaps a couple of hundred — a manageable amount for testing toxicities.

The project is still in its early days — making sure that the same assay yields the same results in different labs. Eventually, however, those pathways could be used in cell-based assays to serve as bellwethers of toxicity. “We’d know if we triggered one of those pathways that something bad would happen, and we’d know what that adverse event would be,” says David Jacobson-Kram, who evaluates ways to predict toxicity at the Food and Drug Administration in Silver Spring, Maryland. He warns that a molecule that seemed harmless to cells in culture might behave differently in the body — for example if the liver converted it to a toxin. Nonetheless, he says, the toxome project could save time, money and animals. “Do I think this paradigm has promise?” he asks. “Absolutely.”

INTEGROME

The key to unravelling biology's greatest mysteries depends less on inventing new 'omes, says Kolker, than on combining those that are already there. “One approach won't solve it,” he says. Enter the integrome: information from all the 'omes thrown into one pot for an integrated analysis, along with any other relevant data for good measure. “That's the real deal, it's going to be more and more important,” says Kolker.

Consider Google Maps. Separate lists of petrol stations, restaurants and street names are far less useful than one map showing that a particular petrol station is on the same street as a particular restaurant. But many conventional 'omics studies stop at list-making — genes, proteins or RNA transcripts. These can ignore networks and so may not reveal, for example, that changes in disparate genes actually converge on the same pathway.

Ideker has shown that it is possible to analyse disparate 'omics data automatically⁶. He created software that interrogated four collections of such data for patterns, and then used the results to work out independently what the relevant genes were doing. Not only did the software recapitulate parts of existing genome resources (for instance, identifying components of cellular

THE GOOD, THE BAD AND THE UGLY

Does your 'ome
meet the criteria?

GOODOME

Encapsulates a new focus
(Interactome: all interactions between biomolecules)

Refers to a comprehensive collection (Transcriptome: everything transcribed from DNA to RNA)

Easy to say (Phenome: comprehensive physical characteristics of an organism)

Easy to understand
(Lipidome: all an organism's fatty molecules)

BADOME

Renames existing field
(Nutriome: study of nutrients)

Limited in scope
(Museome: sequenced DNA from objects in museum archives)

Unpronounceable
(tRNome: collection of transfer RNAs)

Obscure
(Predatasome: genes used by predatory proteobacteria while invading other bacteria)

machinery that help to dispose of spent proteins), but it started filling in gaps by finding similar patterns of organization for genes with unknown functions. “We trolled the transcriptome and interactome data and inferred the entire hierarchical structure of the components in a cell,” says Ideker. “I’m more excited about this technology than I’ve been about anything in a long, long time.” Such algorithms will not supplant human data curators, but they can pick up patterns that would be missed by humans or text-mining software that extracts relationships from published papers, he says. “Cells don’t speak English; they speak data.”

Last year, Michael Snyder, a geneticist at Stanford University in California, published his personal integrome⁷ (although he called it an “integrative personal omics profile” — and others dubbed it the narcissome), combining data for his genome, transcriptome, proteome and metabolome (see *Nature* <http://doi.org/hrq>; 2012). The genomic profile revealed that Snyder had a risk variant for diabetes; during the study he was diagnosed with the disease and fought off two viral infections, which were reflected in increased activity of genes associated with inflammation. The 'omes also revealed changes in pathways not previously associated with diabetes or infection, says Snyder. “Had you only followed transcriptome or proteome, you would have only got part of the picture.”

Gerstein agrees that integrated data sets are the way forward. “The future is going to be putting these things together in networks to understand personal genomes,” he says. The word ‘integrome’, however, just doesn’t sit right with him. “What is an integrome? The whole of all integrations? I don’t think so.” Integrate is a verb, he explains. “Most of the other 'omes are collections of nouns.”

McCray has some rules of thumb for what constitutes a useful 'ome word: one that is meaningful, sounds pleasing and is easily understood by an educated audience (see “The good, the bad and the ugly”). But it is unlikely that many scientists will take notice of the rules. The proliferation of words simply reflects the pace of the science, says McCray. Language typically changes slowly, but the rapid spread of the -ome and -omics suffixes is “recapitulating in a decade what normally takes a half century. It speaks to the intense interest and funding in the field.” ■

Monya Baker is a reporter for *Nature* in San Francisco, California.

1. Kohane, I. S., Masys, D. R. & Altman, R. B. *J. Am. Med. Assoc.* **296**, 212–215 (2006).
2. Green, R. C. *et al. Genet. Med.* **14**, 405–410 (2012).
3. Uetz, P. *et al. Nature* **403**, 623–627 (2000).
4. Venkatesan, K. *et al. Nature Meth.* **6**, 83–90 (2009).
5. Wang, X. *et al. Nature Biotechnol.* **30**, 159–164 (2012).
6. Dutkowski, J. *et al. Nature Biotechnol.* **31**, 38–45 (2013).
7. Chen, R. *et al. Cell* **148**, 1293–1307 (2012).

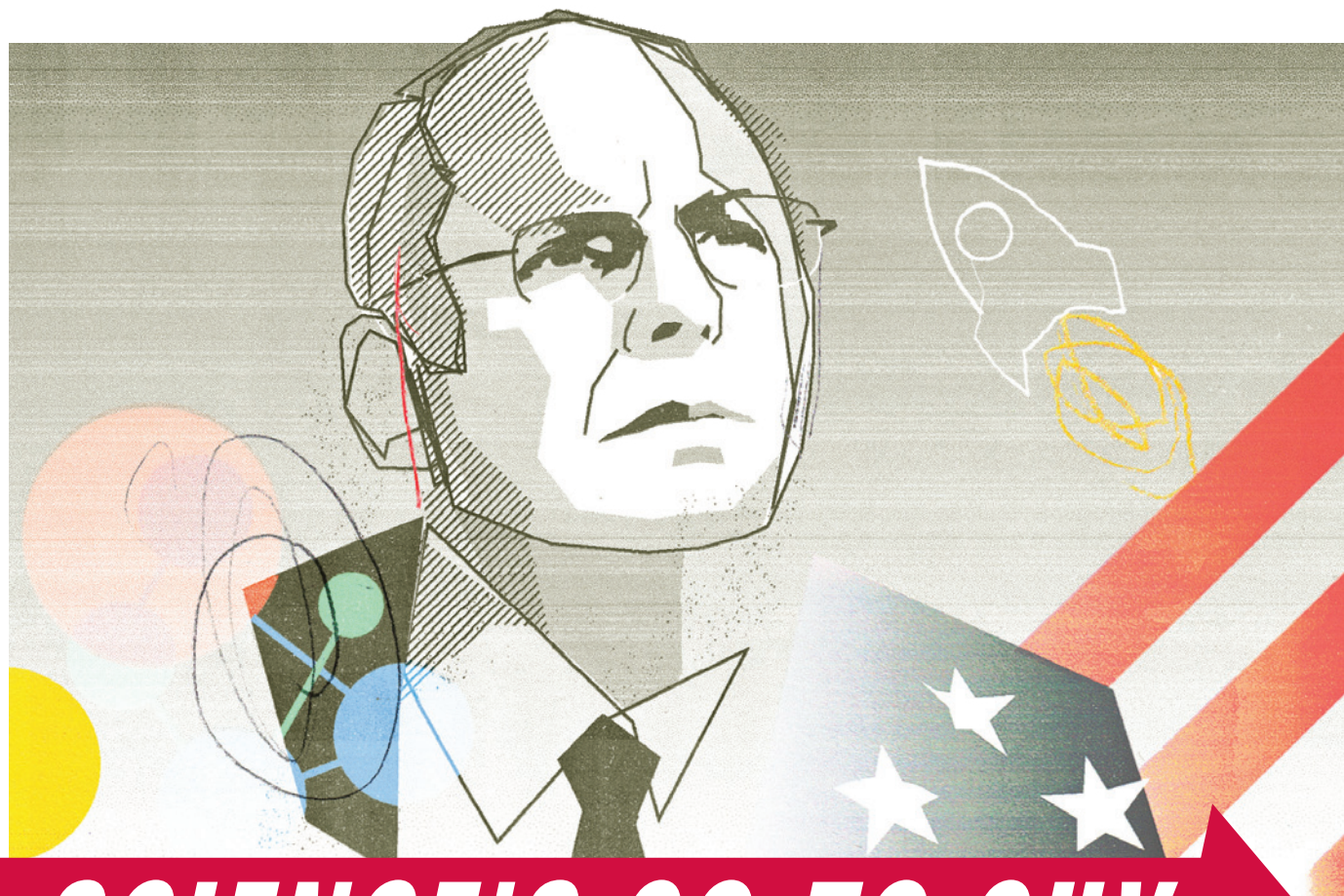


ILLUSTRATION BY PADDY MILLS; BASED ON PHOTO BY PAUL E. ALERS/NASA

SCIENCE'S GO-TO GUY

With the ear of politicians and the respect of researchers, Norman Augustine is the most influential non-scientist in US science.

BY EUGENIE SAMUEL REICH

Of the many requests for advice that stream in from the scientific community, Norman Ralph Augustine says he responds to those that meet one of three criteria: "They're a cause you believe in; they're for a friend; or they'll be fun."

Augustine, 77, says that he got the line from a friend who was advising him on what to do on his retirement as chairman of the aerospace firm Lockheed Martin, back in 1998. He never expected that following the advice would lead him to a new career, as an unpaid adviser to the scientific community. Yet the role meets all three criteria. Augustine enjoys science. He has a lot of friends in science. And it is unquestionably a cause that he believes in.

Science as a cause may sound like a contradiction in terms, and in many ways it is. But the contradiction lies at the heart of the Augustine enigma. The man who has advised NASA on its space programme, three US presidents on science and technology policy and the US Congress on

the urgent need for more science and education funding (see 'Linked in') has largely avoided the critical attention that the scientific community normally turns on its movers and shakers.

It helps that Augustine is not just a tireless advocate for science, but also disarmingly and naturally folksy. In 2010, while testifying to Congress about a study he had led five years earlier on the importance of science and engineering, Augustine suggested off the cuff that cutting science funding to help the economy was like saving an overloaded aeroplane by removing an engine. US President Barack Obama's team liked the analogy so much that the president used the same line to raise a laugh from Congress when he made his own pitch for increasing science funding in his 2011 State of the Union address.

Today, that 2005 study, known as *Rising Above the Gathering Storm* (RAGS), remains one of the most influential science-policy reports in a generation, and it continues to help guide US science spending on science education and research. It also propelled Augustine into an ever-expanding role at the intersection of science and government. Among his many current duties, he leads a panel that reviews science management at the National Institutes of Health (NIH), and one that will appoint a new director for the Fermi National Accelerator Laboratory (Fermilab) in Batavia, Illinois. From health to energy, Augustine "is the go-to person for a fair judgement on a technical matter", says Neal Lane, a physicist at Rice University in Houston, Texas, and former

head of the US National Science Foundation in Arlington, Virginia.

Augustine has his critics. Some say that he sometimes advances policies — for example, easing visa limits on foreign postdocs — that benefit US universities and businesses but harm individual American scientists. “He represents a particular set of views: of the chief executive and scientific establishment,” says Ron Hira, a labour economist at Rochester Institute of Technology in New York.

But with the success of *RAGS* and other Augustine studies, it is not hard to understand why leaders in the US scientific community are increasingly turning to him to head their panels, says David Goldston, a former staff member on the congressional committee that implemented some of the recommendations of *RAGS* and a policy expert at the National Resources Defense Council in Washington DC. “It’s like a popular television show. You want to do the sequel.”

RIISING ABOVE

Although he has earned the respect of scientific leaders, Augustine has never worked in science, does not have a PhD and has limited personal experience doing research. After getting a master’s degree in aeronautical engineering at Princeton University in New Jersey in 1959, he briefly studied gas flows at Douglas Aircraft Company in Long Beach, California, before moving into management.

In the 1960s and 1970s, Augustine bounced back and forth between jobs in the defence industry and increasingly senior positions in the US Department of Defense, reaching undersecretary of the Army in 1975 under then-president Gerald Ford. In 1987, he became chief executive of aerospace company Martin Marietta, and, in that position, helped to broker what was at the time the largest merger of defence aerospace companies in US history, to form Lockheed Martin in Bethesda, Maryland.

From his first research experience, Augustine says he had been aware of science as the source of US industry’s power to innovate, but it wasn’t until he became chief executive of Lockheed Martin that he took that conviction into the political sphere. In 1996, Augustine gathered the leaders of 20 other corporations, including Hewlett Packard, Ford Motor Company and Motorola, to co-author a letter to then-president Bill Clinton about the importance of government spending on basic research.

They sent the letter to *The New York Times*, Augustine says, but the newspaper rejected it. When other papers did likewise, Augustine bought a full-page advertisement in several papers for his letter. He also began to spend time on Capitol Hill promoting basic research.

Through his stints on government advisory panels, Augustine became friendly with Burton Richter, a physics Nobel laureate at Stanford University in California. They paired up, and found that the idea of a joint briefing on the future of the US economy from a former executive and a Nobel laureate proved irresistible even to very busy congressional staffers. “Norm was more of the star,” says Richter. “I was more of the person who could provide specifics — like Batman and Robin.”

In the beginning, Augustine says, many of their victories came in forestalling threatened cuts to science funding. But the pair began to have success asking for more money in 2005, even though President George W. Bush and the Republicans in Congress were pledging to rein in spending. Augustine’s extensive business background may have helped him to win over some of the Republican lawmakers. That year, he, Richter and others garnered bipartisan support for increasing science funding from the two Democratic and two Republican leaders on the Senate and House science committees.

The leaders asked the US National Academies to produce a report on the top ten things that Congress could do to strengthen science and engineering with a view to improving national competitiveness. Sherwood Boehlert, Republican chairman of the House Committee on Science at the time, says that he was delighted when Augustine was picked to chair the National Academy of Sciences panel that put together the *RAGS* report. “I couldn’t have been happier, it was like something from heaven,” he says. “He’s a national treasure.”

Of the 20 recommended actions in the report, the most notable were calls to recruit 10,000 science and mathematics schoolteachers and to increase federal support for basic research, especially in the physical sciences, by 10% per year for 7 years. Both recommendations were welcomed by senior scientists, who saw them as obvious and long overdue.

But some workforce experts found plenty to dislike in the report, including calls to increase the number of visas for scientific workers. Labour economists have found that temporary visas can lead to the offshoring of jobs because businesses can train foreigners in the United States, then keep them on the payroll when they return home. Hira, who was a reviewer of the report, says that these concerns were given short shrift on the panel, which included eminent scientists and university and corporate leaders, but no representatives of US workers, junior working scientists or economists studying their situations.

Hira and others say that those are striking omissions for a panel tasked with discussing the technical workforce. The first version of the report also ended up including at least one major exaggeration: that China graduated nearly ten times more engineers than the United States (600,000 versus 70,000) — a comparison used to argue for increasing the number of scientists and engineers in the United States. But the Chinese data probably included two-year technical degrees whereas the US figure did not. The error “contributed to the alarm quality of the report”, says Michael Teitelbaum, an economist at the Alfred P. Sloan Foundation in New York, who says that he questioned the numbers in his role as a reviewer. “I don’t know of any serious analyst with an open mind who has concluded there are shortages in the science and technology workforce,” he says. In fact, many US scientists and engineers were struggling to find high-quality jobs in academia and industry, a trend that continues today.

The *RAGS* committee had been given an incredibly tight deadline of just 13 weeks. National Academies spokesman Bill Kearney says that the panel operated with much the same rigour as other academy committees. But participants recall some differences from standard procedures. Charles Vest, who served on the *RAGS* panel and is now president of the National Academy of Engineering, says that some of the most compelling facts in the report about the United States being out-competed by other countries came not from careful reviews of economic and science-policy research literature, but from newspaper clippings that Augustine had collected over the years. Not all of those items were fact-checked by academy staff.

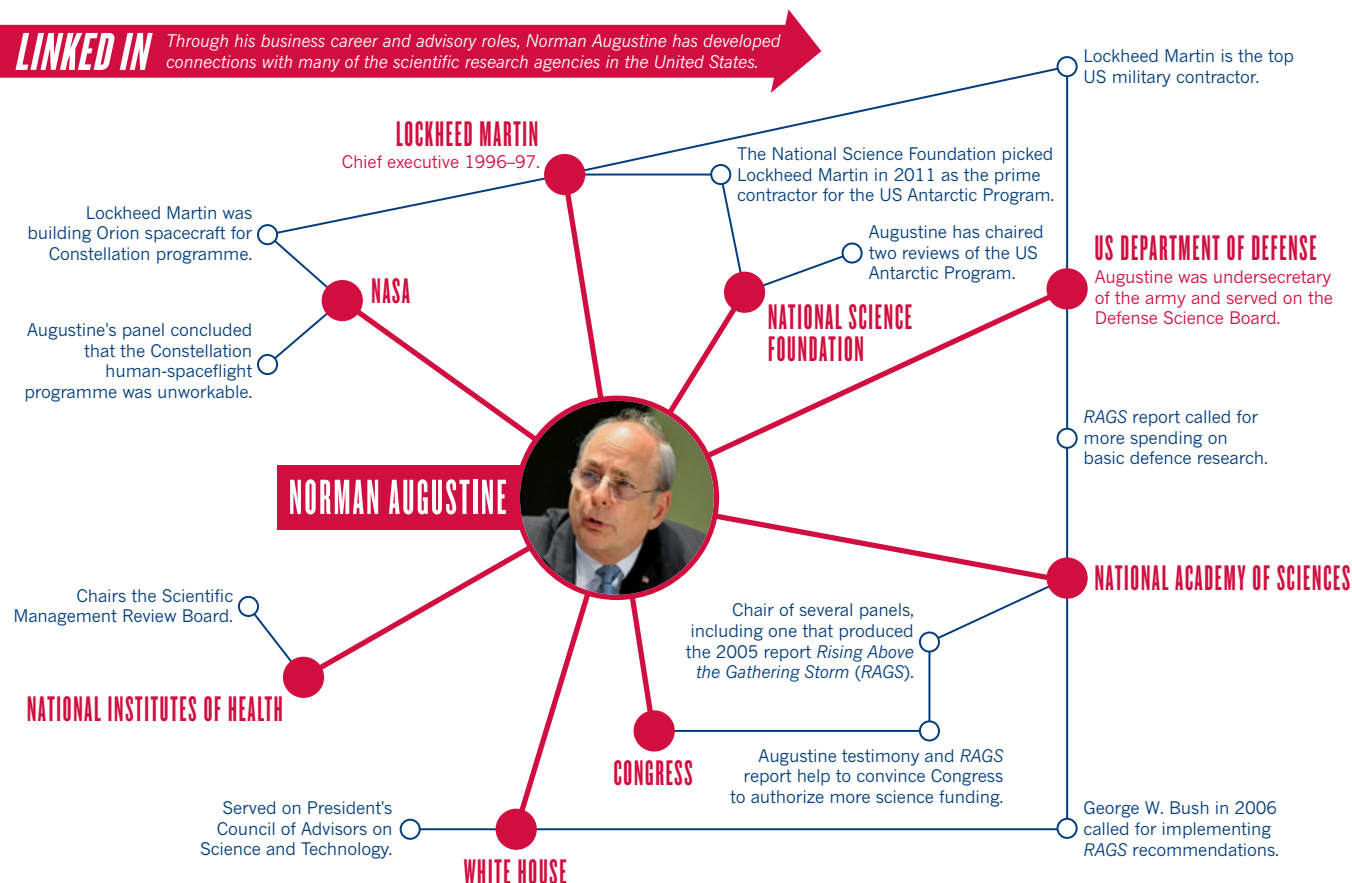
The final version of *RAGS*, released in 2007, corrected the Chinese figures — but by that point the report had already made its mark. The conclusions were roundly welcomed by academic leaders, whose institutions would benefit from the increased funding and influx of foreign students and postdocs.

And it had a much wider impact than that. In his 2006 State of the Union address, Bush announced what he called the “American Competitiveness Initiative”, which took up many of the *RAGS* recommendations as White House policy. A year later, Congress passed legislation called America Creating Opportunities to Meaningfully Promote Excellence in Technology, Education, and Science (COMPETES), which set a goal of increasing research investment in science funding agencies by 10% per year, just as *RAGS* had recommended.

Mike Quear, who helped to draft the America COMPETES legislation as a Democratic congressional staff member, says that the rationale of *RAGS* was understood by Congress and the White House precisely because it had been communicated by Augustine in clear, common-sense terms, without using ideas from economics that could be disputed and without pandering to constituencies such as postdoc unions. “That was Norm’s effectiveness,” Quear says. “He was like a big stone rolling down a hill. No one wanted to get in his way.” When Augustine came to testify on the report, his unscripted remarks were a hit on Capitol Hill. Augustine also cemented his testimony with political friendships. Boehlert says that when Augustine realized that the congressman was a self-described “baseball nut”, he began to quiz him about sports trivia.

“He was like a big stone rolling down a hill. No one wanted to get in his way.”

LINKED IN Through his business career and advisory roles, Norman Augustine has developed connections with many of the scientific research agencies in the United States.



Augustine didn't quit after the legislative victory. When Congress failed to provide funding for elements of the COMPETES act or implement some of his recommendations on school education, Augustine prepared another report, in 2010, just as America COMPETES came up for reauthorization, that called attention to the shortcomings. Those reports continue to carry weight on Capitol Hill, where science agencies have generally fared better in terms of funding than other agencies.

The success of RAGS has brought Augustine invitations to join a wide variety of science advisory boards. Lane says that community leaders who want to get something done turn to Augustine because they know that any report he writes will be read by the right people in Congress. "The chair has to be politically tuned-in," he says — and Augustine is.

Yet Augustine has also been accused of being used by establishment figures to provide external validation for their plans. For example, he leads the NIH Scientific Management Review Board, which was asked in 2010 to assess plans for a new translational research centre. Francis Collins, the NIH chief, was pushing hard for the centre — but many researchers were worried about Collins's proposal to dismantle the National Center for Research Resources (NCRR), which oversees important elements of US research infrastructure, to make way for his brainchild.

Jeremy Berg, director of the National Institute of General Medical Sciences and a member of the review board at the time, e-mailed Augustine, warning that the reputation of the board would be damaged if it didn't assert its independence from Collins and take a hard look at the implications of abolishing the NCRR. Three days later, however, the board voted through Collins's plan with little examination of what might happen to the NCRR. "I never heard from Norm," says Berg, the only person on the board who opposed the creation of the translational medicine institute. Augustine says that the board heard from a number of stakeholders before reaching its decision.

But the unease that some researchers felt about the swiftness of that reorganization points to another concern about Augustine's advisory work. His background leads him to view scientific organizations from a

business model, a perspective that can conflict with the way that science actually works. Research is often economically unproductive, for example, and the aims of university and government leaders do not always align with the needs of working scientists. Some organizations seeking Augustine's advice have therefore brought in other experts to complement his outlook. Last year, Augustine and Teitelbaum co-chaired a National Academy of Sciences panel on the defence science workforce to produce a more nuanced report than the discussion in RAGS. Yet nothing has swayed Augustine from the same basic conclusion he reached long ago: "If America wants to compete, it needs to double the research budget — in which case more scientists will be needed."

To those who say that he simply supports the scientific establishment, Augustine counters that he is independent enough to say what he thinks. And he has demonstrated that before. In 2009, a panel that Augustine chaired for NASA concluded that the agency could not complete the Constellation human-spaceflight programme, which upset NASA leaders and possibly his former colleagues at Lockheed Martin, a major space contractor. More recently, public accountability watchdogs complained that Augustine should not have been chosen to review a controversial fracking study at the University of Texas at Austin because he had been on the board of the oil and gas company ConocoPhillips in Houston, Texas. Yet in December, Augustine's panel issued a bruising critique of the study. Indeed, it is difficult to predict from Augustine's private interests how he will vote on any given topic.

But friends say that there is one thing they can predict: Augustine's recommendations will be motivated by a strong sense of patriotism. His love of science stems from his devotion to country, from his sense of science's place in the nation and in the global economy, which is precisely why his words have traction with politicians. "It's incorrect to refer to Norm as an advocate for science," says Vest. "He's an advocate for what he thinks the United States needs." ■

Eugenie Samuel Reich is a correspondent with *Nature* in Boston.

BOB GATHANY, THE HUNTSVILLE TIMES/AP

COMMENT

NEUROSCIENCE Researchers and designers should make brain games **p.425**



ARCHITECTURE Ersatz new cities overlook local genius **p.427**

THEATRE Does a lean new version of Brecht's idealistic *Life of Galileo* work? **p.428**

CREATIVITY Opportunities for scientific genius are nowhere near exhausted **p.430**

MAXWELL MACKENZIE/NAS



The US National Academy of Sciences has a long history of advising the nation on a range of scientific issues.

Move with the times

The US National Academy of Sciences has to become more nimble and responsive if it is to survive another 150 years, says **Marjory S. Blumenthal**.

In 1987, I became the executive director of the Computer Science and Technology Board at the US National Academy of Sciences (NAS) in Washington DC, charged with building and managing the new unit. I was to work to: develop and assure the quality of reports, which compile expert advice by the board on various issues in information technology (IT); build a portfolio of projects; and, in time, hire staff to work with committees under the board's aegis.

During my first weeks on the job, reality set in. I was told that three previous boards

dedicated solely to IT issues had been shut down. One had run out of funding, one had run out of ideas for new reports and the other had run out of both. Three years later, a telecommunications board with roots in the 1960s failed to secure funding from the US government and was absorbed by my group, which since then has been known as the Computer Science and Telecommunications Board.

These cautionary tales haunted me throughout my 16-year tenure at the NAS. And the day-to-day realities of developing,

conducting and overseeing 'academy studies' has taught me that support for the academy is not guaranteed, and that if its components don't stay useful and competitive, they are unlikely to survive.

This concern has never been more acute. The NAS, the first independent body to provide the US government with advice on science (natural and social), engineering and medicine, turns 150 on 3 March. In 2011, it received more than US\$320 million from private donors and federal funding, the latter being its main source of revenue. But ►

► today, information, even from experts, is much more available and spans a greater range of topics. Venerability is not as compelling as it once was. As politics become more contentious, policy-makers are seeking faster advice, and organizations that offer advice are proliferating.

Twenty-first-century realities demand that the NAS provide expert advice more quickly and do better at explaining its value. If not, then much of the organization could go the way of those ill-fated computer and telecommunications boards.

ADDED VALUE

The premium NAS product is the committee-study report. It is valuable because of the balance of expertise that goes into its drafting and rigorous review. The beauty of the academy is that it brings together experts with varied backgrounds and opinions to create an unbiased set of recommendations.

But reports often take at least 2 years to produce — and thus many are faulted for being slow or late. There are numerous reasons why they take so long; most stem from the standard process to develop them.

Typically, a government organization asks for input on an issue (sometimes one suggested by an NAS board) — for instance, what is cybersecurity, why is enhancing it hard and what can be done to improve it. NAS staff then develop a project proposal and associated budget, and compile a slate of volunteer experts (usually from academia and industry) who provide a range of perspectives and opinions on the problem. After meetings and discussions, the committee is expected to come to a consensus. Projects have tentative deadlines, and how well they are met depends on the interactions among committee members, the committee chair and the staff.

The process involves multiple layers of expert review and approval: of project proposals (including budgets), committee nominations and draft reports. Plus, there are many layers of internal review — for

instance, boards are overseen by divisions, the next tier in the hierarchy. This is great for quality assurance — all of the 60 or so reports in which I was involved benefited from the review — but it is time-consuming. There are a great number of steps and each one depends on external, volunteer experts who typically have busy lives and fit in their committee (or board or division or report-review) service as an ‘extra-curricular’ activity. The odds of every participant doing his or her job on time are low. Furthermore, coming to consensus takes time.

For example, the project that produced *Signposts in Cyberspace* (2005), a report about how to assign domain names to new websites, was a perfect storm of challenges. The project was slow to launch owing to delays in government funding and difficulties in finding neutral experts. Designating a website .com, .org or any of a number of terms might seem like a simple task, but these labels serve a gating function for how individuals or entities represent themselves online. The associated cauldron of technical, commercial, political and advocacy issues, which continues to boil, made composing a committee and finding a neutral chair particularly hard.

The report — which recommended ways to add to the stock of ‘top-level domains’ such as .com, and other improvements — took 7 years to produce after the congressional request. Although the committee’s emphases and arguments evolved over time to maintain relevance, those who disagreed with the report invoked lateness as a criticism.

FIVE CHANGES

The NAS could overcome this internal bureaucracy and hold its own against external competition by making five changes:

Streamline its structure. The organization should eliminate unnecessary internal review. For instance, some boards can manage their own project development, so do not require oversight from divisions.

Empower staff. They can help to complete reports quickly. This may involve negotiating more effectively with experts who are not meeting their deadlines, or even contributing more to the writing. The key is to lessen the time that staff spend waiting passively for volunteer input. In some parts of the academy, such as the

Institute of Medicine, that approach already works well.

“Twenty-first-century realities demand that the NAS provide expert advice more quickly and do better at explaining its value.”

Make meetings more effective.

Projects may meet as frequently as every four weeks. Cutting back on meetings is very

hard to do well, because the purpose of the NAS is to bring together experts with different points of view, making consensus difficult and time-consuming. But on some projects, I was able to forge a consensus with one big meeting and a series of smaller ones, which probably saved at least 6 months.

Experiment with technology. Committee members and staff could, for example, use blogs, wikis and other social media to share and respond to what is being generated. The NAS could even make some tools public so that people beyond the board can provide input, along with a system that enables the academy to distil out high-value comments with ease. Technology may also help to bring in more international experts, transcending the challenge of funding and organizing face-to-face meetings. This would render the advice of the organization more pertinent for a global audience.

Act as a clearing house. The tradition of layering expertise and balancing biases suggests that the NAS could be an ideal host for structuring, motivating (including by finding ways to give credit) and vetting science and engineering opinions that could come from either known expert communities or from a more varied and diffuse set of participants.

Although there is now more competition than there was 150 years ago, other organizations that offer expert advice tend to be staffed by advocates who are trying to advance a particular point of view. The NAS must become more vocal in explaining why its processes work, and it should experiment with alternative ways to produce high-quality, authoritative and unbiased analysis. A major anniversary is a great occasion for an innovation initiative of its own. ■

Marjory S. Blumenthal is associate provost at Georgetown University in Washington DC. e-mail: blumentm@georgetown.edu



President Abraham Lincoln at the signing of the academy's charter in 1863.

ILLUSTRATION BY ANDY MARTIN



Games to do you good

Neuroscientists should help to develop compelling video games that boost brain function and improve well-being, say **Daphne Bavelier** and **Richard J. Davidson**.

In the month after its release, the video game *Call of Duty: Black Ops* had been played for the equivalent of 68,000 years worldwide. Children in the United States played an average of 1 hour and 13 minutes of video games every day in 2009 — a nearly threefold increase from 10 years earlier¹. And people of all ages are playing. Only 18% of US gamers are under 18 years old; nearly one-third are over 50.

Video games are associated with a variety of negative outcomes, such as obesity, aggressiveness, antisocial behaviour and, in extreme cases, addiction². At the same time, evidence is mounting that playing games can have beneficial effects on the brain.

After spending an hour a day, 5 days a week for 8–10 weeks spotting snipers and evading opponents in shooter games such as *Call of Duty* or *Unreal Tournament*, young adults saw more small visual details

in the middle of clutter and more accurately distinguished between various shades of grey³. After 10 hours stretched over 2 weeks spent chasing bad guys in mazes and labyrinths, players were better able to rotate an image mentally⁴, an improvement that was still present six months later and could be useful for activities as varied as navigation, research chemistry and architectural design. After guiding small rodents to a safe exit amid obstacles during a version of the game *Lemmings* that was designed to encourage positive behaviour, players were more likely in simulated scenarios to help another person after a mishap or to intervene when someone was being harassed⁵.

Because gaming is clearly here to stay, some scientists are asking how to channel people's love of screen time towards positive effects on the brain and behaviour by designing video games specifically intended

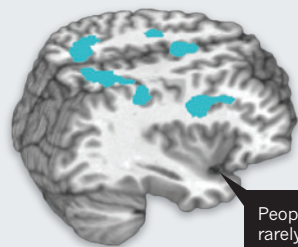
to train particular aspects of behaviour and brain function. One game, for example, aims to treat depression by introducing cognitive behavioural therapy while users fight off negative thoughts in a fantasy world⁶. In *Re-mission*, young cancer patients blast cancer cells and fight infections and the side effects of therapy — all to encourage them to stick with treatment (see www.re-mission.net).

Last year, we and other scientists studying the brain met entertainment-media experts to discuss ways of using interactive technology such as video games to further our understanding of brain functions and to provide new, engaging rehabilitation tools, in particular for boosting attention and well-being. The meeting was hosted by the White House Office of Science and Technology Policy and sponsored by the US National Science Foundation (see go.nature.com/t9mvqc).

BRAIN GAME

When searching for a particular object in a sea of shapes, people who played video games regularly showed less activation of the brain regions linked to attention, a sign that their brains were performing the task more efficiently.

● Brain networks associated with attention



People who rarely played video games



People who played at least 5 hours of action video games per week

To make the sort of video games that might one day improve empathy and positive social interaction, or decrease anxiety and sharpen attention, the developments outlined below will be necessary.

EXPLORING THE BRAIN

First, game designers and brain scientists must determine which game components foster brain plasticity, to guide the design of tomorrow's video games. This is not intuitive. For instance, playing hours of action video games seems to have no effect on players' ability to react reflexively to loud noises, even though that type of attention is frequently solicited during the game³. By contrast, action gamers are better able to deliberately allocate their attention to one part of their environment, ignoring other sources of distraction (see 'Brain game'). This is a quality known as attentional control, and is not obviously associated with chasing zombies³.

Another key challenge is to map the effects of video games in the brain, because many overlapping skills are called on during even a few seconds of gaming. Neuroscience is still in its infancy when it comes to mapping complex behaviour, but video-game designers could create controls that help researchers to systematically vary how much of each skill is needed during gameplay, enabling them to map the corresponding brain circuit.

WORKING TOGETHER

Second, the next generation of neuroscientists must collaborate better with the games industry. Universities could facilitate links by creating new multidisciplinary programmes that subvert rigid departmental boundaries and bring together experts ranging from artists and psychologists to programmers and neuroscientists. Stronger links to professional game designers would also facilitate the development of therapeutic games that people actually want to play as much as *Call of Duty*.

The games industry could help tremendously by adding brain scientists to their teams. These researchers could assist the

industry in enhancing players' experience, while gaining insights into players' behaviour by studying the industry's large gameplay records, which track players' actions and responses to various game components. Every year, Valve, a game company based in Bellevue, Washington, involves a psychology graduate student from the nearby University of Washington in Seattle in their gameplay research.

GETTING TO MARKET

Third, experts must develop a path for academics to bring potentially therapeutic games to market, similar to the translational process that takes drugs from the lab to the clinic. No such path exists for games, but some academics are trying. For example, neuroscientist Adam Gazzaley and his colleagues at the University of California, San Francisco, have developed a game to ameliorate age-related decline in attention, by asking adults to play a driving game in which they avoid various distractions along the way. Before and after playing, the researchers measure a player's brain function and test their ability to resist distraction.

Gazzaley is a founding adviser to a new company — Akili Interactive Labs in Boston, Massachusetts, for which one of us (D.B.) serves on the advisory board — that aims to pursue the development, large-scale validation and commercialization of this game to improve resistance to distraction.

EXPERIMENTAL DESIGN

Finally, those in the field should recognize that researching the impact of gaming on the brain is inherently difficult. Presenting a video or computer game to a participant in a research study necessarily requires that they are aware of the intervention. We must therefore develop standards to evaluate the impact of gaming on brain and behaviour

to avoid false claims of benefits. Control interventions should be matched to the experimental version on as many variables as possible, including the amount of game-playing, the difficulty level and the interest value. Placebo controls are not possible, so optimal designs probably involve having several comparison groups, including an active gameplaying comparison and perhaps other, more typical interventions, such as drug therapy. And even if participants are not blinded, experimenters should be.

It is important to note that even if experts can design a new breed of video games that benefit brain function, it will not provide a carte blanche for video-game bingeing. Exposures that show beneficial effects — 5 hours of gaming per week for 2–10 weeks — are a fraction of the time that most young gamers play. And violent, negative content can have detrimental effects on social and emotional skills, calling for much caution⁷. An important challenge for both academics and the games industry is to collaborate on the development of games as compelling as those in which many young people now indulge, but that help to cultivate positive qualities such as empathy and cooperation^{8,9}.

Gradually, this work will begin to address the burning social question of how technology is having an impact on our brains and our lives, and enable us to make evidence-based choices about the technologies of the future, to produce a new set of tools to cultivate positive habits of mind. ■

Daphne Bavelier is in the Department of Brain and Cognitive Sciences, University of Rochester, Rochester, New York 14627-0268, USA, and the Department of Psychology and Education Sciences, University of Geneva, Switzerland. **Richard J. Davidson** is at the Center for Investigating Healthy Minds, University of Wisconsin, Madison, Wisconsin 53705-2280, USA.
e-mails: daphne@bcs.rochester.edu; rjdavids@wisc.edu

1. Rideout, V. J., Foehr, U. G. & Roberts, D. F. *Generation M²: Media in the Lives of 8- to 18-Year-Olds* (Kaiser Family Foundation, 2010); available at go.nature.com/sb7pjp.
2. Strasburger, V. C., Jordan, A. B. & Donnerstein, E. *Pediatrics* **125**, 756–767 (2010).
3. Green, C. S. & Bavelier, D. *Curr. Biol.* **22**, R197–R206 (2012).
4. Feng, J., Spence, I. & Pratt, J. *Psychol. Sci.* **18**, 850–855 (2007).
5. Greitemeyer, T. & Osswald, S. *J. Pers. Soc. Psychol.* **98**, 211–221 (2010).
6. Merry, S. N. et al. *Br. Med. J.* **344**, e2598 (2012).
7. Bavelier, D., Green, C. S., Han, D. H., Renshaw, P. F. & Merzenich, M. M. *Nature Neurosci.* **12**, 763–768 (2011).
8. Davidson, R. J. & McEwen, B. S. *Nature Neurosci.* **15**, 689–695 (2012).
9. Klimecki, O. M., Leiberg, S., Lamm, C. & Singer, T. *Cerebral Cortex* <http://dx.doi.org/10.1093/cercor/bhs142> (2012).

D. B. declares competing financial interests: see go.nature.com/jmunrh for details.



The replica Eiffel Tower in the suburb of Tianducheng in Shanghai, China.

URBAN PLANNING

Monumental knock-offs

Mike Davis on a chronicle of four ‘instant’ cities modernized by mimicking the West.

In 1914, Patrick Geddes arrived in Madras, India, in the waning phase of a plague pandemic that had killed 10 million people on the subcontinent. Geddes, a pioneer of urban planning from Scotland, had been invited to lecture on his ideas and, later, to evaluate the government’s draconian proposal to ‘sanitize’ cities through slum clearance, street widening and the installation of public latrines.

Geddes did something surprising. After four years visiting dozens of cities across India, he produced a series of reports extolling the superiority of native urbanism over British *idées fixes*. He concluded that the official sanitation crusade was a huge threat to the cultural and environmental foundations of Indian town life. He prescribed “conservative surgery”: providing communities with the resources to cleanse and repair themselves, improve rather than remove slums, and plant gardens in demolition sites. He advocated collecting human waste and trenching it in public vegetable and fruit gardens, rather

than dumping it into streams or latrines.

His ideas achieved small-scale successes in Lucknow, Baroda and Indore. The larger urban-reform movement in India collapsed after the First World War, in part because of the immense cost of building New Delhi on an imperial scale.

Geddes was not an anti-modernist; indeed, he was an enthusiast for concrete and electricity. But he rejected the hubris of British engineers who, ignorant of local ‘webs of life’, proposed for India the same drastic palliatives that had been applied to industrial British cities such as Liverpool and Glasgow. Geddes’ work poses an enduring question: why do politicians, bankers and developers



A History of Future Cities
DANIEL BROOK
W. W. Norton: 2013.
480 pp. \$27.95

continue to ignore the local genius of non-Western architectures and urban life, and promote generic urban modernity?

This is a question that Daniel Brook should have tackled in *A History of Future Cities*, his fascinating parallel social histories of St Petersburg, Shanghai, Mumbai and Dubai as deliberately constructed facsimiles of the distant modernities of Amsterdam, London and Las Vegas. These ‘instant’ cities are light years away from the tinkering, incremental urbanism advocated by Geddes, which thrives today in self-built slums. The global middle classes, especially in Asia, seem to prefer theme-park cities with replicas of the Eiffel Tower (in Tianducheng, a suburb of Shanghai) and gated subdivisions copied from *The Real Housewives of Orange County* (in Ju Jun, for example, near Beijing).

Brook is undismayed by the popularity of simulated landscapes and monumental knock-offs. Unlike Geddes, he does not see urban conservation as the precondition ▶

► of modernization. Authentic modernity, Brook argues, is usually the conquest and transformation of a copy of somewhere else. From a historical perspective, “impersonation is often just a first step, not a final destination in a place’s development”. To illustrate this thesis, he traces the “idea of Dubai” back to the building of St Petersburg as a copy of Amsterdam, and later through Shanghai and Bombay (now Mumbai) as artificial iterations of English cities.

My experience of reading this book, however, would have been much happier without the introduction. In it, Brook, in my view, depicts sophisticated Chinese and Indian civilizations almost as if they were stunned hunter-gathers seeing iron tools for the first time: “to their Chinese and Indian inhabitants these strange new buildings and the cosmopolitan cities themselves were, by turns, confusing, threatening, and inspiring.” Likewise, Brook’s assertion that “the idea of Dubai ... is the idea of our time: the Asian Century, which is also the Urban Century” would make a good slogan for the side of an Emirates passenger jet; but I dread to think that a debt-ridden absolute monarchy exploiting foreign labour might be the shape of things to come.

Once past the clichés, the studies of St Petersburg, Shanghai and Bombay begin to grip (Dubai is too recent a phenomenon and fits awkwardly into the narrative structure). Brook describes how imposed modernity, combined with epic inequality, eventually triggered three-way struggles between the colonial or autocratic state, an aggressive and modernizing local bourgeoisie, and radical labour movements anchored in the new factories. Such conflicts, albeit occurring at great human cost, generated the extraordinary, if brief-lived energies of avant-garde Leningrad, Jazz Age Shanghai and Art Deco Bombay.

Will history repeat itself in a similar pattern in Dubai, Abu Dhabi, New Songdo or others of today’s instant cities? I think that such a question is equivalent to asking what time the revolution will begin in Las Vegas, the utopia of tack. Brook tends to confuse cosmopolitan modernity with malls, skyscrapers and theme parks, especially with the strange claim that “Dubai represents the world as it is”. Rather than searching to “catch the glimpses of utopia within the dystopia”, as he recommends, I think it would be more fruitful, as Geddes advised, to focus on the solidarities and practices of daily life. ■

Mike Davis is a writer and urban historian based in San Diego, California. e-mail: michael.davis@ucr.edu



Ian McDiarmid plays the title role in Mark Ravenhill’s new translation.

ARTS

Reinventing Galileo

Philip Ball weighs up an exuberant Royal Shakespeare Company production of Bertolt Brecht’s *Life of Galileo*.

It is one of the central works of drama about science, and one of the most controversial. Bertolt Brecht’s *Life of Galileo* has been criticized for misrepresenting history, science and Galileo Galilei himself, with some validity. The real question, however, is whether the play works, theatrically and psychologically.

Shakespeare, after all, took vast liberties with history, yet such is his way with human portraiture that no one complains. Shakespeare and Galileo were born within a few weeks of each other in 1564 — a coincidence that the Royal Shakespeare Company (RSC) understandably makes much of for its latest production of Brecht’s play. More significantly, the play shows Brecht at his most Shakespearean, with Galileo the wily, tragically compromised sensualist redeemed by self-insight that others lack — he is, as Adam Gopnik suggested in a recent article in *The New Yorker*, a kind of intellectual Falstaff.

The exuberance and wit of this production owe much to the new translation by RSC writer-in-residence Mark Ravenhill. Ravenhill has commented on the “comic sensibility in Brecht’s language which I think [is] often overlooked”, but which he and director Roxana Sibert have found in abundance. In the title role, Ian McDiarmid is sly and worldly yet succeeds in pulling off the crucial feat of making Galileo loveable. It is with the basic fabric of the play, not its realization, that the questions lie.

In retrospect, we can see that Brecht set himself an impossible task, because even now

there is no consensus on Galileo. Many scientists still prefer the narrative that prevailed when Brecht first wrote the play in 1937–39, of a martyr

persecuted by the Catholic Church for his pursuit of truth about the arrangement of the cosmos. A more measured view now holds, recognizing that a less pugnacious man might have navigated the currents of the papal court more skilfully. It is certainly not to excuse the bullying, dogmatic church to point out that Galileo’s evidence for a heliocentric Universe was equivocal and in some respects (his interpretation of the tides) wrong.

Galileo’s mathematical approach, rightly adored by physicists today, was not, as some older science historians had it, the right way to do science. It was the right approach for celestial and terrestrial mechanics, but useless for chemistry, botany, zoology and much else. And although Einstein claimed that Galileo’s rejection of logical deduction devoid of empirical input was essential to modern science, that rejection did not begin with Galileo.

Brecht must take some blame for making Galileo seem more original than he was. He fell for the idea of a scientific revolution in which great men begin thinking in a totally new way. Complaints about historical accuracy could seem carping when appraising a work of art, but Brecht himself attested of the first version of the play that “I was trying here to follow history”. Brecht was in any case

A Life of Galileo

DIRECTED BY ROXANA SILBERT
Swan Theatre,
Stratford-upon-Avon,
UK.
Until 30 March 2013

disingenuous, because that original version was evidently informed by, and widely interpreted as a comment on, the political climate of the time. Brecht fled Nazi Germany after the Reichstag fire in 1933, and his cunning Galileo who subverts the ideology of the authorities — recanting on heliocentrism in order to continue his work in secret — was regarded as a symbol of anti-Nazi resistance.

That, however, is not the Galileo of the revised 1947 version — the one most often performed, and used here. Although Brecht was already reworking the play in 1944, the bombing of Hiroshima and Nagasaki transformed his view of scientists. “Overnight the biography of the founder of the new system of physics read differently,” he wrote. He felt that the Manhattan Project scientists had betrayed their moral obligations, and criticized even Einstein as a politically naive “eternal schoolboy”. Regardless of the merits of that view, it is the play’s downfall.

Now Galileo, confronting his former student Andrea, launches into a diatribe on how, by focusing on science for science’s sake, “you might jump for joy at some new achievement, only to be answered by a world shrieking in horror”. Nothing in Galileo’s former conduct has prepared this (anachronistic) concern about the social applications of science, leaving us with a confusing portrait.

On 30 October 1947, when the new version premiered, Brecht got a taste of Galileo’s ordeal: he testified before the US House Committee on Un-American Activities. He left for Europe the following day, accused of having compromised artistic freedom and with perhaps a keener appreciation that ideological interference in art and science is not confined to dictatorships.

Brecht’s other impossible task was to explain how science is done. He succumbs to the view that you just need to think clearly, believe your eyes and trust in reason. He then has to skirt around the problem that your eyes tell you that the Sun, not Earth, moves. What’s more, philosophers such as Paracelsus and Bernardino Telesio had been relying on experience, rather than on Aristotle, for a hundred years before Galileo, but had reached rather different ‘truths’. Nor was there any ‘scientific method’ in Galileo’s time, just as there is none today: the ad hoc combination of hypothesis, assumption, experiment, theory, logic and intuition will not reduce to any formula.

The RSC’s production is spirited and visually inventive. But the play itself is pulled between too many irreconcilable poles to make a coherent whole. It is perhaps the history of the play, rather than the text itself, that reveals the most about the difficult relationship between science and the cultures in which it is embedded. ■

Philip Ball is a writer based in London.
e-mail: p.ball@btinternet.com

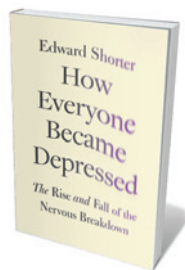
Books in brief



The Future: Six Drivers of Global Change

Al Gore RANDOM HOUSE 592 pp. \$30 (2013)

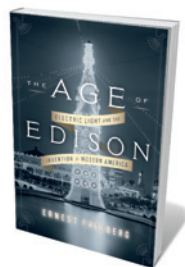
Seven years on from his climate-change documentary *An Inconvenient Truth*, Al Gore takes on six planetary paradigm shifts. The former US vice-president pulls few punches in analysing economic globalization, the balance of power, the Internet, population and resources, biotechnology and digitization, and environmental crises. The idea that Net-based “public squares” could add significantly to the democratic process may be optimistic. But Gore’s data synthesis impresses — as do his cogent critiques of scientific and political myopia, such as the corrosion of self-governance by market forces.



How Everyone Became Depressed: The Rise and Fall of the Nervous Breakdown

Edward Shorter OXFORD UNIVERSITY PRESS 272 pp. \$29.95 (2013)

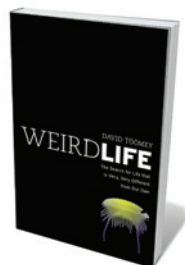
Historian of psychiatry Edward Shorter wonders at the disappearance of ‘nerves’ from psychiatry, arguing that today’s classification of mood disorders is deeply problematic. Data from the US National Center for Health Statistics for 2005–08, for instance, showed that more than 22% of US women were on antidepressants. To rationalize treatment, Shorter calls for a relabelling of major depression as “melancholia”, and more acuity in seeing that many ‘depressives’ actually suffer from whole-body nervous conditions.



The Age of Edison: Electric Light and the Invention of Modern America

Ernest Freeberg PENGUIN 368 pp. \$27.95 (2013)

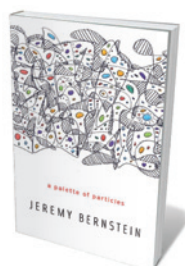
American geekery had a shining moment in 1879, when Thomas Edison unveiled the incandescent light bulb. The invention literally electrified the country, drawing rural residents to the bright lights of the burgeoning cities and illuminating surgeries, fairgrounds and more. But as Ernest Freeberg’s history shows, Edison was no lone genius: funding, patenting and a science-savvy public all played a part in his invention of modern research and development. As for the dazzling bulb, we are still grappling with its energy-guzzling ways.



Weird Life: The Search for Life That Is Very, Very Different from Our Own

David Toomey W. W. NORTON 288 pp. \$25.95 (2013)

At least 30 billion species have inhabited Earth, David Toomey tells us — each extraordinary in some way, like the extremophile bacteria that cluster at sea-floor vents. Yet all arose from a single ancestor. Toomey leads us into a speculative world of life outside that singular club. We visit the “shadow biosphere” of as-yet-only-imagined microbes posited by astrobiologists; the possibility of microbial life in Venusian clouds; doppelgangers in the multiverse; and much, much more. Weird indeed, and not a little wonderful.



A Palette of Particles

Jeremy Bernstein BELKNAP 224 pp. \$18.95 (2013)

Physicist Jeremy Bernstein pays homage to the subatomic, tinting particles according to era of discovery. So electrons, neutrons and neutrinos are assigned primary colours; the muons through to quarks, secondary colours; and the Higgs boson, neutrino cosmology and squarks, tachyons and the graviton, pastels. The abstractions come alive as Bernstein meshes history and science with anecdotes on everyone from Murray Gell-Mann to Richard Feynman. A colourful chronicle backed by 50 years in the field.

Correspondence

Scientific genius: in different guises

Dean Keith Simonton's contention that scientific genius is extinct (*Nature* 493, 602; 2013) may itself be based on an extinct — or at least dying — concept of genius.

In the past, geniuses were lone scientists who distilled extant knowledge to spawn innovation. Simonton lays part of the blame for their extinction on modern team science (see K. Börner *et al. Sci. Transl. Med.* 2, 49cm24; 2010). But a different kind of genius can exist inside a team. An example might be the member who instinctively optimizes the group's complementary expertise to elicit a ground-breaking discovery.

Even more radical forms of genius are conceivable. The hallmark combination of knowledge and process can create a form of collective genius (A. W. Woolley *et al. Science* 330, 686–688; 2010). And as scientists become more connected with each other and technology, genius could emerge from a hybrid of human and machine intelligence.

There is no need to bemoan the demise of the lone genius. Rather, we should be fostering and studying more contemporary forms of scientific genius.

Stephen M. Fiore *University of Central Florida, Orlando, Florida, USA.*
sfiore@ist.ucf.edu

Scientific genius: will continue to thrive

Dean Keith Simonton's contention that scientific genius is extinct (*Nature* 493, 602; 2013) invites comparison with Lord Kelvin's famous speech to the British Association for the Advancement of Science in 1900, in which he remarked, "There is nothing new to be discovered in physics now. All that remains is more and more precise measurement." The discoveries of quantum mechanics and relativity soon made nonsense of this hubristic claim.

Simonton suggests that these

were the last new fields, and that disciplines founded since are simply hybrids of existing ones. But science does not proceed in the way followed by the journalist in Charles Dickens's *The Pickwick Papers* (1836), who, when asked to write on Chinese metaphysics, combined the information he read "for metaphysics under the letter M, and for China under the letter C" from the *Encyclopaedia Britannica*.

Information theory, for example, founded by Claude Shannon in 1948, is surely a field in its own right — albeit with applications to many different fields. Other emergent fields include network theory and the science of complex systems, which are providing insight into systems from organisms to societies and ecosystems. Opportunities for scientific genius and surprising discoveries are nowhere near exhausted.

Len Fisher *University of Bristol, Bristol, UK.*
len.fisher@bristol.ac.uk

Don't belittle the rebound effect

We disagree with Kenneth Gillingham and colleagues' contention that the rebound effect — in which greater consumption offsets the energy saved by increasing efficiency — is exaggerated (*Nature* 493, 475–476; 2013). We and others have shown rebound effects as large as 60% (see, for example, M. Frondel *et al. Energy Econ.* 34, 461–467; 2012).

In our view, energy-efficiency standards are among the least cost-effective ways of lowering carbon emissions (see H. Allcott *Am. Econ. Rev.* 101, 98–104; 2011). For example, the costs of the US Corporate Average Fuel Economy standard are more than ten times higher than a petroleum tax that induces the same reduction in oil consumption (R. W. Crandall *J. Econ. Persp.* 6, 171–180; 1992). This is mainly because of the rebound effect:

the standard actually encourages driving by marginally lowering its cost, unlike a tax.

The greater cost-effectiveness of a tax could be undermined by coupling it with an efficiency standard, as Gillingham *et al.* suggest, because of interaction effects between the two.

Manuel Frondel, Colin Vance *Rhineland-Westphalia Institute for Economic Research, Essen, Germany.*
vance@rwi-essen.de

Guarding children's genetic privacy

Your coverage of genetic privacy issues (*Nature* 493, 451 and *Nature* 494, 7; 2013) does not address concerns relating to DNA collected from children, who have contributed thousands of biobank samples worldwide.

Open sharing of genotype and phenotype information is crucial for advancing research into childhood diseases, but depends on consent from patients or their parents. Children cannot themselves consent to participation in research with long-term privacy implications. However, parental consent is currently founded on unrealistic promises of anonymity and confidentiality.

For the responsible conduct of research, parents need to be made fully aware of the risk of identifiability before granting consent on their children's behalf (J. E. Lunshof *et al. Nature Rev. Genet.* 9, 406–411; 2008).

Stringent research protocols are necessary to protect child donors (D. Gurwitz *et al. Science* 325, 818–819; 2009). But we should not prohibit the publication of sequencing information that could save lives. For example, mutations in calmodulin gene sequences are associated with some sudden infant deaths (L. Crotti *et al. Circulation* <http://doi.org/kjz>; 2013).

Jeantine E. Lunshof *Harvard Medical School, Boston, Massachusetts, USA.*

jelunshof@genetics.med.harvard.edu

David Gurwitz *Tel Aviv University, Israel.*

'Antifragility' as a mathematical idea

In his review of my book *Antifragile*, Michael Shermer mischaracterizes the concept of 'antifragility' (*Nature* 491, 523; 2012).

'Fragility' can be defined as an accelerating sensitivity to a harmful stressor: this response plots as a concave curve and mathematically culminates in more harm than benefit from random events. 'Antifragility' is the opposite, producing a convex response that leads to more benefit than harm.

We do not need to know the history and statistics of an item to measure its fragility or antifragility, or to be able to predict rare and random ('black swan') events. All we need is to be able to assess whether the item is accelerating towards harm or benefit. The relation of fragility, convexity and sensitivity to disorder is thus mathematical (N. N. Taleb and R. Douady *Quant. Finance*, in the press) and not derived from empirical data, as Shermer implies.

Shermer's suggestion that I should offer "a checklist of things companies or countries can do to prepare for black-swan events" overlooks 50 or so such heuristics based on the identification of convex responses.

Nassim N. Taleb *Polytechnic Institute of New York University, New York, USA.*
ntaleb@poly.edu

CLARIFICATION

The Correspondence headline 'Avoid constructing wind farms on peat' (J. Smith *et al. Nature* 489, 33; 2012) is misleading: it is developments on non-degraded, pristine peats that should be avoided.

ASTROPHYSICS

Black holes in a spin

The implications of the X-ray emission patterns of galaxies hosting supermassive black holes have been contentious. Data from NASA's NuSTAR telescope seem to resolve the issue — at least for one such galaxy. [SEE LETTER P.449](#)

CHRISTOPHER S. REYNOLDS

Supermassive black holes, with masses of millions to billions times that of our Sun, are believed to exist at the centre of essentially every galaxy. When these monsters feast upon the gas (and possibly the stars!) within galactic centres, they release enormous quantities of energy, producing a phenomenon called an active galactic nucleus (AGN). Far from being dark and difficult to detect, the black holes in AGNs are the most luminous spectacles in the Universe. On page 449 of this issue, Risaliti *et al.*¹ report observations of the AGN at the centre of the nearby galaxy NGC 1365 (Fig. 1) using the Nuclear Spectroscopic Telescope Array (NuSTAR), a newly deployed X-ray observatory and NASA's latest addition to its fleet of space telescopes. By exploiting NuSTAR's ability to measure the high-energy X-ray spectrum of an AGN with unprecedented accuracy, the authors obtain an unambiguous measurement of the spin rate of this supermassive black hole, finding a spin that is at least 84% of the maximum theoretically allowed value.

Why should we care so much about these supermassive black holes or their spin? To start with, their very presence is a mystery that draws in the curious astrophysicist. It now seems clear that the first black-hole 'seeds' were created just a few hundred million years after the Big Bang, although the process that created them is still not understood. Weighing in at a mere 10,000 solar masses or so, these seeds then gorged upon the gas within the young galaxies and grew rapidly into the behemoths that we see today. Furthermore, our understanding of galaxy formation and evolution is intimately linked to our understanding of supermassive black holes. The energy released by a growing supermassive black hole can be so powerful that it disrupts the normal growth of the host galaxy; in extreme cases, the AGN can terminate all subsequent growth of the galaxy.

Although essentially every detail of this feasting process is uncertain, the spin of a supermassive black hole can help us unravel the mystery of its growth². If a black hole grew in one (or a small number of) dramatic feeding event(s), it would acquire the angular momentum of the inflowing matter and would



Figure 1 | Spiral galaxy NGC 1365. Risaliti *et al.*¹ have measured the spin rate of the supermassive black hole that lurks at the centre of NGC 1365, shown here in an optical image obtained with the Very Large Telescope.

be spinning very fast. On the other hand, growth through the infall of small, randomly oriented packets of gas (or even small black holes) would produce black holes that rotate much more slowly³. In this way, the black-hole spin is a 'fossil remnant' of its formation processes.

Black-hole spin — which reveals itself in the twisting of space-time close to the hole's event horizon, beyond which no matter or light can escape — is a difficult quantity to measure. Our handle on spin comes from the fact that a spinning black hole 'draws in' the inner edge of the accretion disk, the flat rotating disk through which gas flows into the black hole. Because the accretion disk can get closer to the black hole when the black hole is spinning, the disk's emissions are more strongly affected

by the gravity of the black hole, producing an enhancement in the gravitationally induced redshifting of the disk's emission spectrum^{4,5}. Through a detailed spectral analysis of the X-ray emission from the accretion disk, we can model these effects and determine the black-hole spin.

Black-hole spin measurements using this technique have been conducted^{6,7} for several years using the 0.5–10-kiloelectronvolt part of the X-ray spectrum accessible with the sensitive spectrographs on previous X-ray missions such as the Chandra X-ray Observatory, XMM-Newton and Suzaku. However, these measurements remained somewhat controversial because of the existence of an alternative interpretation of this part of the X-ray spectrum. In this view, the X-ray-emitting

accretion disk is partially obscured by multiple layers of gas. These absorbing layers would introduce complexity into the X-ray spectrum that could mimic the effects of rapid black-hole spin⁸. This has cast a cloud (literally) over measurements of the spins of supermassive black holes.

The new data from NuSTAR have finally resolved this issue, at least in this particular AGN, NGC 1365. Using the superior high-energy X-ray capabilities of NuSTAR, Risaliti *et al.* have produced a high-quality spectrum of the photons with energies in the range 3–80 keV. Above 10 keV, the signal-to-noise ratio of the spectrum is unprecedented and allows a direct face-off between the alternative, gas-absorption models and the more standard (spin-sensitive) models. The authors find that, for the gas-absorption models to work, the accretion disk would have to be blanketed by a thick layer of gas such that only 2–3% of the generated X-rays actually make it out of the system. Following this picture to its logical conclusion, the intrinsic emission in this AGN would have to be so luminous that the associated radiation pressure would blow the AGN apart. Although indirect arguments against gas-absorption models had been put forward previously^{5,9,10}, this is by far the cleanest observational demonstration that such models fail.

With this cloud removed, it seems an unavoidable result that at least some supermassive black holes are spinning rapidly and must have grown in rapid accretion events. This raises fundamental theoretical questions about how gas is fed onto a supermassive black hole without fragmenting into smaller packets (or even stars) that would randomize its angular momentum³. These results also encourage us to push further and deeper with our X-ray observations, necessitating the development of more powerful X-ray observatories, so that we can use the diagnostic power of black-hole spin to uncover the story of supermassive-black-hole growth. ■

Christopher S. Reynolds is in the Department of Astronomy and the Joint Space Science Institute, University of Maryland, College Park, Maryland 20742, USA. e-mail: chris@astro.umd.edu

1. Risaliti, G. *et al.* *Nature* **452**, 449–451 (2013).
2. Volonteri, M., Madau, P., Quataert, E. & Rees, M. J. *Astrophys. J.* **620**, 69–77 (2005).
3. King, A. R. & Pringle, J. E. *Mon. Not. R. Astron. Soc.* **373**, L90–L92 (2006).
4. Tanaka, Y. *et al.* *Nature* **375**, 659–661 (1995).
5. Fabian, A. C. *et al.* *Mon. Not. R. Astron. Soc.* **277**, L11–L15 (1995).
6. Miller, J. M. *et al.* *Astrophys. J.* **606**, L131–L134 (2004).
7. Brenneman, L. W. & Reynolds, C. S. *Astrophys. J.* **652**, 1028–1043 (2006).
8. Miller, L., Turner, T. J. & Reeves, J. N. *Astron. Astrophys.* **483**, 437–452 (2008).
9. Reynolds, C. S. *et al.* *Mon. Not. R. Astron. Soc.* **397**, L21–L25 (2009).
10. Reynolds, C. S. *Astrophys. J.* **759**, L15 (2012).

VIROLOGY

Phages hijack a host's defence

The discovery that some viruses use a defence mechanism known as a CRISPR/Cas system beautifully illustrates the evolutionary tit-for-tat between viruses and the bacteria they infect. [SEE LETTER P.489](#)

MANUELA VILLION & SYLVAIN MOINEAU

If you belong to the most abundant biological entity on the planet, you need a few tricks to stay on top. The global population of bacterial viruses (bacteriophages, or phages) has been estimated to be 10^{31} , outnumbering their bacterial hosts by tenfold¹. Bacteria have developed a formidable arsenal of sophisticated strategies to neutralize viruses², but phages always seem to find a way to evolve, persist and abound. Studies of the complex evolutionary dynamics between phages and bacteria led to the discovery³ of a widespread bacterial defence system called CRISPR/Cas. On page 489 of this issue, Seed *et al.*⁴ report the remarkable finding that some phages that infect the bacterial pathogen *Vibrio cholerae* have also acquired a functional CRISPR/Cas system in their own genome which allows them to neutralize an unrelated antiviral system in their bacterial host.

CRISPR (clustered regularly interspaced short palindromic repeats) sequences are often flanked by *cas* (CRISPR-associated) genes⁵. These directly repeating nucleotide sequences are separated by short stretches of non-repetitive DNA called spacers. CRISPR/Cas regions have been found in 40% of bacterial species and 90% of archaea. These CRISPR/Cas-harboring microorganisms can acquire small pieces of DNA directly from the genomes of invading phages³ or plasmids⁶ (small non-chromosomal DNA molecules that can be transmitted between bacteria) and insert them as spacers within a CRISPR site. The spacers are then transcribed and processed, leading to the production of small RNA molecules called CRISPR RNAs (crRNAs). The crRNAs and Cas proteins act together as a surveillance system that is primed to quickly target — through base-pairing — similar nucleic acids from subsequent invaders, and then to cleave them⁶. Thus, the bacteria gain genetic information from invaders and use it to mount a defence. This process is reminiscent of our own immune system and, as a result, CRISPR/Cas has been called an adaptive microbial immune system.

A few stealthy phages have been discovered that can bypass this bacterial protection mechanism through mutation or deletion of

CRISPR-targeted regions⁷ or through acquisition of anti-CRISPR genes⁸. Metagenomic studies have also identified CRISPR/Cas systems in viral genomes (see, for example, ref. 9), but their biological relevance has not been proposed. Enter Seed and colleagues, who elegantly demonstrate that phage genomes are not just ammunition and targets for CRISPR/Cas sequences — certain *V. cholerae* phages have hijacked the entire system for their own defence and persistence.

V. cholerae is the cause of cholera, which affects hundreds of thousands of people each year¹⁰. Phages are among the factors that may modulate the burden of cholera in endemic regions, so understanding the interactions between the bacteria and their infecting phages is of interest. Seed *et al.* analysed the genomes of 11 phages isolated from stool samples of patients with cholera, and

“These results demonstrate that phages can hijack a functional, adaptive immune-evasion system to benefit their own multiplication.”

found that five contained a CRISPR/Cas system. When the authors examined the sequence of the spacers in the phages, they found that they matched regions in the genome of the host bacteria. Specifically, the spacer sequences matched an 18-kilobase ‘genomic island’ that is also present in several other strains of *V. cholerae*.

This genomic element resembles phage-inducible chromosomal islands (PICIs), which are found in some bacteria, including some *Staphylococcus aureus* strains. In *S. aureus*, these regions are known as SaPIs, and they represent pathogenicity islands that contain virulence-factor-encoding genes¹¹. When a SaPI-containing cell is infected by certain phages, the SaPI sequence excises from the bacterial chromosome, circularizes and replicates — presumably to exit the infected bacterium. During this process, the bacterium also activates a largely uncharacterized defence system in an attempt to stop phage propagation, and thereby ensure its own persistence and the persistence of the surrounding phage-susceptible bacterial population¹². Seed

et al. demonstrate that the 18-kb element in *V. cholerae* also circularizes after phage infection, and that it encodes an active anti-phage system. Consequently, the authors refer to it as a PICI-like element, or PLE.

Further studies of one of the isolated phages, which carried a CRISPR/Cas system with two PLE-targeting spacers, showed that it could replicate and kill a PLE-harboring *V. cholerae* strain that had been isolated from the same stool sample. However, Seed and colleagues show that a mutant version of this phage that lacks the matching spacer cannot replicate in the PLE-harboring strain, but can replicate in a mutated *V. cholerae* strain lacking the PLE, further supporting the targeted action of the system.

The authors also performed an elaborate set of experiments to confirm the hallmarks of an active CRISPR/Cas system. For example, they show that crRNAs are transcribed and processed from the phages, and that derivative phages that have acquired new CRISPR spacers targeting the PLE can be isolated. Overall, these results demonstrate that phages can hijack a functional, adaptive immune-evasion system to benefit their own multiplication. And, as stated by the authors, because bacterial cell death and DNA damage are inherent in virulent phage infection, CRISPR-mediated DNA cleavage of the targeted bacterial genome does not have a negative impact on phage proliferation.

Seed and colleagues' study illustrates another extraordinary turn of events in the evolution of phages and bacteria, in which the phages defeat the bacteria outright by using one of its own weapons against it. How frequently such an event occurs and whether a phage that contains a CRISPR/Cas system stays stable remains to be seen. Nevertheless, these findings will certainly fuel selected applications. For example, the discovery of other phages with a CRISPR/Cas system that targets host genes or more phages with anti-CRISPR genes⁸ may provide additional leverage to design an efficient cocktail of natural or engineered phages to prevent or treat bacterial contamination or infection. On the other hand, this finding suggests that biotechnological industries that rely solely on CRISPR/Cas systems to protect key bacterial strains from phage infection should be ready to go back to the drawing board. Because, as always, phages will find a way. They may already have. ■

Manuela Villion and Sylvain Moineau are in the Département de biochimie, microbiologie et bio-informatique, Faculté des sciences et de génie, Université Laval, Québec G1V 0A6, Canada. S.M. is also in the Groupe de recherche en écologie buccale, Faculté de médecine dentaire, and the Félix d'Hérelle Reference Center for Bacterial Viruses, Université Laval.
e-mail: sylvain.moineau@bcm.ulaval.ca

1. Suttle, C. A. *Nature* **437**, 356–361 (2005).
2. Labrie, S. J., Samson, J. E. & Moineau, S. *Nature Rev. Microbiol.* **8**, 317–327 (2010).
3. Barrangou, R. *et al. Science* **315**, 1709–1712 (2007).
4. Seed, K. D., Lazinski, D. W., Calderwood, S. B. & Camilli, A. **494**, 489–491 (2013).
5. Wiedenheft, B., Sternberg, S. H. & Doudna, J. A. *Nature* **482**, 331–338 (2012).
6. Garneau, J. E. *et al. Nature* **468**, 67–71 (2010).
7. Deveau, H. *et al. J. Bacteriol.* **190**, 1390–1400 (2008).
8. Bondy-Denomy, J., Pawluk, A., Maxwell, K. L. & Davidson, A. R. *Nature* **493**, 429–432 (2013).
9. Minot, S. *et al. Genome Res.* **21**, 1616–1625 (2011).
10. World Health Organization. *Wkly Epidemiol. Rec.* **87**, 289–304 (2012).
11. Novick, R. P., Christie, G. E. & Penadés, J. R. *Nature Rev. Microbiol.* **8**, 541–551 (2010).
12. Ram G. R. *et al. Proc. Natl Acad. Sci. USA* **109**, 16300–16305 (2012).

SPEECH SCIENCE

Tuned to the rhythm

Rhesus macaques' responses to computer-animated images of lip-smacking monkey faces suggest that the jaw, tongue and lip oscillations that characterize human speech may have evolved from rhythmic primate facial expressions.

W. TECUMSEH FITCH

Language is a multifaceted jewel, with some facets better studied than others. Although the evolution of syntax and vowel production is much discussed, other aspects of spoken language remain relatively neglected. In particular, the origins of the periodic oscillations that produce the alternation of consonants and vowels that make up syllables — a central feature of all spoken languages — have remained mysterious, because most primate calls are produced with just a single opening of the mouth. Writing in *Proceedings of the National Academy of Sciences*, Ghazanfar and colleagues¹ offer an intriguing perspective on this question by studying a class of visual display, termed lip-smacking, that is found in many non-human primates. The authors show that rhesus macaques are 'tuned' to a natural lip-smacking frequency range that is similar to the oscillation frequency of speech, supporting the hypothesis that the origin of human speech rhythms lies not in ancestral primate vocal displays, but rather in rhythmic facial expressions.

The jaw, tongue and lip oscillations in human speech occur at roughly six times per second (6 hertz), and speech perception is optimal when syllable rates flow in this natural rhythm^{2,3}. Ghazanfar *et al.* tested whether the same is true for monkeys, whose natural lip-smacking rhythm occupies a similar 3–8-Hz frequency range. The authors offered rhesus macaque 'viewers' a choice between two computer-animated lip-smacking displays: one at 6 Hz and another at an abnormally fast or slow rate (Fig. 1). They found that macaques spent more time watching the 6-Hz animations. What's more, many of the monkeys lip-smacked back to the monitor, showing that they indeed interpreted the monkey avatar's behaviour as lip-smacking. These results show a clear and convincing preference

for natural-rate monkey facial movements. However, their significance for speech evolution may be less obvious.

There are two main hypotheses for the evolutionary origin of human speech⁴. The first and most widespread is that speech is derived from primate vocalizations, which were harnessed or co-opted to convey linguistic information. In support of this idea, the same vocal production system (lungs, larynx and vocal tract) is used to produce both primate calls and speech. A problem is that human speech is unique among primate vocalizations in being a very flexible, learned signal, whereas most primate calls have a strong, species-specific genetic determination. The 'vocal origins' hypothesis favours evolutionary continuity of vocal production over a hypothetical discontinuity in vocal control and vocal learning.

The second, and less intuitive, hypothesis builds on the fact that the lips, jaws and tongue generate not just vocal, but also visual, signals — and, unlike the larynx, these articulators are under learned voluntary control in non-human primates. This led evolutionary neuroscientist Peter MacNeilage to suggest⁵ that speech rhythms originated not in the vocal but in the visual domain. In a sense, he argued, speech starts out (in babies' babbling, for example) as a lip-smacking oscillation superimposed on a vocal signal. This rhythmic stream is then differentially modified, by learned tongue and lip movements, into the vowels and consonants of speech. Support for this hypothesis comes from previous work demonstrating that the detailed kinematics of lip-smacking are strikingly similar to those of speech⁶. But Ghazanfar and colleagues' work adds support from the domain of perception, indicating that perceptual tuning for the two signal classes is also consistent with MacNeilage's hypothesis.

The approach pioneered by Ghazanfar *et al.*

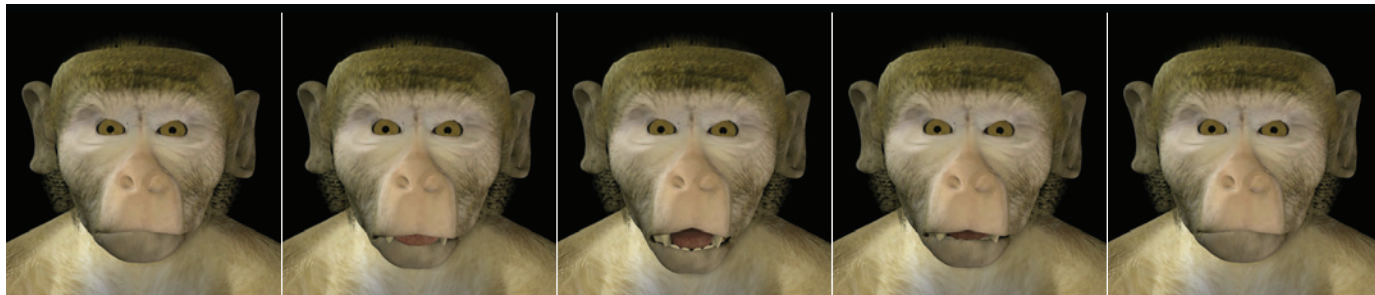


Figure 1 | From the mouths of monkeys. A frame sequence from a video clip of computer-simulated monkey faces producing lip-smacking movements that Ghazanfar *et al.*¹ showed to rhesus macaques. The authors compared the macaques' responses to lip-smacking at their natural 6-hertz rhythm, which matches the syllable rate of human speech, with lip-smacking at faster (10 Hz) or slower (3 Hz) frequencies.

offers many possibilities for further work. Particularly intriguing would be to attempt the same procedure with chimpanzees. A positive result in this or other primate species would increase the chance that 6-Hz lip-smack tuning is shared by common descent in many primates. Equally interesting will be to explore whether watching lip-smacking evokes synchronized neuronal oscillations in the visual cortex. A major advantage of studying macaques over humans is that neuroscientists can perform both brain imaging and direct recording of cortical-neuron activity⁷. This would allow the neural processes underlying such rhythms to be investigated in greater detail.

If accumulating evidence ends up supporting MacNeilage's hypothesis, it will have fascinating implications for the evolution of spoken language. A long tradition has focused on details of human vocal-tract anatomy — in particular, our descended larynx — as a key prerequisite for human speech. But many studies suggest that the importance of anatomy has been overestimated, and that factors of neural control are dominant⁴. Humans have a uniquely well-developed capacity for vocal learning, which entailed forging new neural links between the auditory cortex and the motor cortex⁸. MacNeilage's hypothesis suggests that the evolutionary route by which these links were formed was circuitous, and initially involved co-opting visual-communication circuitry that was already present and under voluntary cortical control in our primate ancestors. Adding some laryngeal phonation, as occurs in an infrequent macaque call termed a girney, would be enough to render these visual signals audible. A second evolutionary step would have been the development of our unique cortical-brainstem connections⁹, giving us increased control over the larynx. These may have evolved to more effectively exploit the acoustic bandwidth offered by the rapidly oscillating vocal tract, yielding the speech signal we know today.

Although speech is just one facet of language, and not necessarily even the most important one, its neural and evolutionary basis is becoming increasingly well

understood. These new results suggest that the evolutionary history of speech and other aspects of language may have been full of odd turns and surprises. ■

W. Tecumseh Fitch is in the Department of Cognitive Biology, University of Vienna, 1010 Vienna, Austria.
e-mail: tecumseh.fitch@univie.ac.at

1. Ghazanfar, A. A., Morrill, R. J. & Kayser, C. *Proc. Natl Acad. Sci. USA* **110**, 1959–1963 (2013).
2. Drullman, R., Festen, J. M. & Plomp, R. J. *Acoust.*

- Soc. Am.* **95**, 2670–2680 (1994).
3. Smith, Z. M., Delgutte, B. & Oxenham, A. J. *Nature* **416**, 87–90 (2002).
4. Fitch, W. T. *The Evolution of Language* (Cambridge Univ. Press, 2010).
5. MacNeilage, P. F. *Behav. Brain Sci.* **21**, 499–511 (1998).
6. Ghazanfar, A. A., Takahashi, D. Y., Mathur, N. & Fitch, W. T. *Curr. Biol.* **22**, 1176–1182 (2012).
7. Logothetis, N. K., Pauls, J., Augath, M., Trinath, T. & Oeltermann, A. *Nature* **412**, 150–157 (2001).
8. Rilling, J. K. *et al. Nature Neurosci.* **11**, 426–428 (2008).
9. Jürgens, U., Kirzinger, A. & von Cramon, D. Y. *Cortex* **18**, 125–139 (1982).

ENVIRONMENTAL SCIENCE

The shape of nitrogen to come

An analysis reveals the huge impact of human activity on the nitrogen cycle in China. With global use of Earth's resources rising per head, the findings call for a re-evaluation of the consumption patterns of developed societies. [SEE LETTER P.459](#)

MARK A. SUTTON & ALBERT BLEEKER

Although Earth's atmosphere consists of nearly 80% dinitrogen (nitrogen gas, N₂), most living organisms cannot use this form of the element and require it to be converted into usable forms, such as ammonia. Humans have long exploited the ability of leguminous crops to fix dinitrogen into usable reactive nitrogen compounds, improving soil fertility. But the amount of reactive nitrogen produced in this way is now greatly exceeded by that produced industrially¹. Together with nitrogen oxides, another form of reactive nitrogen produced as a by-product of combustion processes, nitrogen compounds released into the environment by human activity are weaving a web of unforeseen consequences. On page 459 of this issue, Liu *et al.*² quantify the massive scale of these changes to the nitrogen cycle across China, which are a direct result of increases in human activities such as food production, travel and energy consumption*.

In a study remarkable for the scale of its achievement, Liu *et al.* have shown how increases in the rate of the release to the atmosphere of nitrogen oxides (NO_x) and ammonia (NH₃) have been matched by increases in the amounts of atmospheric reactive nitrogen (N_r) deposition, measured in precipitation. To do this, they drew on more than 300 published data sets of N_r deposition from across China spanning 30 years (from 1980 to 2010). Most importantly, the authors went on to show how nitrogen uptake by plants and its levels in leaves have changed across China as a consequence.

The focus of the study was to provide quantified evidence of biogeochemical and biological change, but Liu and colleagues' results can also be considered as indicators of a pan-dimensional modification to the nitrogen cycle. The components of this modification include: the formation of

*This article and the paper under discussion² were published online on 20 February 2013.

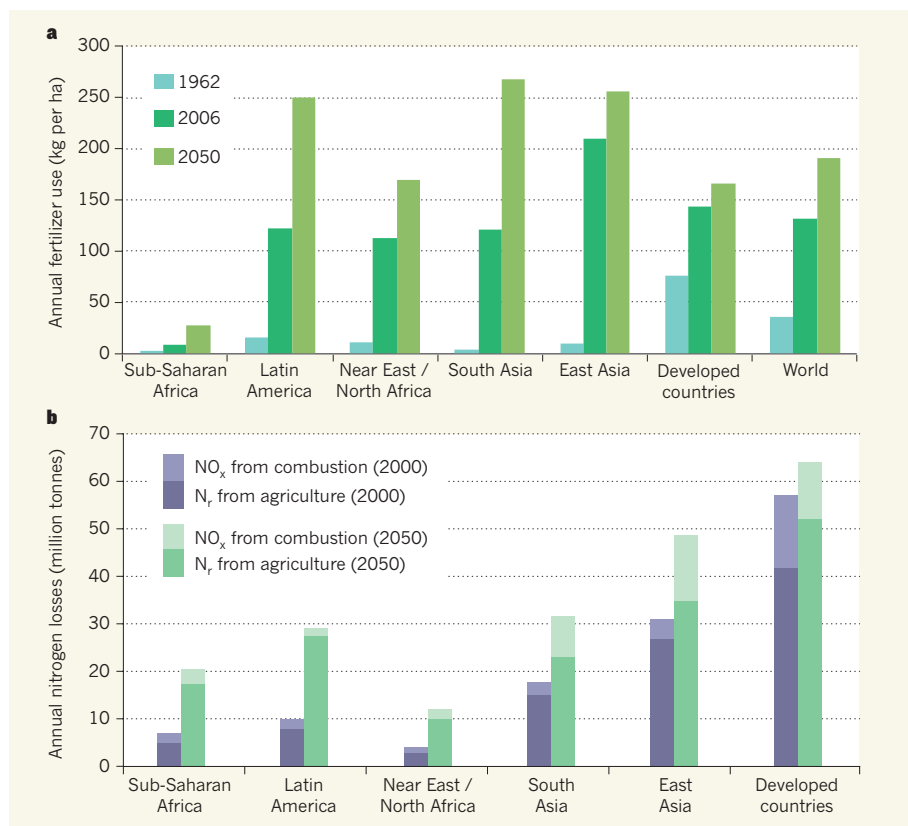


Figure 1 | Fertilizer use and nitrogen losses to the environment. **a**, Estimated and projected global fertilizer use⁷ for fertilizers that contain nitrogen, phosphorus and potassium compounds. **b**, Total estimated losses to the environment of nitrogen oxides (NO_x) in emissions from combustion sources and of reactive nitrogen (N_r) from agricultural activities for 2000 and 2050. Estimates of NO_x for 2050 are the mean of the A1 and A2 emission scenarios⁹ (originally developed for the Intergovernmental Panel on Climate Change's Special Report on Emission Scenarios); estimates of N_r are the mean of the Global Orchestration and Technogarden scenarios of the Millennium Ecosystem Assessment⁸.

nitrogen-containing fine particulate matter in air, which poses a substantial threat to human health; the contribution of NO_x to the formation of ground-level ozone, which causes crop losses; increased emissions of nitrous oxide (N₂O), a greenhouse gas; and extreme levels of water pollution by nitrates and other forms of N_r (refs 3–5). Concern over water pollution was highlighted during the 2008 Beijing Olympics, when a massive algal 'green tide' severely disrupted training for sailing events.

Liu *et al.* report a 60% increase in atmospheric N_r deposition in China since 1980. However, their results are based on the amount of N_r sampled by open rain collectors, and, as the authors recognize, the total amount deposited will be several times larger. For example, most rain is captured by these samplers, but snowfall is only partially caught. N_r-containing gases, fine particles and fog are also caught, but the amount of N_r captured from these components is much less than that deposited on plant canopies. The total annual N_r deposition to Chinese ecosystems will therefore often be more than 80 kilograms of nitrogen per hectare — several times larger than the rain-collector data.

To assess the effects of increased nitrogen

deposition on vegetation, the researchers drew on data from crop-fertilizer trials, which typically include control measurements of crop production without fertilizer. By combining data from sites across China, they estimate that a 15% increase in nitrogen uptake by plants has occurred since 1980 (see Fig. 3b of the paper²). In principle, the additional N_r inputs resulting from NO_x emissions could have increased crop productivity. However, the authors did not report the net change in crop growth, which leaves open the question of whether the fertilization effect provided by increased N_r deposition outweighs the growth-reduction effect of NO_x-related ground-level ozone. For natural ecosystems, the extra nutrients remain a major threat to biological diversity⁶.

Rates of nitrogen fertilization in China are among the highest in the world — fostered by the country's subsidy of fertilizer manufacturing, which was established to address food-security concerns. However, this reliance on

NATURE.COM
For more on nitrogen
pollution in China,
visit:
go.nature.com/kx5ztz

fertilizers has decreased the extent to which nitrogen from manure and sewage is recycled, reducing the efficiency of nitrogen use overall.

Fertilizer use in China can be compared with estimates of regional and global rates of total fertilization⁷ (which includes fertilizers containing nitrogen, phosphorus and potassium compounds; Fig. 1a) from the Food and Agriculture Organization (FAO) of the United Nations. In the 1960s, fertilizer inputs were largest in developed countries, at 75 kg per ha. By 2006, East Asia (including China) had taken the lead, with average inputs at around 200 kg per ha, and local values often five times higher. Liu *et al.* show how this has combined with a 3.2-fold increase in livestock and a 20.8-fold increase in vehicles since 1980, together leading to substantial increases in N_r pollution in China.

It must be emphasized, however, that nitrogen is not only a problem in China. The FAO estimates suggest that there will be a further 50% increase in global fertilizer consumption by 2050 as a result of trends in population, improved diets and increased consumption of animal products. At the same time, projections based on scenarios that emphasize population and economic growth^{8,9} suggest a global increase in nitrogen losses to the wider environment of 70% by 2050 (Fig. 1b). By 2050, estimates⁷ suggest that average fertilizer inputs in Latin America and South Asia will approach Chinese levels, and major increases will also occur in North Africa and the Near East.

Regional increases in N_r losses are broadly similar and projections indicate a substantial worsening of nitrogen-pollution effects, including increased NO_x emissions in Asia, unless action is taken. In fact, these projections may be conservative. If the current trends reported by Liu *et al.* are extrapolated, an 85% increase in NH₃ and a 200–240% increase in NO_x emissions in China is possible by 2050.

Liu and colleagues' data and the projections shown in Figure 1 highlight the urgency for global action to tackle increasing nitrogen levels. But there is still no global international convention that defines targets for better management of global nitrogen and nutrient cycles, as highlighted in a recent report¹⁰. The authors of that report (who include ourselves) have proposed a shared aspirational goal to improve nitrogen-use efficiency by 20% by the year 2020; a cost-benefit calculation suggests that this would provide net savings equivalent to around US\$170 billion. This will require changes in industrial and agricultural practices, and a re-evaluation of the consumption patterns of Western society. But achieving all of this will require countries to get organized, and to start taking the nitrogen challenge seriously. ■

Mark A. Sutton is at the NERC Centre for Ecology and Hydrology (CEH), Edinburgh Research Station, Edinburgh EH26 0QB, UK. **Albert Bleeker** is at the Energy research Centre of the Netherlands (ECN), 1755ZG

Petten, the Netherlands. M.A.S. and A.B. are also at the International Nitrogen Initiative, co-hosted at the CEH and ECN.
e-mails: ms@ceh.ac.uk; a.bleeker@ecn.nl

- Galloway, J. N. *et al.* *Science* **320**, 889–892 (2008).
- Liu, X. *et al.* *Nature* **494**, 459–462 (2013).
- Sutton, M. A. *et al.* in *The European Nitrogen Assessment* (eds Sutton, M. A. *et al.*) xxiv–li (Cambridge Univ. Press, 2011).
- Suddick, E. C., Whitney, P., Townsend, A. R. & Davidson, E. A. *Biogeochemistry* <http://dx.doi.org/10.1007/s10533-012-9795-z> (2012).
- Kim, T. W., Lee, K., Najjar, R. G., Jeong, H. D. & Jeong, H. J. *Science* **334**, 505–509 (2011).
- Bleeker, A., Hicks, K., Dentener, F., Galloway, J. & Erisman, J. W. *Environ. Pollut.* **159**, 2280–2288 (2011).
- Alexandratos, N. & Bruinsma, J. *World Agriculture Towards 2030/2050: The 2012 Revision* (FAO, 2012).
- Bodirsky, B. L. *et al.* *Biogeosciences* **9**, 4169–4197 (2012).
- Alcamo, J. *et al.* in *Ecosystems and Human Well-being Vol. 2* (eds Carpenter, S. R., Pingali, P. L., Bennett, E. M. & Zurek, M. B.) 297–373 (Island, 2005).
- Sutton, M. A. *et al.* *Our Nutrient World: The Challenge to Produce More Food and Energy with Less Pollution* Ch. 8, 95–108 (Centre for Ecology and Hydrology, 2013).

NUTRITION

When guests turn hostile

The impact of a diet, no matter how rich it is, depends crucially on the host's resident gut microbes. Treatment of severe malnutrition with antibiotics may affect the composition of this microbiota to favour better use of nutrients.

RUTH E. LEY

Malnutrition affects an estimated one in four children worldwide¹ and severe forms of it are commonly treated with nutrient-rich therapeutic foods. Yet 10–15% of children do not respond to this treatment. Two papers, published in the *New England Journal of Medicine* (Trehan *et al.*)² and *Science* (Smith *et al.*)³, implicate gut microbes as an additional dimension in the nutrition–disease relationship and suggest treatments for overcoming undesirable nutritional effects caused by these prolific inhabitants of humans.

There is mixed evidence⁴ that antibiotics may aid recovery from malnutrition, suggesting that they could be used in combination with nutritional supplements to treat some of the non-responders. Malnutrition, however, also directly affects the gut microbes that live in harmony with their human host. When food is plentiful, an adult carries roughly a kilogram of such microbes, whose combined activities enhance the host's daily calorie harvest⁵. This 'microbial organ' requires energy for its own maintenance, however, and so takes a cut. When food is scarce, common gut bacteria can subsist on the host's mucus⁶, indicating that this mutualism could turn parasitic if the going gets tough. So, could gut microbes exacerbate the effects of malnutrition?

One clue comes from Trehan and colleagues' study². They investigated the effects of combining ready-to-use therapeutic food (RUTF) with antibiotics to treat malnutrition. This work was conducted in Malawi, where more than 50% of children show stunted growth due to poor nutrition. Of 3,212 children whom the

authors identified with severe acute malnutrition, more than 2,700 were randomly selected for treatment with RUTF plus either of two antibiotics — amoxicillin and cefdinir — or a placebo drug. The logistics required to conduct a field study of this magnitude, and the strict follow-ups, in rural Malawi and all in just one year, are quite remarkable.

Although antibiotics had little effect on how

quickly the malnourished children recovered, they significantly reduced the death rate during the time of the follow-up — a 35% and 44% reduction for amoxicillin and cefdinir, respectively. Trehan *et al.* propose that the antibiotics might have prevented life-threatening, systemic infections that can occur during malnutrition. Another possibility is that these drugs somehow acted on the gut microbiota, such that the altered microbiota contributed to the recovery.

Smith *et al.*³ independently explored the possibility that the specific composition of the microbiota can affect recovery from severe malnutrition by studying faecal samples from 317 Malawian twin pairs, from birth to 36 months of age. In 43% of these twins, one sibling suffered from a type of severe acute malnutrition called kwashiorkor, whereas the other did not. Moreover, of the 317 pairs, 15% were identical twins.

Twins offer a means to control for environmental exposures, as they are raised together, and to infer the effects of genetics, by comparing identical twins with fraternal twins. When assessing the faecal microbiota from a subset of the healthy and diseased twin pairs, Smith and colleagues discovered that discordance (that is, the situation when one twin has the condition and the other does not) for moderate or severe malnutrition was the same in identical versus fraternal twin pairs. This finding emphasizes the importance of non-genetic factors in kwashiorkor.

The authors also found that kwashiorkor was associated with what seemed to be a functionally immature microbiota — one that was more similar to the microbiota of a younger child, with greater levels of actinobacteria. Although administration of a RUTF diet promoted functional maturation of this microbial population, unfortunately, the effect did not persist once the treatment was stopped. Why the effect was transient is uncertain. It could be that the immune system of the sick children had not encountered a more mature microbiota during a critical developmental period, when it was learning to recognize a 'normal' microbiota. It therefore might consider that a microbiota rich in actinobacteria is normal, aiding its re-establishment.

An intriguing question is whether an abnormal microbiota is the cause of or a risk factor for kwashiorkor. To address this, Smith *et al.* introduced into germ-free mice the gut microbiota from either children with kwashiorkor or healthy children. The mice were maintained on a typical (nutritionally poor) Malawi diet for a week before the introduction of the microbes and for three weeks after. They were then given RUTF for two weeks before moving them back to the Malawi diet.

The results were sobering. The 'kwashiorkor microbiota' induced a precipitous weight loss when combined with the Malawi diet. What is worse, even though the mice with this microbiota showed improvement in both weight



Figure 1 | A Malawian child with kwashiorkor.

gain and microbiota composition when on the RUTF diet, once back on the Malawi diet they lost weight and their microbiota reverted.

The impact of the gut microbiota on host health went beyond weight loss. Gut microbiota of those with kwashiorkor showed a wide variety of metabolic derangements that were only partially ameliorated while the animals were eating RUTF. Moreover, the kwashiorkor microbiota contributed to abnormal sulphur metabolism and hindered energy metabolism by the host.

These two studies point to the complexity of our own interactions with resident microbiota, which can influence the nutritional quality of our diets. It remains unclear, however, whether the increased survival of severely malnourished children when given antibiotics is due to an improvement in their microbiota. Regardless of the answer, the risks associated with the widespread use of antibiotics call for careful evaluation of long-term outcomes of this treatment. Taking Smith and colleagues' lead, perhaps mice could be used as experimental vessels to elucidate the mechanisms underlying the positive effects of antibiotics. This should aid optimization of treatment for the children who suffer long-term complications associated with malnutrition.

Although the papers discussed here indicate that intentional manipulation of the gut microbiota could eventually form part of the treatment for RUTF-unresponsive, malnourished children, antibiotics are a blunt tool for altering the composition of the microbiota, as their effects can differ substantially between individuals⁷. A more feasible approach might be bacteriotherapy, which involves infusing a healthy microbiota directly into the patient's gut. This approach has had great success in treating gut infections with *Clostridium difficile*⁸, but it is intensive and costly as it requires a clinical procedure. A formulation more like a probiotic, in which a select microbiota is taken orally as a supplement, is probably more practical on a large scale. The best preventive treatment, of course, is to provide proper nourishment throughout childhood. ■

Ruth E. Ley is in the Departments of Microbiology and of Molecular Biology and Genetics, Cornell University, Ithaca, New York 14853, USA.
e-mail: rel222@cornell.edu

- Black, R. E. *et al.* *Lancet* **371**, 243–260 (2008).
- Trehan, I. *et al.* *N. Engl. J. Med.* **368**, 425–435 (2013).
- Smith, M. I. *et al.* *Science* **339**, 548–554 (2013).
- Alcoba, G. *et al.* *PLoS ONE* **8**, e53184 (2013).
- Bäckhed, F., Ley, R. E., Sonnenburg, J. L., Peterson, D. A. & Gordon, J. I. *Science* **307**, 1915–1920 (2005).
- Sonnenburg, J. L. *et al.* *Science* **307**, 1955–1959 (2005).
- DeThlefsen, L. & Relman, D. A. *Proc. Natl Acad. Sci. USA* **108**, 4554–4561 (2011).
- van Nood, E. *et al.* *N. Engl. J. Med.* **368**, 407–415 (2013).

PARASITOLOGY

Rejuvenation through stem cells

The discovery that schistosomes possess adult stem cells could explain the long-term persistence of these parasitic worms in humans. Targeting a protein produced by the cells might damage schistosome defences. [SEE LETTER P.476](#)

EDWARD J. PEARCE

Schistosomes are nasty. These multicellular parasitic worms infect more than 200 million individuals worldwide, living and laying eggs within their hosts' blood vessels. The eggs become trapped in major organs such as the liver and intestine, causing prolonged inflammatory reactions¹. And despite aggressive immune responses by the infected host, the pathogens persist for 6–10 years on average, but sometimes for much longer. Such robustness strongly implies that schistosomes can replace or repair tissues that have been damaged through ageing or by host immune mechanisms, although how this occurs was unknown. On page 476 of this issue, Collins *et al.*² lift the curtain on this mystery, reporting that schistosomes possess a widely distributed population of adult stem cells that can differentiate into many cell types*.

A close relative of schistosomes are the free-living planarians; the two groups are members of the phylum Platyhelminthes (flatworms). Planarians have exceptional regenerative powers and so have become valuable teaching tools and models for studying stem-cell biology. In these organisms, the only proliferating somatic (non-germ) cells are stem cells called neoblasts, which have a distinctive morphology and are destroyed by radiation.

Experts in studying planarians, Collins and colleagues focused on *Schistosoma mansoni* — a parasitic flatworm that is poorly understood and difficult to work with — to determine whether it too possesses adult stem cells. They discovered dividing cells that were lost on exposure to radiation and that resembled planarian neoblasts in appearance, localization and gene-expression profile. Remarkably, the cells could self-renew to sustain their own

*This article and the paper under discussion² were published online on 20 February 2013.

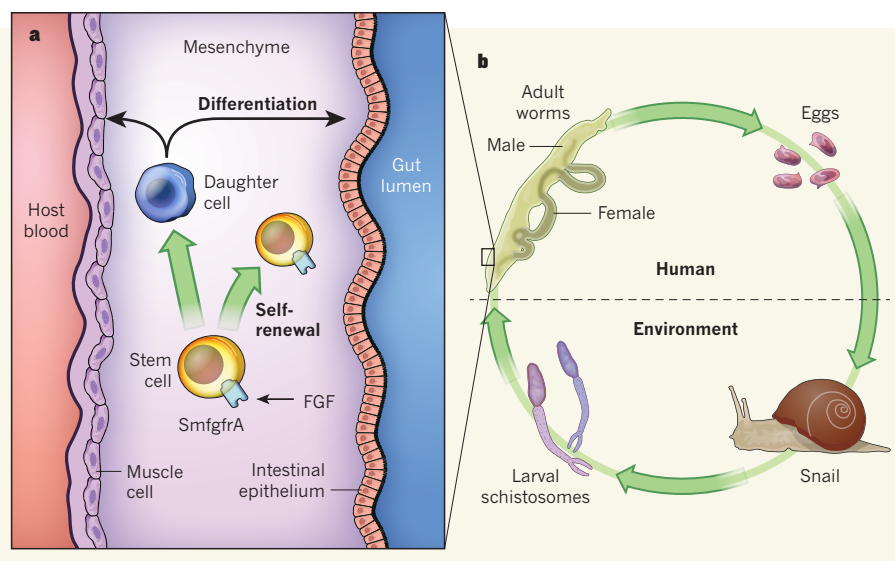


Figure 1 | Schistosome survival strategies and life cycle. **a**, Collins *et al.*² have identified adult stem cells in the mesenchymal tissue of male schistosomes, which underlies the intestinal epithelium. These 'neoblasts' can self-renew through a process that may involve activation of the gene *SmgfrA*, which encodes a FGF-receptor-like protein, *SmgfrA*. They can also produce daughter cells capable of differentiating into multiple cell types, including muscle and intestinal epithelial cells. **b**, Schistosomes have a complex life cycle. In their mammalian host (humans or, in the laboratory, mice), they reproduce sexually, with the female parasite producing eggs. The eggs pass into the environment through the host's urine or faeces, eventually hatching to release larval stages that infect an intermediate host, the aquatic snail. It is in snails that the infectious larvae form, and they mature into adult parasites once they have entered their human host.

population numbers while simultaneously seeding daughter cells into new lineages, such as muscle and intestinal epithelium — truly stem-cell-like behaviour.

The authors also identified *SmfgfrA*, a gene that they found is preferentially expressed in *S. mansoni* adult stem cells and which encodes a receptor for the parasite's version of fibroblast growth factor (FGF; Fig. 1a). FGFs promote proliferation and maintain the 'stemness' of stem cells in other systems, most notably in cultures of human embryonic stem cells³. Following this lead, Collins *et al.* show that inhibiting *SmfgfrA* expression results in both loss of proliferating mesenchymal stem cells underlying the parasite's intestinal epithelium, and a reduction in the expression of gene transcripts normally found at high levels in neoblasts.

The discovery that FGF-receptor-mediated signalling is crucial for the maintenance of adult schistosome stem cells is noteworthy not just because it links stemness in organisms at opposite extremes of multicellular complexity — schistosomes and humans. It also suggests a potential means of interfering with this parasite's life cycle (Fig. 1b).

Treatment of schistosomiasis currently relies exclusively on the drug praziquantel, which is both safe and commonly available, especially thanks to funding from the Bill & Melinda Gates Foundation and Merck. However, the widespread availability and repetitive use of this drug, coupled with the fact that it often fails to clear infection completely, have led to concerns about the development of drug resistance⁴. Indeed, schistosomes can repair surface damage caused by subcurative doses of praziquantel, making the search for alternative treatments a priority. Because stem cells may have a crucial role in praziquantel resistance, it is appealing to envisage the development of drugs that inhibit *SmfgfrA*, or other genes essential for maintaining schistosomal adult stem cells, as adjuncts to existing therapy.

The list of intriguing questions that arise from this work is long. For instance, when do neoblasts form during schistosomal embryogenesis? What is their role in the various stages of the parasite's life cycle? And is the cells' ability to self-renew exhaustible under appropriate immune or metabolic pressure?

But perhaps the most tantalizing question is what is happening in female parasites. Schistosomes are unusual among Platyhelminthes in having two sexually distinct forms. Yet Collins and colleagues conducted their studies almost entirely on adult male organisms.

A remarkable feature of schistosome biology is that female parasites live enclosed within a specialized canal on the ventral surface of the male's body, and they rely on this niche to reach, and maintain, sexual maturity. The molecular basis for this reliance is unclear, but an organ called the vitellarium, which produces cells that are packaged into the egg with the fertilized ovum, is highly sensitive to the

presence of the male; it shrinks to a vestigial form in females that have become separated from their partners.

Vitellarial tissues can regrow if females mate again, possibly owing to the presence of vitellarium-specific stem cells called S1 cells⁵. How S1 cells are related to the neoblast-like cells identified by Collins *et al.* is unknown, but is potentially addressable using the approaches pioneered by the authors' lab. Such studies would be exciting, as they promise to reveal how the vitellarium responds to the presence of the male parasite. Given that egg production by schistosomes is central to both the transmission of infection (Fig. 1) and the development of disease, elucidating this process may also have practical value.

Working from a baseline established in planarians, Collins *et al.* have taken full advantage of advances in our understanding of the schistosome genome⁶ and the development of reverse-genetics approaches in

these organisms⁷. They have thereby made a highly informative and valuable cross-cultural foray from studying stem cells in free-living worms to studying them in parasitic worms². Rejuvenating indeed! ■

Edward J. Pearce is in the Department of Pathology and Immunology, Washington University in St Louis School of Medicine, St Louis, Missouri 63110, USA.
e-mail: edwardpearce@path.wustl.edu

1. King, C. H. & Dangerfield-Cha, M. *Chronic Illness* **4**, 65–79 (2008).
2. Collins, J. J. III *et al.* *Nature* **494**, 476–479 (2013).
3. Gotoh, N. *Curr. Stem Cell Res. Ther.* **4**, 9–15 (2009).
4. Doenhoff, M. J. *et al.* *Parasitology* **136**, 1825–1835 (2009).
5. Erasmus, D. A., Popiel, I. & Shaw, J. R. *Parasitology* **84**, 283–287 (1982).
6. Protasio, A. V. *et al.* *PLoS Negl. Trop. Dis.* **6**, e1455 (2012).
7. Krautz-Peterson, G., Bhardwaj, R., Faghiri, Z., Tararam, C. A. & Skelly, P. J. *Parasitology* **137**, 485–495 (2010).

CANCER

Stress mixes chromosomes

Chromosome-segregation errors during cell division may play a key part in tumour evolution. The long-awaited identification of a common genetic defect causing such errors comes with an interesting conceptual twist. SEE LETTER P.492

ANIEK JANSSEN & RENÉ H. MEDEMA

The classical view of cancer holds that the disease's characteristics arise through sequential acquisition of transforming mutations that eventually produce a cell that is well equipped for unrestricted proliferation in a given environment. Proliferation of this cell would therefore be expected to produce tumours comprised largely of cells of the same genetic make-up. But in reality, the cells in solid tumours display tremendous genetic variation, termed intratumour heterogeneity. Understanding the molecular basis of this heterogeneity will help to decipher the cellular pathways that promote tumour formation and progression, and could lead to the development of specific anticancer therapies. On page 492 of this issue, Burrell and co-workers¹ uncover a recurrent genetic defect in colorectal cancers that could initiate tumour heterogeneity. Their data provide a novel perspective on the origin of this aspect of cancer biology.

The genetic variation present in heterogeneous tumours is thought to be induced both by minor DNA mutations and by changes in the number and structure of chromosomes — referred to as chromosomal

instability (CIN)². Structural CIN produces gross chromosomal rearrangements, which may result from improper repair of damaged DNA³. Numerical CIN produces abnormal numbers of chromosomes (a situation called aneuploidy) and has been attributed to various defects occurring during cell division⁴. Cell division in normal, healthy cells leads to equal distribution of the replicated chromosomes between the two daughter cells. By contrast, cancer cells that exhibit chromosome instability (CIN⁺ cells) frequently missegregate their chromosomes, and this results in daughter cells with deviant chromosome numbers⁵. Interestingly, the two types of CIN are also intertwined: structural CIN can lead to numerical CIN^{6–8} and vice versa^{9,10}. Although CIN was identified in tumours almost two decades ago⁵, a common genetic cause has remained elusive until now.

“The data reveal that replication stress leads to structural and numerical chromosomal instability in most colorectal cancers.”

Burrell *et al.* describe a region on 18q, the longer arm of chromosome 18, that is subject

to frequent loss of one of its two copies in CIN⁺ colorectal-cancer cells. They observed this copy-number loss in more than 80% of CIN⁺ cell lines deriving from colorectal cancers and in samples taken from aneuploid colorectal tumours. The authors also identify three new genes within this region that function to suppress CIN: *PIGN*, *MEX3C* and *ZNF516*. They show that silencing of each of these genes triggers numerical and structural CIN in non-CIN⁺ colorectal-cancer cells, indicating that reduced expression of any one of these genes can produce a CIN⁺ phenotype. Thus, the authors have managed to identify the first common recurrent genetic defect associated with CIN.

But there is much more to this story. CIN has generally been assumed to be the consequence of dysfunction during mitotic cell division that causes whole-chromosome segregation errors. However, Burrell *et al.* show that the induction of CIN upon loss of *PIGN*, *MEX3C* or *ZNF516* can be ascribed to general defects in DNA replication, such as stalling of the replication fork (the site of unwinding of double-stranded DNA during replication) or slower replication. They also show that reducing such replicative stress in cultured cells in which *PIGN*, *MEX3C* or *ZNF516* has been silenced — by adding nucleosides to the cell cultures — leads to a reduction in segregation errors. A similar attenuation of segregation errors was seen after nucleoside treatment of CIN⁺ colorectal-cancer cells that have 18q copy-number loss.

Thus, the authors' data reveal that replication stress leads to structural and numerical CIN in most colorectal cancers, thereby challenging the widely held view that mitotic defects are the cause of numerical CIN. Instead, it seems that the defects in DNA replication cause DNA damage and aberrant chromosome structures, which in turn affect proper transmission of these chromosomes to daughter cells (Fig. 1). Such chromosome-segregation errors could subsequently promote further structural chromosomal aberrations, through the acquisition of DNA damage during cytokinesis (the final splitting of a dividing cell into two daughter cells) or the formation of micronuclei (cellular organelles containing chromosomal fragments)^{9,10}.

Despite the protective mechanisms that shield against replication-stress-induced DNA errors during cell division^{11,12}, Burrell and colleagues' careful analysis of colorectal-cancer cell lines confirms that chromosome missegregations in these cells are largely the result of replication errors. It remains to be seen, however, whether replication stress is the main driver of aneuploidy in cancer. We do not know how daughter cells deal with the damaged chromosomes that are caused by segregation errors induced by replication stress, and whether the resulting structural changes are propagated through subsequent cell cycles. In this respect, it will be interesting

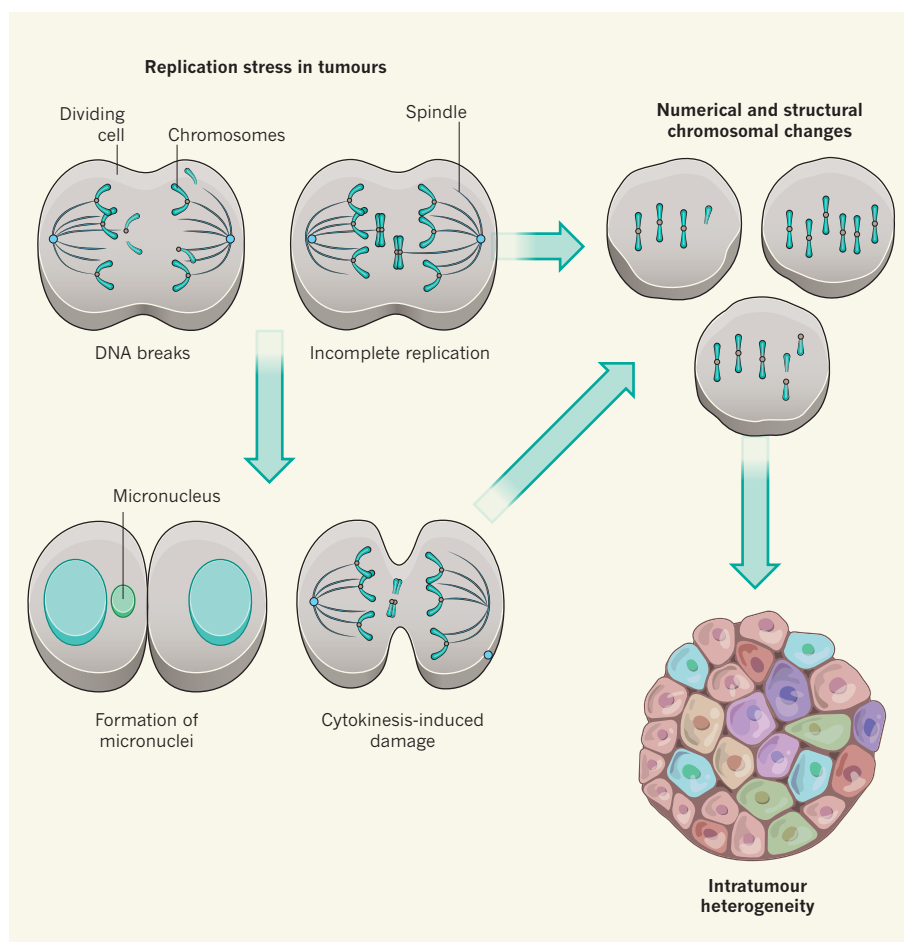


Figure 1 | Replication stress causes chromosomal abnormalities. Burrell *et al.*¹ show that many colorectal-cancer cells have lost one copy of a small region of chromosome 18 and that this mutation leads to faulty DNA replication during cell division. These replication defects cause breaks in the DNA or incomplete replication, which can lead to chromosome-segregation errors upon cell division, resulting in numerical and structural chromosomal abnormalities in the daughter cells. The segregation errors may also lead to structural chromosomal changes through aberrant replication in micronuclei (abnormal cellular organelles containing fragments of chromosomes) or by chromosomal breaks induced during cytokinesis (the final splitting of a dividing cell into two daughter cells). Burrell and colleagues propose that consecutive rounds of replication stress and chromosome-segregation errors may promote intratumour genetic heterogeneity.

to test whether the addition of nucleosides can suppress further changes in cell ploidy in CIN⁺ cells that have 18q loss.

Burrell and colleagues' data suggest that replication stress could promote a rapid 'genetic drift' within a tumour, through connected rounds of structural and numerical chromosomal changes (Fig. 1). Suppressing replicative stress in tumours could inhibit this genetic drift and might prevent the acquisition of resistance to therapies. Such resistance can arise when some cells of a tumour acquire resistance-conferring mutations that give them a proliferative advantage. Combining therapies that target replication stress with conventional therapies could therefore be beneficial in the treatment of CIN⁺ tumours. ■

Aniek Janssen and René H. Medema are in the Division of Cell Biology, the Netherlands Cancer Institute, 1066 CX Amsterdam, the Netherlands. **A.J.** is also in the

Department of Medical Oncology, University Medical Center Utrecht, and **R.H.M.** is also at the Cancer Genomics Center, the Netherlands.

e-mail: r.medema@nki.nl

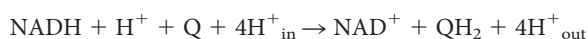
1. Burrell, R. A. *et al.* *Nature* **494**, 492–496 (2013).
2. Lengauer, C., Kinzler, K. W. & Vogelstein, B. *Nature* **396**, 643–649 (1998).
3. Thompson, S. L. & Compton, D. A. *Chromosome Res.* **19**, 433–444 (2011).
4. Holland, A. J. & Cleveland, D. W. *Nature Rev. Mol. Cell Biol.* **10**, 478–487 (2009).
5. Lengauer, C., Kinzler, K. W. & Vogelstein, B. *Nature* **386**, 623–627 (1997).
6. Ichijima, Y. *et al.* *PLoS ONE* **5**, e8821 (2010).
7. Chan, K. L., Palmieri-Pallag, T., Ying, S. & Hickson, I. D. *Nature Cell Biol.* **11**, 753–760 (2009).
8. Pampalona, J., Soler, D., Genescà, A. & Tusell, L. *Genes Chromosomes Cancer* **49**, 368–378 (2010).
9. Janssen, A., van der Burg, M., Szuhai, K., Kops, G. J. P. L. & Medema, R. H. *Science* **333**, 1895–1898 (2011).
10. Crasta, K. *et al.* *Nature* **482**, 53–58 (2012).
11. Harrigan, J. A. *et al.* *J. Cell Biol.* **193**, 97–108 (2011).
12. Lukas, C. *et al.* *Nature Cell Biol.* **13**, 243–253 (2011).

Crystal structure of the entire respiratory complex I

Rozbeh Baradaran¹, John M. Berrisford^{1†}, Gurdeep S. Minhas¹ & Leonid A. Sazanov¹

Complex I is the first and largest enzyme of the respiratory chain and has a central role in cellular energy production through the coupling of NADH:ubiquinone electron transfer to proton translocation. It is also implicated in many common human neurodegenerative diseases. Here, we report the first crystal structure of the entire, intact complex I (from *Thermus thermophilus*) at 3.3 Å resolution. The structure of the 536-kDa complex comprises 16 different subunits, with a total of 64 transmembrane helices and 9 iron–sulphur clusters. The core fold of subunit Nqo8 (ND1 in humans) is, unexpectedly, similar to a half-channel of the antiporter-like subunits. Small subunits nearby form a linked second half-channel, which completes the fourth proton-translocation pathway (present in addition to the channels in three antiporter-like subunits). The quinone-binding site is unusually long, narrow and enclosed. The quinone headgroup binds at the deep end of this chamber, near iron–sulphur cluster N2. Notably, the chamber is linked to the fourth channel by a ‘funnel’ of charged residues. The link continues over the entire membrane domain as a flexible central axis of charged and polar residues, and probably has a leading role in the propagation of conformational changes, aided by coupling elements. The structure suggests that a unique, out-of-the-membrane quinone-reaction chamber enables the redox energy to drive concerted long-range conformational changes in the four antiporter-like domains, resulting in translocation of four protons per cycle.

Complex I (also known as NADH:ubiquinone oxidoreductase) has a central role in the respiratory chain in mitochondria and many bacteria^{1–7}. It catalyses the transfer of two electrons from NADH to ubiquinone (Q), coupled to the translocation of four protons (current consensus value^{8,9}) across the bacterial or inner mitochondrial membrane:



The transfer of two electrons from NADH to oxygen, through complexes I, III (*bc*₁) and IV (cytochrome *c* oxidase), results in the translocation of ten protons across the membrane¹⁰, creating the proton motive force (PMF) for the synthesis of ATP by ATP synthase¹¹. Complex I is a reversible machine¹² that is able to use PMF and ubiquinol to reduce NAD⁺.

Mutations in complex I subunits lead to the most common human neurodegenerative diseases^{5,13}. The enzyme is also a key source of reactive oxygen species in mitochondria¹⁴, which can lead to mitochondrial DNA damage, and are implicated in Parkinson's disease¹⁵ and ageing¹⁶.

Complex I is one of the largest known membrane proteins. The mitochondrial enzyme consists of 44 different subunits (~980 kDa in total)^{17,18}. The simpler prokaryotic version normally comprises 14 ‘core’ subunits (~550 kDa total), highly conserved from bacteria to humans^{1,2,5,19,20}, suggesting that the mechanism is also conserved. Both enzymes contain equivalent redox components and have a similar L-shaped structure, formed by the hydrophilic and membrane domains^{2,5,21}. The ~30 ‘accessory’ subunits of the mitochondrial enzyme mostly form a protective shell around the core^{3,22,23}, although some may have a specialized functional role^{23–25}.

We determined the first structures of the eight-subunit hydrophilic domain of *T. thermophilus* complex I at up to 3.1 Å resolution^{26,27}. It contains all the redox centres of the enzyme: non-covalently bound

flavin mononucleotide (FMN) and nine iron–sulphur (Fe–S) clusters. NADH transfers two electrons to FMN as a hydride ion and then electrons are transferred one by one, along the uniquely long (95 Å) chain of seven conserved Fe–S clusters, to the quinone-binding site (Q site) at the interface with the membrane domain.

We subsequently determined the architecture of the entire *T. thermophilus* complex I at 4.5 Å resolution, with the membrane domain resolved at the level of arrangement of subunits and α -helices²¹. X-ray analysis at 6.3 Å resolution of the *Yarrowia lipolytica* mitochondrial enzyme was published later²⁸, but no subunits were identified and no models were deposited from this work owing to limited resolution. Currently all information on atomic structures of complex I is from our studies.

Recently we determined the 3.0 Å resolution structure of the membrane domain from *Escherichia coli* complex I²⁹. The three largest subunits, NuoL, NuoM and NuoN (known as Nqo12, Nqo13 and Nqo14 in *T. thermophilus*, respectively; Supplementary Table 3), are homologous to each other and to Na⁺/H⁺ antiporter complex (Mrp) subunits^{30,31}. Each contains 14 conserved transmembrane (TM) helices and a putative proton-translocation channel²⁹. However, the crystals lacked NuoH (Nqo8 and ND1 in *T. thermophilus* and humans, respectively), the only core subunit of unknown structure.

The overall architecture of complex I suggests that the coupling mechanism involves long-range conformational changes: there are no cofactors in the membrane and the antiporter-like subunits (hereafter termed ‘antiporters’ for brevity) are distant from the interface with the hydrophilic domain^{21,29}. Exactly how these changes are coupled to redox reactions remains unclear, although mechanical coupling elements have been suggested^{21,28,29}. Notably, Fe–S cluster N2, which donates electrons to the quinone, is ~25–30 Å away from the membrane surface²¹, suggesting that the quinone has to move out of the membrane to accept electrons. Nqo8 is the most conserved membrane subunit of complex I (Supplementary Fig. 1), forming the

¹Medical Research Council Mitochondrial Biology Unit, Wellcome Trust/MRC Building, Hills Road, Cambridge CB2 0XY, UK. [†]Present address: European Bioinformatics Institute, Cambridge CB10 1SD, UK.

interface with the hydrophilic domain and contributing to the Q site³². This subunit emerged only once during evolution, joining hydrogenase and antiporter modules of complex-I-related enzymes²⁰. Clearly, the atomic structure of the entire complex, including Nqo8, holds the key to understanding the enigmatic coupling mechanism.

Determination of structures

The diffraction of crystals of the entire *T. thermophilus* complex has been improved to 3.3 Å resolution (Methods). Crystals are, however, twinned and so to overcome the problem of model bias we crystallized the isolated *T. thermophilus* membrane domain. These crystals were non-twinned and contained subunit Nqo8. The structure was solved at 3.3 Å resolution by molecular replacement with our *E. coli* model (Protein Data Bank (PDB) code, 3RKO) (Supplementary Tables 1, 2 and Supplementary Fig. 2). It contains seven subunits (Nqo12 (16), Nqo13 (14), Nqo14 (14), Nqo10 (5), Nqo11 (3), Nqo7 (3) and Nqo8 (9), in which the numbers in parentheses indicate the number of TM helices in each subunit). Antiporters Nqo12–14 show an arrangement of helices (Supplementary Fig. 3) and key residues similar to the *E. coli* structure: each subunit contains two inverted-symmetry related half-channels. The cytoplasm-linked TM4–8 half-channel contains a central lysine on the discontinuous, thus flexible, TM7 (here termed Lys TM7) and its pK_a-modulating glutamate on TM5 (here termed Glu TM5), whereas the periplasm-linked TM9–13 half-channel contains a central lysine (Glu in Nqo13) on discontinuous TM12 (here termed Lys TM12) (Fig. 1b). The half-channels are linked into a single full proton-translocation channel by charged residues, including a

lysine from the broken (partly unwound in the middle) TM8 (His in Nqo12). The long connecting helix HL, from the carboxy-terminal extension of Nqo12, is straighter in *T. thermophilus* than in *E. coli* (Supplementary Fig. 3). On the opposite side of the domain, the β-hairpin–helix connecting element (βH) shows a very similar arrangement in both species. Thus, both previously proposed coupling elements²⁹ seem to be common complex I features.

T. thermophilus Nqo8 contains eight conserved TM helices and an additional C-terminal TM helix. Unexpectedly, TM1 of Nqo7 (NuoA) is in a different position compared to the *E. coli* structure, forming a part of the Nqo8 helical bundle (Fig. 1a and Supplementary Fig. 3). Presumably, when NuoH dissociates in *E. coli*, this helix moves closer to the remaining subunits.

The *T. thermophilus* membrane domain structure was then used with the hydrophilic domain structure (PDB code, 319V) to solve the structure of the entire complex by molecular replacement. The 3.3 Å resolution structure (Fig. 1a) of the 536-kDa complex contains 9 hydrophilic subunits with 9 Fe–S clusters and 1 FMN molecule, as well as 7 membrane subunits with 64 TM helices (Supplementary Tables 1 and 2). This includes the novel assembly factor-like hydrophilic subunit Nqo16, essential for crystallization but not necessary for activity (Supplementary Discussion). Although many assembly factors for mitochondrial complex I are known³³, this is, to our knowledge, the first example for bacterial complex I.

Features at the interface between the two main domains, missing in the individual structures, were resolved in that of the entire complex, including loops from Nqo4, Nqo7 and Nqo8 (Supplementary Figs 4 and 5). The Q site is found, as expected^{21,34}, at the interface of Nqo4, Nqo6 and Nqo8, and is described below. Most of the interactions between the two domains involve Nqo8 (Supplementary Discussion and Supplementary Table 4), including the highly conserved first cytoplasmic loop. Another highly conserved Nqo8 loop (third cytoplasmic loop) lines the quinone cavity. The first cytoplasmic loop from Nqo7 (NuoA) wraps around Nqo8, stabilizing the interface between the domains.

Subunit Nqo8 (ND1) forms part of a proton channel

The fold of Nqo8 is unusual, with some TM helices very short (TM5, 14 residues), others very long (TM1, 35 residues), and with nearly all helices highly tilted relative to membrane normal (Fig. 2). Unexpectedly, TM helices 2–6 can be superimposed (root mean squared deviation 2.1–2.6 Å over ~140 residues, PDBeFOLD) on to the antiporters' half-channel TM helices 4–8 or 9–13 (Fig. 2c). This similarity is not apparent from the sequence (~11–18% identity). Although in the antiporters most helices are roughly normal to the membrane, TM helices 2–6 from Nqo8 are tilted considerably, up to 45°. By contrast, TM1 is tilted in the opposite direction, so that it crosses TM6 at nearly 90°. TM9 is peripheral, consistent with its absence in most species.

In Nqo8, charged residues are found in similar positions to key antiporter residues: Glu 130 and Glu 163 in the Glu TM5 position and Glu 213 and Glu 248 near Lys TM7 (Fig. 2c). Overall, Nqo8 contains many more charged residues in the membrane (Fig. 3a) compared to the antiporters, and many of these residues (including Glu 163 and Glu 213) are conserved in complex I and in membrane-bound hydrogenases (Supplementary Figs 1 and 6). They form an unusual chain (or 'funnel') of charged residues leading from the Q site to a remarkable network of four interacting carboxylates deep in the membrane (Glu 130, Glu 163 and Glu 213 from Nqo8, plus conserved 7(Asp 72) (in which prefix indicates subunit)). The charged network congregates around the highly conserved broken 10(TM3), a hotspot for human disease mutations²⁹. On the other side of the break, conserved 10(Tyr 59) interacts with essential 11(Glu 32), part of a fourth proton-translocation channel proposed previously²⁹. Nqo11 superimposes with helices 4–6 from the antiporter half-channels, overlaying Glu 32 with Glu TM5 (ref. 29).

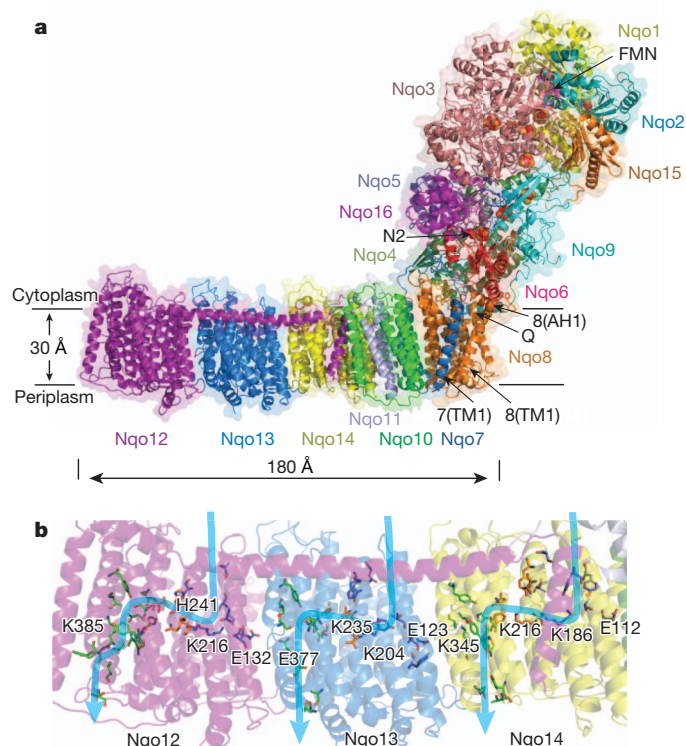


Figure 1 | Structure of the entire complex I from *T. thermophilus*. **a**, An overview. FMN and Fe–S clusters are shown as magenta and red–orange spheres, respectively, with cluster N2 labelled. Key helices around the entry point (Q) into the quinone-reaction chamber, and approximate membrane position, are indicated. **b**, Putative proton-translocation channels in the antiporter-like subunits. Polar residues lining the channels are shown as sticks with carbon in dark blue for the first (N-terminal) half-channel, in green for the second (C-terminal) half-channel and in orange for connecting residues. Key residues—Glu TM5 and Lys TM7 from the first half-channel, Lys/His TM8 from the connection and Lys/Glu TM12 from the second half-channel—are labelled. Approximate proton-translocation paths are indicated by blue arrows.

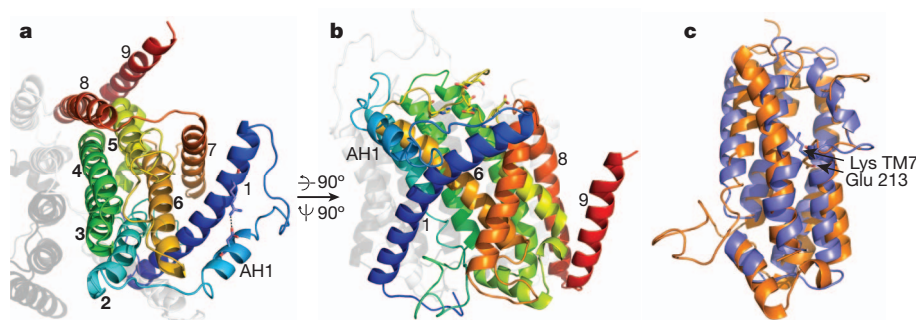


Figure 2 | Fold of subunit Nqo8. Coloured blue to red from N to C terminus. Neighbouring subunits Nqo7 and Nqo10 are shown in light and dark grey, respectively. **a**, View from the cytoplasm. TM helices are numbered, with helices corresponding to the antiporter half-channel in bold. The conserved salt bridge Arg 36–Asp 62, supporting amphipathic helix AH1, is shown. **b**, Side

view. Charged residues from the conserved third cytoplasmic loop, mainly lining the Q cavity, are shown as sticks. **c**, Alignment of TM helices 2–6 of Nqo8 (orange) with TM helices 4–8 of Nqo13 (blue). Lys TM7 from Nqo13 and Glu 213 from Nqo8 TM5 are shown as sticks.

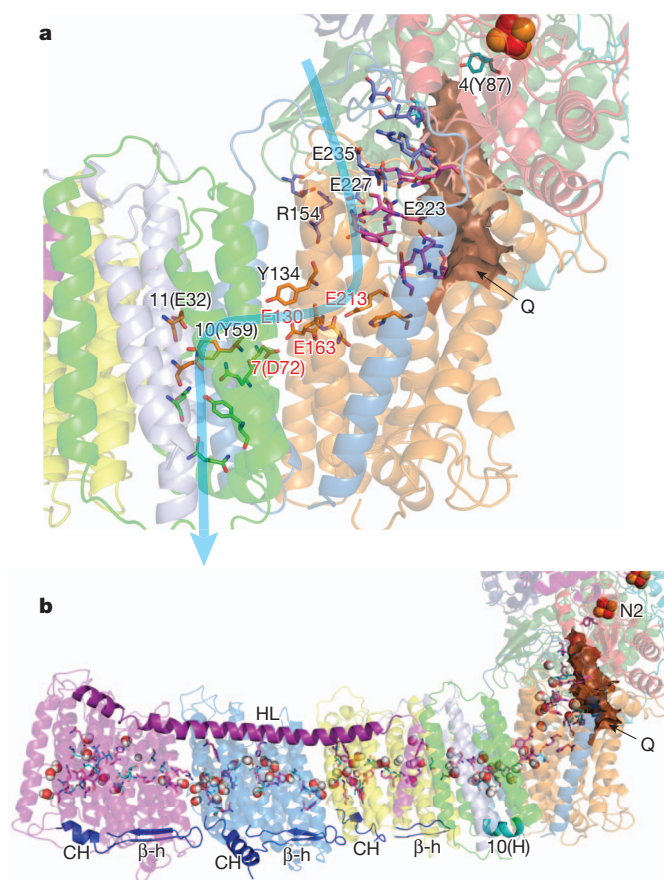


Figure 3 | E-channel and central hydrophilic axis. **a**, E-channel (fourth proton-translocation channel). Charged and polar residues constituting the channel are shown as sticks. Central residues are shown with carbon in yellow, those forming a link to the Q site in magenta, those that link to the cytoplasm in blue, those that link to the periplasm in green and those interacting with the quinone headgroup in cyan. Key residues are labelled, with the Glu/Asp quartet in red. Number prefix indicates subunit (omitted for Nqo8). Approximate proton-translocation path is indicated by blue arrow. Quinone cavity is shown with surface in brown. **b**, Central axis of charged and polar residues. Residues shown are either central to half-channels or are forming the connection between them (charged residues have carbon in magenta, polar in cyan). Most of them are located near the breaks in key helices TM7, TM8 and TM12 (antiporters), 10(TM3) and 8(TM5). Predicted waters nearby, modelled using Dowser software⁴⁴, are shown as spheres. Connecting elements are shown in solid colours: helix HL in magenta and the β H element in blue, with the C-terminal helix CH²⁹ and the β -hairpin (β -h) from each antiporter labelled. The contacting Nqo10 helix is labelled 10(H). Subunits are coloured as in Fig. 1.

Thus, the first half-channel formed by Nqo8 is linked to the second half-channel in Nqo10 and Nqo11, with 8(TM5) and 10(TM3) in the roles of the key discontinuous antiporter helices TM7 and TM12. This strongly suggests that input from the cytoplasm into the fourth channel is not, as previously proposed²⁹, at the interface between Nqo14 and Nqo11 (which in *T. thermophilus* is more clearly closed from the cytoplasm than in *E. coli*), but is through Nqo8 instead. As with the amino-terminal half-channel of the antiporters, the Nqo8 half-channel is closed from the periplasm by large hydrophobic residues but is connected through an extensive network of polar residues both to the cytoplasm and to the Q site. Furthermore, similarly to the C-terminal half-channel of the antiporters, the Nqo10/Nqo11 half-channel is blocked from the cytoplasm, but is connected to the periplasm by polar residues. The two half-channels are linked into a single channel by the Glu/Asp quartet and putative water molecules (Fig. 3). We refer to it here as the ‘E-channel’ owing to abundance of glutamates in its centre. Many residues in the E-channel are conserved and essential for activity (Supplementary Table 7). Therefore it is, unexpectedly, arranged similarly to the three channels within the antiporters. This implies that proton-pumping stoichiometry in complex I is indeed 4 (not 3, as proposed recently³⁵).

Unique quinone–reaction chamber

To determine exactly where quinone binds, intact complex I was co-crystallized, or crystals soaked with the quinone analogues piericidin A (a complex I inhibitor) and decylubiquinone. Although *in vivo* *T. thermophilus* complex I uses menaquinone-8, it is also fully active with decylubiquinone²¹, and, in contrast to *E. coli* complex I³⁶, the *T. thermophilus* enzyme does not contain any bound endogenous quinone after purification. X-ray data (Supplementary Table 1) clearly show (Fig. 4a, b) that piericidin A and decylubiquinone bind in a very similar manner, ~ 15 Å away from the membrane surface, at the deep end of a long narrow cavity. In this position, the quinone headgroup is ~ 12 Å (centre-to-centre) from the Fe–S cluster N2, appropriate for efficient electron transfer³⁷. One of the decylubiquinone ketone groups is, as predicted^{26,34}, hydrogen bonded to 4(Tyr 87), whereas another interacts, unexpectedly, with 4(His 38). Both residues are invariant and essential for activity^{34,38}.

One of the most surprising structural features is that this 30-Å long chamber is completely enclosed from the solvent, with only a narrow (approximately $2\text{--}3 \times 4\text{--}5$ Å) apparent entry point for the quinone, framed by helices TM1, TM6 and amphipathic AH1 from Nqo8 (Figs 1a and 4), as well as TM1 from Nqo7. All residues facing the lipid bilayer here are hydrophobic, but the inside of the chamber is lined, unexpectedly, mostly by hydrophilic residues, especially in the area (‘front’) facing the tip of the membrane domain (to the left in Fig. 4d). However, at the opposite side (‘back’), a hydrophobic patch formed, surprisingly, mainly by residues from hydrophilic subunits

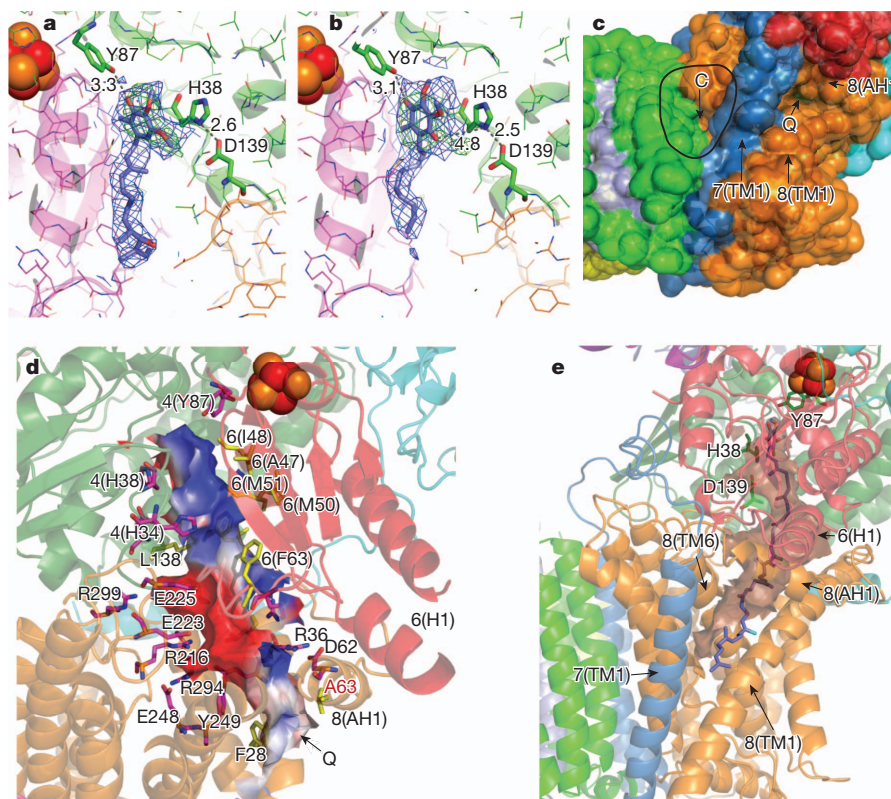


Figure 4 | Quinone-reaction chamber. Subunits are coloured as in Fig. 1. Fe–S cluster N2 is shown as red–orange spheres. **a, b**, Experimental electron density ($2mF_o-DF_c$ in blue, contoured at 1σ , and mF_o-DF_c in green, contoured at 3σ) and models obtained from crystals with bound piericidin A (**a**) and decylubiquinone (**b**). Difference electron density was calculated before ligand modelling. Nqo4 residues interacting with the headgroup are indicated. Potential polar interactions are shown labelled with distances in ångström. **c**, Surface (solvent-accessible) representation of the interface between two main domains. The empty crevice (C, circled; Supplementary Discussion) between Nqo10 and 7(TM1)/Nqo8, as well as helices framing the entry point to the quinone site (Q) are indicated. **d**, Quinone-reaction chamber, with its internal

solvent-accessible surface coloured red for negative, white for neutral and blue for positive surface charges. Charged residues lining the cavity are shown with carbon in magenta and hydrophobic residues in yellow. Residues are labelled with prefix indicating subunit (omitted for Nqo8). Ala 63, the site of the primary Leber's hereditary optic neuropathy disease mutation⁴⁵, is labelled in red. **e**, Theoretical model of bound ubiquinone-10. Carbon atom in cyan indicates the eighth isoprenoid unit. Nqo4 residues interacting with the headgroup are indicated. The quinone chamber is shown with surface in brown and helices framing its entry point are indicated. Movable helix 6(H1)²⁷, interacting with 8(AH1), is also labelled.

Nqo4 and Nqo6, extends towards the entrance, sufficient to accommodate the quinone tail. The cavity front is mostly negatively charged, whereas the back is neutral and the 'top' (near cluster N2) is positively charged (Fig. 4d). The ionizable residues lining the chamber are all highly conserved (Supplementary Fig. 6 and Supplementary Table 8) and mutations in many of these residues lead to human diseases and loss of complex I activity⁵ (Supplementary Tables 5 and 6).

As the quinone chamber is long and narrow, it will restrict the quinone tail to an extended conformation. Thus, knowing the headgroup position, we can model the mode of binding of native ubiquinone with eight or ten isoprenoid units (Fig. 4e). Remarkably, only the last one to three isoprenoid units will protrude out of the cavity into the lipid. The passage around the entrance is narrower than the rest of the cavity, so that the quinone tail will block solvent access to the cavity, sealing the reaction chamber. That is an unexpected feature and suggests that slight structural re-arrangements are necessary to allow the quinone headgroup to move in and out of the cavity.

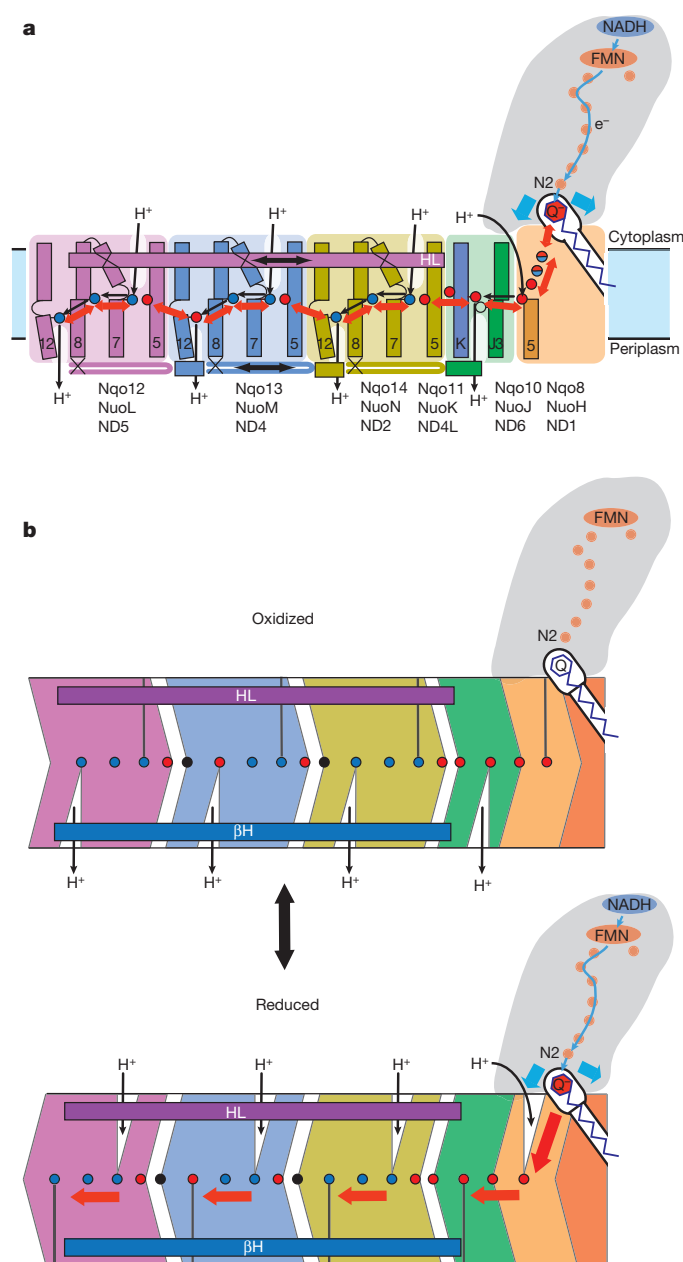
Thus, complex I contains a unique, long enclosed reaction chamber, where nearly the entire quinone molecule can be accommodated, in contrast to other membrane proteins, in which Q sites are usually open (Supplementary Discussion). It is possible that sealing off the cavity has functional importance, although it is not necessary for proton pumping *per se*, as pumping proceeds with short-tailed ubiquinone-1 and decylubiquinone^{8,12}. However, even with short-tailed quinones, steric restrictions in the cavity will not allow solvent access to the bound headgroup. Previously, a second quinone-binding site

in complex I has been discussed³⁹, but structural data argues strongly against its existence (Supplementary Discussion).

Coupling mechanism

The structure provides clear implications for the mechanism of coupling between electron transfer and proton translocation in complex I, described in Supplementary Discussion and summarized in brief here. Although a part of the redox energy in complex I is used upon reduction of cluster N2 (ref. 27), most of it is released during quinone chemistry²⁰. Upon quinone reduction, either Q^{2-} or key charged residues nearby are likely to remain unprotonated in order to drive conformational changes. The enclosed quinone-reaction chamber is well suited for this purpose: owing to tight protein packing near the bound headgroup, the quinone can be protonated only through the coordinating 4(Tyr 87) and 4(His 38). Notably, the charged species can exist in the chamber because it is relatively hydrophilic and distal from the membrane. The Q site is linked to the Glu/Asp quartet in the centre of the E-channel by a hydrophilic funnel, so these negatively charged species can interact electrostatically, driving conformational changes in this channel. Additional driving force is probably provided by moving upon N2 reduction Nqo4 and Nqo6 helices^{27,40}, which directly interact with flexible parts of Nqo8.

One of the most fascinating features of the structure is that the hydrophilic funnel is then continued, through a series of conserved residues, all the way to the tip of Nqo12. Interacting charged and polar residues, surrounded by a 'river' of water molecules, form a



continuous hydrophilic axis in the middle of the membrane, spanning the entire length of the membrane domain (Fig. 3b). Its residues are found in the half-channels and in the connections between them and most are on or near the breaks in discontinuous helices, allowing for the flexibility along this axis, linking membrane subunits in an overall conformational cycle. Tight coupling observed between proton translocation and quinone chemistry²⁹ can be explained if opening of the Q-site entrance to allow quinone in and out forms a part of this cycle.

Conformational changes probably involve both the previously described coupling elements (helix HL and β H element²⁹) and the central hydrophilic axis. The architecture of this axis, discussed previously²⁹ but visible only now in its full extent, suggests that it probably has a prominent role in the cycle. The most plausible scenario is that the electrostatically (and N2)-driven E-channel drives conformational changes first in the neighbouring antiporter Nqo14 (NuoN), which in its turn drives distal subunits Nqo13 (NuoM) and Nqo12 (NuoL), all through the central axis. The extent of the movement of the two coupling elements during the catalytic cycle is currently unclear, but they probably contribute at least to the coordination between the three antiporters. The concerted conformational changes

(conformational switch⁴¹) would lead to changes in pK_a (Supplementary Table 9) and solvent exposure of key residues, resulting in proton translocation (Fig. 5).

The view that anionic ubiquinol is the main driving force for the conformational changes is supported by evolutionary considerations, now including the antiporter fold of Nqo8: membrane-bound proton-translocating hydrogenases, ancestors of complex I²⁰, do not use quinone and probably evolved when soluble hydrogenase attached to the antiporter complex (which is driven essentially by membrane polarization). Sealing of the interface between the two complexes, containing charged nickel-iron centre reaction intermediates and thus mimicking membrane polarization, would immediately result in coupling of the oxidoreductase and proton-translocation activities.

We can now finally begin to make sense of the enormous complexity of this molecular machine and understand how it evolved, with all pieces of the puzzle falling into place. The three new and unexpected features of the structure—a sealed Q chamber, an antiporter-like Nqo8 fold and a hydrophilic funnel connecting quinone site to the E-channel—combine to suggest that redox-driven conformational changes propagate to four proton channels through the unique central hydrophilic axis, aided by coupling elements. Mutations in any core complex I subunit, whether known to cause human disease or introduced in model studies, can now be understood on a structural basis: observed effects are consistent with the proposed mechanism (Supplementary Discussion, Supplementary Fig. 7 and Supplementary Tables 5 and 6). Further details of conformational changes and how exactly they lead to proton translocation will need clarification from structures of different redox states of the enzyme and time-resolved studies.

METHODS SUMMARY

Intact complex I from *T. thermophilus* was purified as described previously²¹, except that the DEAE column was replaced by a Mono-S column. The membrane and hydrophilic domains were separated on a gel-filtration column after treatment of intact complex I with 300 mM sodium acetate, pH 4.0, 100 mM NaCl and 50 mM EDTA.

Crystals were grown using either hanging drop (membrane domain in *n*-undecyl- β -maltoside) or sitting drop (intact complex in *n*-tridecyl- β -maltoside) crystallization. The structure of the membrane domain was solved by molecular replacement with the *E. coli* model (PDB code, 3RKO), followed by Rosetta_MR protocol in PHENIX⁴² and DEN (deformable elastic network) refinement in CNS⁴³. Subunit Nqo8 was built manually. The structure of the entire complex was solved by molecular replacement with this membrane domain model and the previous

hydrophilic domain model (PDB code, 3I9V). Anomalous data from the Fe edge (using the intrinsic Fe-S clusters) allowed modelling of novel features at the interface of the domains. Both structures were refined to excellent statistics (Supplementary Table 1) in cycles of manual re-building and refinement in PHENIX with secondary structure/NCS restraints and using TLS.

Full Methods and any associated references are available in the online version of the paper.

Received 4 September; accepted 21 December 2012.

Published online 17 February 2013.

- Walker, J. E. The NADH:ubiquinone oxidoreductase (complex I) of respiratory chains. *Q. Rev. Biophys.* **25**, 253–324 (1992).
- Yagi, T. & Matsuno-Yagi, A. The proton-translocating NADH-quinone oxidoreductase in the respiratory chain: the secret unlocked. *Biochemistry* **42**, 2266–2274 (2003).
- Brandt, U. Energy converting NADH:quinone oxidoreductase (complex I). *Annu. Rev. Biochem.* **75**, 69–92 (2006).
- Ohnishi, T. Iron-sulfur clusters/semiquinones in complex I. *Biochim. Biophys. Acta* **1364**, 186–206 (1998).
- Sazanov, L. A. Respiratory complex I: mechanistic and structural insights provided by the crystal structure of the hydrophilic domain. *Biochemistry* **46**, 2275–2288 (2007).
- Hirst, J. Towards the molecular mechanism of respiratory complex I. *Biochem. J.* **425**, 327–339 (2010).
- Sazanov, L. A. *A Structural Perspective on Respiratory Complex I: Structure and Function of NADH:Ubiquinone Oxidoreductase* (Springer, 2012).
- Galkin, A. S., Grivennikova, V. G. & Vinogradov, A. D. H⁺/2e stoichiometry in NADH-quinone reductase reactions catalyzed by bovine heart submitochondrial particles. *FEBS Lett.* **451**, 157–161 (1999).
- Galkin, A., Droese, S. & Brandt, U. The proton pumping stoichiometry of purified mitochondrial complex I reconstituted into proteoliposomes. *Biochim. Biophys. Acta* **1757**, 1575–1581 (2006).
- Moser, C. C., Farid, T. A., Chobot, S. E. & Dutton, P. L. Electron tunneling chains of mitochondria. *Biochim. Biophys. Acta* **1757**, 1096–1109 (2006).
- Watt, I. N., Montgomery, M. G., Runswick, M. J., Leslie, A. G. & Walker, J. E. Bioenergetic cost of making an adenosine triphosphate molecule in animal mitochondria. *Proc. Natl Acad. Sci. USA* **107**, 16823–16827 (2010).
- Vinogradov, A. D. Catalytic properties of the mitochondrial NADH-ubiquinone oxidoreductase (complex I) and the pseudo-reversible active/inactive enzyme transition. *Biochim. Biophys. Acta* **1364**, 169–185 (1998).
- Schapiro, A. H. Human complex I defects in neurodegenerative diseases. *Biochim. Biophys. Acta* **1364**, 261–270 (1998).
- Murphy, M. P. How mitochondria produce reactive oxygen species. *Biochem. J.* **417**, 1–13 (2009).
- Dawson, T. M. & Dawson, V. L. Molecular pathways of neurodegeneration in Parkinson's disease. *Science* **302**, 819–822 (2003).
- Balaban, R. S., Nemoto, S. & Finkel, T. Mitochondria, oxidants, and aging. *Cell* **120**, 483–495 (2005).
- Carroll, J. et al. Bovine complex I is a complex of 45 different subunits. *J. Biol. Chem.* **281**, 32724–32727 (2006).
- Balsa, E. et al. NDUFA4 is a subunit of complex IV of the mammalian electron transport chain. *Cell Metab.* **16**, 378–386 (2012).
- Yip, C. Y., Harbour, M. E., Jayawardena, K., Fearnley, I. M. & Sazanov, L. A. Evolution of respiratory complex I: “supernumerary” subunits are present in the α -proteobacterial enzyme. *J. Biol. Chem.* **286**, 5023–5033 (2011).
- Efremov, R. G. & Sazanov, L. A. The coupling mechanism of respiratory complex I – a structural and evolutionary perspective. *Biochim. Biophys. Acta* **1817**, 1785–1795 (2012).
- Efremov, R. G., Baradaran, R. & Sazanov, L. A. The architecture of respiratory complex I. *Nature* **465**, 441–445 (2010).
- Efremov, R. G. & Sazanov, L. A. Respiratory complex I: ‘steam engine’ of the cell? *Curr. Opin. Struct. Biol.* **21**, 532–540 (2011).
- Angerer, H. et al. A scaffold of accessory subunits links the peripheral arm and the distal proton-pumping module of mitochondrial complex I. *Biochem. J.* **437**, 279–288 (2011).
- Hirst, J., Carroll, J., Fearnley, I. M., Shannon, R. J. & Walker, J. E. The nuclear encoded subunits of complex I from bovine heart mitochondria. *Biochim. Biophys. Acta* **1604**, 135–150 (2003).
- Althoff, T., Mills, D. J., Popot, J. L. & Kuhlbrandt, W. Arrangement of electron transport chain components in bovine mitochondrial supercomplex I₁III₂IV₁. *EMBO J.* **30**, 4652–4664 (2011).
- Sazanov, L. A. & Hinchliffe, P. Structure of the hydrophilic domain of respiratory complex I from *Thermus thermophilus*. *Science* **311**, 1430–1436 (2006).
- Berrisford, J. M. & Sazanov, L. A. Structural basis for the mechanism of respiratory complex I. *J. Biol. Chem.* **284**, 29773–29783 (2009).
- Hunte, C., Zickermann, V. & Brandt, U. Functional modules and structural basis of conformational coupling in mitochondrial complex I. *Science* **329**, 448–451 (2010).
- Efremov, R. G. & Sazanov, L. A. Structure of the membrane domain of respiratory complex I. *Nature* **476**, 414–420 (2011).
- Fearnley, I. M. & Walker, J. E. Conservation of sequences of subunits of mitochondrial complex I and their relationships with other proteins. *Biochim. Biophys. Acta* **1140**, 105–134 (1992).
- Mathiesen, C. & Hagerhall, C. Transmembrane topology of the NuoL, M and N subunits of NADH:quinone oxidoreductase and their homologues among membrane-bound hydrogenases and bona fide antiporters. *Biochim. Biophys. Acta* **1556**, 121–132 (2002).
- Sekiguchi, K., Murai, M. & Miyoshi, H. Exploring the binding site of acetogenin in the ND1 subunit of bovine mitochondrial complex I. *Biochim. Biophys. Acta* **1787**, 1106–1111 (2009).
- Nouws, J., Nijtmans, L. G., Smeitink, J. A. & Vogel, R. O. Assembly factors as a new class of disease genes for mitochondrial complex I deficiency: cause, pathology and treatment options. *Brain* **135**, 12–22 (2012).
- Angerer, H. et al. Tracing the tail of ubiquinone in mitochondrial complex I. *Biochim. Biophys. Acta* **1817**, 1776–1784 (2012).
- Wikström, M. & Hummer, G. Stoichiometry of proton translocation by respiratory complex I and its mechanistic implications. *Proc. Natl Acad. Sci. USA* **109**, 4431–4436 (2012).
- Verkhovsky, M., Bloch, D. A. & Verkhovskaya, M. Tightly-bound ubiquinone in the *Escherichia coli* respiratory Complex I. *Biochim. Biophys. Acta* **1817**, 1550–1556 (2012).
- Page, C. C., Moser, C. C., Chen, X. & Dutton, P. L. Natural engineering principles of electron tunnelling in biological oxidation–reduction. *Nature* **402**, 47–52 (1999).
- Kashani-Poor, N., Zwicker, K., Kerscher, S. & Brandt, U. A central functional role for the 49-kDa subunit within the catalytic core of mitochondrial complex I. *J. Biol. Chem.* **276**, 24082–24087 (2001).
- Ohnishi, T., Nakamaru-Ogiso, E. & Ohnishi, S. T. A new hypothesis on the simultaneous direct and indirect proton pump mechanisms in NADH-quinone oxidoreductase (complex I). *FEBS Lett.* **584**, 4131–4137 (2010).
- Berrisford, J. M., Thompson, C. J. & Sazanov, L. A. Chemical and NADH-induced, ROS-dependent, cross-linking between subunits of complex I from *Escherichia coli* and *Thermus thermophilus*. *Biochemistry* **47**, 10262–10270 (2008).
- Bai, F. et al. Conformational spread as a mechanism for cooperativity in the bacterial flagellar switch. *Science* **327**, 685–689 (2010).
- Adams, P. D. et al. PHENIX: building new software for automated crystallographic structure determination. *Acta Crystallogr. D* **58**, 1948–1954 (2002).
- Brunger, A. T. Version 1.2 of the Crystallography and NMR system. *Nature Protocols* **2**, 2728–2733 (2007).
- Zhang, L. & Hermans, J. Hydrophilicity of cavities in proteins. *Proteins* **24**, 433–438 (1996).
- Huoponen, K., Viikari, J., Aula, P., Nikoskelainen, E. K. & Savontaus, M. L. A new mtDNA mutation associated with Leber hereditary optic neuroretinopathy. *Am. J. Hum. Genet.* **48**, 1147–1153 (1991).

Supplementary Information is available in the online version of the paper.

Acknowledgements This work was funded by the Medical Research Council. We thank the European Synchrotron Radiation Facility (ESRF) and the Swiss Light Source (SLS) for provision of synchrotron radiation facilities. We are grateful to the staff of beamlines ID29, ID23-2 (ESRF) and X06SA (SLS) for assistance.

Author Contributions R.B. purified and crystallized the intact complex; J.M.B. purified and crystallized the membrane domain; G.S.M. performed co-crystallization and soaks with quinone analogues; all authors collected and analysed X-ray data; L.A.S. designed and supervised the project, analysed data and wrote the manuscript, with contributions from all authors.

Author Information The coordinates and structure factors have been deposited in the Protein Data Bank under accession numbers 4HE8 (membrane domain) and 4HEA (entire complex). Reprints and permissions information is available at www.nature.com/reprints. The authors declare no competing financial interests. Readers are welcome to comment on the online version of the paper. Correspondence and requests for materials should be addressed to L.A.S. (sazanov@mrc-mbu.cam.ac.uk).

METHODS

Protein purification. Intact complex I from *T. thermophilus* was purified as described previously²¹, except that the DEAE column was replaced by a Mono S cation-exchange column. Fractions from the ANX column were diluted to ~5 mM NaCl with buffer A (20 mM Bis-Tris, pH 6.0, 0.002% phenylmethylsulphonyl fluoride (PMSF), 2 mM CaCl₂, 10% (v/v) glycerol and 0.05% *n*-tridecyl- β -maltoside (TDM)) and applied to a Mono S HR 16/10 column, equilibrated with buffer A. The protein was eluted with a linear gradient of buffer B (0.5 M NaCl in buffer A), using a Gilson high-performance liquid chromatography (HPLC) system at ~22 °C, and the fractions were assessed by SDS-PAGE. Two peaks of NADH:FeCy activity contained complex I lacking Nqo16 protein in the first peak, eluting at ~80 mM NaCl, and complex I with Nqo16 protein in the second peak, eluting at ~100 mM NaCl. These two peak fractions were pooled separately, concentrated to about 1 ml using 100-kDa molecular-weight cutoff (MWCO) concentrators and each applied to a HiLoad 16/60 Superdex 200 gel-filtration column, equilibrated with GF buffer (buffer A with 100 mM NaCl). Fractions from each run were pooled on the basis of purity (assessed by SDS-PAGE), concentrated to about 25 mg ml⁻¹ and an additional 15% glycerol added for storage in liquid nitrogen. Only the protein containing Nqo16 was crystallizable.

The membrane and hydrophilic subunits were separated by treatment of intact complex I at pH 4.0. Purified complex I (2 mg) was incubated in 300 mM sodium acetate, pH 4.0, 100 mM NaCl, 50 mM EDTA buffer, 25% (v/v) ethylene glycol and 0.03% (w/v) *n*-undecyl- β -maltoside (UDM) for 3 h at ~22 °C. The protein solution was loaded into a HiLoad 16/60 Superdex 200 gel-filtration column equilibrated with buffer M (20 mM Bis-Tris, pH 6.0, 2 mM CaCl₂, 100 mM NaCl, 10% ethylene glycol and 0.03% UDM). Fractions containing the membrane domain were pooled on the basis of purity (assessed by SDS-PAGE), concentrated to about 10 mg ml⁻¹ using 100-kDa MWCO concentrators and used immediately for crystallization trials. In addition to membrane domain subunits, the preparation contained the hydrophilic subunits Nqo4, Nqo5, Nqo6 and Nqo9, which dissociated upon crystallization.

Crystallization. Crystals of intact *T. thermophilus* complex I were grown at 23 °C using sitting drop crystallization. First, purified complex I (18 mg ml⁻¹ in 20 mM Bis-Tris, pH 6.0, 2 mM CaCl₂, 100 mM NaCl, 0.002% PMSF, 25% glycerol and about 2% TDM) was incubated with additional TDM detergent (final concentration of about 4% (w/v)) at ~22 °C, and then mixed at 2:1 (v/v) ratio with crystallization reagent comprising 100 mM Bis-Tris, pH 6.0, 19–24% (w/v) polyethylene glycol (PEG) 4000, 100 mM KCl, 100 mM glutaric acid, pH 6.0, and 2.2 mM fos-choline-8, fluorinated. The addition of extra TDM before crystallization trials improved the size of the rod crystals (to about 50 × 50 × 500–700 μ m). Crystals used for the iron peak data collection were grown in similar conditions, except that the fos-choline-8 additive in the crystallization reagent was replaced by either 0.6% (w/v) *n*-dodecyl- β -maltoside or 7.6 mM 4-cyclohexyl-1-butyl- β -D-maltoside (CYMAL-4). Different detergent additives promoted crystal growth to a variable extent but they did not affect diffraction properties. Crystals were fully grown within 1 week. They did not tolerate dehydration and were cryoprotected in 100 mM Bis-Tris, pH 6.0, 9% PEG 4000, 50 mM KCl, 50 mM glutaric acid, pH 6.0, 25% ethylene glycol and 0.01% TDM before plunging into liquid nitrogen.

Crystals of the membrane domain of *T. thermophilus* complex I were grown at 17 °C using hanging drop crystallization. Purified membrane domain (10 mg ml⁻¹ in 20 mM Bis-Tris, pH 6.0, 2 mM CaCl₂, 100 mM NaCl, 10% ethylene glycol and about 1% UDM) was mixed with crystallization reagent comprising 100 mM phosphate-citrate buffer, pH 4.5, 26% (v/v) PEG 300 and 5 mM 3-[(3-cholamidopropyl)dimethylammonio]-1-propanesulphonate (CHAPS) at 1:1 (v/v) ratio. Crystals grew for about 2 weeks and were rectangular shaped (about 100 × 100 × 500–700 μ m). Crystals were dehydrated and cryoprotected in 100 mM phosphate-citrate, pH 4.5, 26% PEG 300, 30% PEG 3350, 0.03% UDM, 5 mM CHAPS and 7% ethylene glycol for 6 h before plunging into liquid nitrogen.

Data collection and processing. Data from crystals of the entire complex were collected (using several points along the crystal to minimize radiation damage) at 100 K with a Pilatus 6M detector at beamline ID29 at the European Synchrotron Radiation Facility (ESRF). Image data were processed with XDS and XSCALE⁴⁶, which helped to deal with the problem of reflections overlap due to a large unit cell. Data from crystals of the membrane domain were collected at 100 K with an ADSC Q210 detector at ESRF beamline ID29. Image data were processed with iMosflm⁴⁷ and SCALA from the CCP4 suite⁴⁸.

Crystals of the entire complex I belong to the *P*₂₁ space group, with two molecules per asymmetric unit (ASU) and 69% solvent content. Crystals are pseudo-merohedrally twinned with twin fractions approaching 0.5 (ref. 21). Data from three isomorphous crystals were combined to achieve maximal resolution and completeness (Supplementary Table 1). Overall, resolution extends

to about 3.3 Å by CC0.5 criterion⁴⁹, although diffraction along axis *b* is weaker. Using the Diffraction Anisotropy Server (<http://services.mbi.ucla.edu/anisocscale/>)⁵⁰, the data set was anisotropically scaled and truncated to 3.3 Å, 3.5 Å and 3.3 Å resolution, where the *F*/ σ ratio drops to ~2.6–2.8 along the *a**, *b** and *c** axes, respectively. Owing to twinning, model bias presented a problem when using the relatively diverse (~30–35% identity) model of the *E. coli* membrane domain for molecular replacement. To overcome this, we crystallized the isolated *T. thermophilus* membrane domain. Crystals were in the *P*₁ space group and not twinned. Packing resembles that of the *E. coli* membrane domain²⁹, with two molecules per ASU and 66% solvent content. Crystals contained subunit Nqo8, in contrast to the *E. coli* case. The diffraction was also anisotropic and so the best data set, of about 3.3 Å overall resolution, was anisotropically scaled and truncated to 3.6 Å, 3.4 Å and 3.3 Å resolution along the *a**, *b** and *c** axes, respectively.

Structure solution and refinement. From trials with many heavy atoms for experimental phasing, tungsten derivatives of the membrane domain crystals were obtained. However, W atoms were wedged between the two domains and so disrupted the packing, resulting in lower resolution. Therefore, the structure of the membrane domain was solved by molecular replacement with our *E. coli* model (Protein Data Bank (PDB) code, 3RKO)²⁹. Initially, individual subunits were refined as rigid bodies in Phaser⁵¹, sequence replaced for *T. thermophilus* with CHAINSAW⁴⁸ and side chains re-built with SCWRL4 (ref. 52). This model was re-built by one cycle of the Rosetta_MR protocol in PHENIX⁴², followed by DEN (deformable elastic network) refinement in CNS⁴³, resulting in *R*/*R*_{free} = 31.5/36.6%. Improved electron density (both calculated and density-modified) allowed for cycles of manual building of subunit Nqo8 and re-building of some regions in other subunits in *Coot*⁵³, followed by refinement in PHENIX with secondary structure/NCS (non-crystallographic symmetry) restraints and using TLS (translation, libration and screw-motion parameterization). The final model was refined to *R*/*R*_{free} = 20.9/26.3% (Supplementary Table 1). It contained 2,144 residues (Supplementary Table 2) and two bound UDM molecules per domain. All nine TM helices of Nqo8 were resolved in the structure, but the long highly conserved cytoplasmic loops 1 (TM1–2) and 3 (TM5–6) were disordered.

The structure of the entire complex in twinned *P*₂₁ crystals was solved by molecular replacement (using Phaser) with the new structure of the *T. thermophilus* membrane domain and the previously described structure of the hydrophilic domain (PDB code, 3I9V). First, to exploit anomalous signal from intrinsic Fe–S clusters, we used combined data from two rare crystals with relatively low twin fraction (~0.4), collected at Fe peak wavelength (Supplementary Table 1). Jelly body refinement of the initial model with SAD target function in REFMAC⁵⁴ resulted in improved electron density for novel features at the interface of the two domains, missing in either starting structure (including Nqo16). Then, manual model building was followed with cycles of refinement in PHENIX against the best native data set, with secondary structure/NCS restraints and using TLS. The structure was refined at 3.3 Å resolution to *R*/*R*_{free} = 20.2%/23.9% (*R* factors are lower than usual owing to twinning). One complex contained 4,780 residues, nine Fe–S clusters and one FMN molecule (Supplementary Table 2). Both the membrane domain and the entire complex structures were validated in MolProbity⁵⁵ and were found to be of better-than-average quality for the resolution (Supplementary Table 1).

Co-crystals of intact complex I with piericidin A were obtained by mixing protein and inhibitor at a 1:1 molar ratio before crystallization. The co-crystal was further soaked in 100 μ M piericidin A (added from 10 mM stock in 100% dimethylsulphoxide) for approximately 4 h, before cryo-cooling. Decylubiquinone soaks were performed by soaking native complex I crystals overnight in solution containing 500 μ M decylubiquinone (added from 50 mM stock in 100% ethanol). Crystals were otherwise treated and data processed as for native crystals. Molecular replacement with the intact complex structure in Phaser was followed by refinement in REFMAC for 40 cycles with Jelly body restraints (sigma 0.02). This resulted in a significant drop of *R*_{free}; however, the models were not re-built manually and should be considered preliminary. A strong positive difference electron density (shown in green in Fig. 4a, b) identified the position of the aromatic ring of the compounds; they were modelled into the electron density, added to the initial structure and REFMAC refinement repeated, resulting in the models shown in Fig. 4a, b.

Bioinformatics. Structure-based multiple sequence alignment was performed in CLUSTALW v1.83 (ref. 56) with the profile alignment option. Water molecules were modelled using Dowser software⁵⁴. When applied to the *E. coli* membrane domain structure (PDB code, 3RKO), a similar 'river' of waters was predicted, with crystallographic waters, where observed, coinciding with those modelled. Conservation scores for Supplementary Fig. 6 were calculated with the ConSurf server⁵⁷, with sequences for alignment selected to be between 90% and 30% similar, resulting in about 300–400 sequences per subunit. Figures were prepared in PyMOL. Surface charges were calculated with APBS plug-in in PyMOL.

46. Kabsch, W. *XDS*. *Acta Crystallogr. D* **66**, 125–132 (2010).
47. Batty, T. G. G., Kontogiannis, L., Johnson, O., Powell, H. R. & Leslie, A. G. W. *iMOSFLM*: a new graphical interface for diffraction-image processing with *MOSFLM*. *Acta Crystallogr. D* **67**, 271–281 (2011).
48. The *CCP4* suite: programs for protein crystallography. *Acta Crystallogr. D* **50**, 760–763 (1994).
49. Evans, P. R. An introduction to data reduction: space-group determination, scaling and intensity statistics. *Acta Crystallogr. D* **67**, 282–292 (2011).
50. Strong, M. *et al.* Toward the structural genomics of complexes: crystal structure of a PE/PPE protein complex from *Mycobacterium tuberculosis*. *Proc. Natl Acad. Sci. USA* **103**, 8060–8065 (2006).
51. McCoy, A. J. *et al.* *Phaser* crystallographic software. *J. Appl. Crystallogr.* **40**, 658–674 (2007).
52. Krivov, G. G., Shapovalov, M. V. & Dunbrack, R. L. Jr. Improved prediction of protein side-chain conformations with *SCWRL4*. *Proteins* **77**, 778–795 (2009).
53. Emsley, P. & Cowtan, K. *Coot*: model-building tools for molecular graphics. *Acta Crystallogr. D* **60**, 2126–2132 (2004).
54. Murshudov, G. N. *et al.* *REFMAC5* for the refinement of macromolecular crystal structures. *Acta Crystallogr. D* **67**, 355–367 (2011).
55. Chen, V. B. *et al.* *MolProbity*: all-atom structure validation for macromolecular crystallography. *Acta Crystallogr. D* **66**, 12–21 (2010).
56. Thompson, J. D., Higgins, D. G. & Gibson, T. J. *CLUSTAL W*: improving the sensitivity of progressive multiple sequence alignment through sequence weighting, position-specific gap penalties and weight matrix choice. *Nucleic Acids Res.* **22**, 4673–4680 (1994).
57. Ashkenazy, H., Erez, E., Martz, E., Pupko, T. & Ben-Tal, N. *ConSurf 2010*: calculating evolutionary conservation in sequence and structure of proteins and nucleic acids. *Nucleic Acids Res.* **38**, W529–W533 (2010).

A rapidly spinning supermassive black hole at the centre of NGC 1365

G. Risaliti^{1,2}, F. A. Harrison³, K. K. Madsen³, D. J. Walton³, S. E. Boggs⁴, F. E. Christensen⁵, W. W. Craig^{5,6}, B. W. Grefenstette³, C. J. Hailey⁷, E. Nardini⁸, Daniel Stern⁹ & W. W. Zhang¹⁰

Broad X-ray emission lines from neutral and partially ionized iron observed in active galaxies have been interpreted as fluorescence produced by the reflection of hard X-rays off the inner edge of an accretion disk^{1–7}. In this model, line broadening and distortion result from rapid rotation and relativistic effects near the black hole, the line shape being sensitive to its spin. Alternative models in which the distortions result from absorption by intervening structures provide an equally good description of the data^{8,9}, and there has been no general agreement on which is correct. Recent claims¹⁰ that the black hole^{11,12} (2×10^6 solar masses) at the centre of the galaxy NGC 1365 is rotating at close to its maximum possible speed rest on the assumption of relativistic reflection. Here we report X-ray observations of NGC 1365 that reveal the relativistic disk features through broadened Fe-line emission and an associated Compton scattering excess of 10–30 kiloelectronvolts. Using temporal and spectral analyses, we disentangle continuum changes due to time-variable absorption from reflection, which we find arises from a region within 2.5 gravitational radii of the rapidly spinning black hole. Absorption-dominated models that do not include relativistic disk reflection can be ruled out both statistically and on physical grounds.

Previous soft (energy $E < 10$ keV) X-ray observations of NGC 1365 have consistently seen Compton-thin clouds that periodically cross the line of sight, absorbing the 3–5-keV flux, and changing the continuum on timescales of hours^{13,14}. On timescales of a day, the spectrum has been seen to change from a state where a non-thermal continuum (associated with a tenuous coronal plasma) is viewed through a moderate, variably obscuring column to a state where the emission is completely dominated by Compton reflection off a dense material¹⁵. Based on the black-hole mass, and assuming velocities of a few thousand kilometres per second for the obscuring clouds, the inferred size of the X-ray source is a few gravitational radii, $R_g = GM/c^2$, where G is the gravitational constant, M is the black hole's mass, and c is the speed of light¹³.

The orbiting X-ray observatory XMM-Newton¹⁶ (X-ray Multi-Mirror Mission—Newton) and the space-based X-ray telescope NuSTAR¹⁷ (the Nuclear Spectroscopic Telescope Array) simultaneously observed the galaxy NGC 1365 with an exposure of around 130 ks from 25 to 27 July 2012 Universal time. These broadband X-ray data (0.5–79 keV) have sufficient statistics to study spectral variability on the relevant few-hour timescales. We find the low-energy ($E < 3$ keV) component to be constant, and dominated by thermal emission from an optically thin plasma (see Supplementary Information). Previous imaging observations from the space telescope Chandra X-ray Observatory show that this soft component is spatially extended, and physically distinct from the variable emission¹⁸. We restricted our analysis to the hard components observed above 3 keV.

The 3–79-keV spectrum shows strong emission features typical of relativistic disk reflection (Fig. 1). However, previous work has demonstrated that the 5–7 keV distortion can be also be explained by varying absorbers along the line of sight partially covering the source. These have been seen before in NGC 1365, and they strongly affect the spectral shape below 10 keV (refs 10 and 13).

In the 3–10-keV XMM band, the flux ratio $F(3–5 \text{ keV})/F(6–10 \text{ keV})$ shows strong time variations, while the $F(7–15 \text{ keV})/F(15–80 \text{ keV})$ ratio in the NuSTAR band is constant over the whole observation (Fig. 2), suggesting that the soft variation is due to variable absorption (see Supplementary Information). This enabled us to perform a time-resolved analysis and to decompose the different spectral components accurately. We broke the observation into four intervals of similar hardness and analysed each simultaneously. We considered two models to explain the spectrum and its variability, one containing a relativistic reflection component from the inner accretion disk and a variable, partially covering absorber, and one employing multiple

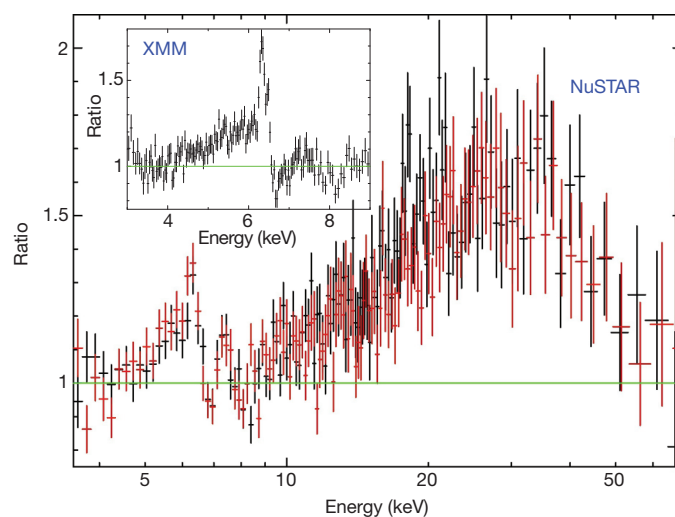


Figure 1 | The broadband 3–79-keV X-ray spectrum of NGC 1365. An absorbed power law has been fitted to the usually featureless continuum intervals 3–4 keV, 7–10 keV and 50–80 keV. The ratios relative to this fit are shown for NuSTAR modules A and B (black and red data in main panel), and for the XMM EPIC/PN instrument (inset). Three prominent features are apparent: an asymmetric excess between 5 and 7 keV, a broad prominent excess between 10 and 79 keV, and a series of absorption lines between 6.7 and 8.3 keV. These absorption lines are due to absorption by a highly ionized plasma²⁶, which we include in all the spectral models discussed below. The two excesses are typical signatures of relativistically blurred emission. Quoted errors refer to a 90% confidence level.

¹INAF—Osservatorio Astronomico di Arcetri, Largo Enrico Fermi 5, 50125 Firenze, Italy. ²Harvard-Smithsonian Center for Astrophysics, 60 Garden Street, Cambridge, Massachusetts 02138, USA. ³Cahill Center for Astrophysics, 1216 East California Boulevard, California Institute of Technology, Pasadena, California 91125, USA. ⁴Space Science Laboratory, University of California, Berkeley, California 94720, USA. ⁵DTU Space—National Space Institute, Technical University of Denmark, Elektrovej 327, 2800 Lyngby, Denmark. ⁶Lawrence Livermore National Laboratory, Livermore, California 94550, USA. ⁷Columbia Astrophysics Laboratory, Columbia University, New York, New York 10027, USA. ⁸Astrophysics Group, School of Physical and Geographical Sciences, Keele University, Keele, Staffordshire ST5 5BG, UK. ⁹Jet Propulsion Laboratory, California Institute of Technology, 4800 Oak Grove Drive, Pasadena, California 91109, USA. ¹⁰NASA Goddard Space Flight Center, Greenbelt, Maryland 20771, USA.

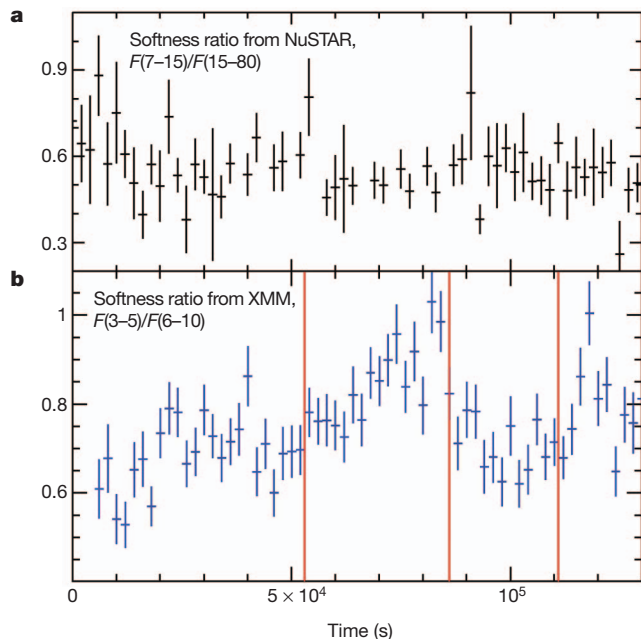


Figure 2 | X-ray spectral variability of NGC 1365. **a**, NuSTAR $F(7\text{--}15\text{ keV})/F(15\text{--}80\text{ keV})$ softness ratio light curve. **b**, XMM $F(3\text{--}5\text{ keV})/F(6\text{--}10\text{ keV})$ softness ratio light curve. The vertical lines delimit four time intervals with significantly different average values of the softness ratio, from which four different spectra have been extracted and analysed simultaneously. These variations are due to absorption variability (see Supplementary Information). The changes of softness ratio within each interval reveal that the absorber has a complex structure; however, its detailed variability on timescales shorter than around 1,000 s is not relevant in the determination of the physical parameters of the other spectral components. Error bars are one standard deviation.

variable absorbers instead. In addition, both models include neutral reflection from a constant, distant screen of gas to reproduce the unresolved, narrow iron emission line at 6.4 keV.

To illustrate the power of the broad energy range in determining model parameters, we first fitted the XMM data alone to both models. With XMM data alone, we could not distinguish between these scenarios, the broadened Fe-line being consistent with both. However, extrapolation of the two models to the 10–80 keV range broke the degeneracy: the absorption-only model failed to reproduce the new NuSTAR data by a large factor, while the model including the relativistic component reproduced the observed spectrum within around 5%, without even re-fitting the data (Fig. 3).

We next considered the possibility that the shape of the hard spectrum arises not from disk reflection, but from an intervening screen of dense absorbing material that can scatter a fraction of the light, but primarily affects the high-energy continuum through absorption. A high equivalent hydrogen column density N_{H} of this gas (far in excess of that found by the fits to XMM only) is required to affect energies above 10 keV. We fitted the broad 3–79-keV band allowing the absorber parameters in model 2 to vary relative to those found with XMM alone. The resulting fit drove the column of the second absorber to $N_{\text{H}} \approx 5 \times 10^{24} \text{ cm}^{-2}$, which reproduces the shape of the hard continuum, but cannot reproduce the spectral variability below 10 keV (see Supplementary Information). We next added a third absorber to model 2, and allowed the parameters of all three to vary. By setting the third absorber to have $N_{\text{H}} = 4\text{--}6 \times 10^{24} \text{ cm}^{-2}$ and to cover at least 40% of the source, we achieved a formally acceptable fit (reduced χ^2 of 1.02). However, this solution was rejected compared with the reflection model: an F -test performed on a ‘merged model’ that includes all the components of the two individual models showed that the probability that the model without relativistic reflection (model 2) is preferred is 8×10^{-5} .

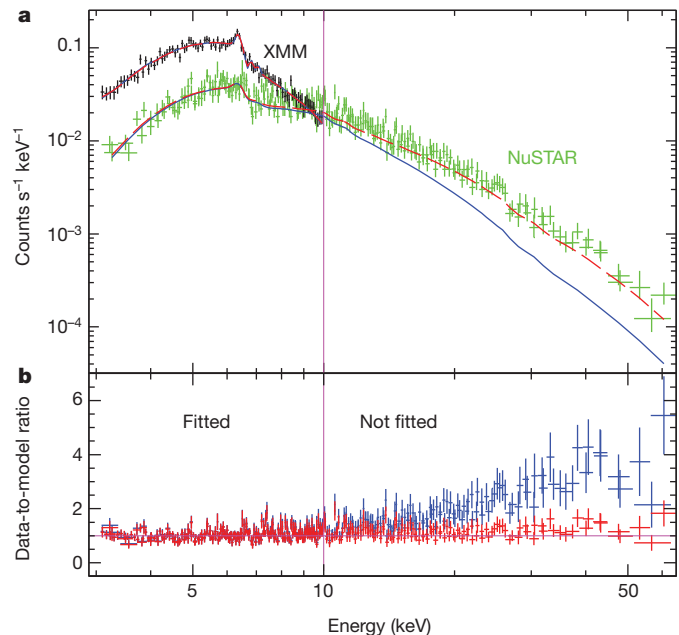


Figure 3 | Comparison between the relativistic reflection model and the multiple absorber model. **a**, XMM and NuSTAR spectral data and models for one of the four time intervals in Fig. 2. The two models contain a relativistic reflection component plus variable partial covering (model 1; red dashed line), and a double partial covering (model 2; blue continuous line). Both models have been fitted to the data only below 10 keV, and reproduce the lower-energy observations equally well. However, the models strongly deviate at higher energies. **b**, Data-to-model ratio for the double partial covering (model 2; blue) and relativistic reflection plus variable absorber (model 1; red) models. The best-fitting partial-covering model using XMM data alone has two absorbers with N_{H} values of $5 \times 10^{22} \text{ cm}^{-2}$ and $3 \times 10^{23} \text{ cm}^{-2}$; these have little influence on the spectrum above 10 keV. Instead, the relativistic reflection component reproducing the broad emission feature below 10 keV also includes a strong Compton reflection component above 10 keV. All errors are at a 90% confidence level.

The three-zone model could also be ruled out on the basis of physical implications that are completely inconsistent with optical, infrared and X-ray observations. These arose when we considered the strong Compton scattering and reprocessing inevitable with the high- N_{H} absorber. For low- N_{H} ($< 10^{24} \text{ cm}^{-2}$) absorbers, the effect of continuum reprocessing can be ignored (and in fact is not included in our models). However, the high-density absorber required to fit the $E > 10\text{-keV}$ data would strongly affect the predicted line and continuum emission. How strongly depends on the geometry.

We considered two extreme bounding possibilities. First, if the solid angle covered is small, the reprocessing into X-ray line emission or infrared flux will be negligible. But, in this case the effect of Compton scattering on the direct emission will strongly (by a factor $\exp(\tau_{\text{C}}) \approx 20\text{--}80$, where τ_{C} is the Compton optical depth) attenuate the intrinsic luminosity. Correcting for this, the implied total luminosity of 0.1–100 keV becomes implausibly high (X-ray luminosity of $1\text{--}3 \times 10^{44} \text{ erg s}^{-1}$, that is, 30–100% of the Eddington limit). This is completely incompatible with other luminosity indicators, such as the optical [O III] 5,007 Å line¹⁹. Second, if the Compton-thick absorber covers a large fraction of the solid angle as seen from the source, there will be strong reprocessing, with two observable effects: a large fraction of the intrinsic luminosity is re-emitted in the infrared part of the spectrum, which is ruled out by high-resolution infrared observations²⁰, and a strong narrow iron emission line²¹ with equivalent width $> 600 \text{ eV}$ should be present, which is ruled out by our measurement: an observed equivalent width of approximately 60 eV (see Supplementary Information).

The observed source variability and unprecedented broad-band spectroscopy enable us to conclude unambiguously that reflection of

a hard continuum off the inner accretion disk edge is producing the neutral Fe-line distortion and strong high-energy Compton reflection continuum. The flux of the relativistic reflection component is higher than the primary continuum at its peak around 30 keV (see Supplementary Information), implying a strong enhancement of the reflection efficiency due to relativistic distortion²² (the highest value with standard disk reflection is about 30%; ref. 23). This high efficiency is consistent with the disk and spin parameters presented below, implying that most of the reflection arises from the inner part of the accretion disk, close to the innermost stable circular orbit.

From the relativistic disk reflection, we can determine the black-hole spin parameter. Allowing all other model parameters (such as disk inclination, ionization state and emissivity profile) to vary, we found the minimum spin to be $a^* \geq 0.84$ at 90% confidence (Fig. 4), where a^* is the dimensionless spin parameter, $a^* = Jc/GM^2$ (where J is the black hole's angular momentum), equivalent to an innermost disk edge at ≤ 2.5 gravitational radii. These results are consistent with the ones from previous observations of NGC 1365 (ref. 10) from the X-ray astronomy satellite Suzaku. In that analysis, however, the relativistic model was assumed to be valid, and a complete comparison with the absorption-only scenario was not attempted, owing to the low statistics, especially at high energies (see Supplementary Information for further details).

Having tested this model (model 1) against the possible alternative (model 2, the multiple variable absorber), and having left all the model parameters unconstrained, the main potential source of residual systematic error is due to assuming truncation of the disk at the innermost stable circular orbit. However, recent magneto-hydro-dynamical simulations suggest that emission from within the innermost stable circular orbit is negligible²⁴. Other errors could be introduced by assuming a constant, power-law emissivity profile, but the steepness of this profile suggests that its exact shape at radii larger than twice the innermost stable circular orbit is unimportant. The analysis therefore provides robust support for high spin values in active galactic nuclei², constraining galaxy evolution and black-hole growth models²⁵.

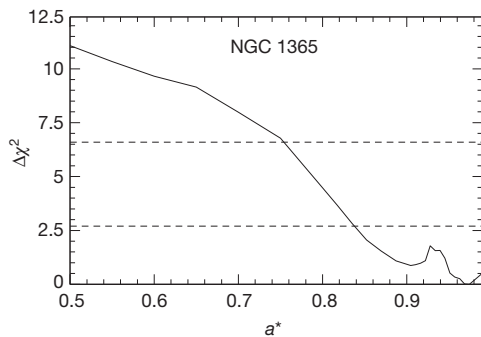


Figure 4 | Error contour for the spin parameter of the supermassive black hole in NGC 1365. The χ^2 contour was obtained while allowing all model parameters to vary. The adopted best-fitting model consists of a power law with photon index $\Gamma = 1.92^{+0.04}_{-0.26}$, a neutral absorber with N_H varying in the range $2.2\text{--}2.8 \times 10^{23} \text{ cm}^{-2}$, a ionized absorber with ionization parameter of about 3.5 and $N_H \approx 10^{23} \text{ cm}^{-2}$, a relativistically blurred reflection by a disk with inner radius less than $2.5R_g$ and spin parameter a^* as shown in the plot. The ionization state of the disk, its inclination, its iron abundance and the normalization of the reflection component are degenerate, and so are only loosely constrained; they also strongly affect the uncertainties on the spin parameter. To emphasize the importance of correctly considering systematic effects, if (based on previous work on Suzaku data²⁷) we limit the disk inclination to $55\text{--}60^\circ$, the error on the spin measurement drops: $a^* = 0.97^{+0.01}_{-0.04}$. Analogously, we would obtain an error of the order of ± 0.01 if we fitted the whole data set with a model that does not allow for absorption variability.

Received 29 October 2012; accepted 16 January 2013.

- Brenneman, L. W. & Reynolds, C. S. Relativistic broadening of iron emission lines in a sample of active galactic nuclei. *Astrophys. J.* **702**, 1367–1386 (2009).
- Walton, D. J., Nardini, E., Fabian, A. C., Gallo, L. C. & Reis, R. C. Suzaku observations of ‘bare’ active galactic nuclei. *Mon. Not. R. Astron. Soc.* **428**, 2901–2920 (2013).
- Fabian, A. C., Rees, M. J., Stella, L. & White, N. E. X-ray fluorescence from the inner disc in Cygnus X-1. *Mon. Not. R. Astron. Soc.* **238**, 729–736 (1989).
- Laor, A. Line profiles from a disk around a rotating black hole. *Astrophys. J.* **376**, 90–94 (1991).
- Brenneman, L. W. & Reynolds, C. S. Constraining black hole spin via X-ray spectroscopy. *Astrophys. J.* **652**, 1028–1043 (2006).
- Chiang, C.-Y. & Fabian, A. C. Modelling the broad-band spectra of MCG-6-30-15 with a relativistic reflection model. *Mon. Not. R. Astron. Soc.* **414**, 2345–2353 (2011).
- Fabian, A. C. *et al.* Broad line emission from iron K- and L-shell transitions in the active galaxy 1H0707–495. *Nature* **459**, 540–542 (2009).
- Miller, L., Turner, T. J. & Reeves, J. N. An absorption origin for the X-ray spectral variability of MCG-6-30-15. *Astron. Astrophys.* **483**, 437–452 (2008).
- Miller, L., Turner, T. J., Reeves, J. N. & Baito, V. X-ray reverberation in 1H0707–495 revisited. *Mon. Not. R. Astron. Soc.* **408**, 1928–1935 (2010).
- Brenneman, L. W., Risaliti, G., Elvis, M. & Nardini, E. An examination of the spectral variability in NGC 1365 with Suzaku. *Mon. Not. R. Astron. Soc.* **429**, 2662–2676 (2013).
- Kaspi, S. *et al.* The relationship between luminosity and broad-line region size in active galactic nuclei. *Astrophys. J.* **629**, 61–71 (2005).
- Schulz, H., Komossa, S., Schmitz, C. & Mücke, A. Clues on the obscured active nucleus of NGC 1365. *Astron. Astrophys.* **346**, 764–768 (1999).
- Risaliti, G. *et al.* Variable partial covering and a relativistic iron line in NGC 1365. *Astrophys. J.* **696**, 160–171 (2009).
- Maolino, R. *et al.* ‘Comets’ orbiting a black hole. *Astron. Astrophys.* **517**, A47 (2010).
- Risaliti, G. *et al.* Occultation measurement of the size of the X-ray-emitting region in the active galactic nucleus of NGC 1365. *Astrophys. J.* **659**, L111–L114 (2007).
- Jansen, F. *et al.* XMM-Newton observatory. I. The spacecraft and operations. *Astron. Astrophys.* **365**, L1–L6 (2001).
- Harrison, F. A. *et al.* The Nuclear Spectroscopic Telescope Array High Energy X-Ray Mission. *Astrophys. J.* (submitted); <http://arxiv.org/abs/1301.7307>.
- Wang, J. *et al.* Imaging the circumnuclear region of NGC 1365 with Chandra. *Astrophys. J.* **694**, 718–733 (2009).
- Bassani, L. *et al.* A three-dimensional diagnostic diagram for Seyfert 2 galaxies: probing X-ray absorption and Compton thickness. *Astrophys. J. Suppl.* **121**, 473–482 (1999).
- Alonso-Herrero, A. *et al.* Probing the nuclear and circumnuclear activity of NGC 1365 in the infrared. *Mon. Not. R. Astron. Soc.* **425**, 311–324 (2012).
- Murphy, K. D. & Yaqoob, T. An X-ray spectral model for Compton-thick toroidal reprocessors. *Mon. Not. R. Astron. Soc.* **397**, 1549–1562 (2009).
- Miniutti, G. & Fabian, A. C. A light bending model for the X-ray temporal and spectral properties of accreting black holes. *Mon. Not. R. Astron. Soc.* **349**, 1435–1448 (2004).
- Magdziarz, P. & Zdziarski, A. Angle-dependent Compton reflection of X-rays and gamma-rays. *Mon. Not. R. Astron. Soc.* **273**, 837–848 (1995).
- Reynolds, C. S. & Fabian, A. C. Broad iron-K α emission lines as a diagnostic of black hole spin. *Astrophys. J.* **675**, 1048–1056 (2008).
- Volonteri, M., Madau, P., Quataert, E. & Rees, M. J. The distribution and cosmic evolution of massive black hole spins. *Astrophys. J.* **620**, 69–77 (2005).
- Risaliti, G. *et al.* Highly ionized iron absorption lines from outflowing gas in the X-ray spectrum of NGC 1365. *Astrophys. J.* **630**, L129–L132 (2005).
- Walton, D. J., Reis, R. C. & Fabian, A. C. Explaining the hard excesses in active galactic nuclei. *Mon. Not. R. Astron. Soc.* **408**, 601–606 (2010).

Supplementary Information is available in the online version of the paper.

Acknowledgements This work was supported under NASA grant number NNG08FD60C, and made use of data from the Nuclear Spectroscopic Telescope Array (NuSTAR) mission, a project led by Caltech, managed by the Jet Propulsion Laboratory, and funded by the National Aeronautics and Space Administration. We thank the NuSTAR Operations, Software and Calibration teams for support with execution and analysis of these observations. This work also made use of observations obtained with XMM-Newton, an ESA science mission with instruments and contributions directly funded by ESA Member States and NASA.

Author Contributions G.R. is the Principal Investigator of the XMM observations of NGC 1365. He led the XMM data analysis and joint spectral analysis, modelling and interpretation of the results. F.A.H. is the Principal Investigator of NuSTAR and led observation planning, execution and participated in scientific interpretation and manuscript preparation. D.J.W. analysed NuSTAR data and participated in modelling and interpretation. K.K.M. led NuSTAR calibration analysis for NGC 1365. D.S. is the NuSTAR Project Scientist and participated in definition and interpretation of the observations. B.W.G. assisted in adaptation of the NuSTAR data analysis to NGC 1365. E.N. participated in XMM observations, reduction and interpretation. S.E.B., F.E.C., W.W.C., C.J.H. and W.W.Z. led efforts in design, calibration and implementation of NuSTAR. All authors participated in review of the manuscript.

Author Information Reprints and permissions information is available at www.nature.com/reprints. The authors declare no competing financial interests. Readers are welcome to comment on the online version of the paper. Correspondence and requests for materials should be addressed to G.R. (risaliti@arcetri.astro.it) and F.A.H. (fiona@srl.caltech.edu).

A sub-Mercury-sized exoplanet

Thomas Barclay^{1,2}, Jason F. Rowe^{1,3}, Jack J. Lissauer¹, Daniel Huber¹, François Fressin⁴, Steve B. Howell¹, Stephen T. Bryson¹, William J. Chaplin⁵, Jean-Michel Désert⁴, Eric D. Lopez⁶, Geoffrey W. Marcy⁷, Fergal Mullally^{1,3}, Darin Ragozzine^{4,8}, Guillermo Torres⁴, Elisabeth R. Adams⁴, Eric Agol⁹, David Barrado^{10,11}, Sarbani Basu¹², Timothy R. Bedding¹³, Lars A. Buchhave^{14,15}, David Charbonneau⁴, Jessie L. Christiansen^{1,3}, Jørgen Christensen-Dalsgaard¹⁶, David Ciardi¹⁷, William D. Cochran¹⁸, Andrea K. Dupree⁴, Yvonne Elsworth⁵, Mark Everett¹⁹, Debra A. Fischer¹², Eric B. Ford⁸, Jonathan J. Fortney⁶, John C. Geary⁴, Michael R. Haas¹, Rasmus Handberg¹⁶, Saskia Hekker^{5,20}, Christopher E. Henze¹, Elliott Horch²¹, Andrew W. Howard²², Roger C. Hunter¹, Howard Isaacson⁷, Jon M. Jenkins^{1,3}, Christoffer Karoff¹⁶, Steven D. Kawaler²³, Hans Kjeldsen¹⁶, Todd C. Klaus²⁴, David W. Latham⁴, Jie Li^{1,3}, Jorge Lillo-Box¹¹, Mikkel N. Lund¹⁶, Mia Lundkvist¹⁶, Travis S. Metcalfe²⁵, Andrea Miglio⁵, Robert L. Morris^{1,3}, Elisa V. Quintana^{1,3}, Dennis Stello¹³, Jeffrey C. Smith^{1,3}, Martin Still^{1,2} & Susan E. Thompson^{1,3}

Since the discovery of the first exoplanets^{1,2}, it has been known that other planetary systems can look quite unlike our own³. Until fairly recently, we have been able to probe only the upper range of the planet size distribution^{4,5}, and, since last year, to detect planets that are the size of Earth⁶ or somewhat smaller⁷. Hitherto, no planets have been found that are smaller than those we see in the Solar System. Here we report a planet significantly smaller than Mercury⁸. This tiny planet is the innermost of three that orbit the Sun-like host star, which we have designated Kepler-37. Owing to its extremely small size, similar to that of the Moon, and highly irradiated surface, the planet, Kepler-37b, is probably rocky with no atmosphere or water, similar to Mercury.

The Kepler spacecraft was launched in 2009 with the goal of determining the frequency of rocky planets in the habitable zone around Sun-like host stars in the Galaxy⁹. More than 150,000 stars are continuously monitored for transits of planetary bodies¹⁰. Transit-like signals indicative of three planets¹¹ were detected over the course of 978 days by Kepler in the photometric time series data of the star we designate Kepler-37 (also known as KIC 8478994 and KOI-245).

Kepler-37 is cooler than the Sun¹². Stellar spectral templates were fitted to optical spectra of Kepler-37^{13,14} to determine initial values of the stellar properties. Despite the low luminosity and low-amplitude oscillations associated with cool main-sequence stars¹⁵, we were able to detect solar-like oscillations in the flux time series. Kepler-37 is the densest star where solar-like oscillations have been detected and an asteroseismic analysis of these oscillations allowed us to measure precise stellar properties¹⁶ (for more information, see section 1 of Supplementary Information). Iterating between the asteroseismic and spectroscopically derived stellar properties yielded final values for the radius and mass of 0.770 ± 0.026 solar radii (R_{\odot}) and 0.802 ± 0.068 solar masses (M_{\odot}), respectively. The small uncertainty in the stellar radius is important because this uncertainty limits the precision with which we can measure the planetary radius.

We fitted a transiting planet model¹⁷ with three planets to the Kepler data using a Markov chain Monte Carlo technique¹⁸. The best-fitting

model is shown, plotted over the transit data, in Fig. 1. The transit model yields the ratio of planet radius to stellar radius. Using the asteroseismically derived stellar radius, we determined planet radii of $0.303^{+0.053}_{-0.073} R_{\oplus}$, $0.742^{+0.065}_{-0.083} R_{\oplus}$ and $1.99^{+0.11}_{-0.14} R_{\oplus}$ (where R_{\oplus} is Earth's radius), for the three planets Kepler-37b, Kepler-37c and Kepler-37d, respectively, where the quoted uncertainties are the central 68.3% of the posterior distributions (equivalent to 1σ) and account for both the uncertainty in the ratio of planetary to stellar radius (the dominant term for the inner planet) and the uncertainty in the stellar radius (the dominant term for the outer planet). A full list of planet parameters are given in Supplementary Table 1.

It was not possible to confirm using radial velocities¹⁹ or transit timing variations²⁰ that the three candidate planets are substellar bodies orbiting Kepler-37. We therefore explored possible astrophysical scenarios (blends) that can mimic a planet transit across the disc of Kepler-37 using the BLENDER procedure^{6,21–23}. BLENDER analyses attempt to show that a blend scenario is much less likely than a planet interpretation by creating a wide array of synthetic light curves of various blend scenarios and comparing the goodness of fit to the synthetic light curves with that of the true planet model. Inconsistent fits are rejected, as are fits to scenarios that are ruled out by additional information such as high-contrast imaging, Kepler Input Catalog²⁴ colours and high-resolution spectroscopic observations. Details of the supporting data used by BLENDER are provided in sections 2–5 of Supplementary Information. The final blend probability is compared with the expected frequency of occurrence of real planets (known as the planet prior) to calculate the final probability that the candidate is a true planet. Our planet priors are calculated by looking at the frequency of planets with a size within the 3σ uncertainty range of the measured planet radii. We then apply a correction to the planet prior to account for false positives and incompleteness in the planet catalogue²⁵.

In this study, we consider blends caused by background eclipsing binaries, background stars transited by a planet and physical companions transited by a planet. For Kepler-37d, the only credible blend

¹NASA Ames Research Center, Moffett Field, California 94035, USA. ²Bay Area Environmental Research Institute, 596 First Street West, Sonoma, California 95476, USA. ³SETI Institute, 189 Bernardo Avenue, Mountain View, California 94043, USA. ⁴Harvard-Smithsonian Center for Astrophysics, 60 Garden Street, Cambridge, Massachusetts 02138, USA. ⁵School of Physics and Astronomy, University of Birmingham, Edgbaston B15 2TT, UK. ⁶Department of Astronomy and Astrophysics, University of California, Santa Cruz, California 95064, USA. ⁷Department of Astronomy, UC Berkeley, Berkeley, California 94720, USA. ⁸Astronomy Department, University of Florida, 211 Bryant Space Sciences Center, Gainesville, Florida 32111, USA. ⁹Department of Astronomy, Box 351580, University of Washington, Seattle, Washington 98195, USA. ¹⁰Calar Alto Observatory, Centro Astronómico Hispano Alemán, Calle Jesús Durbán Remón, E-04004 Almería, Spain. ¹¹Departamento Astrofísica, Centro de Astrobiología, ESAC campus, PO Box 78, E-28691 Villanueva de la Cañada, Spain. ¹²Department of Astronomy, Yale University, New Haven, Connecticut 06520, USA. ¹³Sydney Institute for Astronomy, School of Physics, University of Sydney, Sydney, New South Wales 2006, Australia. ¹⁴Niels Bohr Institute, University of Copenhagen, DK-2100 Copenhagen, Denmark. ¹⁵Centre for Star and Planet Formation, Natural History Museum of Denmark, University of Copenhagen, DK-1350 Copenhagen, Denmark. ¹⁶Stellar Astrophysics Centre, Department of Physics and Astronomy, Aarhus University, Ny Munksgade 120, DK-8000 Aarhus C, Denmark. ¹⁷NASA Exoplanet Science Institute, California Institute of Technology, 770 South Wilson Avenue Pasadena, California 91125, USA. ¹⁸McDonald Observatory, University of Texas at Austin, Austin, Texas 78712, USA. ¹⁹National Optical Astronomy Observatory, 950 North Cherry Avenue, Tucson, Arizona 85719, USA. ²⁰Astronomical Institute "Anton Pannekoek", University of Amsterdam, Postbus 94249, 1090 GE Amsterdam, The Netherlands. ²¹Southern Connecticut State University, New Haven, Connecticut 06515, USA. ²²Institute for Astronomy, University of Hawaii, 2680 Woodlawn Drive, Honolulu, Hawaii 96822, USA. ²³Department of Physics and Astronomy, Iowa State University, Ames, Iowa 50011, USA. ²⁴Orbital Sciences Corporation/NASA Ames Research Center, Moffett Field, California 94035, USA. ²⁵White Dwarf Research Corporation, Boulder, Colorado 80301, USA.

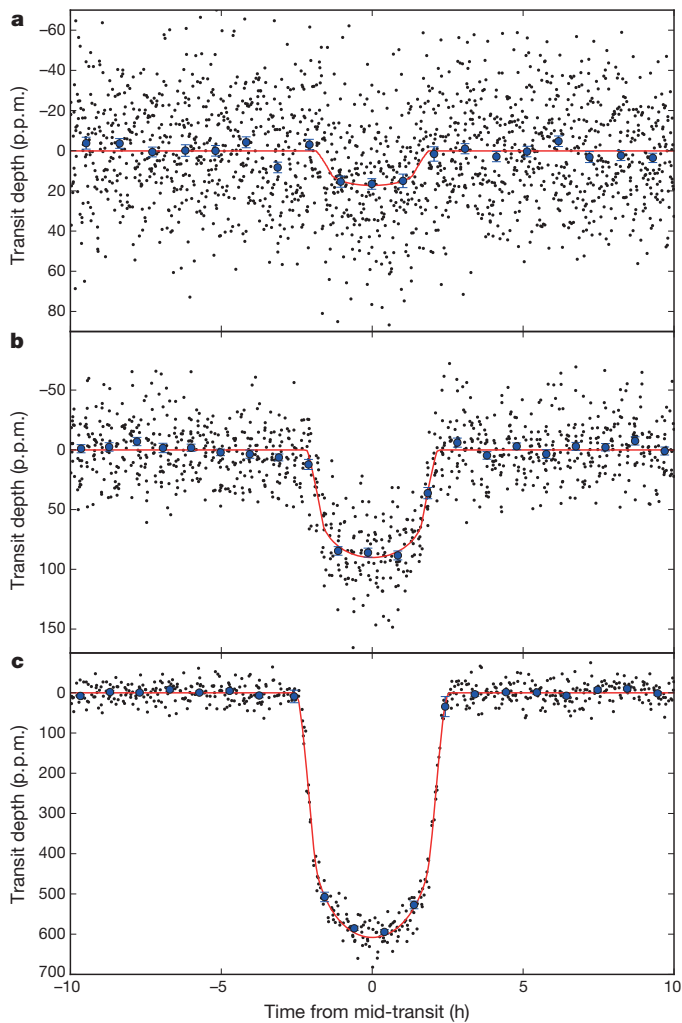


Figure 1 | The transit light curves for the planets orbiting Kepler-37. The transit model fit to the light curve of Kepler-37 was calculated using a four-parameter nonlinear limb-darkening model that allowed for eccentric orbits. Limb-darkening coefficients were interpolated in stellar temperature, surface gravity and metallicity to determine the appropriate values for Kepler-37, and these were kept fixed. A Markov chain Monte Carlo technique was used to sample the planet parameters to account for correlated variables. The mean stellar density determined by our asteroseismic analysis was used as a prior in the analysis. The three panels show the transits of planets Kepler-37b (a), Kepler-37c (b) and Kepler-37d (c). The photometric light curve has been phase-folded on the orbital period of the planets to show the observed data as a function of orbital phase. Individual data points are shown as black dots. The blue dots show the data binned, with 90, 50 and 30 individual data points making up each binned point in a–c, respectively. The error bar size is the standard deviation of the data making up that bin divided by $N^{1/2}$, where N is the number of data points in the bin. The best-fitting transit model from the Markov chain Monte Carlo analysis is shown as the red line. The signal-to-noise ratios of the transits of the planets are 13 (a), 49 (b) and 282 (c).

scenario is a planet transiting a background G- or K-type main-sequence star with a brightness within 3 mag of Kepler-37, with a similar absolute radial velocity, but not seen by high-contrast imaging. The probability of such a source existing is vanishingly small, with an upper limit on the probability of 10^{-10} . We used the Kepler planet catalogue¹¹ to estimate the frequency of occurrence of planets with a similar radius to Kepler-37d, and hence calculate the planet prior. We find that a scenario in which the planet orbits the target star is favoured by a factor of $>10^6$ over false-positive scenarios.

The validation of Kepler-37c proved slightly more challenging owing to the difficulty of calculating a planet prior for such a small

body. The number of Kepler planet candidates orbiting F–M-type dwarfs with a similar size to Kepler-37c is 46, and we predict that the expected number of false positives in this size range²⁵ is 7.36. A total of 138,254 dwarf stars were observed continuously for the duration of the mission included in the Kepler planet catalogue, and the planet prior is therefore $(46 - 7.36)/138,254 = 2.79 \times 10^{-4}$, not accounting for incompleteness. If we assume that a signal this small could be detected from transit across only 6.5% of stars, owing to the noise level in most stars exceeding the signal we detect here, we can boost the planet prior by a factor of $1/0.065 = 15.4$, giving a final planet prior of 4.3×10^{-3} . The blend frequency for this source is calculated by summing all the individual blend probabilities: planets transiting background stars (1.49×10^{-5}), background eclipsing binaries (1.4×10^{-8}) and planets transiting a physically bound companion (3.3×10^{-7}). Therefore, the total blend probability is 1.52×10^{-5} and the odds ratio in favour of the true planet scenario is 287. As is common in BLENDER analyses, we can increase the probability of the true planet scenario because multiplanet systems are likely to be coplanar^{26–28}. This increases the odds ratio by a factor of 8.3, to 2,350, making it equivalent to a confidence level of 99.95%.

For Kepler-37b, using the planet candidate list¹¹ to derive a prior is not appropriate because the list is far from complete at such small planet radii. In this work, we assume that planets of comparable size to Kepler-37b have the same occurrence rate as Earth-size planets²⁵. The size range we use to calculate our planet prior is the 3σ uncertainty range of the radius of Kepler-37b. This assumption is somewhat conservative because for larger planet sizes the occurrence rate increases with decreasing planet size⁴. There are 167 Earth-sized candidates in the Kepler planet candidate list. However, we expect about 21 of these to be false positives²⁵. Given that only 15.5% of the stars observed by Kepler are capable of hosting a detectable Earth-sized planet, we find that $(167 - 21)/(138,254 \times 0.155) = 0.68\%$ of F–K-type dwarf stars are expected to host a transiting Earth-sized planet. We therefore take 0.68% to be our planet prior for Kepler-37b. The blend frequency in this analysis is dominated by background eclipsing binaries between 9 and 11.5 mag fainter than the target (the background eclipsing-binary blend frequency is 1.9×10^{-5} and the blend frequency from all other sources is 7.6×10^{-6}). This results in a total blend frequency of 2.6×10^{-5} . The ratio of the planet prior to blend frequency yields an odds ratio that favours the planet interpretation by a factor of 262. If we consider the coplanarity of the system, the odds ratio is boosted by a factor of 8.97, to 2,350 (a 99.95% confidence in the true planet interpretation).

We ran a dynamical simulation to determine whether this system of three planets is stable. For the initial conditions, we use the observed orbital period and the epoch of first transit for each of the three confirmed planets, and assume coplanar orbits. We adopt masses using the relation $M_p/M_\oplus \approx (R_p/R_\oplus)^{2.05}$ (ref. 27), where M_p and R_p are the planetary mass and radius, respectively, and M_\oplus is Earth's mass. For each planet, we performed 1,000 integrations over 100,000 years, each using initially circular orbits for the planets. All planets were found to be stable over the entire simulation.

Although sub-Mercury-sized planets are expected from theory²⁹ and their space-based detection has previously been predicted³⁰, our detection of Kepler-37b is remarkable given that this transit signal would be detected in the data of fewer than 0.5% of the stars observed by Kepler. Although the detection of one planet cannot be used to determine occurrence rates, it does lend weight to the belief that planet occurrence increases exponentially with decreasing planet size.

Received 20 September 2012; accepted 15 January 2013.

Published online 20 February 2013.

1. Mayor, M. & Queloz, D. A Jupiter-mass companion to a solar-type star. *Nature* **378**, 355–359 (1995).
2. Marcy, G. & Butler, R. P. A planetary companion to 70 Virginis. *Astrophys. J.* **464**, L147–L151 (1996).

3. Fabrycky, D. C. *et al.* Architecture of Kepler's multi-transiting systems: II. New investigations with twice as many candidates. *Astrophys. J.* (submitted); preprint at <http://arxiv.org/abs/1202.6328> (2012).
4. Howard, A. W. *et al.* The occurrence and mass distribution of close-in super-Earths, Neptunes, and Jupiters. *Science* **330**, 653–655 (2010).
5. Howard, A. W. *et al.* Planet occurrence within 0.25 AU of solar-type stars from Kepler. *Astrophys. J.* **201** (suppl.), 15 (2012).
6. Fressin, F. *et al.* Two Earth-sized planets orbiting Kepler-20. *Nature* **482**, 195–198 (2011).
7. Muirhead, P. S. *et al.* Characterizing the cool KOs. III. KOI 961: a small star with large proper motion and three small planets. *Astrophys. J.* **747**, 144 (2012).
8. Archinal, B. A. *et al.* Report of the IAU Working Group on Cartographic Coordinates and Rotational Elements: 2009. *Celestial Mech. Dyn. Astron.* **109**, 101–135 (2011).
9. Borucki, W. J. *et al.* Kepler planet-detection mission: introduction and first results. *Science* **327**, 977–980 (2010).
10. Koch, D. G. *et al.* Kepler mission design, realized photometric performance, and early science. *Astrophys. J.* **713**, L79–L86 (2010).
11. Batalha, N. M. *et al.* Planetary candidates observed by Kepler, III: analysis of the first 16 months of data. *Astrophys. J. Suppl.* (in the press); preprint at <http://arxiv.org/abs/1202.5852> (2012).
12. Ammons, S. M. *et al.* The N2K Consortium. IV. New temperatures and metallicities for more than 100,000 FGK dwarfs. *Astrophys. J.* **638**, 1004–1017 (2006).
13. Valenti, J. A. & Fischer, D. A. Spectroscopic properties of cool stars (SPOCS). I. 1040 F, G, and K dwarfs from Keck, Lick, and AAT planet search programs. *Astrophys. J.* **159** (suppl.), 141–166 (2005).
14. Buchhave, L. A. *et al.* An abundance of small exoplanets around stars with a wide range of metallicities. *Nature* **486**, 375–377 (2012).
15. Kjeldsen, H. & Bedding, T. R. Amplitudes of stellar oscillations: the implications for asteroseismology. *Astron. Astrophys.* **293**, 87–106 (1995).
16. Ulrich, R. K. Determination of stellar ages from asteroseismology. *Astrophys. J.* **306**, L37–L40 (1986).
17. Mandel, K. & Agol, E. Analytic light curves for planetary transit searches. *Astrophys. J.* **580**, L171–L175 (2002).
18. Ford, E. B. Quantifying the uncertainty in the orbits of extrasolar planets. *Astron. J.* **129**, 1706–1717 (2005).
19. Struve, O. Proposal for a project of high-precision stellar radial velocity work. *Observatory* **72**, 199–200 (1952).
20. Holman, M. J. & Murray, N. W. The use of transit timing to detect terrestrial-mass extrasolar planets. *Science* **307**, 1288–1291 (2005).
21. Torres, G., Konacki, M., Sasselov, D. D. & Jha, S. Testing blend scenarios for extrasolar transiting planet candidates. I. OGLE-TR-33: a false positive. *Astrophys. J.* **614**, 979–989 (2004).
22. Torres, G. *et al.* Modeling Kepler transit light curves as false positives: rejection of blend scenarios for Kepler-9, and validation of Kepler-9 d, a superearth-size planet in a multiple system. *Astrophys. J.* **727**, 24 (2011).
23. Fressin, F. *et al.* Kepler-10c, a 2.2-Earth radius transiting planet in a multiple system. *Astrophys. J.* **197** (suppl.), 5 (2011).
24. Brown, T. M., Latham, D. W., Everett, M. E. & Esquerdo, G. A. Kepler Input Catalog: photometric calibration and stellar classification. *Astron. J.* **142**, 112 (2011).
25. Fressin, F. *et al.* The false positive rate of Kepler and the occurrence of planets. *Astrophys. J.* (in the press); preprint at <http://arxiv.org/abs/1301.0842> (2013).
26. Cochran, W. D. *et al.* Kepler-18b, c, and d: a system of three planets confirmed by transit timing variations, light curve validation, warm-Spitzer photometry, and radial velocity measurements. *Astrophys. J.* **197**, 7 (2011).
27. Lissauer, J. J. *et al.* Architecture and dynamics of Kepler's candidate multiple transiting planet systems. *Astrophys. J.* **197** (suppl.), 8 (2011).
28. Lissauer, J. J. *et al.* Almost all of Kepler's multiple planet candidates are planets. *Astrophys. J.* **750**, 112 (2012).
29. Chambers, J. in *Exoplanets* (ed. Seager, S.) 297–317 (Univ. Arizona Press, 2011).
30. Borucki, W. J. *et al.* in *Earths: DARWIN/TPF and the Search for Extrasolar Terrestrial Planets*. Report No. ESA SP-539, 69–81 (ESA Publications Division, 2003).

Supplementary Information is available in the online version of the paper.

Acknowledgements Kepler was competitively selected as the tenth Discovery mission. Funding for this mission is provided by NASA's Science Mission Directorate. Some of this work is based on observations made with the Spitzer Space Telescope, which is operated by the Jet Propulsion Laboratory, California Institute of Technology under a contract with NASA. Support for this work was provided by NASA through an award issued by JPL/Caltech. Kepler flux time series data presented in this paper are available from the Mikulski Archive for Space Telescopes (MAST) at the Space Telescope Science Institute (STScI). Funding for the Stellar Astrophysics Centre is provided by The Danish National Research Foundation. The research is supported by the ASTERISK project funded by the European Research Council. E.A. acknowledges support through an NSF Career grant. D.H. is supported by an appointment to the NASA Postdoctoral Program at Ames Research Center.

Author Contributions T.B. led the work, performed the Markov chain Monte Carlo transit modelling and wrote the manuscript. J.F.R. discovered Kepler-37b and Kepler-37c and performed the initial analysis of the light curve. J.J.L. provided guidance on the false-positive probability and contributed to the manuscript. D.H. discovered the solar-like oscillations and led the asteroseismic analysis. F.F. led the BLENDER analysis. S.T.B. performed pixel-level centroid analysis. W.J.C. led the asteroseismic modelling effort. J.-M.D. and D. Charbonneau obtained and analysed the Spitzer observations and wrote the section in Supplementary Information based on these data. E.D.L. calculated the planetary composition constraints. G.W.M. obtained HIRES spectra (Supplementary Information, sections 1 and 3) and performed the cross-correlation function calculation. F.M. developed a model for assessing false-positive probabilities based on colours. D.R. calculated the coplanarity boost used in BLENDER. G.T. developed the BLENDER technique and was involved in the corresponding analysis. E.R.A. and A.K.D. obtained and analysed the adaptive optics images from the MMT. E.A. identified additional transiting planet candidates in the Kepler-37 system. D.B. and J.L.-B. obtained and analysed the lucky imaging data (Supplementary Information, section 4). S.B., T.R.B., J.C.-D., Y.E., R.H., S.H., C.K., S.D.K., H.K., M.N.L., M.L., T.S.M., A.M. and D.S. were involved in the asteroseismic analysis and modelling. L.A.B. analysed the TrES and HIRES spectra using SPC (Supplementary Information, section 1). J.L.C., M.R.H., J.M.J., T.C.K., J.L., R.L.M., E.V.Q., J.C.S., M.S. and S.E.T. were involved in the target management, processing, analysis and dissemination of Kepler data. D. Ciardi, M.E., E.H. and S.B.H. recorded and analysed the high-contrast imaging data. D.A.F. analysed HIRES spectra using SME. J.C.G. developed the Kepler photometer electronics, built KeplerCam for the KIC and follow-up spectral observations, and developed the TRES echelle spectrograph at SAO for follow-up observations. E.B.F. contributed to the analysis of transit times and eccentricities. J.J.F. assisted in modelling the structure and evolution of the planets. C.E.H. assisted in running BLENDER on the NASA Pleiades supercomputer. A.W.H. and H.I. obtained and analysed the HIRES radial velocity data. R.H. manages the Kepler project. D.W.L. obtained TrES spectra.

Author Information Reprints and permissions information is available at www.nature.com/reprints. The authors declare no competing financial interests. Readers are welcome to comment on the online version of the paper. Correspondence and requests for materials should be addressed to T.B. (thomas.barclay@nasa.gov) or J.F.R. (jason.rowe@nasa.gov).

Giant osmotic energy conversion measured in a single transmembrane boron nitride nanotube

Alessandro Siria¹, Philippe Poncharal¹, Anne-Laure Biance¹, Rémy Fulcrand¹, Xavier Blase², Stephen T. Purcell¹ & Lydéric Bocquet¹

New models of fluid transport are expected to emerge from the confinement of liquids at the nanoscale^{1,2}, with potential applications in ultrafiltration, desalination and energy conversion³. Nevertheless, advancing our fundamental understanding of fluid transport on the smallest scales requires mass and ion dynamics to be ultimately characterized across an individual channel to avoid averaging over many pores. A major challenge for nanofluidics thus lies in building distinct and well-controlled nanochannels, amenable to the systematic exploration of their properties. Here we describe the fabrication and use of a hierarchical nanofluidic device made of a boron nitride nanotube that pierces an ultrathin membrane and connects two fluid reservoirs. Such a transmembrane geometry allows the detailed study of fluidic transport through a single nanotube under diverse forces, including electric fields, pressure drops and chemical gradients. Using this device, we discover very large, osmotically induced electric currents generated by salinity gradients, exceeding by two orders of magnitude their pressure-driven counterpart. We show that this result originates in the anomalously high surface charge carried by the nanotube's internal surface in water at large pH, which we independently quantify in conductance measurements. The nano-assembly route using nanostructures as building blocks opens the way to studying fluid, ionic and molecule transport on the nanoscale, and may lead to biomimetic functionalities. Our results furthermore suggest that boron nitride nanotubes could be used as membranes for osmotic power harvesting under salinity gradients.

The field of nanofluidics has developed recently as a result of the characteristic length scale in fluidic systems being reduced to the nanometre range. From a fundamental point of view, novel transport properties are expected to emerge from the combination of strong confinement and the importance of surface properties on the nanoscale⁴, and such properties may lead to technological breakthroughs. Accordingly, studying the physical and chemical interactions of water and ions with the confining structure is crucial to discovering new fluidic properties, as exemplified by the design of fluidic diodes^{5,6} and nanofluidic transistors⁷. Fast mass and ion transport through carbon nanotubes was recently demonstrated^{8–11}, suggesting that water flow in such carbon-based pipes is nearly frictionless^{12–14}. Several recent molecular simulations have suggested that boron nitride nanotubes (BNNTs), which have the crystallographic structure of carbon nanotubes but have radically different electronic properties¹⁵, show great potential for water and ion transport^{16,17}. However, unlike for carbon nanotubes, nanofluidic transport in BNNTs has not yet been studied experimentally.

In this work, we report the fabrication of a new class of nanofluidic devices and study the fluid transport properties inside a single BNNT. The results may have application in renewable-energy harvesting. Our hierarchical nanofluidic device is made of a single BNNT connecting two reservoirs across an impermeable, solid-state membrane (Fig. 1). This transmembrane nanotube (t-BNNT) configuration combines the advantages of an ideal cylindrical nanopipe geometry with the versatility of solid-state nanopore devices^{18,19}. It allows fluid transport in

the nanopipe to be probed under electric, pressure and chemical forcings, and their combinations. The t-BNNT consists of a single BNNT inserted into a hole in a silicon nitride (SiN) membrane. A single hole with a diameter of between 100 and 200 nm is drilled through the membrane using a FIB. An individual multiwalled BNNT is glued at the extremity of an electrochemically etched tungsten tip and its apex is opened using electric field ion evaporation (Supplementary Methods). The insertion of the nanotube into the hole is realized *in situ* in an SEM by nanomanipulation (Fig. 1a and Supplementary Methods). The movements of the tip are controlled by a home-made nanomanipulator consisting of five-axis piezo-inertial motors, which allows us to insert the nanotube into the membrane with nanometre precision. Once the tube is in place, the hole is sealed with cracked naphthalene using local electron-beam-induced deposition. The tip is then retracted, producing a telescopic sliding of the internal walls of the nanotube (Fig. 1a). This step ensures that the inner surface of the nanotube is atomically flat and that both extremities are fully open, thus avoiding inner defects in the channel. A final inspection using TEM allows the quality and inner diameter of the nanotubes to be checked and measured. We studied tubes with inner radii of $R \approx 15$ – 40 nm and lengths of $L \approx 1$ μ m.

The membrane traversed by the BNNT is then squeezed between two macroscopic fluid reservoirs containing potassium chloride (KCl) solutions of various concentrations, with controlled pH (Fig. 1b). We use Ag/AgCl electrodes to measure the electric current passing through the t-BNNT, with a precision in the picoampere range. In addition to the direct TEM visualization of the system, which allows us to verify the integrity of the transmembrane nanotube both before and after fluidic experimentation, benchmark measurements and experimental cross-checks are systematically performed to ensure that transport occurs exclusively through the BNNT (Supplementary Methods).

Our final interest in this work concerns electrical transport induced by salinity gradients in individual BNNTs, which is known as diffusio-osmosis^{20,21}. However, we start by first characterizing the response of the BNNT to voltage and pressure drops, which provide key information on the BNNT's surface properties. Accordingly, the ion current, I , generated through the t-BNNT under an electric potential drop, ΔV , is first measured as a function of salt concentration (Fig. 2a). The electric conductance, $G = I/\Delta V$, and corresponding conductivity, K , defined as $K = GL/\pi R^2$, are deduced as functions of salt concentration (Fig. 2b). For a given tube, these conductance and conductivity curves show saturation of the conductance for low salt concentration. This observation is a signature of a charged confining surface²², which is in strong contrast with the behaviour reported for carbon nanotubes¹¹. The predicted conductance is⁴

$$G = 2e^2 \mu C_s \frac{\pi R^2}{L} + e \mu \frac{2\pi R}{L} |\Sigma| (1 + \alpha) \quad (1)$$

where C_s is the KCl concentration, e is the electronic charge, $\mu = (\mu_K + \mu_{Cl^-})/2 = 4.8 \times 10^{-11}$ s kg⁻¹ is the KCl mobility and Σ is the surface charge density on the BNNT surface (in C m⁻²). The correction $\alpha = (2\pi\lambda_B \mu \eta)^{-1} \approx 1$ accounts for the electro-osmotic

¹Institut Lumière Matière, UMR5306 University Lyon 1-CNRS, 69622 Villeurbanne, France. ²Institut Néel, UPR CNRS 2940 and Université Joseph Fourier, 38042 Grenoble, France.

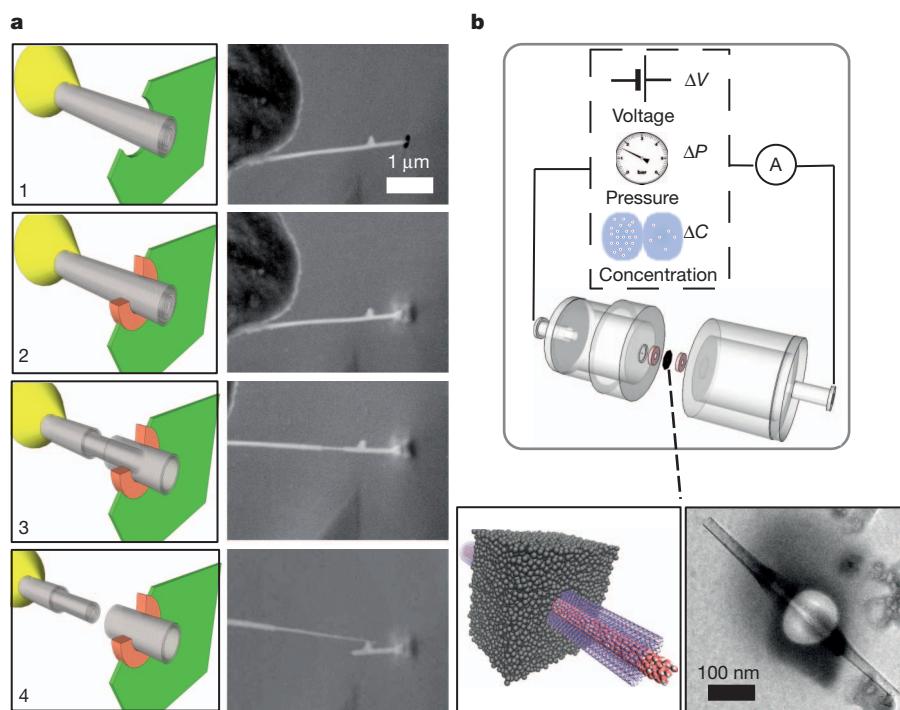


Figure 1 | Hierarchical single nanotube nanofluidic set-up. **a**, *In situ* nanomanipulation of a BNNT (left, sketch; right, scanning electron microscope (SEM) images): 1, insertion of a BNNT (grey) through a nanopore drilled in a SiN membrane (green) using a focused ion beam (FIB); 2, carbon sealing of the FIB-drilled hole using local electron-beam-induced deposition (orange);

contribution to the conductance ($\lambda_B = 0.7$ nm is the Bjerrum length and η is the water viscosity). At low pH (pH 5 in Fig. 2a, b), the calculated surface charge is found to increase slightly as the diameter of the tube is decreased, with a typical value of $\Sigma \approx 0.1$ C m $^{-2}$ (Fig. 2b). Although this surface charge is already very large, we measure a large—and reversible—increase with pH, with Σ rising to 1 C m $^{-2}$ for pH ~ 11 (Fig. 2c), which corresponds to $9e$ nm $^{-2}$ on the BNNT surface. This exceeds typical surface charge densities by at least an order of magnitude²³. Although zeta potential measurements on BN powders have consistently suggested that the BN surface is charged and that the charge is dependent on pH²⁴, the observed chemical reactivity of the BN surface as a function of pH has not been documented up to now. Our results are consistent with a possible chemical equilibrium, $\text{BN}_3 + \text{H}_2\text{O} \rightleftharpoons \text{BN}_3 - \text{OH}^- + \text{H}^+$, in analogy with the reactivity of boric acid, with a corresponding reaction constant K_a .

This unexpected chemical reactivity is supported by preliminary *ab initio* simulations, which demonstrate that an ‘activated’ boron site,

3, telescopic retraction of internal walls of the BNNT; 4, finalized transmembrane BNNT device. **b**, Top, schematic of the experimental set-up for measuring fluid transport through the single BNNT. Bottom, sketch of the final transmembrane BNNT for nanofluidic measurements (left) and its experimental realization, imaged by transmission electron microscopy (TEM) (right).

that is, one with a hydrogen atom bound to a nitrogen atom, can indeed seed water dissociation on a BN sheet (Supplementary Methods). It is well documented²⁵ that defects in the large bandgap of the ionic h-BN system (the planar hexagonal BN sheet) lead to open-shell in-gap states prone to capturing charge. This behaviour echoes that recently described at the non-polar GaN surface, which was shown to generate surface-bound OH^- fragments through spontaneous water dissociation²⁶. In the present situation, a charge regulation model²³ accordingly reproduces the pH dependence of the charge (Fig. 2c), providing a value of $\text{p}K_a \approx 5.5$ for the equilibrium constant (with the density of chargeable sites identified as the surface density of boron in the BNNT, $\Gamma = 18$ nm $^{-2}$; see Supplementary Methods). This value is also consistent with the $\text{p}K_a$ of porous glass, with an expected surface excess of boron²⁷.

The response of the confined fluid to a pressure drop across the t-BNNT furnishes an alternative, sensitive probe to assess the coupled fluid–ion dynamics. By transporting ions in the electric double layer,

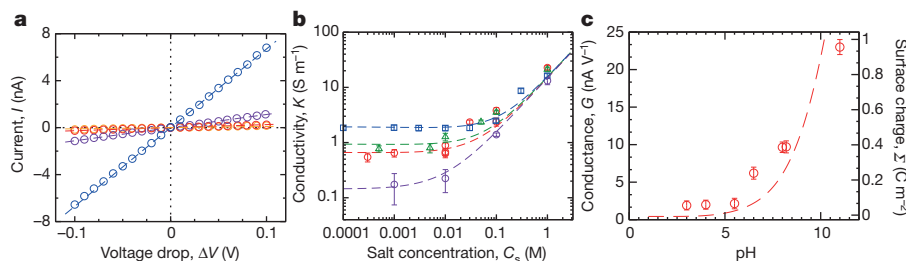


Figure 2 | Electrical conductance and chemical reactivity of the BNNT. **a**, Ion current versus voltage drop for $C_s = 1$ M (blue), 10^{-1} M (purple), 10^{-2} M (orange) and 10^{-3} M (red) at pH 5, for a t-BNNT with $\{R, L\} = \{29$ nm, 900 nm $\}$. Dashed lines are linear fits, from which conductance, $G = I/\Delta V$, and conductivity, $K = GL/\pi R^2$, are determined. **b**, Conductivity versus salt concentration for various t-BNNTs, with $\{R, L\} = \{40$ nm, 1,250 nm $\}$ (purple),

$\{29$ nm, 900 nm $\}$ (red), $\{22$ nm, 1,500 nm $\}$ (green) and $\{15$ nm, 800 nm $\}$ (blue), at pH 5. Dashed lines are predictions using equation (1) with $\Sigma = 25, 85, 90, 125$ mC m $^{-2}$. **c**, Dependence on pH of the conductance and the surface charge, deduced from equation (1), for a t-BNNT with $\{R, L\} = \{29$ nm, 900 nm $\}$ and $C_s = 10^{-2}$ M. Error bars, 1 s.d.

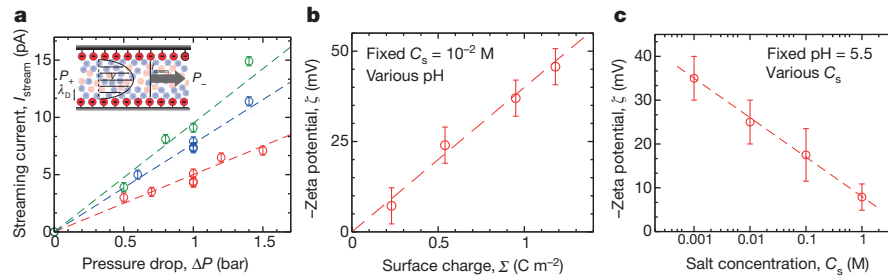


Figure 3 | Pressure-driven streaming. **a**, Streaming current induced by a pressure drop, for a t-BNNT with $\{R, L\} = \{29 \text{ nm}, 900 \text{ nm}\}$, pH 7 (red), 8.5 (blue) and 10 (green), and $C_s = 10^{-2} \text{ M}$. The straight lines are the corresponding linear fits. Inset, sketch of the pressure-driven streaming current. $\Delta P = P_+ - P_-$, pressure drop. **b**, Calculated zeta potential versus

surface charge for $C_s = 10^{-2} \text{ M}$ and pH 5–11.5. The measured surface charge is determined from equation (1) for each pH. The dashed line is a linear fit. **c**, Measured zeta potential versus salt concentration for a t-BNNT with $\{R, L\} = \{40 \text{ nm}, 1,250 \text{ nm}\}$ and pH 5.5. The dashed line is a linear fit of ζ versus $\log(C_s)$. Error bars, 1 s.d.

an electric streaming current, I_{stream} , typically of a few picoamperes, results from the pressure-driven flow (Fig. 3). This provides a measurement of the electro-osmotic mobility and corresponding zeta potential, ζ , here defined by the Smoluchowski relationship²³, $I_{\text{stream}} = -(\epsilon\zeta/\eta)A(\Delta P/L)$, where ϵ is the dielectric permittivity of water, $A = \pi R^2$ is the tube cross-sectional area and ΔP is the applied pressure drop. A pressure drop of up to 1.5 bar is applied between the two fluid reservoirs by means of a voltage-controlled valve (Fig. 1b), and the resulting electric current, $I_{\text{stream}}(\Delta P)$, is measured (Fig. 3a). Like the surface charge, Σ , the corresponding zeta potential is found to increase with pH; in Fig. 3b it is shown to be nearly linearly proportional to $\Sigma(\text{pH})$ as obtained from the independently measured surface conductance. It is also a slowly decreasing function of the salt concentration, varying linearly with $\text{p}C_s = -\log_{10}(C_s)$ (Fig. 3c). Overall, the value of the zeta potential is markedly smaller than the estimated surface potential, as calculated from, for example, the non-linear Poisson–Boltzmann equation (Supplementary Methods). Such behaviour has been reported for other types of charged interface and its origin is the subject of active investigations²⁸.

Together, these first measurements highlight the presence of a very large, pH-sensitive surface charge carried by the inner walls of BNNTs. To our knowledge, values of Σ as high as 1 C m^{-2} have not been reported up to now. We now demonstrate that this property has a key impact on the osmotic transport through the nanotube, whereby an electric current is generated by a difference in salt concentration. This phenomenon is particularly interesting in the context of energy conversion from the mixing of masses of water with different salinities. However, although as much as 0.7 kW h of energy could theoretically be captured per cubic metre of water³, boosting the efficiency of the energy extraction process remains a key challenge.

We use different KCl concentrations, $C_{s,I}$ and $C_{s,II}$, in the range 10^{-3} –1 M in the two reservoirs and measure the resulting electric

current for a variety of concentration ratios, $C_{s,I}/C_{s,II}$. The bare current is corrected for the contribution resulting from the Nernst potential originating in the difference in salt concentration at the two electrodes²⁹ (Supplementary Methods). As shown in Fig. 4a, a very large, osmotically driven current is measured. It is in the nanoampere range, whereas the pressure-driven streaming current is in the picoampere range (Fig. 3). Furthermore, we find that it increases linearly with the logarithm of the salinity ratio, $\Delta\log(C_s) = \log(C_{s,I}/C_{s,II})$:

$$I_{\text{osm}} = K_{\text{osm}} \Delta\log(C_s) \quad (2)$$

Here $K_{\text{osm}} \approx 0.07$ –0.16 nA is the transport coefficient for the nanotube in Fig. 4, with pH ranging from 5.5 to 11, and is almost linearly proportional to the surface charge, Σ (Fig. 4a, inset).

The nanotube is not ion-selective for the configuration presented in Fig. 4a, because no Debye layer overlap occurs here. The origin of the produced current therefore differs from the ion-selective mechanism usually assumed in the osmotic generation of energy, known as reversed electrodialysis, which uses ion exchange membranes to convert a salinity gradient into electric energy^{3,29}. Rather, we suggest that this osmotic current results from the diffusio-osmotic flux induced by the difference in salt concentration at the inner interface of the tube²⁰. Although no global osmotic pressure drop builds up in this permeable configuration, the salt concentration difference builds an osmotic pressure gradient within the diffuse layer at the interfaces^{20,21} (Fig. 4c). Accordingly, the diffusio-osmotic flow, expressed in terms of the diffusio-osmotic velocity, V_{DO} , results from a balance between viscous flow and the osmotic pressure gradient within the Debye layer: $\eta V_{\text{DO}}/\lambda_D \propto \lambda_D k_B T \nabla C_s$. Here $\nabla C_s = \Delta C_s/L$ is the salt concentration gradient, $\lambda_D = (8\pi\epsilon_0\epsilon_r k_B T)^{-1/2}$ is the Debye length, T is the temperature and k_B is the Boltzmann constant. The diffusio-osmotic velocity can then be written as $V_{\text{DO}} = \mu_{\text{DO}} \nabla \log(C_s)$, where $\nabla \log(C_s) =$

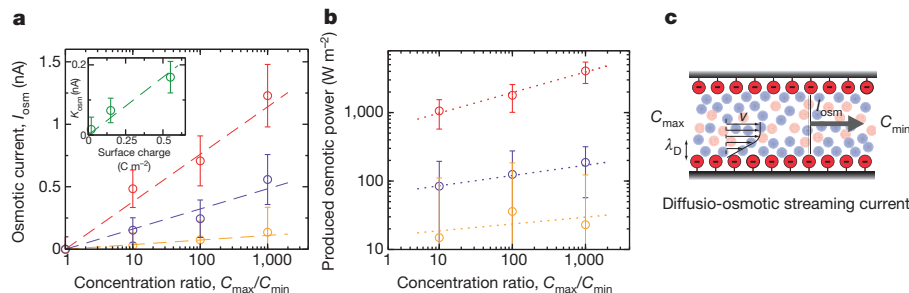


Figure 4 | Osmotic power generation under salinity gradients. **a**, Osmotic streaming current versus concentration difference for a t-BNNT with $\{R, L\} = \{40 \text{ nm}, 1,250 \text{ nm}\}$ and pH 5.5 (yellow), 9.5 (purple) and 11 (red). The experimental points show measurements for various salt concentrations in the two reservoirs, with C_{min} and C_{max} in the range 10^{-3} –1 M. Error bars follow from the corresponding error analysis. Dashed lines are linear fits: $I_{\text{osm}} = K_{\text{osm}} \log(C_{\text{max}}/C_{\text{min}})$. Inset, osmotic mobility versus surface charge.

Surface charge is obtained from independent conductance measurements. The dashed line is a linear fit: $K_{\text{osm}} \approx 0.33 \Sigma$. **b**, Corresponding power density (per unit surface of the BNNT) for the three values of pH. Dotted lines are a guide to the eye. In the present graph, the minimum concentration is fixed to $C_{\text{min}} = 10^{-3} \text{ M}$. **c**, Sketch of the osmotically driven streaming current under a salt concentration difference, $C_{\text{max}} - C_{\text{min}}$.

$\Delta \log(C_s)/L$ and the diffusio-osmotic mobility scales as $\mu_{\text{DO}} \propto k_B T / \eta \lambda_B \approx 10^{-9} \text{ m}^2 \text{ s}^{-1}$ (ref. 20). This diffusio-osmotic flow drags the charges in the double layer at the BNNT interface (Fig. 4c). The predicted osmotic current is written accordingly as $I_{\text{osm}} \propto 2\pi R \Sigma V_{\text{DO}}$:

$$I_{\text{osm}} \approx \frac{2\pi R \Sigma k_B T}{L \eta \lambda_B} \Delta \log(C_s) \quad (3)$$

A rigorous derivation of the osmotic current is given in Supplementary Methods and confirms the scaling described by equation (3). This expression captures the observed functional dependence of the osmotic current on the salinity ratio (Fig. 4a), with a predicted transport mobility (here expressed in nA) proportional to Σ for large surface charge, $K_{\text{osm}}^{\text{theo}} \approx 0.2\Sigma$, in good quantitative agreement with experiments (Fig. 4a, inset).

Furthermore, the complete theoretical model predicts that for small Σ values the osmotic mobility, K_{osm} , decreases to zero like Σ^3 (Supplementary Methods): this points to the unique quality of BN as a confining material, whose giant surface charge generates much larger osmotic current than for alternative materials. Also, the measured osmotic current is larger than the pressure-driven streaming currents plotted in Fig. 3a. This is due to a combination of factors. First, owing to the difference in microscopic origin of the two phenomena, the osmotic mobility is much more sensitive to large surface charges than its electro-osmotic counterpart (Supplementary Methods). Second, the osmotic pressure drop that exists inside the double layer for the osmotically driven phenomenon is much larger than the external pressure drop that can usually be applied. Typically, $\Delta P_{\text{osm}} \approx 50$ bar inside the double layer for $\Delta C_s = 1$ M as compared with the applicable pressure range for pressure-driven flows, ΔP_{ext} , which is at most a few bars. Under such large pressures, a streaming current of up to 0.5 nA could be extrapolated, although the origins of the two phenomena are clearly different. Finally, the predicted linear scaling of I_{osm} as a function of nanotube radius makes the osmotic generation more efficient for smaller tubes than its pressure-driven counterpart, which is proportional to the square of tube radius (Supplementary Methods).

The t-BNNT device thus generates electrical energy from a salinity gradient. The maximum power generated is $P_{\text{max}} = I_{\text{osm}}^2 / 4G_{\text{ion}} = K_{\text{osm}}^2 / 4G_{\text{ion}} [\Delta \log(C_s)]^2$ (ref. 29), which leads to a power density per unit tube surface of $\mathcal{P}_{\text{max}} = P_{\text{max}} / \pi R^2$, reaching 4 kW m^{-2} for the single BNNT (Fig. 4b). This single-nanotube result could be extrapolated to a macroscopic BN membrane³⁰, with a similar BNNT density of $\sim 10^{10} \text{ cm}^{-2}$, for which the predicted power density reaches values in the same range (kW m^{-2}). These values exceed by several orders of magnitude the reported power densities, usually of a few tens of watts per square metre, using classical reversed electrodialysis with alternative exchange membranes³. Our results thus demonstrate the impressive performance of BNNT membranes for energy conversion from the mixing of water masses with different salinities, making them potentially superior to photovoltaics. They open a new avenue in the exploration of new sources of renewable 'blue energy'.

METHODS SUMMARY

The transmembrane nanotube device is realized by *in situ* SEM insertion of a nanotube in a FIB-drilled SiN membrane. The nanotube is opened via *in situ* TEM field evaporation of the apex. The membrane and nanotube are positioned on a five-axis nanomanipulator allowing x - y - z translation (Attocube ANPx-z51) along with θ - ϕ rotation (Attocube ANR51). A first, coarse, approach is performed with 100-nm stick-and-slip steps of the inertial motors. The final insertion of the nanotube in the membrane is done with nanometre precision, by applying a d.c. voltage to the piezoelectric element of the motors. Once inserted, an electron beam is focused on the hole and a gas injection system is used to inject naphthalene (C_8H_8) locally, which is decomposed under electron-beam irradiation and subsequently fills the hole with a water-impermeable and electrically insulating material. The transmembrane nanotube is then squeezed between two reservoirs, allowing for measurements of the ion current induced by voltage drop, pressure drop and salt concentration difference.

Received 4 September; accepted 20 December 2012.

1. Sparreboom, W., van den Berg, A. & Eijkel, J. C. T. Principles and applications of nanofluidic transport. *Nature Nanotechnol.* **4**, 713–720 (2009).
2. Rasaiah, J. C., Garde, S. & Hummer, G. Water in non polar confinement: from nanotubes to proteins and beyond. *Annu. Rev. Phys. Chem.* **59**, 713–740 (2008).
3. Logan, B. E. & Elimelech, M. Membrane-based processes for sustainable power generation using water. *Nature* **488**, 313–319 (2012).
4. Bocquet, L. & Charlaix, E. Nanofluidics, from bulk to interfaces. *Chem. Soc. Rev.* **39**, 1073–1095 (2010).
5. Karnik, R., Duan, C., Castelino, K., Daiguji, H. & Majumdar, A. Rectification of ionic current in a nanofluidic diode. *Nano Lett.* **7**, 547–551 (2007).
6. Siwy, Z. & Fulinski, A. Fabrication of a synthetic nanopore ion pump. *Phys. Rev. Lett.* **89**, 198103 (2002).
7. Schasfoort, R. B. M., Schlautmann, S., Hendrikse, J. & van den Berg, A. Field-effect flow control for microfabricated fluidic networks. *Science* **286**, 942–945 (1999).
8. Majumdar, M., Chopra, N., Andrews, R. & Hinds, B. J. Enhanced flow in carbon nanotubes. *Nature* **438**, 44 (2005).
9. Holt, J. K. *et al.* Fast mass transport through sub-2-nanometer carbon nanotubes. *Science* **312**, 1034–1037 (2006).
10. Whitby, M., Cagnon, L., Thanou, M., & Quirke, N. Enhanced fluid flow through nanoscale carbon pipes. *Nano Lett.* **8**, 2632–2637 (2008).
11. Liu, H. *et al.* Translocation of single stranded DNA through single-walled carbon nanotubes. *Science* **327**, 64–67 (2010).
12. Hummer, G., Rasaiah, J. C. & Noworyta, J. P. Water conduction through the hydrophobic channel of a carbon nanotube. *Nature* **414**, 188–190 (2001).
13. Falk, K., Sedlmeier, F., Joly, L., Netz, R. R., & Bocquet, L. Molecular origin of fast water transport in carbon nanotube membranes: superlubricity versus curvature dependent friction. *Nano Lett.* **10**, 4067–4073 (2010).
14. Joseph, S. & Aluru, N. R. Why are carbon nanotubes fast transporters of water? *Nano Lett.* **8**, 452–458 (2008).
15. Arenal, R., Blase, X. & Loiseau, A. Boron-nitride and boron-carbonitride nanotubes: synthesis, characterization and theory. *Adv. Phys.* **59**, 101–179 (2010).
16. Won, C. Y. & Aluru, N. R. Water permeation through a subnanometer boron nitride nanotube. *J. Am. Chem. Soc.* **129**, 2748–2749 (2007).
17. Hilder, T. A., Gordon, D., Chung, S.-H. & Salt rejection, and water transport through boron nitride nanotubes. *Small* **5**, 2183–2190 (2009).
18. Li, J. *et al.* Nanoscale ion beam sculpting. *Nature* **412**, 166–169 (2001).
19. Dekker, C. Solid state nanopores. *Nature Nanotechnol.* **2**, 209–215 (2007).
20. Anderson, J. L. Colloid transport by interfacial forces. *Annu. Rev. Fluid Mech.* **21**, 61–99 (1989).
21. Fair, J. C. & Osterle, J. F. Reverse electrodialysis in charged capillary membranes. *J. Chem. Phys.* **54**, 3307–3316 (1971).
22. Stein, D., Kruthof, M. & Dekker, C. Surface charge governed ion transport in nanofluidic channels. *Phys. Rev. Lett.* **93**, 035901 (2004).
23. Hunter, R. J. *Foundations of Colloid Science* (Oxford Univ. Press, 1991).
24. Crimp, M. J., Oppermann, D. A. & Krehbiel, K. Suspension properties of hexagonal BN powders: effect of pH and oxygen content. *J. Mater. Sci.* **34**, 2621–2625 (1999).
25. Schmidt, T. M., Baierle, R. J., Piquini, P. & Fazzio, A. Theoretical study of native defects in BN nanotubes. *Phys. Rev. B* **67**, 113407 (2003).
26. Wang, J., Pedroza, L. S., Poissier, A. & Fernandez-Serra, M. V. Water dissociation at the GaN surface: structure, dynamics and surface acidity. *J. Phys. Chem. C* **116**, 14382–14389 (2012).
27. Altug, I. & Hair, M. L. Cation exchange in porous glass. *J. Phys. Chem.* **71**, 4260–4263 (1967).
28. Bonhuis, D. & Netz, R. Unraveling the effects of dielectric and viscosity profiles on electro-osmotic mobility and electric surface conductivity. *Langmuir* **28**, 16049–16059 (2012).
29. Kim, D.-K., Duan, C., Chen, Y.-F. & Majumdar, A. Power generation from concentration gradient by reverse electrodialysis in ion-selective nanochannels. *Microfluid. Nanofluid.* **9**, 1215–1224 (2010).
30. Bechelany, M. *et al.* Synthesis of boron nitride nanotubes by a template-assisted polymer thermolysis process. *J. Phys. Chem. C* **111**, 13378–13384 (2007).

Supplementary Information is available in the online version of the paper.

Acknowledgements L.B. acknowledges support from ERC-AG project Micromegas and the French ANR under the programme P3N. We thank D. Cornu, M. Bechelany, A. Brioude for providing the boron nitride nanotubes, D. Guillot for building the experimental fluidic set-up and P. Vincent for assistance with the SEM. L.B. thanks M.-L. Bocquet for discussions on boron nitride chemistry. We thank L. Auvray, E. Charlaix, C. Cottin-Bizonne, J. Gierak, D. M. Huang, L. Joly, A. Madouri, R. Netz, J. Palacci and C. Ybert for many discussions. We thank the Centre Lyonnais de Microscopie for providing access to the dual-beam FIB.

Author Contributions L.B. conceived the project. P.P. and S.T.P. designed the transmembrane nanotube system. A.S. and P.P. constructed the experimental device with contributions from R.F. and A.-L.B. A.S., A.-L.B. and L.B. designed the fluidic system (with input from P.P.), performed measurements and conducted the experimental analysis. X.B. performed the *ab initio* simulations. L.B. wrote the manuscript with input from all authors.

Author Information Reprints and permissions information is available at www.nature.com/reprints. The authors declare no competing financial interests. Readers are welcome to comment on the online version of the paper. Correspondence and requests for materials should be addressed to L.B. (lyderic.bocquet@univ-lyon1.fr).

Enhanced nitrogen deposition over China

Xuejun Liu^{1*}, Ying Zhang^{1*}, Wenxuan Han¹, Aohan Tang¹, Jianlin Shen¹, Zhenling Cui¹, Peter Vitousek², Jan Willem Erisman^{3,4}, Keith Goulding⁵, Peter Christie^{1,6}, Andreas Fangmeier⁷ & Fusuo Zhang¹

China is experiencing intense air pollution caused in large part by anthropogenic emissions of reactive nitrogen^{1,2}. These emissions result in the deposition of atmospheric nitrogen (N) in terrestrial and aquatic ecosystems, with implications for human and ecosystem health, greenhouse gas balances and biological diversity^{1,3–5}. However, information on the magnitude and environmental impact of N deposition in China is limited. Here we use nationwide data sets on bulk N deposition, plant foliar N and crop N uptake (from long-term unfertilized soils) to evaluate N deposition dynamics and their effect on ecosystems across China between 1980 and 2010. We find that the average annual bulk deposition of N increased by approximately 8 kilograms of nitrogen per hectare ($P < 0.001$) between the 1980s (13.2 kilograms of nitrogen per hectare) and the 2000s (21.1 kilograms of nitrogen per hectare). Nitrogen deposition rates in the industrialized and agriculturally intensified regions of China are as high as the peak levels of deposition in northwestern Europe in the 1980s⁶, before the introduction of mitigation measures^{7,8}. Nitrogen from ammonium (NH_4^+) is the dominant form of N in bulk deposition, but the rate of increase is largest for deposition of N from nitrate (NO_3^-), in agreement with decreased ratios of NH_3 to NO_x emissions since 1980. We also find that the impact of N deposition on Chinese ecosystems includes significantly increased plant foliar N concentrations in natural and semi-natural (that is, non-agricultural) ecosystems and increased crop N uptake from long-term-unfertilized croplands. China and other economies are facing a continuing challenge to reduce emissions of reactive nitrogen, N deposition and their negative effects on human health and the environment.

Atmospheric N deposition results from emissions of reactive nitrogen (N_r) species and their atmospheric transport; it expands the footprint of local alterations to the N cycle³. Although both natural and anthropogenic sources contribute to atmospheric N deposition, anthropogenic N_r emissions (largely from the agricultural, industrial and transport sectors) have increased substantially since the industrial revolution began⁹; they now make the dominant contribution to N deposition in many regions^{3,10}. Increased concentrations of N_r in the atmosphere and, through deposition, in terrestrial or aquatic ecosystems, or both, degrade human health¹ (notably through driving the formation of particulate matter and tropospheric ozone), alter soil and water chemistry³, influence greenhouse gas balance⁴ and reduce biological diversity⁵.

The human and environmental costs associated with anthropogenic N_r are well recognized, and active measures in Western Europe and North America have stabilized or reduced N_r deposition in those regions^{6,11,12}. Even so, very large costs of excess N_r have been reported in the European Union⁸ (€70–320 billion per year) and the United States¹³. In contrast, over the past 30 years China's emissions have increased to the point that it has become by far the largest creator and emitter of N_r globally². However, the rates and trends of N deposition in China since the 1980s are not clear. We would also like to know

the consequences of N deposition, for the people and ecosystems of China, its region and the world.

Following rapid economic growth since the early 1980s, China's gross domestic product was estimated at US\$5.9 trillion in 2010, making China the world's second largest economy after the United States (http://money.cnn.com/news/economy/world_economies_gdp). In around the year 2000, China surpassed the United States and the European Union (combined) in its production and use of N fertilizers. Moreover, less than half of the fertilizer N applied in China is taken up by crops¹⁴; the rest is largely lost to the environment in gaseous (NH_3 , NO , N_2O and N_2) or dissolved (NH_4^+ and NO_3^-) forms^{15,16}. These fluxes—along with N_r emitted during fossil fuel combustion—have resulted in some of the most pronounced air pollution on Earth¹.

Increased N_r emissions must have influenced atmospheric N deposition in and near China, but information on the magnitude, scope and consequences of any change has been lacking. Here we summarize available data nationwide on the bulk deposition of N_r in terrestrial ecosystems. Also, we show that the N cycle has been altered in Chinese ecosystems, both within and outside croplands.

Nitrogen deposition includes wet and dry deposition of both inorganic and organic N forms^{2,17}, but in most cases only the bulk deposition of inorganic N ($\text{NH}_4\text{-N}$ and $\text{NO}_3\text{-N}$) has been measured systematically^{6,18,19}. Bulk N deposition denotes N input from precipitation as measured by an open sampler (Supplementary Methods); it is a relatively simple measure that includes wet deposition and a fraction of the dry deposition, and it is suitable for regional comparisons. We constructed a national data set incorporating all the available bulk N deposition results from monitoring sites throughout China between 1980 and 2010 (Supplementary Fig. 1). This data set was used to test the magnitude and trend of atmospheric N deposition in relation to anthropogenic emissions of reduced and oxidized forms of N.

In spite of site-to-site variability in the data, bulk N deposition increased significantly with time ($P < 0.001$), with an average annual increase of 0.41 kilograms of nitrogen per hectare (kgN ha^{-1}) between 1980 and 2010 (Fig. 1a and Supplementary Table 1). The increase in bulk N deposition was driven mainly by increased volume-weighted N concentrations in rain water ($0.063 \text{ mgN l}^{-1} \text{ yr}^{-1}$ on average; Fig. 1b) because annual precipitation in the study area has not changed significantly in the past 30 years (Supplementary Fig. 2 and Supplementary Table 1). $\text{NH}_4\text{-N}$ was the dominant form in bulk deposition, but the ratio of $\text{NH}_4\text{-N}$ to $\text{NO}_3\text{-N}$ in bulk precipitation decreased significantly with time (Fig. 1c, Supplementary Fig. 3 and Supplementary Table 1). Overall, annual bulk N deposition averaged 13.2 and 21.1 kgN ha^{-1} in the 1980s and 2000s, respectively, showing an increase of approximately 8 kgN ha^{-1} , or 60% ($P < 0.001$).

The increase in overall bulk N deposition and the change in the ratio of $\text{NH}_4\text{-N}$ to $\text{NO}_3\text{-N}$ in precipitation and deposition (Fig. 1) are similar to the increasing trends of anthropogenic gaseous N_r (NH_3 and NO_x) emissions and changes in their ratio since 1980 (Fig. 2a and Supplementary Fig. 4a). The ratio of $\text{NH}_4\text{-N}$ to $\text{NO}_3\text{-N}$ in measured

¹College of Resources & Environmental Sciences, China Agricultural University, Beijing 100193, China. ²Department of Biology, Stanford University, Stanford, California 94305, USA. ³VU University Amsterdam, 1081 HV Amsterdam, The Netherlands. ⁴Louis Bolk Institute, Hoofdstraat 24, 3972 LA Driebergen, The Netherlands. ⁵The Sustainable Soils and Grassland Systems Department, Rothamsted Research, Harpenden AL5 2JQ, UK. ⁶Agri-Environment Branch, Agri-Food and Biosciences Institute, Belfast BT9 5PX, UK. ⁷Institute of Landscape and Plant Ecology, University of Hohenheim, 70593 Stuttgart, Germany.

*These authors contributed equally to this work.

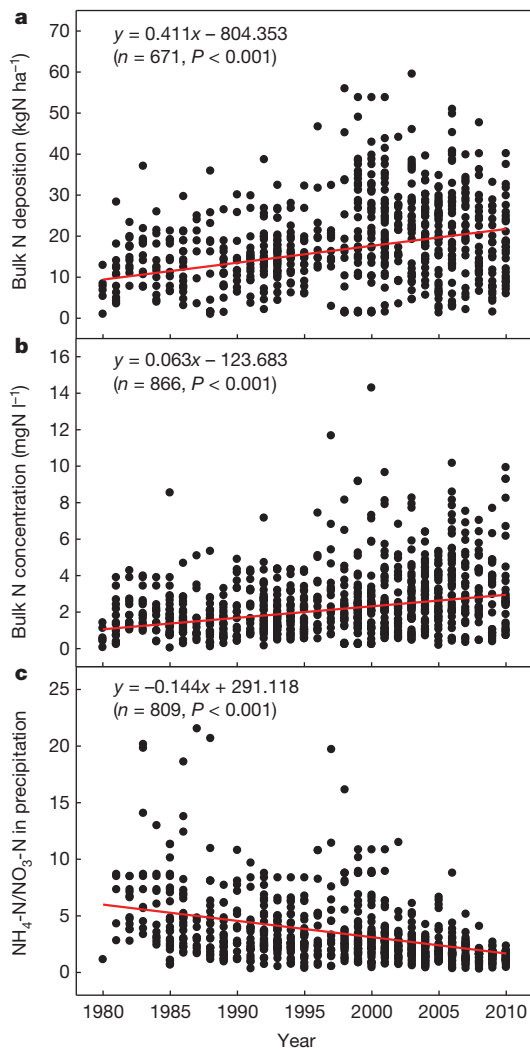


Figure 1 | Trends in N deposition and its components in China between 1980 and 2010. **a**, Bulk N deposition; **b**, bulk N concentration; **c**, ratios of $\text{NH}_4\text{-N}$ to $\text{NO}_3\text{-N}$ in bulk precipitation. In spite of large site-to-site variability, both bulk N deposition and N concentration have increased significantly since 1980, and the ratio of $\text{NH}_4\text{-N}$ to $\text{NO}_3\text{-N}$ in bulk precipitation has decreased significantly according to linear mixed models (all $P < 0.001$; Supplementary Table 1). Data sources are included in Supplementary Information.

bulk deposition decreased from about 5 to 2, and the ratio of $\text{NH}_3\text{-N}$ to $\text{NO}_x\text{-N}$ in calculated emissions decreased from about 4 to 2.5; these changes are highly correlated ($P < 0.01$). Emissions of NH_3 doubled (Fig. 2a), reflecting increased agricultural production in that both the use of N fertilizer and the number of domestic animals (expressed as standard livestock units) have also doubled since the 1980s (Fig. 2b and Supplementary Fig. 4b). Fossil fuel power plants, industrial production and motor vehicles are the major sources of NO_x in China and Asia²⁰. Coal consumption and the number of motor vehicles increased 3.2- and 20.8-fold, respectively, between the 1980s and the 2000s (Fig. 2c and Supplementary Fig. 4c), driving a more rapid percentage increase in NO_x emission than in NH_3 emission (Fig. 2a), although the net increase in emission was still larger for NH_3 than for NO_x (about 6 TgN versus 4 TgN between the 1980s and the 2000s). The ratio of $\text{NH}_4\text{-N}$ to $\text{NO}_3\text{-N}$ in bulk precipitation (Fig. 1c) changed in the same direction and by approximately the same magnitude as the ratio of $\text{NH}_3\text{-N}$ to $\text{NO}_x\text{-N}$ emission over the same period (Fig. 2a), despite uncertainties in ammonia emission inventories^{2,21}.

We analysed the dynamics of bulk N deposition regionally by dividing deposition data into six areas: northern, southeast, southwest, northeast and northwest China and the Tibetan plateau. Human influences

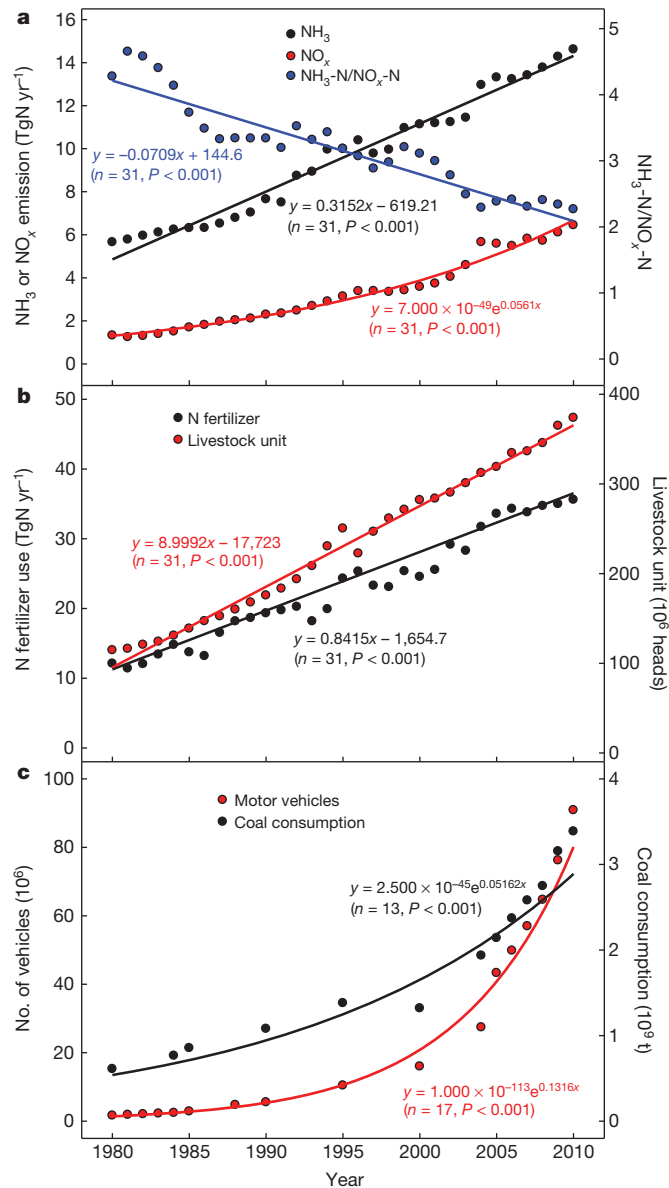


Figure 2 | Trends in NH_3 and NO_x emissions and their main contributors between 1980 and 2010. **a**, NH_3 and NO_x emissions and ratios of $\text{NH}_3\text{-N}$ to $\text{NO}_x\text{-N}$ emission; **b**, number of domestic animals (expressed as livestock units) and N fertilizer consumption; **c**, number of motor vehicles and coal consumption. Data sources are cited in Supplementary Information.

on the N cycle differ substantially among these regions. In general, bulk N deposition showed increasing trends and ratios of $\text{NH}_4\text{-N}$ to $\text{NO}_3\text{-N}$ showed decreasing trends for all six regions between the 1980s and the 2000s (Supplementary Table 1); highly significant ($P < 0.001$) increases in bulk N deposition were found in northern, southeast and southwest China, significant ($P < 0.05$) increases were found in the Tibetan plateau and northeast China, and no significant ($P = 0.199$) increase was found in northwest China (Supplementary Figs 5 and 6). By comparison with the national average, we found both higher overall rates of deposition and higher annual rates of increase in deposition in the industrialized and agriculturally intensified northern, southeast and southwest China. Annual bulk deposition rates were 22.6, 24.2 and 22.2 kgN ha^{-1} in northern, southeast and southwest China in the 2000s, respectively, with average rates of increase of 0.42, 0.56 and 0.53 $\text{kgN ha}^{-1} \text{yr}^{-1}$. A more detailed study²² of all major deposition pathways shows that total annual N wet and dry deposition on the northern China plain (the central area of northern China) was about 80 kgN ha^{-1} . These levels are much higher than those observed in any region in the United

States¹², and are comparable to the maximum values observed in the United Kingdom⁶ and the Netherlands⁷ when N deposition was at its peak in the 1980s⁸.

Extensive long-term environmental inventories and experiments in China allow us to evaluate some of the consequences of this substantial and continuing increase in N deposition. We have summarized results of an ongoing survey of foliar N concentrations from non-agricultural ecosystems throughout China and from detailed studies of crop N uptake from croplands in long-term trials without N fertilizer (described as zero-N plots hereafter), which are used as reference plots in fertilization experiments. The foliar N data set provides information on how changes in N deposition have influenced plant tissue chemistry in unfertilized, non-agricultural ecosystems. Foliar N increased significantly (all $P < 0.001$) between the 1980s and the 2000s for woody, herbaceous and all plant species (Fig. 3a, Supplementary Fig. 7a and Supplementary Table 1). Foliar N increase for all species averaged 32.8% ($24.0 \pm 9.2 \text{ mg g}^{-1}$ (2000s) versus $18.1 \pm 7.2 \text{ mg g}^{-1}$ (1980s)), with a higher increase in herbaceous plants than in woody plants (Fig. 3a). In contrast, foliar phosphorus (P) did not change significantly ($P = 0.085$) over the same period (Supplementary Fig. 7b and Supplementary Table 1). Foliar N is largely determined by plant species and plant N nutritional status; foliar N of specific plant species should be stable in natural and semi-natural ecosystems unless some process changes the availability of N relative to other plant resources²³.

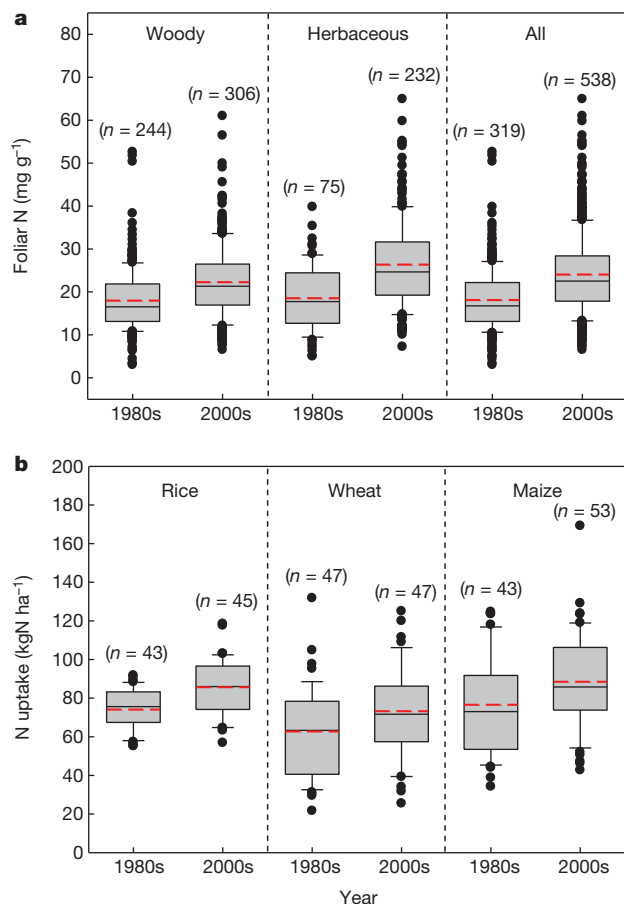


Figure 3 | Comparisons of foliar N concentrations and crop N uptake between the 1980s and 2000s. **a**, Foliar N in woody, herbaceous and all plant species in non-agricultural ecosystems; **b**, N uptake by rice, wheat and maize from zero-N plots in long-term experiments. Both foliar N (all $P < 0.001$) and N uptake (all $P < 0.05$) are significantly higher in the 2000s than in the 1980s. The black and red lines, lower and upper edges, bars and dots in or outside the boxes represent median and mean values, 25th and 75th, 5th and 95th, and <5th and >95th percentiles of all data, respectively.

Plant species in this study were sampled widely (Supplementary Fig. 1) and analysed by standard procedures (Supplementary Information)—and the evaluation of foliar P should correct for any bias towards sampling high-nutrient plant species late in the record (suggesting no apparent changes in the soil environment)—so the increase in foliar N in unfertilized ecosystems most probably represents a widespread increase in plant N nutritional status caused by the cumulative effects of enhanced N deposition.

In agricultural ecosystems, crop N uptake from zero-N plots in long-term experiments is controlled primarily by N deposition, because soil N pools are relatively stable after 5 to 10 years without N fertilization^{22,24}. We summarized the available data on N uptake from zero-N plots in long-term experiments between 1980 and 2010 (Supplementary Information); N uptake by rice, wheat and maize in zero-N plots was significantly higher in the 2000s than in the 1980s (Fig. 3b; all $P < 0.05$). The increase in N uptake averaged 11.3 kgN ha^{-1} across the three major cereals (Fig. 3b and Supplementary Fig. 8).

Overall, the temporal patterns in bulk N deposition, foliar N and N uptake from zero-N plots are consistent with rapidly increased anthropogenic NH_3 and NO_x emissions over the past three decades. The lower ratio of reduced N to oxidized N in measured deposition agrees well with the decrease in the ratio of calculated emissions of NH_3 to NO_x , reflecting a more rapid proportional increase in N_r emissions from industrial and traffic sources than from agricultural sources. All these changes can be linked to a common driving factor, strong economic growth, which has led to continuous increases in agricultural and non-agricultural N_r emissions and, consequently, increased N deposition.

Although we did not measure the impact of atmospheric N_r emissions and deposition from China on the global environment, recent studies indicate that N_r deposited by China may be moving to surrounding marine ecosystems²⁵ and perhaps to tropical and subtropical forests²⁶. Another study²⁷ reported a strong abnormal spring increase in free tropospheric ozone concentrations in western North America between 1995 and 2008, and suggested that NO_x -induced ozone transport from Asia (mainly from China and India) to North America could be a major source.

Clearly, N deposition has increased significantly in China and has affected both non-agricultural and agricultural ecosystems. So far, China's economic growth model has relied mainly on the consumption of raw materials, and it has caused large anthropogenic N_r emissions in addition to other environmental perturbations²⁸. For example, the emitted NH_3 and NO_x gases form secondary aerosols such as NH_4NO_3 in $\text{PM}_{2.5}$ (particulate matter with aerodynamic diameter $\leq 2.5 \mu\text{m}$) under favourable conditions, decrease visibility and damage human health. The Chinese government has recognized the importance of protecting the environment while developing the economy; recently, it approved the first national environmental standard for limiting the amount of $\text{PM}_{2.5}$ (ref. 29).

Our results demonstrate that deposition of reduced forms of N_r continues to be of greatest importance in China (which is responsible for approximately 2/3 of total deposition) but emission and deposition of oxidized N_r are increasing more rapidly. Current environmental policy needs to focus more strongly on reducing present NH_3 emissions from agricultural sources, whereas control of NO_x emissions from industrial and traffic sources will become more important in the near future. It is time for China and other economies to take action to improve N-use efficiency and food production in agriculture and reduce N_r emissions from both agricultural and non-agricultural sectors. These actions are crucial to reducing N deposition and its negative impact locally and globally.

METHODS SUMMARY

Data sets on bulk N deposition, plant foliar N concentration and crop N uptake from non-N-fertilized soils were summarized from published data and measurements across China. Using 315 references and our own deposition monitoring

network (CAUDN), we constructed a nationwide data set of the amount of annual precipitation, volume-weighted N concentrations in precipitation and bulk N deposition, as well as the ratio of $\text{NH}_4\text{-N}$ to $\text{NO}_3\text{-N}$ deposition. A total of 866 data points of annual volume-weighted N concentrations in precipitation and 671 data points of annual bulk N deposition rates at 270 monitoring sites were summarized for the period 1980–2010. To clarify regional variations, bulk N deposition data from six separate regions were also summarized. Additionally, a total of 981 observations of plant foliar N concentration and 859 observations of foliar P were collected from 666 natural and semi-natural terrestrial plant species or varieties at 245 sites distributed across the whole of China (based mainly on ref. 30; Supplementary Fig. 1), and a total of 278 data points of crop N uptake by rice, wheat and maize were summarized from non-N-fertilized soils in long-term experiments. Emissions of national anthropogenic NH_3 and NO_x were summarized from published data² and updated to 2010 (Supplementary information).

Data on N deposition, foliar N and crop N uptake, and other related parameters, were fitted (with year) using linear mixed models or nonlinear regression models for the interval 1980–2010 (SPSS13.0, SPSS Inc.). Differences in these data between the 1980s (1980–1989) and the 2000s (2000–2010) were compared statistically using an unpaired two-tail Student's *t*-test. A significant difference is assumed when the *P* value is <0.05 or as otherwise stated. Further details on the data sets and statistical methods are given in Supplementary Methods.

Full Methods and any associated references are available in the online version of the paper.

Received 25 June 2012; accepted 15 January 2013.

Published online 20 February 2013.

- Richter, D. D., Burrows, J. P., Nüß, H., Granier, C. & Niemeier, U. Increase in tropospheric nitrogen dioxide over China observed from space. *Nature* **437**, 129–132 (2005).
- Liu, X. J. *et al.* Nitrogen deposition and its ecological impacts in China: an overview. *Environ. Pollut.* **159**, 2251–2264 (2011).
- Vitousek, P. M. *et al.* Human alteration of the global nitrogen cycle: sources and consequences. *Ecol. Appl.* **7**, 737–750 (1997).
- Matson, P., Lohse, K. A. & Hall, S. J. The globalization of nitrogen deposition: consequences for terrestrial ecosystems. *Ambio* **31**, 113–119 (2002).
- Clark, C. M. & Tilman, D. Loss of plant species after chronic low-level nitrogen deposition to prairie grasslands. *Nature* **451**, 712–715 (2008).
- Goulding, K. W. T. *et al.* Nitrogen deposition and its contribution to nitrogen cycling and associated soil processes. *New Phytol.* **139**, 49–58 (1998).
- Erisman, J. W. *et al.* The Dutch N-cascade in the European perspective. *Sci. China C* **48**, 827–842 (2005).
- Sutton, M. A. *et al.* *The European Nitrogen Assessment: Sources, Effects and Policy Perspectives* (Cambridge Univ. Press, 2011).
- Galloway, J. N. *et al.* Transformation of the nitrogen cycle: recent trends, questions, and potential solutions. *Science* **320**, 889–892 (2008).
- Schlesinger, W. H. On the fate of anthropogenic nitrogen. *Proc. Natl Acad. Sci. USA* **106**, 203–208 (2009).
- Bleeker, A. *et al.* in *Atmospheric Ammonia: Detecting Emission Changes and Environmental Impacts* (eds. Sutton, M. A., Reis, S. & Baker, S. M. H.) 123–180 (Springer, 2009).
- Holland, E. A., Braswell, B. H., Sulzman, J. & Lamarque, J. F. Nitrogen deposition onto the United States and Western Europe: synthesis of observations and models. *Ecol. Appl.* **15**, 38–57 (2005).
- Compton, J. E. *et al.* Ecosystem services altered by human changes in nitrogen cycle: a new perspective for US decision making. *Ecol. Lett.* **14**, 804–815 (2011).
- Zhang, F. S. *et al.* Nutrient use efficiencies of major cereal crops in China and measures for improvement. *Acta Pedol. Sin.* **45**, 915–924 (2008).
- Zhu, Z. L. & Chen, D. L. Nitrogen fertilizer use in China: contributions to food production, impacts on the environment and best management strategies. *Nutr. Cycl. Agroecosyst.* **63**, 117–127 (2002).
- Ju, X. T. *et al.* Reducing environmental risk by improving N management in intensive Chinese agricultural systems. *Proc. Natl Acad. Sci. USA* **106**, 3041–3046 (2009).
- Erisman, J. W. & Draaijers, G. P. J. *Studies in Environmental Science* Vol. 63, 9 (Elsevier, 1995).
- Frink, C. R., Waggoner, P. E. & Ausubel, J. H. Nitrogen fertilizer: retrospect and prospect. *Proc. Natl Acad. Sci. USA* **96**, 1175–1180 (1999).
- Liu, X. J. *et al.* Nitrogen deposition in agroecosystems in the Beijing area. *Agric. Ecosyst. Environ.* **113**, 370–377 (2006).
- Klimont, Z. *et al.* Projections of SO_2 , NO_x , NH_3 and VOC emissions in East Asia up to 2030. *Wat. Air Soil Pollut.* **130**, 193–198 (2001).
- Schjørring, J. K. Atmospheric ammonia and impacts of nitrogen deposition: uncertainties and challenges. *New Phytol.* **139**, 59–60 (1998).
- He, C. E., Liu, X. J., Fangmeier, A. & Zhang, F. S. Quantifying the total airborne nitrogen-input into agroecosystems in the North China Plain. *Agric. Ecosyst. Environ.* **121**, 395–400 (2007).
- Pitcairn, C. *et al.* Diagnostic indicators of elevated nitrogen deposition. *Environ. Pollut.* **144**, 941–950 (2006).
- Jenkinson, D. S., Poulton, P. R., Johnston, A. E. & Powlson, D. S. Turnover of nitrogen-15-labelled fertilizer in old grassland. *Soil Sci. Soc. Am. J.* **68**, 865–875 (2004).
- Kim, T. W., Lee, K., Najjar, R. G., Jeong, H. D. & Jeong, H. J. Increasing N abundance in the northwestern Pacific Ocean due to atmospheric nitrogen deposition. *Science* **334**, 505–509 (2011).
- Hietz, P. *et al.* Long-term change in the nitrogen cycle of tropical forests. *Science* **334**, 664–666 (2011).
- Cooper, O. R. *et al.* Increasing springtime ozone mixing ratios in the free troposphere over western North America. *Nature* **463**, 344–348 (2010).
- Liu, J. G. & Diamond, J. China's environment in a globalizing world. *Nature* **435**, 1179–1186 (2005).
- Zhang, Q., He, K. B. & Huo, H. Cleaning China's air. *Nature* **484**, 161–162 (2012).
- Han, W. X., Fang, J. Y., Reich, P. B., Woodward, F. I. & Wang, Z. H. Biogeography and variability of eleven mineral elements in plant leaves across gradients of climate, soil and plant functional type in China. *Ecol. Lett.* **14**, 788–796 (2011).

Supplementary Information is available in the online version of the paper.

Acknowledgements We thank X. Chen, A. Bleeker, X. Ju, J. Shen and R. Jiang for their comments on an earlier version of the manuscript or assistance during the manuscript revision, and we thank H. Liu, J. Lü, F. Chen, L. Wu and S. Qiu for providing data from long-term experiments. The authors also acknowledge all those who provided local assistance or technical help to the CAU-organized Deposition Network. This work was financially supported by the Chinese National Basic Research Program (2009CB118606), an Innovative Group Grant from the NSFC (31121062, 41071151, 40973054) and the Sino-German Research Training Group (GK 1070).

Author Contributions X.L. and F.Z. designed the research. X.L., Y.Z., W.H., A.T., J.S. and Z.C. conducted the research (collected the data sets and analysed the data). X.L., Y.Z. and P.V. wrote the manuscript. J.W.E., K.G., P.C., A.F. and F.Z. commented on the manuscript.

Author Information Reprints and permissions information is available at www.nature.com/reprints. The authors declare no competing financial interests. Readers are welcome to comment on the online version of the paper. Correspondence and requests for materials should be addressed to F.Z. (zhangfs@cau.edu.cn).

METHODS

Data sources for bulk N deposition. Bulk N deposition data are from two sources: monitoring results from a regional atmospheric deposition monitoring network (that is, the China Agricultural University-organized Deposition Network (CAUDN)); and results published during the period 1980–2010. Only bulk deposition data for inorganic N ($\text{NH}_4\text{-N}$ and $\text{NO}_3\text{-N}$) were summarized in this study because no dry deposition data for N were reported in China in the 1980s and 1990s². Our data sets include year of monitoring at every site; location of every monitoring site; annual amount of precipitation; concentration and deposition of $\text{NH}_4\text{-N}$, $\text{NO}_3\text{-N}$ and total inorganic N (TIN); and ratios of $\text{NH}_4\text{-N}$ to $\text{NO}_3\text{-N}$ concentration and deposition in precipitation. Some sites that contained only portions of deposition data (that is, only concentration or deposition of inorganic N) were also included in our data sets. Briefly, bulk N deposition samples from the CAUDN were collected using always-open rain gauges (different from wet-only samplers) on a daily basis and measured by colorimetry (that is, continuous flow analysis) or ion chromatography. For literature deposition data, these are the two most common methods for measuring inorganic N ($\text{NH}_4\text{-N}$ and $\text{NO}_3\text{-N}$) concentrations in precipitation (for details, see references in Supplementary Table 2). Bulk deposition rates of $\text{NH}_4\text{-N}$, $\text{NO}_3\text{-N}$ and TIN were then calculated by multiplying N concentration in precipitation by the amount of precipitation¹⁹.

In this paper, we summarize 866 data points of N concentrations in rainwater and 671 data points of bulk N deposition rates from between 1980 and 2010. All of the data originated from publications and our own results from the CAUDN. In all, we collected 315 references on annual N concentration and deposition results (including 276 journal articles, 19 dissertations and 20 monographs) (Supplementary Table 2) in this data set, covering 270 monitoring sites widely distributed in China (Supplementary Fig. 1). The current bulk N deposition data sets are the most complete deposition data sets in China in spite of some minor weaknesses (that is, relatively fewer monitoring sites and data points in northeast China, northwest China and the Tibetan plateau). Therefore, our meta-analysis based on the data set should be reliable. The same results published in different sources (that is, journals, dissertations or monographs) were cited only once and only one reference source was listed in the following priority: English-language journals, Chinese-language journals, dissertations and monographs.

To clarify regional variations, bulk N deposition data were also summarized on a regional basis (Supplementary Fig. 1): northern China, comprising Beijing, Tianjin, Hebei, Henan, Shandong, Shanxi and Shaanxi provinces; southeast China, comprising Shanghai, Jiangsu, Zhejiang, Anhui, Hubei, Hunan, Jiangxi, Fujian, Guangdong, Hong Kong, Macau, Taiwan and Hainan provinces; southwest China, comprising Sichuan, Chongqing, Guizhou, Yunnan and Guangxi provinces; the Tibetan plateau, comprising Tibet and Qinghai provinces; northeast China, comprising Liaoning, Jilin and Heilongjiang provinces; and northwest China, comprising Xinjiang, Inner Mongolia, Ningxia and Gansu provinces.

Data sources for plant foliar N from non-agricultural vegetation types. A total of 981 observations of plant foliar N content and 859 observations of foliar P were collected from 666 natural and semi-natural terrestrial plant species (including woody and herbaceous species, non-N-fixing and N-fixing species, and evergreen and deciduous species, according to various classification methods) between 1980 and 2010 at 245 sites distributed across the whole of China (Supplementary Fig. 1), on the basis of our field measurements and the literature (for details, see references in Supplementary Table 3). Leaves were sampled mainly during the growing season (July to September). Leaf samples were oven-dried, ground and then measured for N concentrations using the Kjeldahl method. To avoid systematic deviation caused by chemical determination, N samples determined with C and N elemental analysers³⁰ (after the year 2000) were not included in our analysis. For the few leaf samples lacking detailed time records, the sampling year was assumed to be two years before the associated paper was first submitted (for example, the sampling year was assumed to be 2004 if the paper was submitted in 2006). Mean foliar N was calculated for each species at the same sites within the same sampling year.

Data sources for crop N uptake from zero-N croplands. A total of 278 data points of crop N uptake were collected from non-N-fertilized (zero-N fertilizer input for at least five years) croplands (described as 'zero-N plots' hereafter) during the 1980s and 2000s across China, on the basis of our field experiments and published data^{22,31–37}. Nitrogen uptake by rice, wheat and maize includes N accumulation in grain plus straw at harvest (normally from May to October) of the three main cereal crops on zero-N plots. Grain and straw samples were oven-dried, ground and measured for N concentrations using the Kjeldahl method when the

harvest process was completed in the field. Nitrogen accumulation in grain or straw was calculated as N concentration multiplied by grain or straw dry matter; crop N uptake was then the sum of grain and straw N accumulation. For a few publications that did not provide crop N uptake data, we used conversion coefficients³⁸ of grain yield for estimating N uptake by rice, wheat and maize, respectively.

Data sources for anthropogenic NH_3 and NO_x emissions and their main contributors. NH_3 and NO_x (sum of NO and NO_2) emission inventories in China during 1980 and 2010 were obtained from all published data available² and updated to 2010 on the basis of data from the National Bureau of Statistics of China (<http://www.stats.gov.cn/english/statisticaldata/yearlydata/>) and the reported NH_3 and NO_x emission factors³⁹; if several emission values were available in one specific year only, an averaged emission value was used. Briefly, China's national emission inventories for NH_3 and NO_x were based on different emission sources and emission factors of specific N_t species. Compared with the NO_x emission inventory (mainly point sources), the NH_3 emission inventory (mainly non-point-source emission) has a relatively large uncertainty^{2,21}. The ratios of $\text{NH}_3\text{-N}$ to $\text{NO}_x\text{-N}$ emission were then calculated on the basis of averaged annual emission data over the period 1980–2010.

Data on N fertilizer use and domestic animal numbers (expressed as livestock units) were from Chinese Agriculture Statistics (1982–2010). The transformation of domestic animal numbers to livestock units was based on some widely used conversion factors in Europe (http://epp.eurostat.ec.europa.eu/statistics_explained/index.php/Glossary:LSU). Data on coal consumption (as standard coal) and motor vehicle numbers were from the National Bureau of Statistics of China (<http://www.stats.gov.cn/english/statisticaldata/yearlydata/>).

Statistical analysis. Annual precipitation; N concentration in precipitation; bulk N deposition; ratios of $\text{NH}_4\text{-N}$ to $\text{NO}_3\text{-N}$ in bulk precipitation; foliar N, foliar P and crop N uptake from zero-N plots; NH_3 and NO_x emissions and ratios of $\text{NH}_3\text{-N}$ to $\text{NO}_x\text{-N}$ emission; N fertilizer use; and numbers of domestic animals, numbers of motor vehicles and coal consumption in China were fitted (with year) by linear mixed models or nonlinear regression models for the interval 1980–2010. We used mixed models^{40,41} instead of simple linear regressions because of the large site-to-site variability. The selection of linear versus nonlinear regression depended on the distribution of the 'scatter diagram' (initially judging the temporal variation followed by a linear or nonlinear trend) and on the correlation coefficients (r) and P values in the linear or nonlinear regression equations⁴¹. Correlation coefficients were tested by a statistical model (SPSS 13.0, SPSS Inc.). Differences between all of the above-mentioned parameters as measured in the 1980s (1980–1989) and the 2000s (2000–2010) were compared statistically using an unpaired two-tail Student's t -test. Significant difference is assumed when the P value is <0.05 or as otherwise stated.

- Guo, L. P. *Study on the Integrated Effects of Long-Term Fertilization under Wheat-Corn Rotation System at Fluvo-aquic Soil in Beijing Area* 63–65. PhD thesis, China Agricultural Univ. (1998).
- Zhao, B. Q. *et al.* Long-term fertilizer experiment network in China: crop yields and soil nutrient trends. *Agron. J.* **102**, 216–230 (2010).
- Miao, Y. X., Stewart, B. A. & Zhang, F. S. Long-term experiments for sustainable nutrient management in China: a review. *Agron. Sustain. Dev.* **31**, 397–414 (2011).
- Fan, M. S. *Integrated Plant Nutrient Management for Rice-upland Crop Rotation System* 43–56. PhD thesis, China Agricultural Univ. (2005).
- Ye, Y. L. *et al.* Effect of long-term fertilizer application on yield, nitrogen uptake and soil $\text{NO}_3\text{-N}$ accumulation in wheat/maize intercropping. *J. Plant Nutr. Fertil. Sci.* **10**, 113–119 (2004).
- Fan, T. L. *et al.* Long-term fertilization on yield increase of winter wheat-maize rotation system in Loess Plateau dryland of Gansu. *J. Plant Nutr. Fertil. Sci.* **10**, 127–131 (2004).
- Liao, Y. L. *et al.* Effects of long-term application of fertilizer and rice straw on soil fertility and sustainability of a reddish paddy soil productivity. *Sci. Agric. Sin.* **42**, 3541–3550 (2009).
- Lu, R. K. *et al.* Nutrients cycle and balance in Chinese typical farm land biological system II. Index of nutrients income in farm land. *Chin. J. Soil Sci.* **27**, 151–154 (1996).
- Olivier, J. G. J., Bouwman, A. F., Van der Hoek, K. W. & Berdowski, J. J. M. Global air emission inventories for anthropogenic sources of NO_x , NH_3 and N_2O in 1990. *Environ. Pollut.* **102**, 135–148 (1998).
- Snijders, T. & Bosker, R. *Multilevel Analysis: an Introduction to Basic and Advanced Modeling* 67–83 (Sage, 1999).
- Littell, R. C., Milliken, G. A., Stroup, W. W. & Wolfinger, R. D. *SAS System for Mixed Models* 525–566 (SAS Institute Inc., 1996).

Evolutionary rescue from extinction is contingent on a lower rate of environmental change

Haley A. Lindsey¹, Jenna Gallie^{1,2,3}, Susan Taylor¹ & Benjamin Kerr¹

The extinction rate of populations is predicted to rise under increasing rates of environmental change^{1–3}. If a population experiencing increasingly stressful conditions lacks appropriate phenotypic plasticity or access to more suitable habitats, then genetic change may be the only way to avoid extinction¹. Evolutionary rescue from extinction occurs when natural selection enriches a population for more stress-tolerant genetic variants^{1,3}. Some experimental studies have shown that lower rates of environmental change lead to more adapted populations or fewer extinctions^{4–9}. However, there has been little focus on the genetic changes that underlie evolutionary rescue. Here we demonstrate that some evolutionary trajectories are contingent on a lower rate of environmental change. We allowed hundreds of populations of *Escherichia coli* to evolve under variable rates of increase in concentration of the antibiotic rifampicin. We then genetically engineered all combinations of mutations from isolates evolved under lower rates of environmental change. By assessing fitness of these engineered strains across a range of drug concentrations, we show that certain genotypes are evolutionarily inaccessible under rapid environmental change. Rapidly deteriorating environments not only limit mutational opportunities by lowering population size, but they can also eliminate sets of mutations as evolutionary options. As anthropogenic activities are leading to environmental change at unprecedented rapidity¹, it is critical to understand how the rate of environmental change affects both demographic and genetic underpinnings of evolutionary rescue.

One of the first real-time evolution experiments demonstrated that evolutionary rescue from extinction is sensitive to the rate of environmental change⁷. In the 1880s, it was shown that protist lineages that had experienced a gradual increase in temperature over 7 years were able to thrive at 70 °C, whereas non-evolved populations rapidly went extinct when suddenly exposed to any temperature above 60 °C (ref. 7). Other experiments have explored the effect of the rate of environmental change on evolution in fruitflies⁹, algae⁶, yeast^{4,5} and bacteria⁸. These pioneering studies have found that gradual change leads to lower levels of extinction or to better adapted populations. However, the precise genetic underpinnings of these evolutionary dynamics have remained unexplored.

We propagated 1,255 populations of *E. coli* via serial transfer under increasing concentrations of the antibiotic rifampicin. The three experimental treatments involved different rates of change: Sudden, Moderate and Gradual. All populations started in antibiotic-free medium and ended at a maximal concentration of rifampicin (190 µg ml^{−1}) (Fig. 1a). The Sudden populations were exposed to the maximal rifampicin concentration after their first transfer and remained at that concentration for the duration of the experiment. The Moderate populations underwent a slower increase in concentration, such that they arrived at the maximal concentration halfway through the experiment and then remained at that concentration. The Gradual populations experienced the slowest increase in antibiotic concentration, reaching the maximum on the last transfer of the experiment.

There were significant differences in the extinction rate among treatments (Pearson's chi-squared test, $\chi^2 = 709.88$, $P < 0.001$; Fig. 1b). As the rate of environmental change increased, the fraction of populations that survived the entire experiment dropped precipitously. Relative to

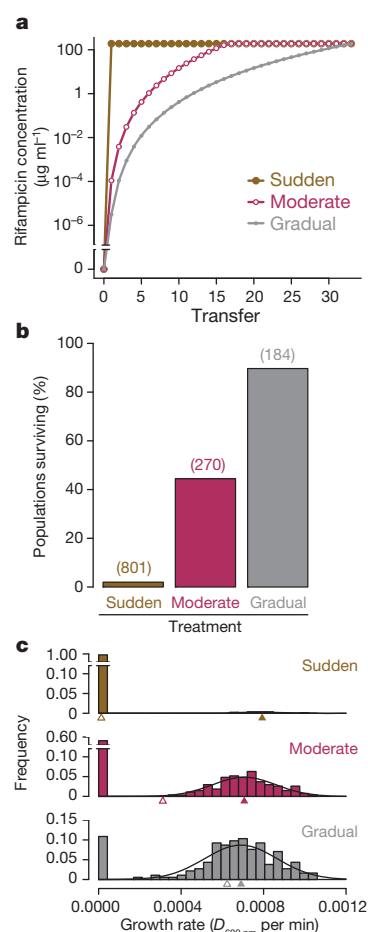


Figure 1 | Survival and growth under different rates of environmental change. **a**, The three experimental treatments. Rifampicin concentration increases from a minimum value (0 µg ml^{−1}) to a maximum value (190 µg ml^{−1}) at different rates within each treatment. **b**, The percentage of populations surviving the experiment in each treatment. The number above each bar is the corresponding number of initial populations. **c**, The growth rate of populations from the end of the experiment. Growth rate is measured in attenuation units ($D_{600 \text{ nm}}$) per minute using a spectrophotometric assay (see Methods). If a population went extinct, its growth rate was assigned to zero. Note that the full range on the ordinate scale (frequency) is different for each treatment. The open triangles give mean growth rate and the closed triangles give mean growth of surviving populations. Growth rate distributions for the surviving populations are shown with maximum likelihood normal curves.

¹Department of Biology and BEACON Center for the Study of Evolution in Action, University of Washington, Seattle, Washington 98195, USA. ²Department of Environmental Microbiology, Eawag, 8600 Dübendorf, Switzerland. ³Department of Environmental Systems Science, ETH Zurich, 8092 Zurich, Switzerland.

populations in the other treatments. Gradual populations spent more time at sub-inhibitory concentrations of rifampicin where mutations conferring resistance could be selected¹⁰. This would give Gradual populations more opportunities for resistance mutations to occur and spread. However, does evolutionary rescue occur by the same set of mutations in all treatments? We found significant differences in growth rate between Gradual and Sudden isolates from the end of the experiment (log likelihood ratio test, $\chi^2 = 12.95$, $P = 0.0015$; Fig. 1c), which indicates that different mutations occurred in different treatments.

Mutations that confer resistance to rifampicin are known to occur in specific regions of the *rpoB* gene, which codes for the β subunit of RNA polymerase^{11–13}. Figure 2a displays the *rpoB* mutations from all 13 surviving Sudden populations and a random sample of 30 Moderate and 30 Gradual populations. All mutations were non-synonymous. The Gradual and Moderate populations have significantly higher nucleotide diversity¹⁴ than the Sudden populations (permutation tests, $P < 0.001$; Fig. 2b).

Interestingly, all isolates in the Sudden treatment possess only single mutations in *rpoB*, whereas the majority of the isolates from the other treatments contain multiple *rpoB* mutations. We identified the first mutation to arise in populations with multiple mutations by sequencing samples frozen at various points in time during the experiment. Of the 44 Gradual and Moderate isolates with multiple mutations, only a single (Moderate) isolate has exactly the same first mutation as any Sudden isolate. When confining the analysis to first mutations only, the Gradual and Moderate isolates continue to have significantly higher nucleotide diversity than the Sudden isolates (permutation

tests, $P < 0.001$). This pattern is consistent with a situation in which more mutations are selectively accessible at lower antibiotic concentrations. Indeed, when we engineer the first *rpoB* mutations from a handful of isolates into a common background, we find that some mutations that are beneficial at lower antibiotic concentrations are no longer advantageous under the highest concentrations (Fig. 2c).

If the first mutations to occur in the Gradual and Moderate treatments are inviable at the maximal concentration of rifampicin (see Fig. 2c), subsequent mutations are required to salvage the lineage at the highest concentration. Such secondary mutations might only be selectively accessible after the first mutation, which might only be selectively accessible under sub-maximal antibiotic concentrations. In such a case, a mutational trajectory accessible under gradual environmental change will be unlikely to occur under rapid change.

The evolutionary trajectory of a population evolving under conditions of strong selection and weak mutation¹⁵ can be envisioned as a series of steps between genotypes differing by a single mutation. Each step in a selectively accessible path involves an increase in genotype fitness. However, because the fitness of genotypes can change with the environment, the historical sequence of environments can qualitatively affect which paths are selectively accessible. Consider a path from one genotype to another that is selectively accessible under a sequence of distinct environments. We call such a path 'historically contingent upon some focal environment(s)' if this path is not selectively accessible in the absence of the focal environment(s) (see Fig. 3).

In the Supplementary Information, we demonstrate that if a path ending at an adaptive peak is historically contingent upon an intermediate environment, then the sign of the fitness effect of some mutations

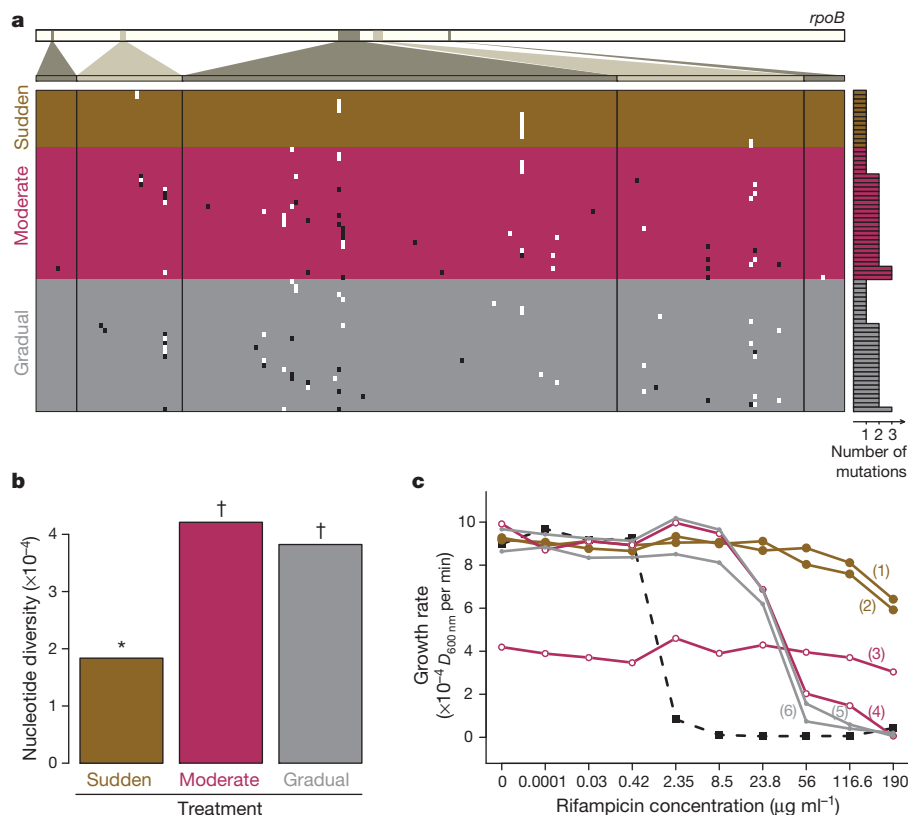


Figure 2 | Mutations and their effects. **a**, The locations of mutations in 73 isolates. The top bar represents the *rpoB* gene. Gene regions with mutations in at least one isolate are magnified for the table. Each isolate is a single row (13 Sudden, 30 Moderate and 30 Gradual). The location of the first mutation to arise in the evolutionary history of the isolate is given by a white mark and subsequent mutations are given by black marks. The number of mutations in each isolate is specified by the size of the small bar to the right of the table. **b**, The index of nucleotide diversity (π) for each treatment. Different symbols (asterisk

and dagger) over the bars indicate significantly different π values by permutation tests. **c**, Mean growth rate of single mutants in different environments. Each of the first mutations to fix in six different populations was engineered into a common background (these mutations were (1) g1546t, (2) g436t, (3) t437a, (4) t1532g, (5) c1527a and (6) c1721t). The treatments have the same representation as in Fig. 1. The growth rates for the ancestral genotype are given by the squares. By comparing engineered mutants with the ancestor, we see that three of the mutations (4, 5 and 6) do not increase growth rate at the highest drug concentration.

must depend on genetic background (sign genetic epistasis¹⁶) and the sign of the fitness effect of some mutations must depend on environment ('sign environmental epistasis'). Environmental epistasis is a genotype by environment ($G \times E$) interaction and can be described as plasticity in the fitness effect of a mutation¹⁷. Figure 3 illustrates both forms of epistasis in the context of historical contingency upon environment. Sign genetic epistasis has been found in a number of different systems^{18–21}, and both forms of sign epistasis have been reported in microbial systems^{13,22}. For an evolutionary path ending on an adaptive peak, sign epistasis is a necessary, but not sufficient, condition to obtain historical contingency upon an intermediate environment; thus, empirical evidence for such contingency requires verification that particular configurations of epistasis exist.

To demonstrate historical contingency directly, we constructed all intermediate genotypes between an ancestor and its descendant and assessed their fitness across a spectrum of environments. We focused on two evolved isolates from different populations in the Gradual treatment, each possessing two mutations in *rpoB* (see Supplementary Information for the analysis of isolates from the Moderate and Sudden treatments). For each isolate, we genetically engineered the

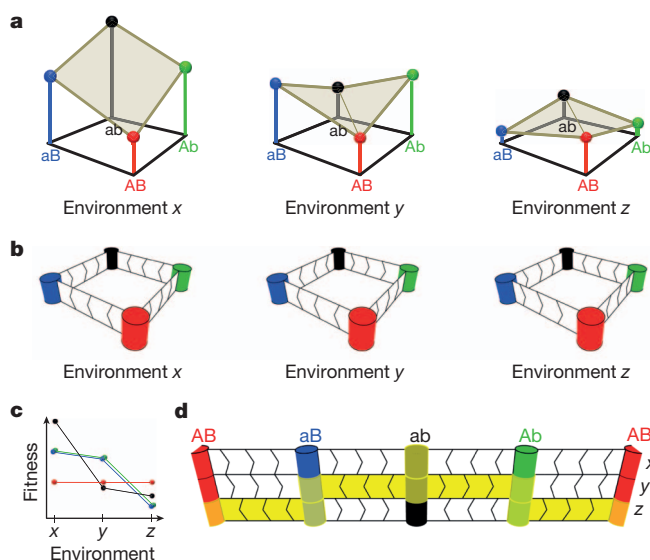


Figure 3 | A two-locus biallelic example illustrating historical contingency upon the environment. **a**, The adaptive landscapes for the four genotypes are depicted in the environments x , y and z . The height of each 'lollipop' gives the fitness of the genotype. When using an additive model, genetic epistasis is present when the fitness of the four genotypes are not embedded in a single plane (for example, sign genetic epistasis occurs in environments y and z , but no genetic epistasis is found in x). **b**, For each environment, selective accessibility between genotypes is indicated as 'flow arrows' between the neighbouring genotypes (cylinders). One genotype is selectively accessible from another in a given environment if a single mutation transforms the latter into the former and if the former has a higher fitness than the latter. **c**, A 'fitness norm of reaction' for the four genotypes is presented. When the trajectories of two mutational neighbours are not parallel, environmental epistasis is present. For example, the mutation from ab to Ab is detrimental in environment x , but beneficial in environment y (sign environmental epistasis). **d**, Imagine stacking the squares from **b**, with the x square on top of the y square and the z square on the bottom. Then slice the red cylinders in half and open up the stack to form the flat wall shown. Suppose the population started fixed for the ab genotype and the environments were experienced in the order $x \rightarrow y \rightarrow z$. Imagine starting on top of the black cylinders and rappelling down the wall, potentially moving horizontally to different cylinders in accord with the flow arrows. A fully descending trajectory would represent a selectively accessible path. The only two selectively accessible paths from genotype ab to genotype AB are highlighted. We note that environment y must be experienced: if a population in environment x was moved directly into environment z , then the genotype AB would be selectively inaccessible from ab . Thus, this is an example where an evolutionary path is historically contingent upon an environment.

four relevant genotypes in a common background using an allele exchange protocol that resulted in scar-free construction of the desired genotypes (see Methods and Supplementary Information).

The growth rate, competitive ability and viability of the engineered strains across a gradient of rifampicin concentrations are shown in Fig. 4. There is clear historical contingency upon intermediate environments for both isolates. For the lineage yielding the first Gradual isolate (Fig. 4a, b), paths from the ancestor to the double mutant through either single mutant are selectively accessible only for intermediate concentrations of rifampicin. For the lineage evolving the second Gradual isolate (Fig. 4c, d), the path actually taken ($ab \rightarrow aB \rightarrow AB$) must be completed piece-wise in different environments. For both lineages, the slow change in concentration of rifampicin was critical to the evolutionary sequence: if the environment changed from an absence of antibiotic to its maximal concentration abruptly (as in the Sudden treatment), the path taken under gradual change would not be available (Fig. 4b, d). We find similar evidence for historical contingency upon intermediate environments in the Moderate isolates (see Supplementary Information). We suggest that even if certain mutations are selectively neutral or deleterious under high levels of stress, they can nonetheless predispose the lineage to gain other mutations that allow it to escape extinction at high stress. Such priming mutations need not drift into a population; rather they can be (powerfully) selected at low levels of stress. This means that the rate of environmental deterioration can qualitatively affect evolutionary trajectories. In our system, we find that rapid environmental change closes off paths that are accessible under gradual change.

In our experiment, demographic factors certainly contribute to the higher prevalence of evolutionary rescue under a gradual increase in the level of stress. Specifically, the population growth rate of the ancestor is positive in the Gradual treatment over the initial set of transfers, whereas it is negative in the Sudden treatment. Thus, there are more chances for mutations to occur in the Gradual treatment. A fraction of isolates in the Gradual and Moderate treatments had only a single mutation in *rpoB*, some of which affected amino acid residues that also were mutated in the Sudden treatment (see Fig. 2a). Barring mutations outside of the sequenced region²³, these mutations could represent single evolutionary steps that both rescue the population under high stress and are advantageous under low stress (see mutations (1), (2) and (3) in Fig. 2c). There will be more of these mutations under lower rates of change because there will be more mutational opportunities in populations with higher growth rates. However, in this article we have also traced out another important factor that can make evolutionary rescue more likely under gradual change. If mutations selected at intermediate levels of stress predispose a lineage to receive additional epistatic mutations conferring viability under higher stress, then gradual change in the environment can 'open up' evolutionary endpoints. We propose that such historical contingency upon the environment is particularly relevant to some current problems resulting from anthropogenic activities, including the rise of antibiotic resistance and extinction in the face of climate change.

The presence of antibiotics in industrial and agricultural waste runoff²⁴ has the potential to select for antibiotic-resistant microbes even when the drugs are present at very low concentrations¹⁰. Our work suggests an additional problem with such exposure: low drug concentrations can evolutionarily 'prime' bacterial populations, by bringing a population (mutationally) closer to genotypes that would enable drug resistance at a high concentration. In a more direct medical context, rifampicin is one of the first-line drugs used to treat tuberculosis^{23,25}. The mutations conferring resistance to rifampicin in our experimental *E. coli* populations are observed in similar genetic locations in *Mycobacterium tuberculosis*^{23,25,26}, indicating that our results may have relevance to this disease system. Specifically, we propose that the manner of change in the concentration of rifampicin within a patient could affect both the persistence and evolution of this pathogen, which has implications for disease management.

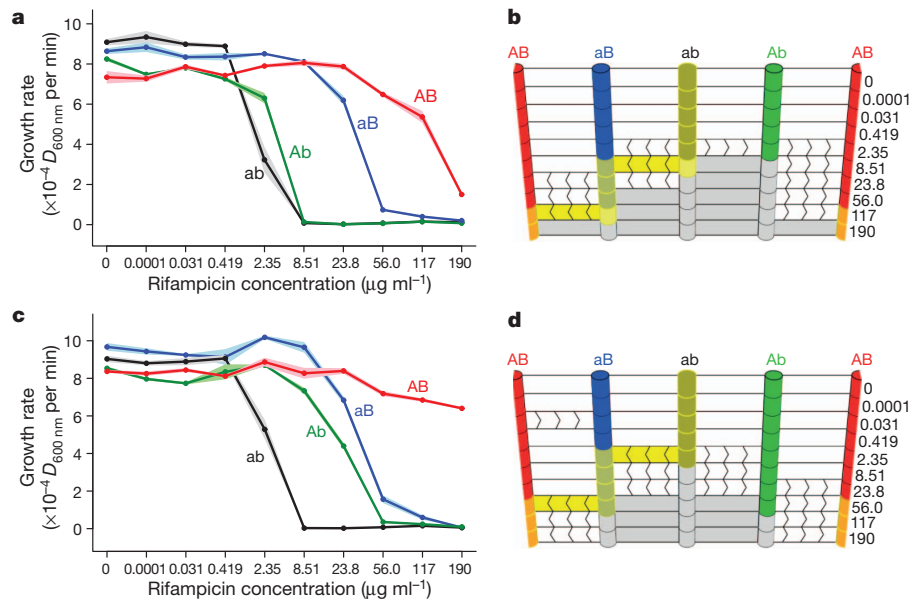


Figure 4 | Selective accessibility from the ancestral genotype to two evolved genotypes in two different Gradual populations. The evolved isolate in the first Gradual population has two mutations in *rpoB*, g428a and c1721t, yielding the amino acid substitutions R143H and S574F, respectively. The four engineered genotypes are denoted ab (bases g428 and c1721), Ab (bases a428 and c1721), aB (bases g428 and t1721) and AB (bases a428 and t1721). The evolved isolate in the second Gradual population also has two mutations in *rpoB*, a443t and c1527a, yielding the amino acid substitutions Q148L and S509R, respectively. The four engineered genotypes for the second isolate case are denoted ab (bases a443 and c1527), Ab (bases t443 and c1527), aB (bases a443 and a1527) and AB (bases t443 and a1527). **a**, The maximum population growth rate for each of the engineered genotypes corresponding to the first isolate across a gradient of rifampicin concentrations. The points are means and the shading gives the standard error. **b**, The 'accessibility wall' for the case of the first isolate. The four genotypes are cylinders of different colours and each horizontal stratum corresponds to a distinct concentration of rifampicin (labels

Whereas extinction of a target population may be the preferred outcome in the case of pathogens, it is generally undesirable for populations threatened by anthropogenic climate change. There is much interest in the fate of current ecological communities under a markedly changing environment^{1,2,27,28}. For logistic reasons, experimental communities in the field are sometimes subjected to a predicted amount of climate change over a greatly compressed time frame. If evolutionary rescue is sensitive to the rate of change, the estimated risk of extinction may depend on the degree of compression²⁸. For instance, it was found that a more gradual increase in ambient CO₂ concentration resulted in a substantially higher species richness in a mycorrhizal fungi community, in comparison to the abrupt change typical of other CO₂ elevation experiments²⁹. Such caveats aside, our study does suggest that there is genuine reason to worry about unusually high rates of environmental change. As the rate of environmental deterioration increases, there can be pronounced increases in the rate of extinction. Our work suggests that this is due not only to the lost mutational opportunities that come with a dwindling population, but also to lost potentiating mutations that would be selected under milder conditions.

METHODS SUMMARY

In total 1,255 populations of *Escherichia coli* B were initiated from a common ancestor and evolved for two months in microtitre wells with minimal glucose (MG), diluting 40-fold every 48 h into fresh media with a rifampicin concentration determined by experimental treatment (Fig. 1a). Any population completely lacking visible cloudiness after a 48-h growth period was considered extinct. From the set of populations surviving the evolution experiment, a random subset was chosen in which isolates were sequenced at the *rpoB* locus. Engineered mutants were created by site-directed mutagenesis and allelic exchange (using a variant of

to the right, μg ml⁻¹). As maximum growth rate is only one component of fitness, we performed pairwise competitions between all mutational neighbours across the gradient of rifampicin to determine selective accessibility (see Methods). Flow arrows indicate that the genotype from which the flow starts decreased its proportion significantly in competition with the genotype to which the flow ends (*t*-test with Bonferroni corrections for multiple comparisons, *P* < 0.05). An edge between cylinders without arrows represents a competition in which neither strain increased in proportion significantly. A grey cylinder indicates that the genotype could not form a turbid population in the relevant concentration of rifampicin (see Methods). A grey edge indicates that neither bordering genotype could form a turbid population in the relevant concentration of rifampicin starting with a population of 10–100 cells. The highlighting shows the actual evolutionary trajectory followed during the experiment. This trajectory was elucidated by sequencing the *rpoB* locus from samples frozen at various time points during the experiment. **c**, **d**, The growth rates (c) and selective accessibility (d) for the case of the second Gradual isolate.

the pKOV vector³⁰). For the growth assay, each strain or population was revived from the freezer via growth in MG over 24 h and then diluted 40-fold into fresh media with rifampicin (see Supplementary Table 1 for concentrations). Attenuation readings (over 24 h at 600 nm) were used to calculate the maximum growth rate. For the pairwise competition assay, two strains were grown separately for 24 h in MG, mixed in equal volume, and then diluted 40-fold into fresh MG with rifampicin (see Supplementary Table 1) and competed for 48 h. The initial and final densities of the competitors were determined by selective plating (one competing strain was neutrally marked with the ability to use arabinose). For the viability assay, each strain was revived from the freezer and then diluted 40-fold and 10⁵-fold into MG with rifampicin (see Supplementary Table 1). Growth was determined visually after 48 h. See the extended methods for further details.

Full Methods and any associated references are available in the online version of the paper.

Received 14 September; accepted 21 December 2012.

Published online 10 February 2013.

- Bell, G. & Collins, S. Adaptation, extinction and global change. *Evol. Appl.* **1**, 3–16 (2008).
- Bellard, C., Bertelsmeier, C., Leadley, P., Thuiller, W. & Courchamp, F. Impacts of climate change on the future of biodiversity. *Ecol. Lett.* **15**, 365–377 (2012).
- Gomulkiewicz, R. & Holt, R. When does evolution by natural selection prevent extinction? *Evolution* **49**, 201–207 (1995).
- Bell, G. & Gonzalez, A. Evolutionary rescue can prevent extinction following environmental change. *Ecol. Lett.* **12**, 942–948 (2009).
- Bell, G. & Gonzalez, A. Adaptation and evolutionary rescue in metapopulations experiencing environmental deterioration. *Science* **332**, 1327–1330 (2011).
- Collins, S. & de Meaux, J. Adaptation to different rates of environmental change in *Chlamydomonas*. *Evolution* **63**, 2952–2965 (2009).
- Dallinger, W. H. The President's Address. *J. R. Microsc. Soc.* **7**, 185–199 (1887).
- Perron, G. G., Gonzalez, A. & Buckling, A. The rate of environmental change drives adaptation to an antibiotic sink. *J. Evol. Biol.* **21**, 1724–1731 (2008).

9. Huey, R., Partridge, L. & Fowler, K. Thermal sensitivity of *Drosophila melanogaster* responds rapidly to laboratory natural selection. *Evolution* **45**, 751–756 (1991).
10. Gullberg, E. *et al.* Selection of resistant bacteria at very low antibiotic concentrations. *PLoS Pathog.* **7**, e1002158 (2011).
11. Reynolds, M. G. Compensatory evolution in rifampin-resistant *Escherichia coli*. *Genetics* **156**, 1471–1481 (2000).
12. MacLean, R. C., Perron, G. G. & Gardner, A. Diminishing returns from beneficial mutations and pervasive epistasis shape the fitness landscape for rifampicin resistance in *Pseudomonas aeruginosa*. *Genetics* **186**, 1345–1354 (2010).
13. Hall, A. R. & MacLean, R. C. Epistasis buffers the fitness effects of rifampicin resistance mutations in *Pseudomonas aeruginosa*. *Evolution* **65**, 2370–2379 (2011).
14. Nei, M. & Li, W. H. Mathematical model for studying genetic variation in terms of restriction endonucleases. *Proc. Natl Acad. Sci. USA* **76**, 5269–5273 (1979).
15. Gillespie, J. H. A simple stochastic gene substitution model. *Theor. Popul. Biol.* **23**, 202–215 (1983).
16. Weinreich, D. M., Watson, R. A. & Chao, L. Perspective: sign epistasis and genetic constraint on evolutionary trajectories. *Evolution* **59**, 1165–1174 (2005).
17. Remold, S. K. & Lenski, R. E. Pervasive joint influence of epistasis and plasticity on mutational effects in *Escherichia coli*. *Nature Genet.* **36**, 423–426 (2004).
18. Weinreich, D. M., Delaney, N. F., DePristo, M. A. & Hartl, D. L. Darwinian evolution can follow only very few mutational paths to fitter proteins. *Science* **312**, 111–114 (2006).
19. Trindade, S. *et al.* Positive epistasis drives the acquisition of multidrug resistance. *PLoS Genet.* **5**, e1000578 (2009).
20. Lalić, J. & Elena, S. F. Magnitude and sign epistasis among deleterious mutations in a positive-sense plant RNA virus. *Heredity* **109**, 71–77 (2012).
21. Kvitek, D. J. & Sherlock, G. Reciprocal sign epistasis between frequently experimentally evolved adaptive mutations causes a rugged fitness landscape. *PLoS Genet.* **7**, e1002056 (2011).
22. Lalić, J. & Elena, S. F. Epistasis between mutations is host-dependent for an RNA virus. *Biol. Lett.* **9**, 20120396 (2013).
23. Comas, I. *et al.* Whole-genome sequencing of rifampicin-resistant *Mycobacterium tuberculosis* strains identifies compensatory mutations in RNA polymerase genes. *Nature Genet.* **44**, 106–110 (2012).
24. Martinez, J. L. Environmental pollution by antibiotics and by antibiotic resistance determinants. *Environ. Pollut.* **157**, 2893–2902 (2009).
25. Gagneux, S. *et al.* The competitive cost of antibiotic resistance in *Mycobacterium tuberculosis*. *Science* **312**, 1944–1946 (2006).
26. Sandgren, A. *et al.* Tuberculosis Drug Resistance Mutation Database. *PLoS Med.* **6**, e1000002 (2009).
27. Bodbyl Roels, S. A. & Kelly, J. K. Rapid evolution caused by pollinator loss in *Mimulus guttatus*. *Evolution* **65**, 2541–2552 (2011).
28. Skelly, D. K. *et al.* Evolutionary responses to climate change. *Conserv. Biol.* **21**, 1353–1355 (2007).
29. Klironomos, J. N. *et al.* Abrupt rise in atmospheric CO₂ overestimates community response in a model plant–soil system. *Nature* **433**, 621–624 (2005).
30. Link, A. J., Phillips, D. & Church, G. M. Methods for generating precise deletions and insertions in the genome of wild-type *Escherichia coli*: application to open reading frame characterization. *J. Bacteriol.* **179**, 6228–6237 (1997).

Supplementary Information is available in the online version of the paper.

Acknowledgements We thank T. Bradshaw, J. Martiny and J. Tewksbury for sharing ideas that inspired this work; the Church laboratory for supplying the pKOV vector; C. Adams, S. DeCew, K. Dickinson, S. Drescher, C. Eshelman, K. Hobbs, C. Muerdter, B. Rogers and C. Shyue for help in the laboratory; and F. Bertels, C. Eshelman, C. Glenney and S. Singhal for comments on the manuscript. This material is based in part on work supported by the National Science Foundation under Cooperative Agreement Number DBI-0939454, a NSF CAREER Award Grant (DEB0952825), and a UW Royalty Research Fund Award (A74107).

Author Contributions B.K. and S.T. designed the evolution experiment; S.T. and H.A.L. performed the evolution experiment; all authors designed and troubleshooted the genetic and phenotypic protocols; H.A.L. performed the genetic work and phenotypic assays; B.K. did the mathematical and statistical analysis, and all authors contributed to the writing of the manuscript.

Author Information Reprints and permissions information is available at www.nature.com/reprints. The authors declare no competing financial interests. Readers are welcome to comment on the online version of the paper. Correspondence and requests for materials should be addressed to B.K. (kerrb@uw.edu).

METHODS

Strains. *Escherichia coli* B (REL606) was used for the evolution experiment. Chemically competent DH5 α - λ pir *E. coli* and One Shot TOP10 *E. coli* (Invitrogen) were used for the genetic engineering protocol.

Growing and storing bacteria. Standard growth conditions: for many parts of the experiment, bacterial growth occurred in 96-well microtitre plates with a final volume of 200 μ l of minimal glucose (MG) medium per well. The growth phase lasted 48 h, during which time the plates were incubated and shaken (380 r.p.m. in a microtitre plate shaker at 37 °C). Transfers to fresh media involved 40-fold dilution.

Storing bacteria: populations were pipetted in their entirety into sterile tubes with 32 μ l of dimethyl sulphoxide and stored at –80 °C. Each frozen isolate was derived from a single colony that was inoculated into 5 ml of lysogeny broth (LB) medium and shaken at 205 r.p.m. overnight at 37 °C. Then 1 ml of the culture was mixed with 160 μ l of 80% glycerol and stored at –80 °C.

Evolution experiment. A single culture of *E. coli* B was used to inoculate 1,255 populations in microtitre wells. All populations were serially propagated for two transfers under standard growth conditions in the absence of rifampicin (to allow for independent mutations to occur in different populations). Each population was then serially propagated under standard growth conditions in the presence of a specific concentration of rifampicin, which was dependent on treatment (Supplementary Table 1). Before each transfer, each population's well was checked carefully for cloudiness. Populations in which two independent observers did not detect any visible growth were declared 'extinct' and were not transferred. Contamination of a media control well on transfer 19 forced us to restart the evolution series from transfer 18 (which had been stored at 4 °C). All populations were frozen periodically throughout the experiment. Three Sudden populations were lost due to a transfer error and one Moderate population could not be revived from 4 °C.

Sequencing. We randomly chose 30 surviving Moderate populations and 30 surviving Gradual populations. A single colony from each of these populations and from all 13 surviving Sudden populations was selected for sequencing. PCR amplification was performed using the primers described in ref. 11. After confirmation via gel electrophoresis, the PCR product was purified using the ExoI/CIAP (calf intestinal alkaline phosphatase) method. Purified products were sequenced (Macrogen) and analysed with Sequencher (version 4.6). For isolates with multiple mutations, the order of appearance was determined by sequencing at various points in the lineage's history.

Genetic engineering. Fragments of *rpoB* containing the desired mutation(s), flanked by 500–2,000 base pairs on either side, were ligated into pCR8/GW/TOPO (Invitrogen) for storage. When the desired mutation could not be amplified alone, it was introduced into a wild-type fragment of *rpoB* in pCR8/GW/TOPO using a Phusion site-directed mutagenesis kit (NEB) and stored in DH5 α - λ pir cells. After sequence confirmation, the resulting fragments were ligated into a customized version of pKOV³⁰ in which bases 1117–4057 were removed and replaced with a BglII restriction site. The desired mutations were then introduced into the ancestral REL606 background using a modified version of previously described two-step allelic exchange methods³⁰ (see Supplementary Information). The ancestral sequence of *rpoB* was reintroduced to each engineered mutant via the same technique. These re-engineered ancestors were used in the growth and competition assays to control for the allelic replacement process.

Growth assay. Spectrophotometric growth assays were performed on all populations that survived the experiment and the engineered strains. Bacteria were revived from the freezer and then diluted 40-fold into fresh MG medium with a pre-specified concentration of rifampicin (Supplementary Table 1). The culture was grown for 24 h at 37 °C in a VersaMax spectrometer (Molecular Devices) with attenuation (*D*) readings taken every 30 min at 600 nm. Using a sliding window of 2 h, the rate of change in *D*_{600 nm} at a focal time point (that is, the first derivative of the *D*_{600 nm} curve) was approximated by the slope of a linear least-square fit to the *D*_{600 nm} data centred on the time point of interest. The growth rate of the strain or population was the average of the top three slopes. Each strain or population was replicated four times (with position in the microtitre plate randomized) and the most deviant replicate was discarded.

Competition assay. In all competitions, one strain possessed the ability to use arabinose (Ara⁺), which was a selectively neutral marker. The Ara⁺ strain forms pink colonies on tetrazolium arabinose agar and grows on minimal arabinose agar, whereas the Ara[–] strain forms red colonies on tetrazolium arabinose agar and does not grow on minimal arabinose agar. The two strains to be competed were revived from the freezer and equal volumes of the two stationary cultures were combined. The co-culture was then diluted 40-fold into MG medium with a pre-specified concentration of rifampicin (Supplementary Table 1) and incubated under standard growth conditions. Dilution and plating was performed on tetrazolium arabinose and minimal arabinose agar at the beginning and end of the 48 h growth phase. Let *d_i(t)* be the bacterial density of strain *i* at time *t*. The competitive index of strain 1 relative to strain 2 is $W_{1,2} = \{d_1(48)d_2(0)\}/\{d_1(0)d_2(48)\}$, which measures how the ratio of competitors changes over a growth cycle. If $W_{1,2} > 1$, then strain 1 has increased in proportion; whereas strain 2 has proportionally increased if $W_{1,2} < 1$. Each competition was replicated four times.

Population viability assay. The engineered strain was revived from the freezer and diluted both 40-fold and 10⁵-fold into fresh MG medium with a pre-specified concentration of rifampicin (Supplementary Table 1). Each diluted culture was incubated under standard growth conditions, and after 48 h, it was checked visually for cloudiness indicating growth. The strain was deemed 'viable' if at least five of six replicate cultures were cloudy and 'inviable' if at most two of six replicate cultures were cloudy (all strains fell into these two classes). A strain viable after 40-fold dilution could persist at the relevant rifampicin concentration under our experimental conditions, whereas a strain viable after 10⁵-fold dilution could increase from rarity at the relevant rifampicin concentration. The ability to increase from rarity implies persistence, but the converse does not necessarily hold.

Sampling rationale. Pilot runs suggested a high extinction rate under the Sudden regime; thus, hundreds of populations were needed to estimate extinction rates and yield survivors for further analysis. Whereas isolates from all Sudden populations were sequenced, we sampled the surviving Moderate and Gradual populations with sufficient depth to estimate nucleotide diversity. Isolates from two populations from each treatment were chosen for genetic reconstruction and growth/competition/viability assays across environments (see Supplementary Information). This final stage was meant to illustrate the phenomenon of 'historical contingency upon environment.' More samples would be required to estimate its average incidence.

Specialized appendages in fuxianhuiids and the head organization of early euarthropods

Jie Yang¹, Javier Ortega-Hernández², Nicholas J. Butterfield² & Xi-guang Zhang¹

The organization of the head provides critical data for resolving the phylogenetic relationships and evolutionary history of extinct and extant euarthropods^{1,2}. The early Cambrian-period fuxianhuiids are regarded as basal representatives of stem-group Euarthropoda^{3–7}, and their anterior morphology therefore offers key insights for reconstructing the ancestral condition of the euarthropod head^{1–3,8–11}. However, the paired post-antennal structures in *Fuxianhuia protensa* remain controversial^{3,8,10}; they have been interpreted as both ‘great appendages’^{1,2} and as gut diverticulae^{4,12,13}. Here we describe *Chengjiangocaris kunmingensis* sp. nov. and *Fuxianhuia xiaoshibaensis* sp. nov. from a new early Cambrian (Stage 3) fossil Lagerstätte in Yunnan, China. Numerous specimens of both species show a unique ‘taphonomic dissection’ of the anterodorsal head shield, revealing the cephalic organization in detail. We demonstrate the presence of a pair of specialized post-antennal appendages (SPAs) in the fuxianhuiid head, which attach at either side of the posteriorly directed mouth, behind the hypostome. Preserved functional articulations indicate a well-defined but restricted range of limb movement, suggestive of a simple type of sweep feeding. The organization of the SPAs in fuxianhuiids is incompatible with the (deutocerebral) anterior raptorial appendages of megacheirans^{2,9,14,15}, and argue against the presence of protocerebral limbs in the fuxianhuiids^{1,2,9}. The positions of the fuxianhuiid antennae and SPAs indicate that they are segmentally homologous to the deutocerebral and tritocerebral appendages of crown-group Euarthropoda respectively^{2,11,16,17}. These findings indicate that antenniform deutocerebral appendages with many podomeres are a plesiomorphic feature of the ancestral euarthropod head.

Phylum Arthropoda

Chengjiangocaris kunmingensis sp. nov.

Etymology. After the city of Kunming, Yunnan Province.

Holotype. Key Laboratory for Palaeobiology, Yunnan University YKLP 12023. A near-complete individual with ‘taphonomically dissected’ head region (Fig. 1d, and Supplementary Figs 2e and 4f).

Referred material. Fifteen additional specimens (Supplementary Table 1).

Locality and horizon. Xiaoshiba area in the suburb of Kunming; Hongjingshao Formation, *Yunnanoccephalus–Chengjiangaspis–Hongshiyanaspis* Biozone (lower part of the Canglangpuan Stage, Cambrian Series 2, Stage 3).

Diagnosis. A species of *Chengjiangocaris* with 26 trunk tergites that narrow posteriorly, including 5 reduced anterior tergites under the head shield. Conical tail-spine with paired tail flukes.

Fuxianhuia xiaoshibaensis sp. nov.

Etymology. After Xiaoshiba, the nearest village to the new locality.

Holotype. YKLP 12027. A complete articulated specimen with ‘taphonomically dissected’ head region (Fig. 2a, b).

Referred material. Eight additional specimens (Supplementary Table 1).

Locality and horizon. Xiaoshiba area in the suburb of Kunming; Hongjingshao Formation, *Yunnanoccephalus–Chengjiangaspis–Hongshiyanaspis* Biozone (lower part of the Canglangpuan Stage, Cambrian Series 2, Stage 3).

Diagnosis. A species of *Fuxianhuia* with 20 anterior trunk tergites bearing prominent pleural folds, including three reduced tergites under head shield, followed by up to 16 narrow posterior tergites lacking pleurae.

The head structure of fuxianhuiids has been proposed as an evolutionary link between that of euarthropods, which bear a deutocerebral first appendage^{16,17}, and the protocerebral condition of onychophorans¹⁸ and Palaeozoic-era lobopodians¹⁹. Most interpretations of the fuxianhuiid head include the presence of antennae, followed ventrally by a pair of specialized post-antennal appendages (SPAs)^{1–3,8,9}. However, an alternative hypothesis proposes that the SPAs are in fact paired gut diverticulae within a head capsule, presenting a fundamentally different account of early euarthropod evolution^{4,12,13}. This debate remains unresolved because detailed information on the fuxianhuiid head is only available from the type species, *Fuxianhuia protensa* from the Chengjiang biota (Heilinpu Formation)^{3,4,8,10–12,20}.

Fuxianhuiid specimens from the Xiaoshiba Lagerstätte, Hongjingshao Formation, Yunnan (Supplementary Fig. 1), China, are distinguished by a unique taphonomic dissection of the shield that covers the head region of these stem-group euarthropods. A substantial percentage (approximately 40%) of carcasses experienced early (pre-burial) degradational softening of the anterior connective tissues, such that head shields were commonly inverted or rotated forwards during final sedimentation events (Supplementary Figs 2 and 3). Exposure of the underlying structures, including internal organs (Fig. 1d, e, h), reveals the cephalic anatomy of fuxianhuiids in exceptional detail.

C. kunmingensis and *F. xiaoshibaensis* share several general aspects of cephalic organization including: a large subtrapezoidal head shield covering the anterior region, with its anterior tip attached to the rest of the body via a subcircular anterior sclerite (Figs 1a–f, h and 2a, b, d, e); an anterior sclerite that occupies the anterior edge of the head and bears a pair of prominent stalked eyes with no signs of ommatidial lenses (Figs 1a, b and 2b); a subtrapezoidal hypostome on the ventral surface that extends approximately one-third of the shield length, following the anterior sclerite (Figs 1c and 2b, c); and a posteriorly directed mouth that opens behind the posterior edge of the hypostome (Figs 1c and 2c). Neither *C. kunmingensis* nor *F. xiaoshibaensis* show any indication of a discrete head capsule beneath the shield¹².

The uniramous antennae of both species attach anteriorly between the posterior border of the anterior sclerite and the anterior edge of the hypostome (Figs 1a–c and 2d, e); the antennae are composed of more than 20 podomeres and taper distally (Figs 1b and 2d, e). Ventrally, the antennae are followed by a pair of enlarged, posteriorly directed, uniramous limbs that attach para-orally at either side of the hypostome, the SPAs. These appendages are composed of three robust podomeres. The base consists of a very short first podomere (P1; the most proximal) which constitutes approximately 15% of the total length. The attachment to the body and the first articulation (A1) of the SPAs are usually concealed by the lateral edges of the hypostome, but can be observed in specimens in which the hypostome is broken (Fig. 2b). The medial podomere (P2) is larger (approximately 35% of the total length) and displays the conspicuous second articulation (A2), often the only

¹Key Laboratory for Palaeobiology, Yunnan University, Kunming 650091, China. ²Department of Earth Sciences, University of Cambridge, Downing Street, Cambridge, CB2 3EQ, UK.

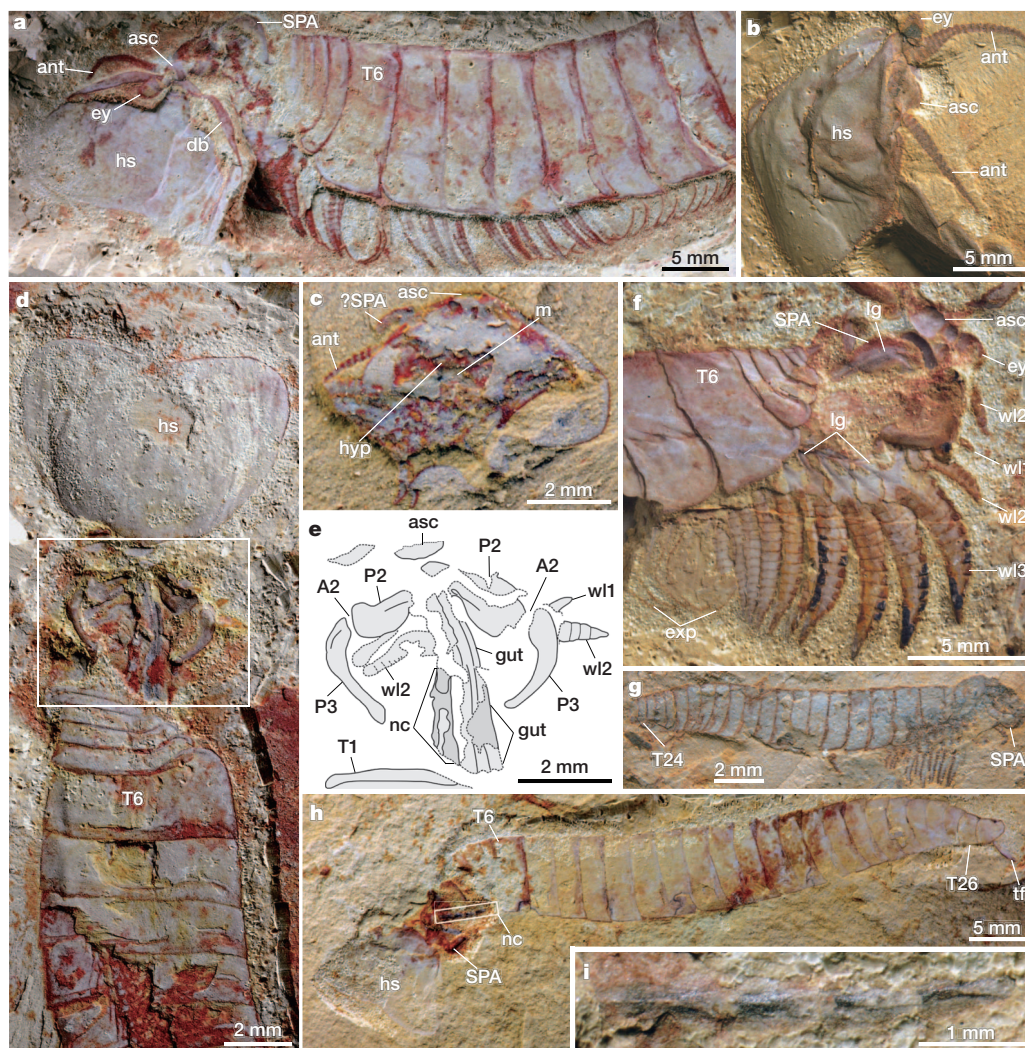


Figure 1 | *Chengjiangocaris kunmingensis* from the early Cambrian (Canglangpuan) Hongjingshao Formation, Yunnan, China. **a**, YKLP 12020 articulated specimen with taphonomically dissected head region (anterior is to the left of the image). **b**, YKLP 12021 isolated head region with *in situ* shield (anterior region is to the right of the image). **c**, YKLP 12022b isolated head with exposed structures (anterior region is to the top of the image). **d**, Holotype YKLP 12023 articulated specimen with taphonomically dissected head region (anterior region is to the top of the image). **e**, Camera lucida drawing of panel **d**. **f**, YKLP 12024 articulated specimen with taphonomically dissected head

region (anterior region is to the right of the image). **g**, YKLP 12025 a complete articulated specimen (anterior region is to the right of the image). **h**, YKLP 12026 complete articulated specimen with taphonomically dissected head region (anterior region is to the left of the image). **i**, Close-up of preserved nerve cord in **h**. A1, articulation 1; ant, antennae; asc, anterior sclerite; db, doublure; exp, exopod; ey, eye; hs, head shield; hyp, hypostome; lg, longitudinal groove; m, mouth; nc, nerve cord; P1, podomere 1; SPA, specialized postantennal appendage; tf, tail flukes; T1, tergite 1; wl1, walking leg 1.

visible joint in well-preserved specimens (Figs 1e and 2b–e and Supplementary Table 1); a longitudinal groove^{3,10} is clear in well-preserved specimens (Figs 1e, f and 2d, e). The distal portion of the SPAs consists of a long (approximately 50% of the total length) and distally tapering podomere (P3) that narrows into a blunt tip. A subchelate termination^{3,8,9} is not apparent.

Variable orientations of distal components of the SPAs indicate that A2 conferred the principal mobility to the limbs (Figs 1d, e and 2c–e). This arrangement, and the absence of gnathobases or other specializations for feeding, suggests that the SPAs had a food-gathering role, performing a simple sweeping motion in which sediment was ploughed directly into the mouth. The antennae with multiple podomeres probably had a sensorial function as opposed to an involvement in feeding⁵.

The digestive tract of the two new species consists of a simple gut that reaches far into the anterior region of the head, overlying the proximal podomeres of the SPAs and extending posteriorly throughout the trunk (Fig. 1d, e and Supplementary Fig. 4d). There is no indication of gut diverticulae^{4,12} or other accessory digestive structures. Four

specimens of *C. kunmingensis* preserve a thin and convex strand of dark material with a distinctive metameric organization beneath the gut (Fig. 1d, e, h, i and Supplementary Fig. 4c). We interpret this as the remains of a simple ventral nerve cord²¹, the first documented case of a preserved post-cephalic central nervous system in a stem-group euarthropod.

All of the post-oral appendages of these two fuxianhuid taxa are biramous, each comprising a simple oval exopod with no lamellae, and an endopod with more than a dozen podomeres. The endopods of *F. xiaoshibaensis* are cylindrical, non-spiniferous walking legs with multiple podomeres, and they have a blunt and undifferentiated termination (Fig. 2c), similar to those of the type species. The post-oral appendages do not extend beyond the shield margins or the pleural folds on the anterior region of the trunk, and there is little variation in size throughout the body; walking legs are absent from the narrow posterior tagma of the trunk. The post-oral appendages of *Chengjiangocaris* differ from those of *Fuxianhuia* by the presence of drastically enlarged conical endopods with acute tips^{10,20}; *C. kunmingensis* is distinguished further by the smaller size of its first two pairs of post-oral

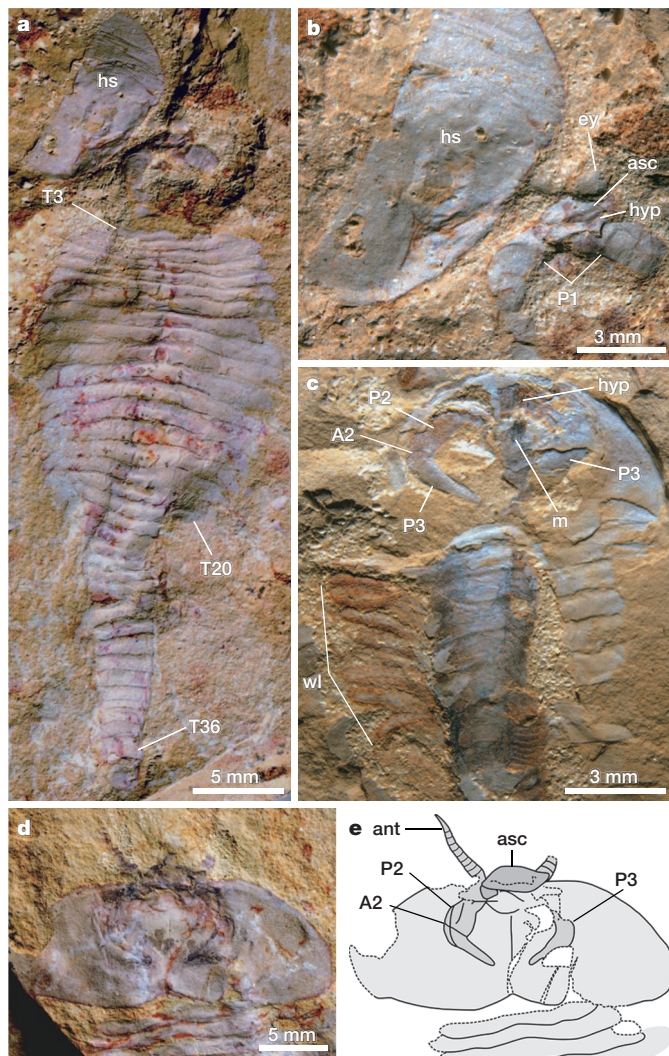


Figure 2 | *Fuxianhuia xiaoshibaensis* from the early Cambrian (Canglangpuan) Hongjingshao Formation, Yunnan, China. Anterior at top of figure. **a**, Holotype YKLP 12027 complete articulated specimen in dorsal view with taphonomically dissected head region. **b**, Close-up of head region in panel **a**. **c**, YKLP 12028 articulated specimen in dorsal view with exposed head and trunk appendages. **d**, YKLP 12029 articulated specimen in dorsal view with preserved head appendages. **e**, Camera lucida drawing of panel **d**. Abbreviations as in Fig. 1.

limbs (Fig. 1d–g), whereas the following ten pairs of limbs have massive endopods with reduced exopod flaps (Fig. 1f). Proximally, the enlarged endopods of *Chengjiangocaris* feature a longitudinal groove⁸ (Fig. 1f), identical to that observed in the SPAs (Fig. 1d–f). In *C. kunmingensis*, each of the first five pairs of post-oral walking legs corresponds to one of the reduced anteriormost trunk tergites (Fig. 1a, d, f). The remaining tergites are polypodous^{3,8,12}, being associated with three or four pairs of walking legs, the endopods of which become progressively reduced in size posteriorly (Fig. 1a, g). Polypody is also evident in *F. xiaoshibaensis* (Fig. 2c), but it is not possible to resolve precisely the association between limb number and the reduced anterior tergites.

The taphonomic dissection of *C. kunmingensis* and *F. xiaoshibaensis* gives a much improved account of fuxianhuiid head anatomy, partly because the details are not obscured by the overlying shield, but also because of the enhanced quality of preservation associated with direct exposure to the surrounding sediment. This phenomenon is readily apparent in the post-oral walking legs of *C. kunmingensis*: the outlines of distal podomeres lying outside the body margin are conspicuously better preserved than the more proximal portions (Fig. 1f).

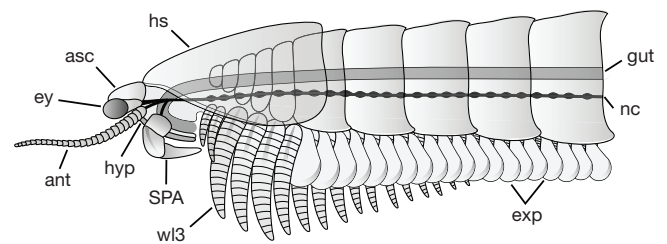


Figure 3 | Reconstruction of *Chengjiangocaris kunmingensis*. Anterior end is to the left of the image. Lateral view showing the organization of the preserved appendages, digestive tract and ventral nerve cord. The reduced exopods on the anterior walking legs are concealed behind the enlarged endopods. Abbreviations as in Fig. 1.

Similarly, the selective effacement of head appendages in association with *in situ* shields—the typical style of fuxianhuiid preservation^{3,4,8,10,12,20}—has previously obscured their anatomical identity (Supplementary Figs 2 and 3).

C. kunmingensis and *F. xiaoshibaensis* provide clear evidence that the fundamental organization of the fuxianhuiid head included a pair of SPAs^{3,8,10,11}. This improved understanding of the structure and organization of the pre-oral appendages in fuxianhuiids leads us to reconsider their segmental affinities (Fig. 3). It has been proposed that the SPAs of fuxianhuiids are segmentally homologous with the ‘short great-appendages’ of megacheirans^{1,2,9}. As such, the SPAs have been widely regarded as deutocerebral^{2,9,14,15}, or possibly even protocerebral¹. Our data show that the morphology and position of the fuxianhuiid SPAs are incompatible with the short great-appendages of megacheirans, which consist of anteriorly attached (pre-oral) and highly specialized raptorial limbs, functionally defined by the presence of elbow-like joints^{14,15}. Although both the SPAs and short great-appendages were probably involved in feeding, the fuxianhuiid SPAs had only a limited range of movement and were restricted under the shield; thus, it is unlikely that they were used for predation in the same way as short great-appendages. The absence of shared structural or positional similarity undermines hypotheses of segmental homology between the fuxianhuiid SPAs and the (deutocerebral^{14,15}) short great-appendages of megacheirans^{1,2,9}.

Identification of the attachment sites of the antennae and SPAs in *C. kunmingensis* and *F. xiaoshibaensis* represent the best means to interpret their segmental affinities. The embryological organization of the pre-oral appendages in Euarthropoda follows a strictly stereotypical pattern^{22–24}: the pre-ocular^{25–28} hypostome–labrum complex overhangs or covers the posteriorly directed mouth; the first pair of deutocerebral^{16,17} limbs is attached anteriorly relative to the hypostome–labrum complex; and the second pair of tritocerebral limbs occupies a para-oral position, and thus attaches at either side of the hypostome–labrum complex. The antennae and SPAs in *C. kunmingensis* and *F. xiaoshibaensis* follow this precise organization, and thus are segmentally homologous to the deutocerebral and tritocerebral appendages of crown-group Euarthropoda, respectively³. There is no compelling evidence for the presence of protocerebral appendages in fuxianhuiids^{1,2,9}.

The information presented here has further implications for understanding the head segmentation of several Cambrian bivalved stem-group euarthropods, such as *Branchiocaris pretiosa* and *Perspicaris dictynna*, which share several components of the cephalic organization with fuxianhuiids^{1,7,10,29}. The widespread distribution of the antenna–SPA configuration observed in the stem lineage suggests that the (deutocerebral) antenniform first appendages represent an ancestral, and relatively stable, feature of the head of stem-group Euarthropoda, and thus are precursors of the derived first appendages found in early representatives of Chelicerata^{14,15} and Mandibulata^{2,9}. The identification of a feeding role for the SPAs in fuxianhuiids, and probably also in taxa such as *Branchiocaris* and *Perspicaris*, indicates that the

tritocerebral appendages are morphologically and functionally mal-leable even in Cambrian representatives.

METHODS SUMMARY

Fossils were photographed with a Nikon D3X fitted with a Nikon AF-S Micro Nikkor 105-mm lens, with a 450-watt inclined incandescent light bulb. Small specimens and close-up images were pictured using a LEICA M205-C stereomicroscope fitted with a Leica DFC 500 digital camera, and directional illumination provided by a LEICA LED5000 MCITM. All of the material described is deposited at the Key Laboratory for Palaeobiology, Yunnan University, Kunming, China.

Received 24 October; accepted 21 December 2012.

- Budd, G. E. A palaeontological solution to the arthropod head problem. *Nature* **417**, 271–275 (2002).
- Scholtz, G. & Edgecombe, G. D. The evolution of arthropod heads: reconciling morphological, developmental and palaeontological evidence. *Dev. Genes Evol.* **216**, 395–415 (2006).
- Chen, J.-Y., Edgecombe, G. D., Ramsköld, L. & Zhou, G.-Q. Head segmentation in early Cambrian *Fuxianhuia*: implications for arthropod evolution. *Science* **268**, 1339–1343 (1995).
- Waloszek, D., Chen, J., Maas, A. & Wang, W. Early Cambrian arthropods—new insights into arthropod head and structural evolution. *Arthropod Struct. Dev.* **34**, 189–205 (2005).
- Waloszek, D., Maas, A., Chen, J. & Stein, M. Evolution of cephalic feeding structures and the phylogeny of Arthropoda. *Palaeogeogr. Palaeoclimatol. Palaeoecol.* **254**, 273–287 (2007).
- Daley, A. C., Budd, G. E., Caron, J.-B., Edgecombe, G. D. & Collins, D. The Burgess Shale anomalocaridid *Hurdia* and its significance for early euarthropod evolution. *Science* **323**, 1597–1600 (2009).
- Budd, G. E. & Telford, M. J. The origin and evolution of arthropods. *Nature* **457**, 812–817 (2009).
- Hou, X.-G. & Bergström, J. *Arthropods of the Lower Cambrian Chengjiang fauna, southwest China*. Fossils and Strata, No. 45, 1–116 (Wiley, 1997).
- Scholtz, G. & Edgecombe, G. D. In *Crustacea and Arthropod Relationships (Crustacean Issues)* (eds Koenemann, S. & Jenner, R.A.) 139–165 (CRC Press, 2005).
- Budd, G. E. Head structure in upper stem-group euarthropods. *Palaeontology* **51**, 561–573 (2008).
- Ma, X., Hou, X.-G., Edgecombe, G. D. & Strausfeld, N. J. Complex brain and optic lobes in an early Cambrian arthropod. *Nature* **490**, 258–261 (2012).
- Bergström, J., Hou, X. G., Zhang, X.-G., Liu, Y. & Clausen, S. A new view of the Cambrian arthropod *Fuxianhuia*. *Geologiska Föreningen* **130**, 189–201 (2008).
- Stein, M. A new arthropod from the Early Cambrian of North Greenland, with a ‘great appendage’-like antennula. *Zool. J. Linn. Soc.* **158**, 477–500 (2010).
- Chen, J.-Y., Waloszek, D. & Maas, A. A new ‘great-appendage’ arthropod from the Lower Cambrian of China and homology of chelicerate chelicerae and raptorial antero-ventral appendages. *Lethaia* **15**, 3–20 (2004).
- Haug, J. T., Waloszek, D., Maas, A., Liu, Y. & Haug, C. Functional morphology, ontogeny and evolution of mantis shrimp-like predators in the Cambrian. *Palaeontology* **55**, 369–399 (2012).
- Mittmann, B. & Scholtz, G. Development of the nervous system in the “head” of *Limulus polyphemus* (Chelicerata, Xiphosura): morphological evidence for a correspondence between the segments of the chelicerae and of the (first) antennae of Mandibulata. *Dev. Genes Evol.* **213**, 9–17 (2003).
- Harzsch, S., Wildt, M., Battelle, B. & Waloszek, D. Immunohistochemical localization of neurotransmitters in the nervous system of larval *Limulus polyphemus* (Chelicerata, Xiphosura): evidence for a conserved protocerebral architecture in Euarthropoda. *Arthropod Struct. Dev.* **34**, 327–342 (2005).
- Eriksson, B. J., Tait, N. N., Budd, G. E., Janssen, R. & Akam, M. Head patterning and Hox gene expression in an onychophoran and its implications for the arthropod head problem. *Dev. Genes Evol.* **220**, 117–122 (2010).
- Liu, J. et al. An armoured Cambrian lobopodian from China with arthropod-like appendages. *Nature* **470**, 526–530 (2011).
- Hou, X. G. et al. *The Cambrian Fossils of Chengjiang, China: the Flowering of Early Animal Life* (Blackwell Publishing, 2004).
- Harzsch, S. & Waloszek, D. Serotonin-immunoreactive neurons in the ventral nerve cord of Crustacea: a character to study aspects of arthropod phylogeny. *Arthropod Struct. Dev.* **29**, 307–322 (2000).
- Olesen, J. Phylogeny of Branchiopoda (Crustacea)—character evolution and contribution of uniquely preserved fossil. *Arthropod Syst. Phyl.* **67**, 3–39 (2009).
- Liu, Y., Maas, A. & Waloszek, D. Early development of the anterior body region of the grey widow spider *Latrodectus geometricus* Koch, 1841 (Theridiidae, Araneae). *Arthropod Struct. Dev.* **38**, 401–416 (2009).
- Liu, Y., Maas, A. & Waloszek, D. Early development of the head region of *Gryllus assimilis* Fabricius, 1775 (Orthoptera, Insecta). *Arthropod Struct. Dev.* **39**, 382–395 (2010).
- Popadić, A., Panganiban, D. R., Shear, W. A. & Kaufman, T. C. Molecular evidence for the gnathobasic derivation of arthropod mandibles and for the appendicular origin of the labrum and other structures. *Dev. Genes Evol.* **208**, 142–150 (1998).
- Posnien, N. F., Bashasab, F. & Bucher, G. The insect upper lip (labrum) is a non-segmental appendage-like structure. *Evol. Dev.* **11**, 440–488 (2009).
- Bitsch, J. & Bitsch, C. The tritocerebrum and the clypeolabrum in mandibulate arthropods: segmental interpretation. *Acta Zool.* **91**, 249–266 (2010).
- Steinmetz, P. R. H. et al. *Six3* demarcates the anterior-most developing brain region in bilaterian animals. *EvoDevo* **1**, 14 (2010).
- Legg, D. A., Sutton, M. D., Edgecombe, G. D. & Caron, J.-B. Cambrian bivalved arthropod reveals origin of arthropodization. *Proc. R. Soc. B* **279**, 4699–4704 (2012).

Supplementary Information is available in the online version of the paper.

Acknowledgements This study is supported by the National Natural Science Foundation of China (41272027), and the PhD Fund of the Ministry of Education of China (20115301110005). J.O.-H. is funded by CONACYT (Consejo Nacional de Ciencia y Tecnología, México), the University of Cambridge Trusts and Darwin College, University of Cambridge. We thank C. Shen, T. Lan and J.-B. Hou for assistance in the field.

Author Contributions The LSID urn:lsid:zoobank.org:pub:B3E00449-6531-4B15-9A36-411C10F1B466 has been deposited in ZooBank. J.Y. discovered the fossil localities, and collected and prepared all the material. J.O.-H. wrote the manuscript with input from the other authors. N.J.B. and X.-g.Z. designed the research.

Author Information Reprints and permissions information is available at www.nature.com/reprints. The authors declare no competing financial interests. Readers are welcome to comment on the online version of the paper. Correspondence and requests for materials should be addressed to X.-g.Z. (xgzhang@ynu.edu.cn).

High salt recruits aversive taste pathways

Yuki Oka¹, Matthew Butnaru¹, Lars von Buchholtz², Nicholas J. P. Ryba² & Charles S. Zuker¹

In the tongue, distinct classes of taste receptor cells detect the five basic tastes; sweet, sour, bitter, sodium salt and umami^{1,2}. Among these qualities, bitter and sour stimuli are innately aversive, whereas sweet and umami are appetitive and generally attractive to animals. By contrast, salty taste is unique in that increasing salt concentration fundamentally transforms an innately appetitive stimulus into a powerfully aversive one^{3–7}. This appetitive–aversive balance helps to maintain appropriate salt consumption^{3,4,6,8}, and represents an important part of fluid and electrolyte homeostasis. We have shown previously that the appetitive responses to NaCl are mediated by taste receptor cells expressing the epithelial sodium channel, ENaC⁸, but the cellular substrate for salt aversion was unknown. Here we examine the cellular and molecular basis for the rejection of high concentrations of salts. We show that high salt recruits the two primary aversive taste pathways by activating the sour- and bitter-taste-sensing cells. We also demonstrate that genetic silencing of these pathways abolishes behavioural aversion to concentrated salt, without impairing salt attraction. Notably, mice devoid of salt-aversion pathways show unimpeded, continuous attraction even to very high concentrations of NaCl. We propose that the ‘co-opting’ of sour and bitter neural pathways evolved as a means to ensure that high levels of salt reliably trigger robust behavioural rejection, thus preventing its potentially detrimental effects on health.

Sodium is an essential ion, and animals have evolved dedicated salt-sensing systems, including prominent detectors in the taste system. Salt taste in mammals can trigger two opposing behavioural responses; low concentrations of salt (<100 mM NaCl, referred to as ‘low salt’) are generally appetitive and elicit behavioural attraction, but high concentrations (>300 mM NaCl, referred to as ‘high salt’) are aversive and provoke strong behavioural rejection. Notably, the attractive salt pathway is selectively responsive to sodium (underscoring the key requirement of NaCl in the diet), whereas the aversive salt pathway functions as a non-selective detector for a wide range of salts^{3,4,6,7}.

For many years, the sensitivity of ENaC (epithelial sodium channel; also known as SCNN1) to the diuretic amiloride^{9–12} has been used as a powerful means to block ENaC function and separate the contributions of the appetitive and aversive salt pathways^{8,10,13}. We reasoned that if we could identify an equivalent pharmacological blocker for the high-salt-sensing pathway, this might provide a valuable tool to dissect the cellular basis of high-salt taste. We therefore recorded chorda tympani taste responses in the presence or absence of various compounds that are known to affect ion-channel function (Supplementary Table 1) and found that allyl isothiocyanate (AITC), a component of mustard oil (and the source of its pungency) significantly suppressed responses to high concentrations of NaCl (Fig. 1a, top panel), without affecting responses to low concentrations of NaCl (see Methods). Identical suppression was observed for KCl, which selectively activates the high-salt pathway (Fig. 1a and Supplementary Fig. 1). Interestingly, AITC also inhibited responses to bitter stimuli without significantly impacting any other taste modality (Fig. 1a, bottom panel, and Supplementary Fig. 2; see Methods for details on conditions). These results suggested that taste receptor cells (TRCs) for bitter taste might be the

target of AITC, and a constituent of the high-salt sensing pathway. Thus, we next asked whether bitter-sensing cells are activated by high-salt stimuli.

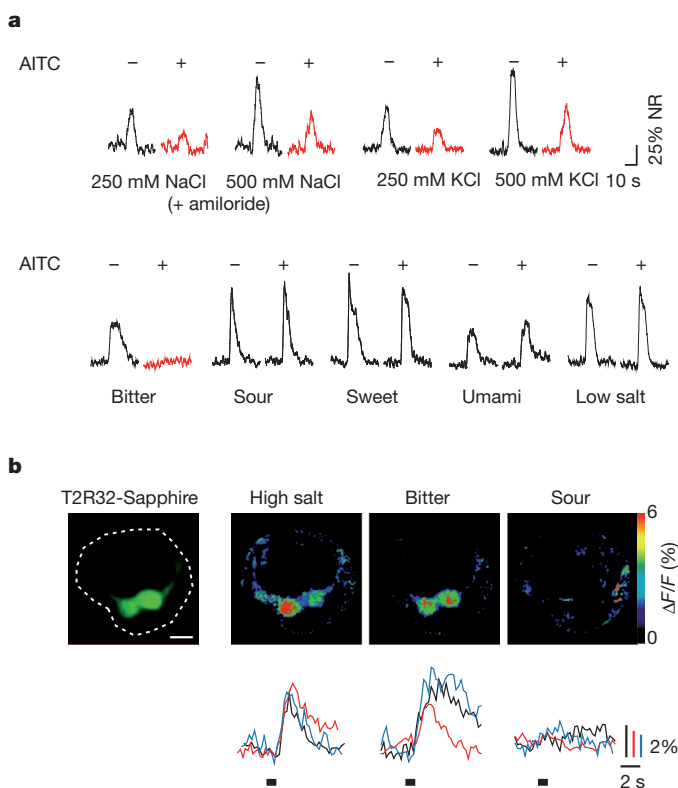


Figure 1 | Bitter receptor cells mediate high-salt taste responses. AITC acts as a selective inhibitor of bitter and high-salt taste responses. **a**, Integrated chorda tympani responses to taste stimuli (see Methods for details) before (–) and after (+) application of AITC; amiloride was used to selectively eliminate the contribution of the ENaC-dependent, low-salt pathways. AITC completely inhibited bitter responses (0.1 mM cycloheximide) and significantly suppressed high-salt responses (250 or 500 mM NaCl + amiloride, and 250 or 500 mM KCl; highlighted in red) but did not affect responses to low-salt (60 mM NaCl) or other taste qualities; representative responses from multiple animals are shown (see also Supplementary Fig. 1). NR, normalized response. **b**, Calcium imaging of taste-cell responses confirmed that T2R32-Sapphire-positive taste cells respond to bitter stimuli (mixture of 1 mM cycloheximide, 1 mM quinine and 10 mM denatonium) and high salt (500 mM KCl), but not to sour stimuli (100 mM citric acid). Shown is a taste bud overlaid with Sapphire fluorescence (dotted circle, left), and three pseudo-coloured images (right panels) depicting its responses to high salt, bitter and sour stimuli, respectively. Scale bar, 10 μ m. Below the imaging panels are representative $\Delta F/F$ traces for these tastants from three additional T2R32-Sapphire-positive cells; black bars beneath the traces denote the window of tastant application. In total, 15 and 12 T2R32-Sapphire-positive cells were activated by bitter and KCl respectively; among these, 11 cells were activated by both compounds but not by sour stimuli (see Supplementary Fig. 4).

¹Howard Hughes Medical Institute and Department of Biochemistry and Molecular Biophysics, and Department of Neuroscience, Columbia College of Physicians and Surgeons, Columbia University, New York, New York 10032, USA. ²National Institute of Dental and Craniofacial Research, National Institutes of Health, Bethesda, Maryland 20892, USA.

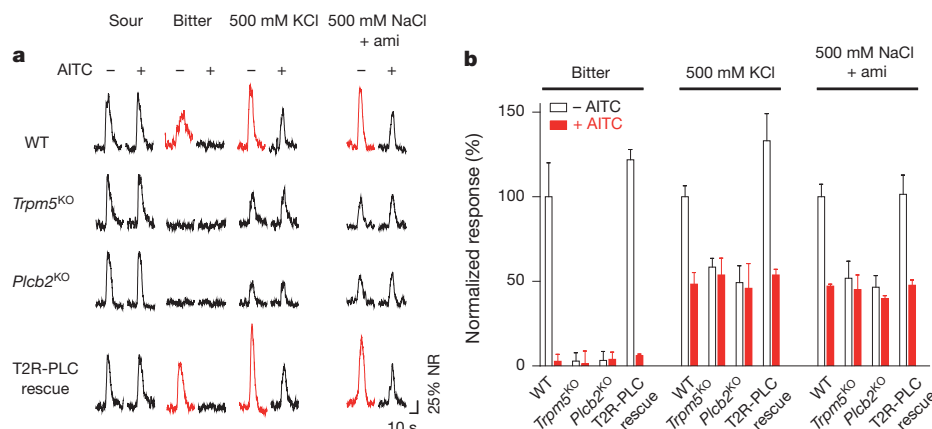


Figure 2 | High-salt responses in bitter cells are TRPM5- and PLC- β 2-dependent. **a**, Representative chorda tympani responses from control (wild type; WT), *Trpm5* knockout (*Trpm5*^{KO}), *Plcb2* knockout (*Plcb2*^{KO}) and T2R32-PLC- β 2-rescue (T2R-PLC rescue) mice before (–) and after (+) application of AITC. Note that both *Trpm5* knockout and *Plcb2* knockout mice lose bitter responses and a significant part of their response to high salt together with all sensitivity to AITC. Expressing PLC- β 2 in just the bitter cells of *Plcb2* knockout mice (T2R-PLC rescue) fully restores normal bitter and high-salt responses as

well as AITC sensitivity (shown by red traces); responses to 500 mM NaCl plus amiloride (ami) were from different animals. **b**, Quantification of normalized responses, before (open bars) and after (red bars) application of AITC (mean \pm s.e.m., $n \geq 3$ mice; see Methods for normalization). AITC treatment almost completely suppressed responses to 0.1 mM cycloheximide and reduced by half the responses to 500 mM KCl and 500 mM NaCl in the presence of 10 μ M amiloride in control and T2R-PLC rescue animals (Student's *t*-test, $P < 0.05$).

We examined salt responses directly using a peeled epithelium preparation that enables functional imaging of TRCs—at single-cell resolution—in response to tastant stimulation⁸. In essence, TRCs from fungiform papillae were loaded with the calcium-sensitive dye, Calcium Green-1 *in vivo*, and then stimulated and imaged *ex vivo*⁸. To ensure that we focused on bitter-sensing cells, we used mice expressing a sapphire variant of the green fluorescent protein (GFP) selectively in T2R-positive cells¹⁴ (T2Rs are the family of G-protein-coupled receptors that mediate bitter-taste sensing) (Supplementary Fig. 3). In these animals, high concentrations of salt indeed activated the GFP-positive cells, which in turn responded to bitter tastants (Fig. 1b and Supplementary Fig. 4).

The finding that high salt activates bitter-sensing cells, and the observation that high salt and bitter stimuli are both blocked by AITC suggest that bitter and high-salt taste may share a common pathway (for example, through the T2R pathway). If this is the case, we would expect *Trpm5* or phospholipase C β 2 (*Plcb2*) knockout mice¹⁵, which lack key components for bitter-taste signalling, to be also defective in high-salt sensing. Indeed, Fig. 2 shows this to be the case: the nerve responses of the knockout animals to high salt are significantly reduced, and are no longer sensitive to AITC. To confirm that the TRPM5- and PLC- β 2-dependent high-salt responses are mediated by bitter receptor cells, we conducted a selective-rescue experiment in which PLC function was restored only to bitter-taste receptor cells of *Plcb2* knockout mice. As expected, expressing a wild-type PLC transgene in bitter receptor cells fully rescued the electrophysiological responses to both bitter and high salt (for example, KCl) to levels indistinguishable from those in wild-type mice (Fig. 2a, b). These results show that bitter-sensing cells mediate the PLC- β 2-dependent high-salt responses, and support the proposal that the aversion to high salt is mediated, at least partly, by activation of the bitter-sensing pathway.

AITC, and *Trpm5* or *Plcb2* knockouts eliminate only approximately 50% of the high-salt neural responses (Fig. 2). Not surprisingly, these animals still retain strong behavioural aversion to high salts¹⁵. Which additional cells mediate the remaining neural responses and behaviour? Given that high salt is strongly aversive and recruits one of the primary aversive taste pathways, we considered that sour taste—the other principal aversive pathway—may mediate the remaining responses.

To examine the involvement of sour-sensing cells in high-salt detection, we inactivated the sour TRCs (PKD2L1-expressing cells¹⁶) by silencing their synaptic machinery. We engineered animals in which

tetanus toxin light chain (TeNT) was targeted to PKD2L1-expressing cells^{17,18} and then assayed their tastant-evoked neural activity in response to salt stimulation. As shown previously¹⁷, silencing PKD2L1-expressing

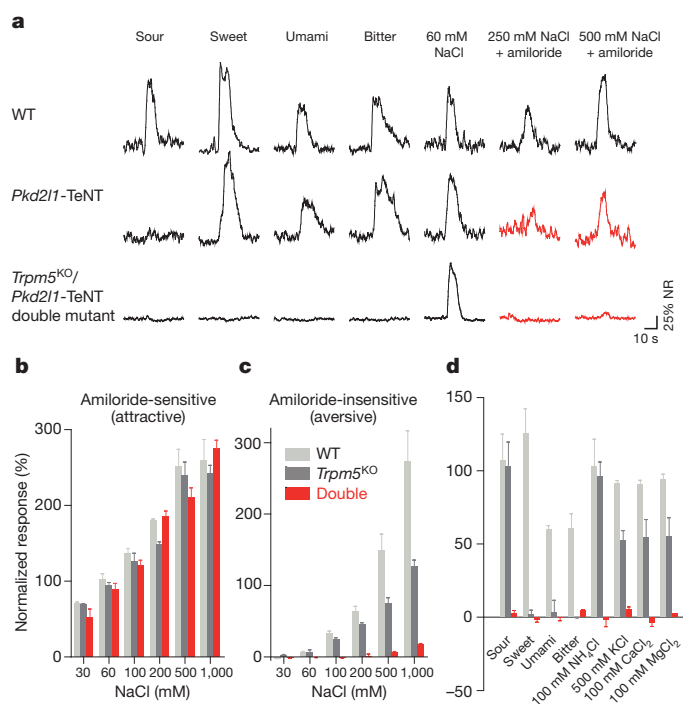


Figure 3 | PKD2L1-expressing cells mediate the residual TRPM5- and PLC- β 2-independent high-salt responses. **a**, Integrated chorda tympani recordings show that silencing PKD2L1 sour-sensing cells affects high-salt taste responses. *Pkd2l1*-TeNT mice have severe deficits in their responses to high salt, but *Trpm5*^{KO}/*Pkd2l1*-TeNT double-mutant animals completely lose all amiloride-insensitive NaCl (high-salt) responses (highlighted as red traces).

b, **c**, Quantification of neural responses shows that double-mutant mice (double) exhibit normal neural responses to low salt (**b**), but lack responses to high salt (**c**) (Student's *t*-test, $P < 0.001$). By contrast, the single mutants (*Trpm5*^{KO}) only show partial loss of responses to high salt. **d**, The double-mutant animals also fail to respond to sweet, bitter, sour and umami as well as non-sodium salts. Data (**b**–**d**) were normalized to the response of 60 mM NaCl and are mean \pm s.e.m., $n \geq 3$ mice.

cells eliminates acid-evoked taste responses (Fig. 3a). However, as shown in Fig. 3, these animals also display a major reduction in their high-salt electrophysiological responses, and further treatment with AITC effectively abolished their remaining high-salt (KCl) responses (Supplementary Fig. 5). Therefore, we reasoned that high-salt taste responses are mediated by the combined action of bitter- and sour-sensing cells, and proposed that genetically blocking both pathways should eliminate high-salt responses. Indeed, double-mutant mice expressing *Pkd2l1*-TeNT and harbouring a *Trpm5* mutation show a near-complete loss of electrophysiological taste responses to a variety of high salts (Fig. 3), including concentrations of NaCl as high as 1,000 mM.

Importantly, if these two cellular pathways are the mediators of behavioural aversion to high salt, then simultaneous silencing of the T2R- and PKD2L1-expressing cells should abolish rejection of concentrated salt solutions. As shown in Fig. 4 and Supplementary Fig. 6, single-mutant mice (*Trpm5*^{-/-} or *Pkd2l1*-TeNT) still retain strong aversion to high salt, demonstrating that activation of either pathway on its own is sufficient to trigger behavioural rejection to salt. However, double-mutant animals show no salt aversion even at concentrations at which controls are strongly repelled. Remarkably, these double

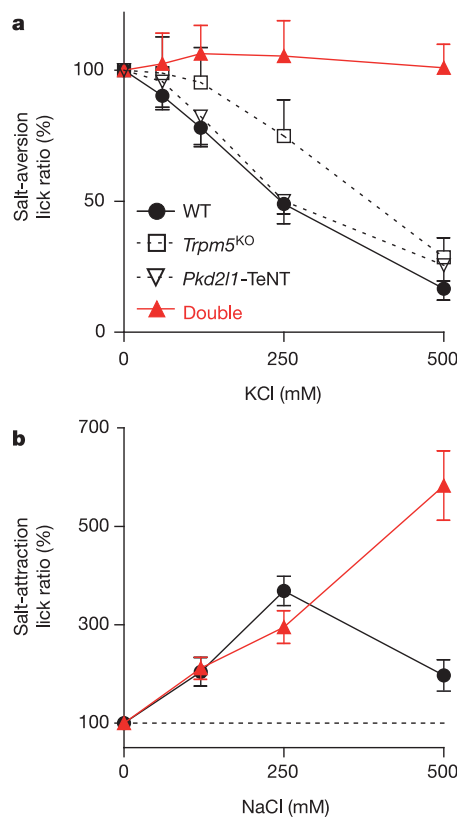


Figure 4 | *Trpm5*^{KO}/*Pkd2l1*-TeNT double-mutant mice show no taste aversion to high salt. Immediate lick assays were used to measure behavioural responses to KCl and NaCl. **a**, Control mice (WT, solid black line) show robust dose-dependent behavioural aversion to increasing concentrations of KCl. By contrast, *Trpm5*^{KO}/*Pkd2l1*-TeNT double-mutant animals do not avoid high-salt stimuli; single mutants behave in the same way as control animals. Two-way analysis of variance (ANOVA) with post-hoc test for individual concentrations revealed significant differences at 500 mM KCl between the double mutants and other genotypes ($P < 0.001$) and at 250 mM KCl between the double mutants and control or *Pkd2l1*-TeNT mice ($P < 0.001$). **b**, After sodium depletion, control mice (black line) show powerful attractive responses to NaCl (see also Supplementary Fig. 7) but the attraction is considerably reduced at higher concentration (500 mM). By contrast, double-mutant animals (red line) show a continuous increase in attraction to NaCl even at concentrations as high as 500 mM NaCl (two-way ANOVA with post-hoc test, $P < 0.001$). Values are mean \pm s.e.m., $n \geq 6$ mice. Horizontal dashed line in **b** denotes baseline (no preference relative to water).

mutants are not simply indifferent to high salt but exhibit unimpeded attraction, even to very high concentrations of salt (for example, levels equivalent to ocean water; approximately 500 mM NaCl; Fig. 4b). Thus, under normal conditions the appetitive–aversive balance for salt, which collectively tunes the animal’s behavioural response to sodium salts, must be orchestrated by the combined activity of the attractive ENaC pathway (which remains in the bitter and sour double mutants) and the repulsive T2R and sour pathways.

The mechanisms by which high salt activates the bitter- and sour-taste receptor cells are not known. However, given that the primary effectors of T2R signalling in bitter cells, PLC- β 2 and TRPM5, are also required for high-salt sensing by the bitter cells, we suggest that either a signalling component in bitter cells (for example, an ion channel), or 1 or more of the approximately 30 T2Rs may be sensitive to high concentrations of salt (perhaps causing the serendipitous transition between the receptor’s inactive and active states)^{19,20}. With respect to the sour-sensing cells, one salient feature is the prominent expression of carbonic anhydrase 4 (CA4)¹⁷, a membrane-bound isoform of carbonic anhydrase. CA4 is likely to be involved in buffering the pH around taste receptor cells ($\text{CO}_2 + \text{H}_2\text{O} \rightleftharpoons \text{HCO}_3^- + \text{H}^+$), and therefore its activity may impact local proton concentration and acid sensing. Notably, carbonic anhydrases are known to be sensitive to high-ionic-strength environments, with high-salt concentrations markedly inhibiting their enzymatic activity^{21,22}. This raises the possibility that CA4 may function as a ‘translator’ of external salts into local pH changes, and thus operate as an important component of the high-salt receptor in sour-sensing cells. Indeed, our results shown in Supplementary Figs 8 and 9 support this proposal by demonstrating that pharmacological inhibition of tongue carbonic anhydrases, or the knockout of CA4, greatly impairs high-salt sensing by the sour-taste receptor cells.

Taken together, our studies reveal that salts activate three different classes of TRCs: the appetitive responses are mediated through the sodium-selective ENaC pathway¹, whereas the rejection of high salt results from the recruitment of the sour- and bitter-taste-sensing pathways. At a cellular level, these results resolve the conundrum of a ‘valence change’ by showing that it is a simple matter of having distinct cell types with well-defined but opposing valences responding to salt. At a physiological level, these findings now provide a simple explanation for the long-standing observation that bitter and sour afferent fibres behave as ‘generalists’, responding not only to bitter and acid stimuli but also to a variety of salts²³. Importantly, we note that the fact that T2R and PKD2L1 cells are also activated by high salt does not imply a change in the logic of taste coding, or in the valence or quality encoded by these TRCs. In fact, if we assume that rodents and humans use similar taste-signalling mechanisms, then it is possible that the bitterness²⁴ and ‘ionic’ taste associated with high concentrations of non-sodium salts in humans may be mediated by the concurrent activation of T2R- and PKD2L1-expressing cells. But why does high salt not taste like a mix of bitter and sour? Sourness represents the detection of protons by at least two separate signalling pathways in the oral cavity: taste (PKD2L1 cells) and non-taste (for example, through TRPV1 or ASIC)^{25–27}, we therefore suggest that the activation of PKD2L1 cells, in the absence of the non-taste acid-sensing pathway, may instead evoke the ionic taste characteristic of high concentrations of non-sodium salts. This proposal re-casts PKD2L1 cells and their corresponding neural line as sensors of ions (for example, protons and potassium), orchestrating different percepts whether activated alone (for example, ionic taste) or in combination (PKD2L1 + non-taste acid sensors = sour taste, whereas PKD2L1 + T2Rs = the taste of KCl and other non-sodium salts).

Future studies using specific inhibitors and activators of each pathway should help to address the contributions of the ENaC-, T2R- and PKD2L1-expressing taste cells to human salt-taste perception, and may serve as a springboard for the development of selective receptor-cell modulators to help to control (and even satisfy) our strong appetite for high salt, but without the potential ill effects of too much sodium.

METHODS SUMMARY

Mice and nerve recordings. T2R32-Sapphire mice are transgenically engineered to express the blue-shifted GFP-derivative, Sapphire²⁸, under the control of the T2R32 promoter (T2R32 is also known as TAS2R139). All other strains have been described previously^{14–17}. Lingual stimulation and recording procedures were carried out as described previously^{8,29}. For pharmacological blocking experiments, 3 mM AITC was applied to the tongue for 5 min before initiation of the recording session; use of higher doses and/or repeated application of AITC often led to less specific inhibition of responses.

Calcium imaging. Calcium imaging from fungiform TRCs was carried out as described previously^{8,30}.

Behavioural assays. Behavioural assays used a custom-made gustometer to measure immediate lick responses as described previously^{8,14,15}. For salt-attraction assays, mice were injected with furosemide (50 mg kg⁻¹) and were placed in their home cage for 3 h without food or water before testing. For salt-aversion assays, mice were deprived of water for 24 h before testing. Three (attraction assay) or two (aversion assay) different concentrations of tastant and water were presented to animals in each experimental session. Data were analysed for statistical significance using a two-way ANOVA with a Bonferroni post-hoc test.

Full Methods and any associated references are available in the online version of the paper.

Received 20 August 2012; accepted 15 January 2013.

Published online 13 February 2013.

- Chandrashekar, J., Hoon, M. A., Ryba, N. J. P. & Zuker, C. S. The receptors and cells for mammalian taste. *Nature* **444**, 288–294 (2006).
- Yarmolinsky, D. A., Zuker, C. S. & Ryba, N. J. P. Common sense about taste: from mammals to insects. *Cell* **139**, 234–244 (2009).
- Beauchamp, G. K., Bertino, M., Burke, D. & Engelman, K. Experimental sodium depletion and salt taste in normal human volunteers. *Am. J. Clin. Nutr.* **51**, 881–889 (1990).
- Duncan, C. J. Salt preferences of birds and mammals. *Physiol. Zool.* **35**, 120–132 (1962).
- Eylam, S. & Spector, A. C. Taste discrimination between NaCl and KCl is disrupted by amiloride in inbred mice with amiloride-insensitive chorda tympani nerves. *Am. J. Physiol. Regul. Integr. Comp. Physiol.* **288**, R1361–R1368 (2005).
- Contreras, R. J. In *Neural Mechanisms in Taste* (ed. Cagan, R. H.) 119–145 (CRC, 1989).
- Lindemann, B. Receptors and transduction in taste. *Nature* **413**, 219–225 (2001).
- Chandrashekar, J. *et al.* The cells and peripheral representation of sodium taste in mice. *Nature* **464**, 297–301 (2010).
- Doolin, R. E. & Gilbertson, T. A. Distribution and characterization of functional amiloride-sensitive sodium channels in rat tongue. *J. Gen. Physiol.* **107**, 545–554 (1996).
- Halpern, B. P. Amiloride and vertebrate gustatory responses to NaCl. *Neurosci. Biobehav. Rev.* **23**, 5–47 (1998).
- Heck, G. L., Mierson, S. & DeSimone, J. A. Salt taste transduction occurs through an amiloride-sensitive sodium transport pathway. *Science* **223**, 403–405 (1984).
- Hettinger, T. P. & Frank, M. E. Specificity of amiloride inhibition of hamster taste responses. *Brain Res.* **513**, 24–34 (1990).
- Spector, A. C., Guagliardo, N. A. & St John, S. J. Amiloride disrupts NaCl versus KCl discrimination performance: implications for salt taste coding in rats. *J. Neurosci.* **16**, 8115–8122 (1996).
- Mueller, K. L. *et al.* The receptors and coding logic for bitter taste. *Nature* **434**, 225–229 (2005).
- Zhang, Y. *et al.* Coding of sweet, bitter, and umami tastes: different receptor cells sharing similar signaling pathways. *Cell* **112**, 293–301 (2003).
- Huang, A. L. *et al.* The cells and logic for mammalian sour taste detection. *Nature* **442**, 934–938 (2006).
- Chandrashekar, J. *et al.* The taste of carbonation. *Science* **326**, 443–445 (2009).
- Yamamoto, M. *et al.* Reversible suppression of glutamatergic neurotransmission of cerebellar granule cells *in vivo* by genetically manipulated expression of tetanus neurotoxin light chain. *J. Neurosci.* **23**, 6759–6767 (2003).
- Gao, Z. G., Jiang, Q., Jacobson, K. A. & Ijzerman, A. P. Site-directed mutagenesis studies of human A_{2A} adenosine receptors: involvement of glu¹³ and his²⁷⁸ in ligand binding and sodium modulation. *Biochem. Pharmacol.* **60**, 661–668 (2000).
- Liu, W. *et al.* Structural basis for allosteric regulation of GPCRs by sodium ions. *Science* **337**, 232–236 (2012).
- Zhu, X. L. & Sly, W. S. Carbonic anhydrase IV from human lung. Purification, characterization, and comparison with membrane carbonic anhydrase from human kidney. *J. Biol. Chem.* **265**, 8795–8801 (1990).
- Baird, T. T., Jr, Waheed, A., Okuyama, T., Sly, W. S. & Fierke, C. A. Catalysis and inhibition of human carbonic anhydrase IV. *Biochemistry* **36**, 2669–2678 (1997).
- Hellekant, G., Ninomiya, Y. & Danilova, V. Taste in chimpanzees II: single chorda tympani fibers. *Physiol. Behav.* **61**, 829–841 (1997).
- Breslin, P. A. & Beauchamp, G. K. Suppression of bitterness by sodium: variation among bitter taste stimuli. *Chem. Senses* **20**, 609–623 (1995).
- Hallock, R. M., Tatangelo, M., Barrows, J. & Finger, T. E. Residual chemosensory capabilities in double P2X2/P2X3 purinergic receptor null mice: intraoral or postgestive detection? *Chem. Senses* **34**, 799–808 (2009).
- Ohkuri, T., Horio, N., Stratford, J. M., Finger, T. E. & Ninomiya, Y. Residual chemoresponsiveness to acids in the superior laryngeal nerve in “taste-blind” (P2X2/P2X3 double-KO) mice. *Chem. Senses* **37**, 523–532 (2012).
- Ugawa, S., Ueda, T., Yamamura, H., Nagao, M. & Shimada, S. Coexpression of vanilloid receptor subtype-1 and acid-sensing ion channel genes in the human trigeminal ganglion neurons. *Chem. Senses* **30** (suppl. 1), i195 (2005).
- Tsien, R. Y. The green fluorescent protein. *Annu. Rev. Biochem.* **67**, 509–544 (1998).
- Nelson, G. *et al.* An amino-acid taste receptor. *Nature* **416**, 199–202 (2002).
- Oka, Y. *et al.* Odorant receptor map in the mouse olfactory bulb: *in vivo* sensitivity and specificity of receptor-defined glomeruli. *Neuron* **52**, 857–869 (2006).

Supplementary Information is available in the online version of the paper.

Acknowledgements We thank E. Vitalis and N. Propp for the generation and maintenance of mouse lines, and K. Mueller for the construction of T2R-Sapphire lines. We also thank J. Chandrashekar, W. Sly and A. Waheed for advice and discussions, and K. Scott and members of our laboratories for comments. Y.O. was supported by the Japan Society for Promotion of Science. This research was supported in part by the intramural research program of the National Institutes of Health and National Institute of Dental and Craniofacial Research (to N.J.P.R.). C.S.Z. is an investigator of the Howard Hughes Medical Institute.

Author Contributions Y.O. designed the study, carried out electrophysiological, biochemical, pharmacological and behavioural experiments, analysed data and wrote the paper; M.B. carried out nerve recordings and behavioural studies; L.v.B. carried out nerve recordings and localization studies. N.J.P.R. and C.S.Z. designed the study, analysed data and wrote the paper.

Author Information Reprints and permissions information is available at www.nature.com/reprints. The authors declare competing financial interests: details accompany the full-text HTML version of the paper at www.nature.com/nature. Readers are welcome to comment on the online version of the paper. Correspondence and requests for materials should be addressed to C.S.Z. (cz2195@columbia.edu) or N.J.P.R. (nick.ryba@nih.gov).

METHODS

Mice. All procedures were carried out in accordance with the US National Institutes of Health (NIH) guidelines for the care and use of laboratory animals, and were approved by the Columbia University or National Institute of Dental and Craniofacial Research Animal Care and Use Committees. T2R32-Sapphire mice are transgenically engineered to express the blue-shifted GFP-derivative, Sapphire²⁸, under the control of the T2R32 promoter (also known as TAS2R139). These mice, generated by K. Mueller, contained 10 kilobase pairs upstream of the T2R32 start codon fused to the GFP reporter. Expression of Sapphire in taste tissue was characterized using double-label *in situ* hybridization (see Supplementary Fig. 3). All other mouse strains have been described previously^{14–17}.

Calcium imaging. Calcium imaging from fungiform TRCs was carried out as described previously^{8,29}. In brief, fungiform TRCs were loaded *in vivo* with 3 kilodaltons Calcium Green-1 dextran (Invitrogen) by electroporating individual taste buds. Tongues were removed 24–36 h after dye loading and the epithelium was peeled enzymatically and placed in a custom recording chamber. The apical surface of the preparation was bathed in a constant flow of artificial saliva, and taste stimuli were delivered by focal application to individual taste buds. Tastants were applied for 1 s, with a minimum of 10 s of artificial saliva between stimuli. Changes in $[Ca^{2+}]_i$ (intracellular calcium concentration) were monitored using a 5-Live confocal microscope (Zeiss) equipped with a $\times 40$ C-Apochromat 1.20 W objective; images were captured at 4 Hz, and $\Delta F/F$ from individual TRCs were analysed and pseudo-coloured as described previously⁸. To identify Sapphire-positive cells in T2R32-Sapphire mice, we used a 405-nm excitation laser to separate Sapphire and Calcium Green-1 fluorescence. Mean cellular fluorescence intensity (F) was calculated for the individual TRCs, and the basal fluorescence (F_0) was assigned to each cell by averaging fluorescence intensity over 3 s just before tastant application. $\Delta F/F$ was calculated as $(F - F_0)/F_0$; taste cells were considered to have responded when $\Delta F/F$ exceeded 3 standard deviations above F_0 within 5 s of tastant application.

Nerve recordings. Lingual stimulation and recording procedures were carried out as described previously^{8,30}; data analysis used the integrated response during the 5 s of tastant stimulation. Compounds used for nerve recordings were: 0.03–1 M NaCl (with and without 10 μ M amiloride) or 0.03–1 M KCl (salty); 20 mM acesulfameK (sweet); 50 mM monopotassium glutamate plus 0.5 mM inosine monophosphate (umami); 0.1 mM cycloheximide (bitter); and 20 mM citric acid (sour). Responses

to 20 mM citric acid (Fig. 1 and Supplementary Fig. 1), 60 mM NaCl (Fig. 3 and Supplementary Figs 7, 8b and 9) or 250 mM KCl before AITC (Aldrich) application (Supplementary Fig. 8a) were used to normalize responses for each experimental series. For Fig. 2, data were normalized to 20 mM citric acid and then scaled to wild-type responses before AITC application. Data were analysed for statistical significance using an unpaired, one-tailed Student's *t*-test and 95% confidence limits.

To compute the amiloride-sensitive salt component, the stimulation regime involved sequential applications of NaCl solutions, first without and then with amiloride (from 5 s before to 5 s after stimulation) in the same experimental series. The amiloride-insensitive component was defined as the response in the presence of amiloride. The fraction of the response inhibited by amiloride was defined as the amiloride-sensitive component (amiloride-sensitive component = response without amiloride – response with amiloride).

For pharmacological inhibition studies using AITC, responses to a series of taste stimuli were measured. Then 3 mM AITC was applied to the tongue at a rate of 6 ml min⁻¹ for 5 min. The tongue was washed with artificial saliva for 1 min and nerve responses to the same series of taste stimuli were measured; responses before and after AITC were compared for each animal. To minimize effects of recovery, responses after AITC were recorded within 15 min of AITC treatment.

For pharmacological studies using bicarbonate, taste responses were measured in the presence or absence of 30 mM KHCO₃, pH 7.4 (applied 5 s before and during tastant stimulation). In dorzolamide (DZA) experiments, responses were monitored before and after incubation of the tongue with 0.5% DZA (w/v) for 5 min. To study the effects of pH on nerve responses, we adjusted the pH of artificial saliva (7.4) to 5.5 with hydrochloric acid.

Behavioural assays. Behavioural assays used a custom-made gustometer to measure immediate lick responses as described previously^{8,14,15}. For salt-attraction assays, mice were injected with furosemide (50 mg kg⁻¹) and were placed in their home cage for 3 h without food or water before testing. For salt-aversion assays, mice were deprived of water for 24 h before testing. Three or four (attraction assay) or two (aversion assay) different concentrations of tastant and water were presented to animals in each experimental session. Differences between knockout and control mice were analysed for statistical significance using a two-way ANOVA with a Bonferroni post-hoc test.

Adult somatic stem cells in the human parasite *Schistosoma mansoni*

James J. Collins III^{1,2}, Bo Wang^{1,3}, Bramwell G. Lambrus¹, Marla E. Tharp¹, Harini Iyer¹ & Phillip A. Newmark^{1,2}

Schistosomiasis is among the most prevalent human parasitic diseases, affecting more than 200 million people worldwide¹. The aetiological agents of this disease are trematode flatworms (*Schistosoma*) that live and lay eggs within the vasculature of the host. These eggs lodge in host tissues, causing inflammatory responses that are the primary cause of morbidity. Because these parasites can live and reproduce within human hosts for decades², elucidating the mechanisms that promote their longevity is of fundamental importance. Although adult pluripotent stem cells, called neoblasts, drive long-term homeostatic tissue maintenance in long-lived free-living flatworms^{3,4} (for example, planarians), and neoblast-like cells have been described in some parasitic tapeworms⁵, little is known about whether similar cell types exist in any trematode species. Here we describe a population of neoblast-like cells in the trematode *Schistosoma mansoni*. These cells resemble planarian neoblasts morphologically and share their ability to proliferate and differentiate into derivatives of multiple germ layers. Capitalizing on available genomic resources^{6,7} and RNA-seq-based gene expression profiling, we find that these schistosome neoblast-like cells express a fibroblast growth factor receptor orthologue. Using RNA interference we demonstrate that this gene is required for the maintenance of these neoblast-like cells. Our observations indicate that adaptation of developmental strategies shared by free-living ancestors to modern-day schistosomes probably contributed to the success of these animals as long-lived obligate parasites. We expect that future studies deciphering the function of these neoblast-like cells will have important implications for understanding the biology of these devastating parasites.

Although classic studies of cell proliferation in *Schistosoma* focused on reproductive tissues^{8,9}, occasional 'undifferentiated' somatic cells that incorporated tritiated thymidine in adult parasites were noted. Encouraged that these cells could represent neoblast-like stem cells, we treated adult *S. mansoni* with the thymidine analogue 5-ethynyl-2'-deoxyuridine (EdU)¹⁰ to examine the distribution of S phase cells in the parasite (Fig. 1a, b). In addition to the expected incorporation in the highly proliferative reproductive organs (testes, ovaries and vitellaria) (Fig. 1a, b and Supplementary Fig. 1), we observed a population of EdU⁺ cells throughout the soma of male and female parasites (Fig. 1a–d). Similar distributions of EdU-incorporating cells were observed whether parasites were given EdU during *in vitro* culture or *in vivo* by intraperitoneal injection of schistosome-infected mice. Analogous to the neoblasts in free-living flatworms^{11,12}, these proliferating somatic cells (PSCs) were restricted to the mesenchyme of male and female worms (Fig. 1c, d), not associated with reproductive organs, and were often found in clusters near the intestine (Supplementary Fig. 2a). We also observed a conspicuous population of PSCs adjacent to the ventral sucker (Supplementary Fig. 2b). PSCs traversed the cell cycle: they initially expressed the cell-cycle-associated transcript histone h2b (Supplementary Fig. 3a–c) and progressed to M phase within 24 h after an EdU pulse (Supplementary Fig. 3d).

Neoblasts are the only proliferating somatic cells in planarians^{4,11} and they possess a distinct morphology: they are round-to-ovoid mesenchymal cells with a high nuclear-to-cytoplasmic ratio, a large nucleolus, and they often extend a cytoplasmic projection^{3,11,13}. To determine whether PSCs share similarities with planarian neoblasts, we examined these cells by dissociating male tissues devoid of germ cells (Fig. 1e). In these preparations we observed a number of distinct differentiated cell types that failed to incorporate EdU, including cells with a low nuclear-to-cytoplasmic ratio, neuron-like cells, and ciliated

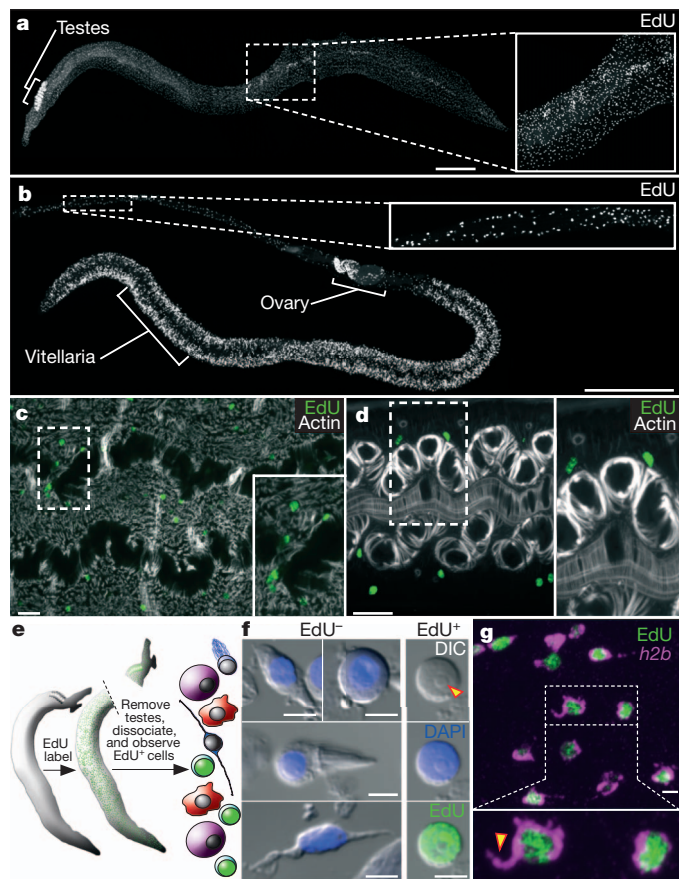


Figure 1 | Proliferation of somatic cells in adult schistosomes. **a, b**, EdU labelling in male (**a**) and female (**b**) parasites. **c, d**, Distribution of mesenchymal PSCs in male (**c**) and female (**d**) parasites. Phalloidin staining for actin shows male enteric and dorso-ventral muscles and female enteric and uterine muscles. **e**, Strategy to characterize PSC morphology. **f**, The morphology of EdU[−] and EdU⁺ cells. The arrowhead indicates a nucleolus. **g**, FISH for histone h2b with EdU labelling. The arrowhead indicates a cytoplasmic projection. **a–d, g** are confocal projections; **a, b** are derived from tiled stacks. Scale bars: **a, b**, 500 μ m; **c, d**, 20 μ m; **f, g**, 5 μ m. Inset magnifications, relative to original: **a, g**, $\times 2.2$; **b**, $\times 2.6$; **c**, $\times 1.6$; **d**, $\times 1.7$.

¹Howard Hughes Medical Institute and Department of Cell and Developmental Biology, University of Illinois at Urbana-Champaign, Urbana, Illinois 61801, USA. ²Neuroscience Program, University of Illinois at Urbana-Champaign, Urbana, Illinois 61801, USA. ³Institute for Genomic Biology, University of Illinois at Urbana-Champaign, Urbana, Illinois 61801, USA.

cells (Fig. 1f). By contrast, we found that EdU incorporation was restricted to a neoblast-like population of cells with scant cytoplasm ($n = 136$ out of 137 cells) and often a prominent nucleolus (Fig. 1f). We also inspected PSCs within the mesenchyme using EdU to label nuclei and fluorescent *in situ* hybridization (FISH) to detect histone h2b messenger RNA in the cytoplasm of proliferative cells. Consistent with our results from tissue macerates, EdU⁺ cells possess a narrow rim of cytoplasm surrounding their nucleus, and these cells often display a cytoplasmic projection (Fig. 1g). These observations highlight morphological similarities between proliferating cells in schistosomes and planarian neoblasts.

Previous studies have exploited the sensitivity of planarian neoblasts to γ -irradiation as a means to identify neoblast-enriched transcripts^{14–16}. Using this strategy to identify PSC-expressed genes, we exposed parasites to various dosages of γ -irradiation and determined that 100–200 Gy were sufficient to block EdU incorporation (Fig. 2a). Because of their high ratio of somatic tissue to reproductive tissue and their large number of PSCs relative to female worms (compare insets in Fig. 1a and b), our remaining studies, unless otherwise noted, focused on male parasites. By comparing the transcriptional profiles of irradiated and non-irradiated parasites by RNA-seq (Fig. 2b), we identified 128 genes with significantly downregulated expression (≥ 2 -fold, $P < 0.05$) 48 h after irradiation (Fig. 2c and Supplementary Table 1). Highlighting the efficacy of this approach to identify transcripts specific to proliferating cells, we found that genes expressed in differentiated tissues, such as the intestine (*S. mansoni* cathepsin B (ref. 17)), were unaffected by irradiation. By contrast, our list of downregulated genes was enriched for factors involved in the cell cycle (Supplementary Fig. 4 and Supplementary Table 1).

In addition to identifying cell-cycle-associated factors, systematic comparison of irradiation-sensitive genes with neoblast-enriched transcripts^{14,15,18,19} uncovered a number of interesting similarities

(Supplementary Table 1). For instance, homologues of genes known to regulate planarian neoblasts such as *p53*, a sox-family transcription factor, fibroblast growth factor receptors, and argonaute 2 (*ago2*)^{14,20–22}, were significantly downregulated in irradiated schistosomes (Supplementary Fig. 4 and Supplementary Table 1). Another distinctive feature of neoblasts^{3,14,22}, and the somatic stem cells of other invertebrates²³, is that they often express post-transcriptional regulators associated with germline development (for example, *vasa*, *piwi*, *tudor* and *nanos*). Although *vasa*-like genes have been reported in *Schistosoma*, no true *vasa* orthologue has been identified²⁴. Similarly, *piwi* and *tudor* genes seem to be absent from schistosomes (data not shown). However, we identified a *nanos* orthologue (*S. mansoni nanos-2* (*Smnanos-2*)) that was downregulated in somatic tissue after irradiation (Supplementary Fig. 4 and Supplementary Table 1). Because these genes represented potential regulators of PSC behaviour and could serve as useful markers for these cells, we examined their expression by whole-mount *in situ* hybridization. We detected *Smago2-1*, *Smnanos-2* and *SmfgrA* transcripts in cells scattered throughout the mesenchyme (Fig. 2d and Supplementary Fig. 5) in a pattern similar to that of cells incorporating EdU (Fig. 1a). This mesenchymal expression was radiation sensitive (Fig. 2d), indicating that these genes are expressed in proliferating cells. Consistent with

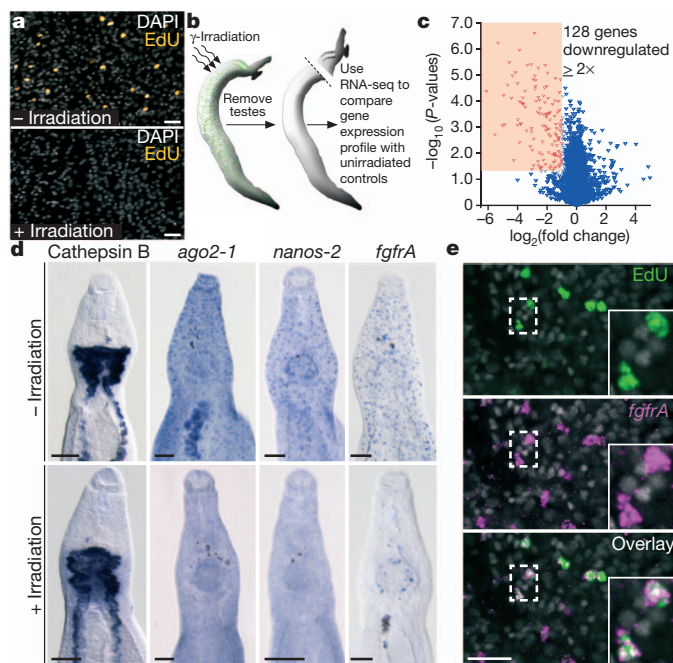


Figure 2 | Transcriptional profiling identifies genes expressed in proliferative cells. **a**, EdU incorporation is abrogated at d3 after irradiation. **b**, Strategy to identify PSC-expressed genes. **c**, Volcano plot showing expression differences in control versus irradiated parasites. $n = 3$ for each group. **d**, Whole-mount *in situ* hybridization for various transcripts in unirradiated and d5 post-irradiation parasites. $n > 3$ parasites. **e**, EdU labelling and FISH for *SmfgrA*. A total of 1,988 out of 2,000 EdU⁺ PSCs were *SmfgrA*⁺ after a 20–22-h pulse ($n = 20$ male parasites). **a**, **e** are confocal projections. Scale bars: **a**, **e**, 20 μ m; **d**, 100 μ m. Inset magnification, relative to original: **e**, $\times 2.6$.

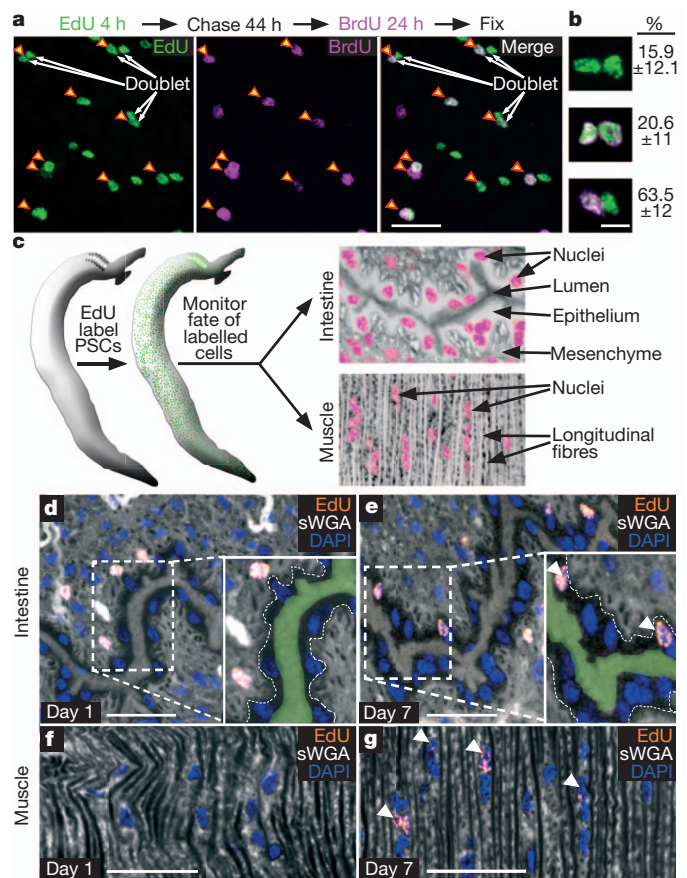


Figure 3 | PSCs self-renew and differentiate. **a**, EdU and BrdU double labelling. Arrowheads indicate EdU⁺BrdU⁺ nuclei. Arrows indicate EdU⁺ 'doublets'. **b**, Percentage (\pm s.d.) EdU⁺ doublets (green) that are BrdU⁻ (top), BrdU⁺-BrdU⁺ (middle, BrdU is magenta), or BrdU⁺-BrdU⁺ (bottom). $n = 21$ parasites. **c**, Strategy to monitor cellular differentiation. **d–g**, EdU and succinylated wheat germ agglutinin (sWGA) labelling showing EdU⁺ cells in male intestine (**d**, **e**) or dorsal musculature (**f**, **g**) at d1 (**d**, **f**) and d7 (**e**, **g**) following a pulse. Insets in **d**, **e**, show intestinal basal surface (dashed lines) and lumen (green). Arrowheads in **e** and **g** show EdU⁺ intestinal cells (**e**) or muscle cells (**g**). Images are confocal projections. Scale bars: **a**, **d–g**, 20 μ m; **b**, 5 μ m. Inset magnifications, relative to original: **d**, **e**, $\times 1.5$.

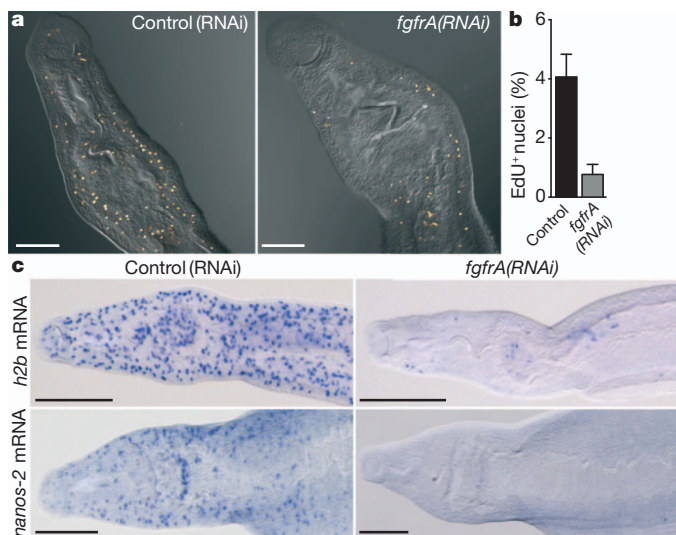


Figure 4 | *SmfgfrA* is required for the maintenance of somatic stem cells. **a**, EdU labelling and DIC images in control and *SmfgfrA*(RNAi) parasites at RNAi d17. **b**, Percentage of EdU⁺ nuclei/total nuclei in dissociated tissues from control (RNAi) ($n = 3,002$ nuclei) and *SmfgfrA*(RNAi) ($n = 3,642$ nuclei) parasites. Error bars indicate 95% confidence intervals, $P < 0.0001 \chi^2$. **c**, Whole-mount *in situ* hybridization for histone h2b (top row) and *Smnanos-2* (bottom row) transcripts in control (left column) versus *SmfgfrA*(RNAi) (right column) parasites at RNAi d20–21. $n > 5$ parasites per experiment. Scale bars: **a**, 100 μm ; **c**, 200 μm .

this idea, we found that after an EdU pulse, >99% of EdU-incorporating somatic cells also expressed *SmfgfrA* (Fig. 2e).

To determine whether PSCs are stem cells, we assessed their ability both to self-renew and to produce differentiated cell types. To examine self-renewal, we administered sequential pulses of EdU and 5-bromo-2'-deoxyuridine (BrdU) to parasites *in vitro*. Because nearly all PSCs that incorporate EdU are *SmfgfrA*⁺, the ability of EdU⁺ cells to incorporate BrdU in subsequent cell cycles would suggest that *fgfrA*⁺ PSCs self-renew (that is, divide and produce more *fgfrA*⁺ PSCs). For these experiments we chose a chase period of 44 h, as this time frame should give many EdU⁺ PSCs sufficient time to divide (Supplementary Fig. 3d). Consistent with PSCs possessing the capacity for self-renewal, we found that 41% of cells that initially incorporate EdU are BrdU⁺ 3 days after an initial EdU pulse (Fig. 3a). Furthermore, we observed that many EdU⁺ cells were distributed in pairs, or 'doublets' (Fig. 3a); we suggest that most of these doublets are the products of cell division (Supplementary Discussion and Supplementary Fig. 6). In these EdU⁺ doublets, a disproportionately large fraction displayed asymmetric BrdU incorporation (that is, one nucleus is EdU⁺BrdU⁺, whereas the other is EdU⁺BrdU⁻) (Fig. 3b and Supplementary Discussion). This observation suggests that division progeny have an asymmetric capacity to proliferate. Whether this represents stem-cell-like asymmetric division or temporal differences in the ability of these cells to re-enter the cell cycle requires further experimentation. Nevertheless, these data are consistent with PSCs (or some PSC subpopulation) being capable of self-renewal.

To examine the capacity of PSCs to differentiate, we performed EdU pulse-chase experiments *in vivo*. For these experiments, schistosome-infected mice were injected with EdU and the distribution of EdU⁺ cells was monitored at early (day (d) 1) and late (d7) time points (Fig. 3c). We successfully used this pulse-chase approach to monitor the differentiation of schistosome germ cells (Supplementary Fig. 7). Visualizing the syncytial epithelium of the schistosome intestine at d1, we did not observe EdU⁺ intestinal nuclei in male or female parasites (Fig. 3d, 0 EdU⁺/3,151 DAPI⁺ nuclei, 14 mixed sex parasites, $n = 5$ mice), confirming that cells in the intestine do not proliferate. After a 7-day chase, however, ~2.5% of the intestinal nuclei were EdU⁺

(Fig. 3e, 56 EdU⁺/2,189 DAPI⁺ nuclei, 10 mixed sex parasites, $n = 3$ mice). This observation suggests that cells initially labelled with EdU have the capacity to migrate into the intestine and differentiate into new intestinal cells. Similarly, we were able to monitor the differentiation of new cells in the body wall muscles. At d1 no EdU⁺ nuclei were observed in the male body wall musculature (Fig. 3f, 0 EdU⁺/1,882 DAPI⁺ nuclei, 13 male parasites, $n = 6$ mice), whereas at d7 ~10% of the muscle cell nuclei were EdU⁺ (Fig. 3g, 55 EdU⁺/584 DAPI⁺ nuclei, 6 male parasites, $n = 3$ mice). Because virtually all cells that initially incorporate EdU are *SmfgfrA*⁺, we suggest that these double-positive cells probably represent the only source of new intestinal and muscle cells and, thus, represent a collectively multipotent population of neoblast-like stem cells. Whether all *SmfgfrA*⁺ PSCs are multipotent or whether they exist as lineage-restricted progenitors remains unclear.

Although progress has been made in identifying transcriptional¹⁴ and post-transcriptional²² regulators of planarian neoblasts, little is known about the signal transduction networks functioning within these cells. Because the expression of FGF receptor family members in proliferative cells is conserved between planarians^{14,21} and schistosomes, we speculated that FGF signalling could regulate these cells in *S. mansoni*. To examine this idea, we disrupted *SmfgfrA* in *in vitro*-cultured adult parasites using RNA interference (RNAi) (Supplementary Fig. 8). We found that inhibition of *SmfgfrA* resulted in reduced EdU incorporation (Fig. 4a, b and Supplementary Table 2) and down-regulation of cell-cycle-associated transcripts (Fig. 4c and Supplementary Fig. 8). To resolve whether this effect is due to reduced cell proliferation or a failure to maintain neoblast-like cells, we monitored the expression of PSC markers *Smago2-1* and *Smnanos-2* in *SmfgfrA*(RNAi) parasites. *SmfgfrA* RNAi treatment resulted in a marked reduction in the number of cells expressing *Smnanos-2* (Fig. 4c) as well as significantly reduced mRNA levels for *Smago2-1* and *Smnanos-2* (Supplementary Fig. 8b). Together, these results indicate that *SmfgfrA* promotes the long-term maintenance of neoblast-like cells in *S. mansoni*. FGF signalling is known to influence multiple processes, such as cell proliferation, differentiation and survival; furthermore, it has key roles in various stem-cell populations²⁵. Our results suggest a conserved role for FGF signalling in controlling stem-cell behaviour in these parasites and demonstrate the feasibility of using RNAi to abrogate adult gene expression and manipulate neoblast-like cells in *S. mansoni*.

Adult schistosomes can modulate growth in response to host immune signals²⁶ and male–female pairing status²⁷ and they can regenerate damaged tissues after sublethal doses of the anti-schistosomal drug praziquantel²⁸. These observations reveal the developmental plasticity of schistosomes, and suggest that these parasites can use distinct developmental programs in response to a range of external stimuli. Future studies characterizing the role of neoblast-like cells in diverse contexts could address long-standing gaps in our knowledge of schistosome biology and may reveal novel therapeutic strategies for treating and eliminating schistosomiasis.

METHODS SUMMARY

EdU detection in adult parasites was performed using Alexa 488 azide (Invitrogen) as described previously¹⁰. To observe the morphology of PSCs, single-cell suspensions were obtained by incubating minced male parasites in trypsin-EDTA (Sigma); cell suspensions were fixed in 4% formaldehyde and spread on microscope slides. For *in situ* hybridizations, parasites were fixed in 4% formaldehyde for 4.5 h and processed essentially as described previously²⁹. Immunofluorescence and histological staining were performed similar to previous studies³⁰. For transcriptional profiling, male parasites were γ -irradiated, cultured *in vitro* for 48 h and processed for RNA-seq (Illumina). Transcriptional differences between irradiated and mock-irradiated controls were assessed using CLC Genomics Workbench (version 4, CLC Bio). For RNAi, *in vitro* cultured parasites were soaked with dsRNA (20–30 $\mu\text{g ml}^{-1}$) freshly added on days 1–3 and every 5–6 days thereafter. A 1.5-kb dsRNA derived from an irrelevant bacterial sequence was used as a negative control. Experiments with and care of vertebrate animals were performed in accordance with protocols approved by the Institutional Animal Care and Use

Committee (IACUC) of the University of Illinois at Urbana-Champaign (protocol approval number 10035).

Full Methods and any associated references are available in the online version of the paper.

Received 3 September 2012; accepted 18 January 2013.

Published online 20 February 2013.

1. Chitsulo, L., Engels, D., Montresor, A. & Savioli, L. The global status of schistosomiasis and its control. *Acta Trop.* **77**, 41–51 (2000).
2. Basch, P. F. *Schistosomes: Development, Reproduction, and Host Relations* (Oxford Univ. Press, 1991).
3. Wagner, D. E., Wang, I. E. & Reddien, P. W. Clonogenic neoblasts are pluripotent adult stem cells that underlie planarian regeneration. *Science* **332**, 811–816 (2011).
4. Newmark, P. A. & Sánchez Alvarado, A. Not your father's planarian: a classic model enters the era of functional genomics. *Nature Rev. Genet.* **3**, 210–219 (2002).
5. Brehm, K. *Echinococcus multilocularis* as an experimental model in stem cell research and molecular host-parasite interaction. *Parasitology* **137**, 537–555 (2010).
6. Protasio, A. V. *et al.* A systematically improved high quality genome and transcriptome of the human blood fluke *Schistosoma mansoni*. *PLoS Negl. Trop. Dis.* **6**, e1455 (2012).
7. Berriman, M. *et al.* The genome of the blood fluke *Schistosoma mansoni*. *Nature* **460**, 352–358 (2009).
8. Den Hollander, J. E. & Erasmus, D. A. *Schistosoma mansoni*: DNA synthesis in males and females from mixed and single-sex infections. *Parasitology* **88**, 463–476 (1984).
9. Nollen, P. M., Floyd, R. D., Kolzow, R. G. & Deter, D. L. The timing of reproductive cell development and movement in *Schistosoma mansoni*, *S. japonicum*, and *S. haematobium*, using techniques of autoradiography and transplantation. *J. Parasitol.* **62**, 227–231 (1976).
10. Salic, A. & Mitchison, T. J. A chemical method for fast and sensitive detection of DNA synthesis *in vivo*. *Proc. Natl Acad. Sci. USA* **105**, 2415–2420 (2008).
11. Newmark, P. A. & Sánchez Alvarado, A. Bromodeoxyuridine specifically labels the regenerative stem cells of planarians. *Dev. Biol.* **220**, 142–153 (2000).
12. Forsthoefel, D. J., Park, A. E. & Newmark, P. A. Stem cell-based growth, regeneration, and remodeling of the planarian intestine. *Dev. Biol.* **356**, 445–459 (2011).
13. Baguña, J. & Romero, R. Quantitative analysis of cell types during growth, degrowth and regeneration in the planarians *Dugesia mediterranea* and *Dugesia tigrina*. *Hydrobiologia* **84**, 181–194 (1981).
14. Wagner, D. E., Ho, J. J. & Reddien, P. W. Genetic regulators of a pluripotent adult stem cell system in planarians identified by RNAi and clonal analysis. *Cell Stem Cell* **10**, 299–311 (2012).
15. Solana, J. *et al.* Defining the molecular profile of planarian pluripotent stem cells using a combinatorial RNAseq, RNA interference and irradiation approach. *Genome Biol.* **13**, R19 (2012).
16. Eisenhoffer, G. T., Kang, H. & Sánchez Alvarado, A. Molecular analysis of stem cells and their descendants during cell turnover and regeneration in the planarian *Schmidtea mediterranea*. *Cell Stem Cell* **3**, 327–339 (2008).
17. Caffrey, C. R., McKerrow, J. H., Salter, J. P. & Sajid, M. Blood 'n' guts: an update on schistosome digestive peptidases. *Trends Parasitol.* **20**, 241–248 (2004).
18. Onal, P. *et al.* Gene expression of pluripotency determinants is conserved between mammalian and planarian stem cells. *EMBO J.* **31**, 2755–2769 (2012).
19. Labbé, R. M. *et al.* A comparative transcriptomic analysis reveals conserved features of stem cell pluripotency in planarians and mammals. *Stem Cells* **30**, 1734–1745 (2012).
20. Pearson, B. J. & Sánchez Alvarado, A. A planarian p53 homolog regulates proliferation and self-renewal in adult stem cell lineages. *Development* **137**, 213–221 (2010).
21. Ogawa, K. *et al.* Planarian fibroblast growth factor receptor homologs expressed in stem cells and cephalic ganglia. *Dev. Growth Differ.* **44**, 191–204 (2002).
22. Rouhana, L., Shibata, N., Nishimura, O. & Agata, K. Different requirements for conserved post-transcriptional regulators in planarian regeneration and stem cell maintenance. *Dev. Biol.* **341**, 429–443 (2010).
23. Juliano, C. & Wessel, G. Versatile germline genes. *Science* **329**, 640–641 (2010).
24. Skinner, D. E. *et al.* Vasa-like DEAD-box RNA helicases of *Schistosoma mansoni*. *PLoS Negl. Trop. Dis.* **6**, e1686 (2012).
25. Lanner, F. & Rossant, J. The role of FGF/Erk signaling in pluripotent cells. *Development* **137**, 3351–3360 (2010).
26. Davies, S. J. *et al.* Modulation of blood fluke development in the liver by hepatic CD4⁺ lymphocytes. *Science* **294**, 1358–1361 (2001).
27. Severinghaus, A. E. Sex studies on *Schistosoma japonicum*. *Q. J. Microsc. Sci.* **71**, 653–702 (1928).
28. Shaw, M. K. & Erasmus, D. A. *Schistosoma mansoni*: structural damage and tegumental repair after *in vivo* treatment with praziquantel. *Parasitology* **94**, 243–254 (1987).
29. Collins, J. J. III *et al.* Genome-wide analyses reveal a role for peptide hormones in planarian germline development. *PLoS Biol.* **8**, e1000509 (2010).
30. Collins, J. J. III, King, R. S., Cogswell, A., Williams, D. L. & Newmark, P. A. An atlas for *Schistosoma mansoni* organs and life-cycle stages using cell type-specific markers and confocal microscopy. *PLoS Negl. Trop. Dis.* **5**, e1009 (2011).

Supplementary Information is available in the online version of the paper.

Acknowledgements We thank R. Roberts-Galbraith, M. Issigonis and L. Rouhana for comments on the manuscript; R. King for sharing the cathepsin B plasmid and unpublished protocols; and A. Hernandez for assistance with Illumina sequencing. Schistosome-infected mice were provided by the NIAID Schistosomiasis Resource Center and the Biomedical Research Institute through NIAID contract no. HHSN2722010000051. This work was supported by: NIH F32 HD062124 (J.J.C.) and NIH R21 AI099642 (P.A.N.). P.A.N. is an investigator of the Howard Hughes Medical Institute.

Author Contributions J.J.C., B.W., B.G.L., M.E.T. and H.I. performed experiments. J.J.C. and B.W. analysed data. J.J.C. and P.A.N. designed the study and wrote the paper.

Author Information RNA-seq analyses have been deposited in the NCBI Gene Expression Omnibus under accession number GSE42757. Reprints and permissions information is available at www.nature.com/reprints. The authors declare no competing financial interests. Readers are welcome to comment on the online version of the paper. Correspondence and requests for materials should be addressed to P.A.N. (pnewmark@life.illinois.edu).

METHODS

Parasite acquisition and culture. Adult *S. mansoni* (6–8 weeks after infection) were obtained from infected mice by hepatic portal vein perfusion³¹ with 37 °C DMEM (Mediatech) plus 5% fetal calf serum (FBS, Hyclone/Thermo Scientific Logan). Parasites were rinsed several times in DMEM + 5% FBS and cultured (37 °C/5% CO₂) in Basch's Medium 169 (ref. 32) and 1× antibiotic-antimycotic (Gibco/Life Technologies). Media was changed every 1–3 days.

EdU labelling. For *in vitro* labelling, parasites were cultured in Basch's Medium 169 supplemented with 10 µM EdU (Invitrogen) diluted from a 10 mM stock in DMSO. Unless otherwise noted, animals were pulsed for 18–24 h. For *in vivo* labelling, schistosome-infected mice (6–8 weeks after infection) were given a single intraperitoneal injection (100–200 mg EdU per kg body weight) with 5 mg ml⁻¹ EdU dissolved in PBS and then collected at various time points after injection.

In situ hybridization. Male and female parasites were separated by incubation (2–3 min) in a 0.25% solution of the anaesthetic ethyl 3-aminobenzoate methanesulphonate (Sigma-Aldrich) dissolved in Basch's Medium 169 or phosphate buffered saline (PBS). Relaxed parasites were then killed in a 0.6 M solution of MgCl₂ and fixed for 4.5 h in 4% formaldehyde dissolved in PBSTx (PBS + 0.3% Triton X-100). After fixation, parasites were dehydrated in MeOH and stored at -20 °C. Samples were rehydrated by incubation in 1:1 MeOH:PBSTx followed by incubation in PBSTx. Rehydrated samples were bleached for 1–2 h in formaldehyde bleaching solution (0.5% Formamide, 0.5% SSC, and 1.2% H₂O₂), rinsed with PBSTx, treated with proteinase K (2–10 µg ml⁻¹, Invitrogen) for 20–30 min at room temperature and post-fixed for 10–15 min in 4% formaldehyde in PBSTx. Samples were hybridized at 52–55 °C and otherwise processed as previously described^{29,33}. Plasmids used for riboprobe synthesis were generated as described previously²⁹ using oligonucleotide primers listed in Supplementary Table 3.

Immunofluorescence, histological staining and EdU detection. Parasites were relaxed, killed, fixed, dehydrated and rehydrated as described above and bleached in 6% H₂O₂ dissolved in PBS for 0.5–2 h. Dehydration and bleaching were omitted for samples labelled with phalloidin. Samples were then treated with Proteinase K and post-fixed as described above. Immunofluorescence, lectin and phalloidin staining were performed as described previously³⁰. Rabbit anti-phospho-histone H3 Ser 10 (anti-pH3) (D2C8, Cell Signaling), rhodamine-conjugated sWGA (Vector Laboratories), and Alexa Fluor 568 phalloidin (Invitrogen) were used at 1:1,000, 1:100 and 1:100, respectively. EdU detection was performed essentially as previously described^{10,34} with 100 µM Alexa Fluor 488 or Alexa Fluor 594 azide conjugates. All imaging was performed as described previously^{29,30}. To quantify intestinal cell differentiation, the number of EdU⁺ and DAPI⁺ intestinal nuclei were determined from 12 consecutive confocal sections imaged from the intestine. To quantify muscle cell differentiation, the number of EdU⁺ and DAPI⁺ nuclei were determined from 4 to 9 consecutive confocal sections through the dorsal muscle layer of male parasites.

Tissue dissociation and EdU detection. After an overnight pulse with 10 µM EdU, the heads and testes of adult male *S. mansoni* were removed and the remaining tissue added to dissociation solution (Hanks Balanced Salt Solution with 3.5× trypsin-EDTA (from 10× stock, Sigma-Aldrich)) and minced with a razor blade. These tissue fragments were incubated in ~4 ml of dissociation solution for 45–60 min at room temperature on a rocker and gentle pipetting was used to break up large tissue fragments. This mixture was passed over two sets of cell strainers (100 and 40 µm, BD) and dissociated cells were collected by centrifugation (250g for 5 min). Pelleted cells were fixed in 4% formaldehyde in PBS for 30 min, spotted on Superfrost Plus microscope slides (Fisher Scientific), permeabilized for 30 min with PBSTx, and EdU was detected as described above with 10 µM Alexa Fluor 488 azide.

To quantify the ratio of EdU⁺ to total DAPI⁺ nuclei in RNAi knockdowns, eight male parasites were processed as above and tiled images of EdU and DAPI labelling were captured on a Zeiss LSM 710 (Plan-Apochromat 20x/0.8). Numbers of EdU⁺ and DAPI⁺ nuclei were quantified using the Image-based Tool for Counting Nuclei (ITCN) plugin for ImageJ³⁵.

γ-Irradiation and transcriptional profiling. Parasites (d43 after infection) were collected from mice, suspended in Basch medium 169, and exposed to 200 Gy of γ-irradiation using a Gammacell-220 Excel with a Co⁶⁰ source (Nordion). Control parasites were mock irradiated. Parasites were cultured in Basch Medium 169 and 48 h after irradiation males were separated from female parasites using ethyl 3-aminobenzoate methanesulphonate. After separation, the head and testes of males were removed and purified total RNA was prepared from the remaining tissue from pools of 14–18 parasites using Trizol (Invitrogen) and DNase treatment (DNA-free

RNA kit, Zymo Research). Three independent biological replicates were performed for both control and irradiated experimental groups. Individually tagged libraries for RNA-seq were prepared (TruSeq RNaseq Sample prep kit, Illumina), pooled in a single lane, and 100-bp reads were generated using an Illumina HiSeq2000. Library preparation and Illumina sequencing were performed at the W.M. Keck Center for Comparative and Functional Genomics. The resulting reads were mapped to the annotated *S. mansoni* genome⁶ (v5.0) and differences in gene expression were determined using CLC Genomics Workbench (CLC bio). Statistical enrichment of Gene Ontology terms was determined in CLC Genomics Workbench using a hypergeometric test that is similar to the GStat test described in previous studies³⁶. To examine similarities between proteins encoded from irradiation-sensitive transcripts in *S. mansoni* and genes expressed in planarian neoblasts, we compared our schistosome data set with both neoblast-enriched and 'whole' transcriptomes^{14,15,18,19} using standalone tBLASTn. Schistosome proteins sharing no similarity to translated planarian mRNAs (e-value cutoff >1 × 10⁻⁵) were omitted from analysis. Assignment of whether protein pairs were orthologous, homologous, paralogous, or unrelated was assessed manually on an individual basis. Data and evidence supporting protein similarity are provided in Supplementary Table 1.

EdU/BrdU double labelling. Parasites labelled with 10 µM EdU and BrdU were fixed in Methacarn (6:3:1 methanol:chloroform:glacial acetic acid) or processed for *in situ* hybridization. After a 45-min 2N HCl treatment, EdU was detected and parasites were processed for anti-BrdU immunofluorescence (anti-BrdU 1:500, clone MoBU, Invitrogen). We observed no crossreactivity between this antibody and EdU.

To quantify the level of BrdU/EdU overlap and measure centre-to-centre distances between nuclei, three-dimensional confocal stacks from EdU/BrdU-labelled animals were re-sampled to give isotropic voxels, and subjected to Gaussian filtering and background-subtraction. Labelled nuclei were segmented with Imaris (Bitplane Inc.) using parameters empirically determined to minimize the need for manual corrections; typically, fewer than 5% of the total nuclei required correction. The three-dimensional coordinates of the nuclei were exported and analysed with MATLAB. Overlapping EdU- and BrdU-labelled nuclei were defined as nuclei with centre-to-centre distances <1 nuclear size (~4 µm). Statistical analyses were performed in Origin (OriginLab).

RNA interference. Although procedures have been previously described^{17,38}, RNAi experiments with adult parasites were based on methods optimized for schistosomula³⁹. Briefly, *in vitro* cultured parasites were soaked with 20–30 µg of dsRNA freshly added on days 1–3 and every 5–6 days thereafter. As a negative control, animals were soaked with dsRNA synthesized from the *ccdB* and *camR*-containing insert of pJC53.2 (ref. 29). dsRNA synthesis was performed as previously described²⁹. Sequences used to generate dsRNAs are provided in Supplementary Fig. 9. To measure mRNA levels, total RNA from control and knockdown parasites (~8 male posterior somatic fragments) was reverse transcribed (iScript cDNA Synthesis kit, Bio-Rad) and quantitative real-time PCR was performed on an Applied Biosystems Step One Plus instrument using GoTaq qPCR Master Mix with SYBR green (Promega). Transcript levels were normalized to the mRNA levels of proteasome subunit beta type-4 (*smp_056500*). Relative quantities were calculated using the ΔΔCt calculation in the Step One Plus software. Oligonucleotide primer sequences are listed in Supplementary Table 3.

- Lewis, F. Schistosomiasis. *Curr. Protoc. Immunol.* Ch. 19, Unit 19 11 (2001).
- Basch, P. F. Cultivation of *Schistosoma mansoni* *in vitro*. I. Establishment of cultures from cercariae and development until pairing. *J. Parasitol.* **67**, 179–185 (1981).
- Cogswell, A. A., Collins, J. J. III, Newmark, P. A. & Williams, D. L. Whole mount *in situ* hybridization methodology for *Schistosoma mansoni*. *Mol. Biochem. Parasitol.* **178**, 46–50 (2011).
- Neef, A. B. & Luedtke, N. W. Dynamic metabolic labeling of DNA *in vivo* with arabinosyl nucleosides. *Proc. Natl Acad. Sci. USA* **108**, 20404–20409 (2011).
- Abramoff, M. D., Magelhaes, P. J. & Ram, S. J. Image processing with ImageJ. *Biophotonics Int.* **11**, 36–42 (2004).
- Falcon, S. & Gentleman, R. Using GStats to test gene lists for GO term association. *Bioinformatics* **23**, 257–258 (2007).
- Skelly, P. J., Da'dara, A. & Harn, D. A. Suppression of *cathepsin B* expression in *Schistosoma mansoni* by RNA interference. *Int. J. Parasitol.* **33**, 363–369 (2003).
- Boyle, J. P., Wu, X. J., Shoemaker, C. B. & Yoshino, T. P. Using RNA interference to manipulate endogenous gene expression in *Schistosoma mansoni* sporocysts. *Mol. Biochem. Parasitol.* **128**, 205–215 (2003).
- Štefanić, S. *et al.* RNA interference in *Schistosoma mansoni* schistosomula: selectivity, sensitivity and operation for larger-scale screening. *PLoS Negl. Trop. Dis.* **4**, e850 (2010).

Dynamics extracted from fixed cells reveal feedback linking cell growth to cell cycle

Ran Kafri¹*, Jason Levy²*, Miriam B. Ginzberg¹, Seungeun Oh¹, Galit Lahav¹ & Marc W. Kirschner¹

Biologists have long been concerned about what constrains variation in cell size, but progress in this field has been slow and stymied by experimental limitations¹. Here we describe a new method, ergodic rate analysis (ERA), that uses single-cell measurements of fixed steady-state populations to accurately infer the rates of molecular events, including rates of cell growth. ERA exploits the fact that the number of cells in a particular state is related to the average transit time through that state². With this method, it is possible to calculate full time trajectories of any feature that can be labelled in fixed cells, for example levels of phosphoproteins or total cellular mass. Using ERA we find evidence for a size-discriminatory process at the G1/S transition that acts to decrease cell-to-cell size variation.

Size is an obvious and distinguishing feature of cells, characteristic of their physiology and pathology. A barrier to studying size control in mammalian cells is the inaccuracy in measuring size, growth rate, and the dynamics of pathways controlling growth and proliferation¹. To

overcome these obstacles we developed ERA, a procedure for extracting dynamics and regulatory relationships from a single image of a population of individual fixed cells. ERA makes use of the fact that, at steady state, the number of cells in any particular molecular state is related to the rate at which cells transit through that state². Using this method, we calculated the dynamics of cell growth and cell cycle progression and investigated the processes that limit size variation.

To determine precise cell cycle dynamics from a single image of fixed cells, we considered the fact that unsynchronized proliferating cells are often found to be in a quasi-steady state, in which the proportion of cells in each phase of the cell cycle is stable (Fig. 1). We determine cell cycle position by measuring the levels of both DNA and a fluorescent reporter of the geminin degron (mAG-hGem)³. In the context of the present study, mAG-hGem serves as a marker for the activity of the anaphase-promoting complex (APC) in its active APC^{Cdh1} form (hereafter termed APC for simplicity). The scatter plot in Fig. 1a demonstrates the well-known decrease in APC activity in late G1 (resulting in mAG-hGem accumulation), which is followed by doubling of DNA in S phase. Reactivation of APC at mitosis results in a sharp fall in mAG-hGem fluorescence followed by cytokinesis, during which DNA levels drop by one half (Fig. 1). For populations

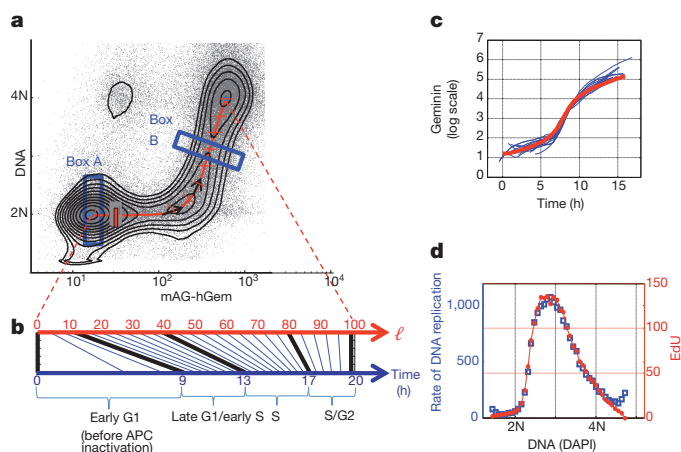


Figure 1 | Dynamic information from static data using ERA. **a**, Levels of DNA (DAPI) and geminin (mAG-hGem) in an unsynchronized, exponential population of HeLa cells. The black contour lines denote the distribution, f , of cells within the DNA/geminin plane. Also shown is the average cell cycle trajectory, ℓ (red). The different densities of cells in boxes A and B result from the different rates at which cells traverse those regions. **b**, The transformation of the cell cycle axis, ℓ , to a real-time axis. For convenience we chose 100 units of ℓ to represent a complete path from the beginning of G1 to the end of G2. **c**, **d**, Comparison of ERA with direct dynamical measurements. Accumulation of mAG-hGem was followed in ten individual live cells by time-lapse microscopy (blue lines) and compared to the dynamics of mAG-hGem calculated from fixed cells using ERA (red) (**c**). DNA-replication rate was measured by exposing cells to a 20-min pulse of EdU before fixation. Average levels of EdU fluorescence per cell (indicating rate of DNA replication) are plotted (blue) as a function of DAPI, giving a measure of the mean rate of DNA replication as a function of passage through S. For comparison, ERA was used to calculate DNA-replication rates directly from fixed cells not treated with EdU (red). N denotes number of chromosome sets.

BOX 1

The ERA balance equation

ERA rests on the fact that at steady state the difference, $-n_t \nabla \cdot (fv)$, between the rates at which cells enter and leave any given molecular state must be balanced by the increase in cell count in that state. n_t is the total number of cells in the population at time t , f is the proportion of cells in the given state (indicated by the black contour lines in Fig. 1a), and v is the rate at which cells pass through that state. As f does not change with time, the number of cells at any given state as a function of time is $fn_t = fn_0 e^{\alpha t}$. These considerations result in a simple balance equation:

$$-\nabla \cdot (fv) + B = \alpha f \quad (1)$$

in which α is the proportion of cells dividing per unit time and B is a term accounting for cell division (see Supplementary Materials). As we will show, equation (1) can be used to derive accurate time profiles from a single measurement on a population of fixed cells. If more parameters are measured, the dimensionality of the plot increases but the analyses remain the same.

Equation (1) is free of any mechanistic assumptions or free variables and is grounded only on a basic conservation principle akin to conservation of mass. Equation (1) and its implementations throughout this study are based on two main assumptions outlined in detail in the Supplementary Materials: (1) the representation axes (which in the present study are DNA and APC activity) appropriately represent both individual and collective cell behaviour; and (2) the steady-state assumptions described above apply.

¹Department of Systems Biology, Harvard Medical School, Boston, Massachusetts 02115, USA. ²Department of Mathematics and Statistics, University of Ottawa, Ottawa, Ontario K1N 6N5, Canada.

*These authors contributed equally to this work.

12 h after fixation that have not reached confluence, the distribution, f , of cells in the plane defined by these two measurements is independent of the time at which cells were sampled and fixed, as shown in Supplementary Materials. The existence of a stationary-state condition imposes a quantitative relationship between the proportion of cells in different regions of the plot and the rates of molecular events (that is, changes in DNA and APC activity). For example, in Fig. 1, because every cycling cell passes through the labelled regions A and B, the higher cell count in region A must mean that cells traverse this region at slower rates than in region B (see Box 1).

Our goal in this study was to use equation (1) (Box 1) to determine the growth rate of cells at different points in the cell cycle; in other words to solve for v . To solve equation (1) we reduced the number of dimensions from DNA (first dimension) and APC activity (second dimension) to a single dimension, ℓ , representing cell cycle progression over time (see Box 2). Although ℓ is not directly measured, it can be calculated from f , which is obtained experimentally (see Supplementary Materials). Figure 1a shows ℓ (red curve) superimposed on the single-cell measurements.

Figure 1c compares mAG-hGem dynamics of live cells obtained from time-lapse microscopy to dynamics of fixed cells calculated by ERA. There is near-perfect agreement. To further demonstrate the utility of ERA, we compared the rate of DNA replication obtained by labelling live cells with 5-ethynyl-2'-deoxyuridine (EdU) to the rate of DNA replication obtained by ERA of 4',6-diamidino-2-phenylindole (DAPI)-stain intensity in fixed cells (Fig. 1d). As with the previous example, we obtained a considerable overlap between the measurements. Both examples show that ERA calculations can resolve dynamics to a timescale on the order of minutes.

To characterize cell-growth dynamics during the cell cycle we quantified the protein mass of individual cells by measuring the total fluorescence intensity from cells stained with a succinimidyl ester dye (Alexa Fluor 647 succinimidyl ester; SE-A647), which covalently reacts

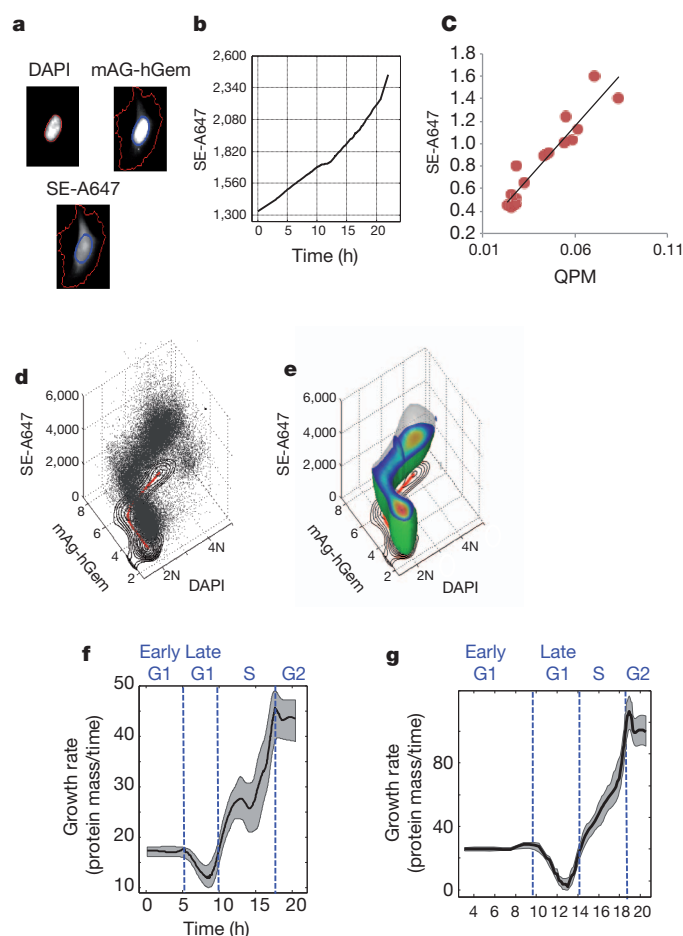


Figure 2 | Calculation of growth as a function of cell cycle progression using ERA. **a**, Cells were stained and imaged for DNA content (DAPI), the geminin degen (mAG-hGem) and for protein content (SE-A647). **b**, Growth during cell cycle progression, computed by ERA. **c**, Comparison of SE-A647 fluorescence intensity with quantitative phase microscopy measurements in single cells. Each data point represents a single cell measured for both protein content (SE-A647) and phase retardation (QPM). **d**, A scatter plot for the levels of DNA (DAPI), geminin (mAG-hGem) and cell size (SE-A647) in an unsynchronized population of HeLa cells. Also shown is the projection of the two-dimensional distribution of geminin and DNA overlaid with ℓ . **e**, The three-dimensional probability distribution from the data shown in **d**. **f, g**, Growth rate versus time for HeLa cells (**f**) and retinal pigment epithelial (RPE1) cells (**g**) calculated by ERA. Confidence intervals (grey) of ± 1 standard error are shown as described in Supplementary Materials.

BOX 2

Reducing the dimensionality of equation (1)

Confining equation (1) to the cell cycle trajectory, ℓ , and integrating results in an expression (equation (2)) that relates measured probability density, f , to the rate of progression through the cell cycle, ω , we have:

$$\omega(\ell) = \alpha \frac{2 - F(\ell)}{f(\ell)} \quad (2)$$

in which $F(\ell) = \int_1^\ell f(\ell) d\ell$. Furthermore, because $\omega(\ell) \equiv \frac{d\ell}{dt}$, we can use results of equation (2) to calculate a complete time axis for the dynamics of the measured processes using:

$$t(\ell_0) = \int_{\ell=1}^{\ell_0} \frac{1}{\omega} d\ell \quad (3)$$

in which $t(\ell_0)$ is the time it takes for a cell starting at position $\ell = 1$ (G1) to reach position ℓ_0 on the cell cycle axis, ℓ . As shown in Fig. 1, equations (1)–(3) transform a single, non-temporal measurement on fixed cells into temporal trajectories represented on time axis, t . Figure 1b shows the nonlinear transformation (the ERA transform) of a path, ℓ , defined by molecular events, onto a time axis. We conveniently chose 100 units of ℓ to represent a complete path from G1 to G2. We do not include M (metaphase) in this analysis because the number of cells in M is very small. Real time enters this calculation through the doubling time of the population, $\tau = \frac{\log(2)}{\alpha}$. For solutions of ERA in more than two dimensions see Supplementary Materials.

with lysyl groups. This is a good measure of protein mass⁴ and correlates well with physical measurements of dry mass by quantitative phase microscopy (QPM), which has accuracy of better than 1%⁵ (Fig. 2c). From these measurements, we assembled a three-dimensional single-cell data set simultaneously reporting cell size and cell cycle stage for millions of fixed cells (Fig. 2a, d, e). As expected, our data show an approximate doubling in protein fluorescence in a single cell cycle (Fig. 2b).

For four very different cell lines, the growth in mass during the cell cycle, as calculated by ERA, produced very similar trajectories that are neither linear nor exponential (Fig. 2f, g and Supplementary Materials). The results show that growth rates increase with progression through the cell cycle and reach a maximum during G2, consistent with a recent study using QPM⁶. What was previously unknown is a transient slowdown in protein-accumulation rate at the G1/S transition in all cell lines (Fig. 2f, g). Because this slowdown occurs for a relatively short time, it is not surprising that it was not detected in previous time-course measurements on synchronized populations. Further, by aligning cells using

molecular markers of cell cycle progression rather than time, ERA avoids the clouding effects of imperfect synchronization. Plots of growth rate as a function of mass are similar to those obtained recently with the suspended microchannel resonator⁷ (Supplementary Materials).

The existence of stable and narrow distributions of cell size suggests cell-autonomous feedbacks controlling size variability. To search for such feedbacks we calculated the joint dependency of growth rate, v , on size, s , and cell cycle position, ℓ (Fig. 3). The size distribution within any interval along the cell cycle path ℓ , $\Delta_\ell = (\ell - w, \ell + w)$, is governed exclusively by (Fig. 3a): (1) the size distribution of cells entering the interval from the previous cell cycle stage; (2) the size distribution of cells leaving the interval into a later cell cycle stage; and (3) cell growth within the interval. Such a formulation allows the construction of a three-term balance equation relating growth rate to cell size within the interval (see Box 3).

Figure 3b plots how v depends on s at three different points in the cell cycle; late G1 ($\ell = 20$), the G1/S transition ($\ell = 40$) and late S phase ($\ell = 80$). A notable result of this analysis is the shift to a negative slope of growth rate versus cell size for cells around the G1/S transition (see slope for $\ell = 40$). This negative slope is unexpected as it suggests that at this point small cells have higher growth rates than larger cells. This

BOX 3

Analysing growth as a function of size

To obtain the size distributions of cells entering and leaving a given interval we consider the size distributions of cells positioned at the borders of that interval (Fig. 3a). These distributions are formally approximated by the conditional probability distributions, $F(s|\ell - w)$ and $F(s|\ell + w)$, in which $F(s|\ell - w)$ is the cumulative probability distribution of cell size, s , among cells in the state $\ell - w$ at the entrance to the interval $\Delta_\ell = (\ell - w, \ell + w)$ (marked red in Supplementary Fig. 13), and similarly with $F(s|\ell + w)$. The width, $\Delta_\ell = 2w$, represents the resolution limit of the calculation. Using this construction we obtain an equation for the rate of cell growth as a function of cell size and cell cycle position:

$$v(s, \Delta_\ell) = \alpha \frac{(2 - \lambda_A)F(s|\ell - w) - (2 - \lambda_A - \lambda_B)F(s|\ell + w) - F(s|\Delta_\ell)\lambda_B}{f(s|\Delta_\ell)\lambda_B} \quad (4)$$

in which $F(s|\Delta_\ell) = F(s|(\ell - w, \ell + w))$ is the size distribution within the interval Δ_ℓ , λ_A is the fraction of cells occupying all cell cycle stages preceding Δ_ℓ , and λ_B is the fraction of cells in Δ_ℓ . We use the notations F and f to refer to cumulative and non-cumulative probability distributions, respectively. To further evaluate how the growth-rate/cell-size dependency relates to cell cycle progression, we translate ℓ along the cell cycle axis and repeatedly solve equation (4) for all points on ℓ .

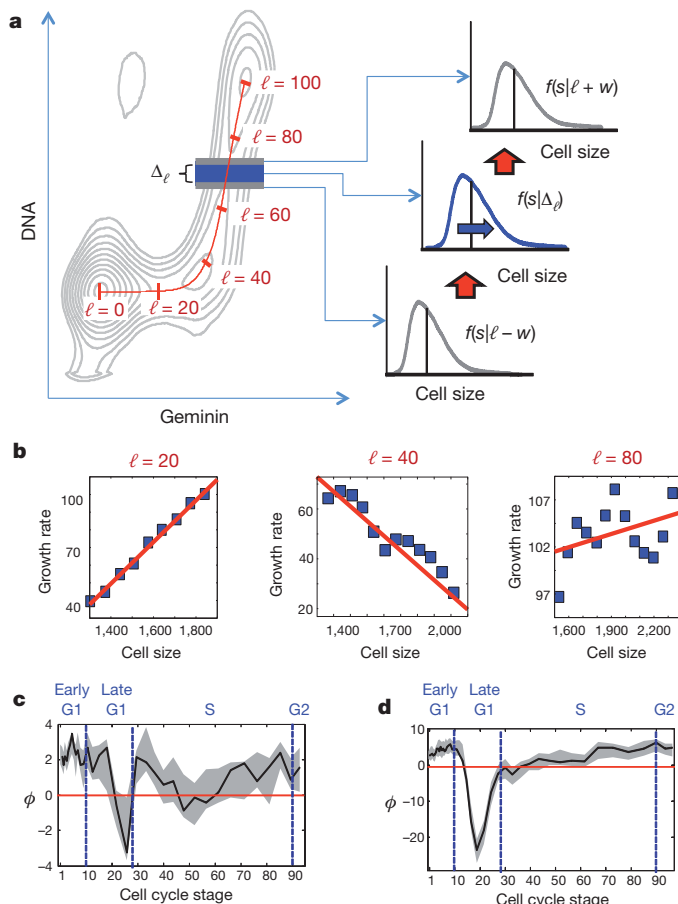


Figure 3 | Rate of cell growth as a function of size and cell cycle. Size discrimination at the G1/S transition. **a**, Calculation of growth rate as a function of size for a defined interval, Δ_ℓ , on the cell cycle axis, ℓ . To calculate feedback regulation as a function of cell size, the size distributions of cells entering and leaving Δ_ℓ are estimated from the sizes of cells on the boundary of Δ_ℓ . **b**, Plots of growth rate versus cell size at late G1 ($\ell = 20$), the G1/S transition ($\ell = 40$) and late S phase ($\ell = 80$). **c**, **d**, The slope, ϕ , of growth rate versus cell size plotted as a function of ℓ , for HeLa cells (**c**) and RPE1 cells (**d**). The red horizontal line positioned at $\phi = 0$ is added to emphasize the distinction between positive and negative slopes (positive and negative feedbacks). Blue vertical lines demarcate borders between different stages of cell cycle. Confidence intervals (grey): 90% in **c**; ± 1 standard deviation in **d**.

cell-size-dependent growth rate implies a negative feedback linking growth rate to cell size, effectively constraining cell-to-cell size variability in the population.

Figure 3c, d shows the slope, ϕ , of the growth rate versus cell size as a function of the cell cycle progression axis, ℓ . A positive ϕ implies that larger cells have higher growth rates than smaller cells, whereas a negative ϕ implies the opposite. $\phi = 0$ indicates that growth is independent of cell size. Calculating ϕ for four different cell lines (Fig. 3c, d and Supplementary Materials) yields feedback spectra that consistently acquire negative values at the G1/S transition.

The strict interpretation that cell size negatively feeds back on growth rate at G1/S depends on the assumption that progression along ℓ is independent of cell size (see Supplementary Materials). This is not the only possibility. An alternative interpretation is that size variation is limited not by repressing the growth rate of large cells but by inhibiting the rate at which small cells progress along the cell cycle. Whichever of these interpretations is correct, equation (4) identifies fingerprints of a cell-size discriminatory process, occurring at the G1/S transition, that distinguishes small and large cells and results in an increase in the homogeneity of cell size in the proliferating population. These results support very early findings suggesting cell-size regulation at the G1/S transition⁸.

To test further whether growth at G1/S is different for large and small cells, we treated HeLa cells for 1 h with a proteasome inhibitor (MG132), a translation inhibitor (cycloheximide), or an mTOR inhibitor (rapamycin). If growth rates and cell cycle progression were independent of cell size, both large and small cells would be equally affected by any treatment. Our results show that MG132 increased the variation in the size of cells at G1/S (Fig. 4b). Cycloheximide had the opposite effect (Fig. 4c). mTOR inhibition also decreased cell-to-cell size variability, but to a lesser extent than cycloheximide (Fig. 4d). These results indicate that the decrease in cell-size variance is at least partially driven by a cell-size discriminating proteasome activity. The possibility that size variation is further controlled by size-dependent translation activity seems less likely in light of the decreased size variation following cycloheximide treatment.

Proliferating cells in an unsynchronized population are distributed among different molecular states (that is, cell cycle stages). In situations in which this distribution does not change with time and in which

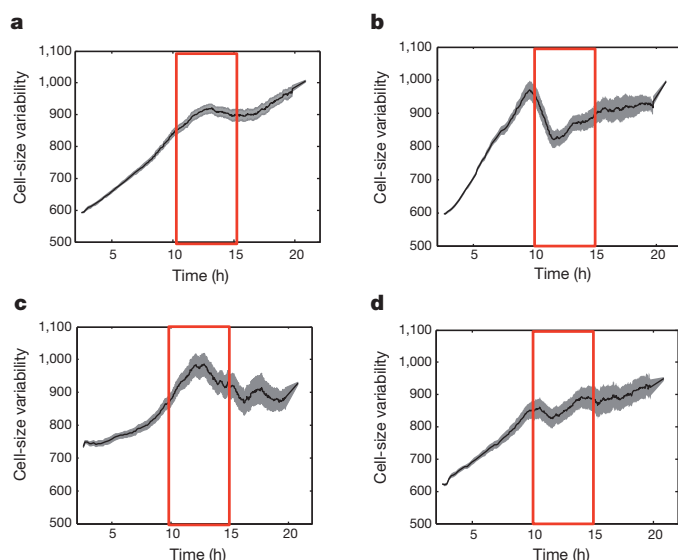


Figure 4 | Effects of drug treatments on size variability at G1 exit. Cell-size variability (full width/half maximum) as a function of cell cycle time for HeLa cells incubated for 1 h with 0.001 v/v dimethylsulphoxide (a), 1 μ M cycloheximide (b), 10 μ M MG132 (c) and 100 nM rapamycin (d). Confidence intervals are shown in grey.

individual cells shift from state to state in a defined sequence, it is possible to calculate dynamical features from simple static single-cell measurements^{9,10}, which may be obtained from microscopy or flow cytometry. We have shown that both our primary measurements and the functions derived from them are time invariant (see Supplementary Materials), thereby meeting these criteria. Others¹¹ previously suggested that data from fixed cells could, in principle, be used to extract dynamic information; we have now provided an explicit mathematical framework to make this analysis possible. Using ERA we show that cell-to-cell size variation is regulated by a negative feedback at the G1/S transition. We can also use ERA to characterize other dynamic processes that cannot in general be measured in real time in living cells, such as the temporal changes in phosphoproteins during the cell cycle (Supplementary Materials).

METHODS SUMMARY

Reagents, cells and antibodies are described in Supplementary Information. Cells were plated and fixed at 10^5 cells per ml in 15-cm dishes. They were fixed in

paraformaldehyde, permeabilized and stained with $0.04 \mu\text{g ml}^{-1}$ succinimidyl-ester-linked Alexa dyes diluted in DMSO (Alexa Fluor 647 carboxylic acid, succinimidyl ester; Invitrogen; A-21016). Slides were imaged with a Nikon Ti Inverted Fluorescence Microscope with Perfect Focus controlled by Nikon Elements software. We used the scan-slide function to image the full area of the slide at $\times 20$ magnification. Image analysis was performed with custom-written software (EnsembleThresher). The details of the software and the calculation of the ERA parameters are discussed in detail in Supplementary Information.

Received 30 December 2011; accepted 10 January 2013.

1. Mitchison, J. M. Growth during the cell cycle. *Int. Rev. Cytol.* **226**, 165–258 (2003).
2. Deen, W. M. *Analysis of Transport Phenomena* 2nd edn (Oxford University Press, 2012).
3. Sakaue-Sawano, A. et al. Visualizing spatiotemporal dynamics of multicellular cell-cycle progression. *Cell* **132**, 487–498 (2008).
4. Mitchison, J. M. *The Biology of the Cell Cycle* 128 (University Press, 1971).
5. Popescu, G. et al. Optical imaging of cell mass and growth dynamics. *Am. J. Physiol. Cell Physiol.* **295**, C538–C544 (2008).
6. Mir, M. et al. Optical measurement of cycle-dependent cell growth. *Proc. Natl Acad. Sci. USA* **108**, 13124–13129 (2011).
7. Son, S. et al. Direct observation of mammalian cell growth and size regulation. *Nature Methods* **9**, 910–912 (2012).
8. Killander, D. & Zetterberg, A. A quantitative cytochemical investigation of the relationship between cell mass and initiation of DNA synthesis in mouse fibroblasts *in vitro*. *Exp. Cell Res.* **40**, 12–20 (1965).
9. Hendrix, R. W. & Zwaan, J. Cell shape regulation and cell cycle in embryonic lens cells. *Nature* **247**, 145–147 (1974).
10. Tzur, A., Kafri, R., LeBleu, V. S., Lahav, G. & Kirschner, M. W. Cell growth and size homeostasis in proliferating animal cells. *Science* **325**, 167–171 (2009).
11. Jacobberger, J. W., Avva, J., Sreenath, S. N., Weis, M. C. & Stefan, T. Dynamic epitope expression from static cytometry data: principles and reproducibility. *PLoS ONE*, e30870 (2012).

Supplementary Information is available in the online version of the paper.

Acknowledgements We thank A. Klein, Y. Merbl, S. Tal and J. Toettcher for consistent and valuable insights at the beginning of and throughout this project. We thank J. Waters and the staff of The Nikon Imaging Center at Harvard Medical School for help and support. We especially thank R. Ward for her critique of the paper and the National Institute of General Medical Sciences (GM26875) for support of this work.

Author Contributions R.K. and J.L. developed the method (ERA) for extracting dynamic information and calculating feedback spectra from fixed populations, designed algorithms, wrote all image-processing software and analysed data. R.K. designed all experiments and wrote the manuscript. J.L. contributed significantly to all conceptual challenges and to writing the manuscript. M.B.G. contributed conceptually on levels of the study, made many important measurements and calculations and contributed to the writing of the manuscript. S.O. provided interferometry-derived cell mass measurements. G.L. and M.W.K. contributed to the formulation of the problem, development of the ideas and the writing of the manuscript.

Author Information Reprints and permissions information is available at www.nature.com/reprints. The authors declare no competing financial interests. Readers are welcome to comment on the online version of the paper. Correspondence and requests for materials should be addressed to M.W.K. (marc@hms.harvard.edu).

GLI activation by atypical protein kinase C ι/λ regulates the growth of basal cell carcinomas

Scott X. Atwood¹, Mischa Li¹, Alex Lee¹, Jean Y. Tang¹ & Anthony E. Oro¹

Growth of basal cell carcinomas (BCCs) requires high levels of hedgehog (HH) signalling through the transcription factor GLI¹. Although inhibitors of membrane protein smoothened (SMO) effectively suppress HH signalling, early tumour resistance illustrates the need for additional downstream targets for therapy^{1–6}. Here we identify atypical protein kinase C ι/λ (aPKC- ι/λ) as a novel GLI regulator in mammals. aPKC- ι/λ and its polarity signalling partners⁷ co-localize at the centrosome and form a complex with missing-in-metastasis (MIM), a scaffolding protein that potentiates HH signalling^{8,9}. Genetic or pharmacological loss of aPKC- ι/λ function blocks HH signalling and proliferation of BCC cells. *Prkci* is a HH target gene that forms a positive feedback loop with GLI and exists at increased levels in BCCs. Genome-wide transcriptional profiling shows that aPKC- ι/λ and SMO control the expression of similar genes in tumour cells. aPKC- ι/λ functions downstream of SMO to phosphorylate and activate GLI1, resulting in maximal DNA binding and transcriptional activation. Activated aPKC- ι/λ is upregulated in SMO-inhibitor-resistant tumours and targeting aPKC- ι/λ suppresses signalling and growth of resistant BCC cell lines. These results demonstrate that aPKC- ι/λ is critical for HH-dependent processes and implicates aPKC- ι/λ as a new, tumour-selective therapeutic target for the treatment of SMO-inhibitor-resistant cancers.

To identify new druggable targets in the HH pathway, we used the scaffold protein MIM, which potentiates GLI-dependent activation downstream of SMO (ref. 9), as bait in a biased proteomics screen of factors involved in HH signalling and ciliogenesis. Two of the hits were polarity proteins not previously linked to the HH pathway: aPKC- ι/λ , a serine/threonine kinase, and PARD3, a scaffolding protein and aPKC- ι/λ substrate (Supplementary Fig. 1a). Reciprocal immunoprecipitation of aPKC- ι/λ and PARD3 pulled down MIM, suggesting a specific interaction (Supplementary Fig. 1b). Because MIM is a centrosome-associated protein that promotes ciliogenesis⁸, we fractionated centrosomes and found that aPKC- ι/λ , along with PARD3 and PARD6A, co-fractionated and co-immunoprecipitated with MIM in γ -tubulin-positive fractions that mark centrosomes (Fig. 1a and Supplementary Fig. 1c). MIM partly co-localizes with aPKC- ι/λ -complex members at the basal body in dermal fibroblasts, keratinocytes and the well-characterized mouse BCC cell line ASZ001¹⁰ (Fig. 1b), where aPKC- ι/λ and MIM interact through co-immunoprecipitation (Fig. 1c). Loss of aPKC- ι/λ or MIM protein suppressed HH signalling, because messenger RNA (mRNA) levels of the HH target gene *Gli1* were reduced and ciliogenesis was inhibited (Fig. 1d, e and Supplementary Fig. 1d, e).

Because the kinase activity is necessary for many of the cellular functions of aPKC- ι/λ (refs 7, 11), we used a myristoylated aPKC

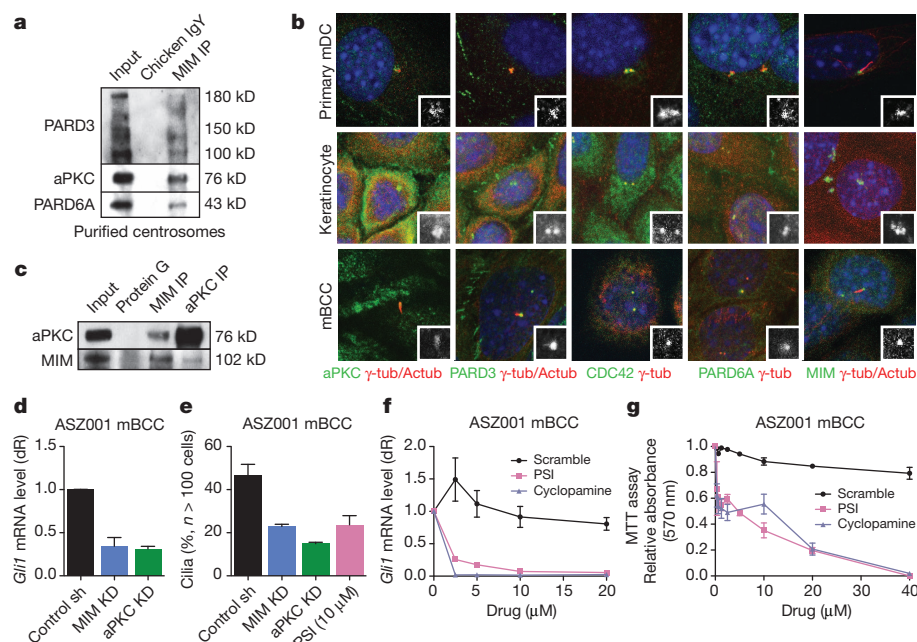


Figure 1 | aPKC- ι/λ is a centrosome-associated protein that regulates HH signalling. **a**, MIM and aPKC- ι/λ interact in purified centrosomes. IgY, immunoglobulin-Y. **b**, MIM and aPKC- ι/λ complexes localize at the centrosome (γ -tub, γ -tubulin) versus primary cilia (Actub, acetylated tubulin) of mouse dermal cells (mDC), mouse keratinocytes and mouse BCC cells (mBCC). **c**, MIM

and aPKC- ι/λ interact in BCC cells. **d–f**, *Gli1* mRNA levels ($n = 3$) or cilia percentage ($n = 3$) after *MIM* or aPKC- ι/λ short hairpin (sh) RNA knockdown, or aPKC or SMO inhibition in BCC cells. KD, knockdown. **g**, Cell proliferation was decreased in BCC cells ($n = 3$) after PSI or cyclopamine treatment, but not after treatment with myristoylated scrambled peptide. Error bars, s.e.m.

¹Program in Epithelial Biology, Stanford University School of Medicine, Stanford, California 94305, USA.

peptide inhibitor (PSI) to suppress kinase activity¹² (Supplementary Fig. 1f). PSI, but not a myristoylated scrambled peptide, inhibited HH signalling in BCC cells in a dose-dependent manner similar to the SMO antagonist cyclopamine (Fig. 1f). PSI, the pan-PKC inhibitor Go6983 and genetic loss of aPKC- ι/λ expression also resulted in dose-dependent inhibition of cell growth in BCC cells, leading to cell death according to MTT assay (Fig. 1g and Supplementary Fig. 1g, h). PSI inhibited BCC cell growth at a concentration similar to that of cyclopamine, with a half-maximal inhibitory concentration (IC_{50}) of 5 μ M. Primary cilia were reduced by 50% in PSI-treated BCC cells (Fig. 1e), indicating that aPKC activity is critical to both HH signalling and ciliogenesis in BCC cells. Interestingly, PSI did not affect proliferation in several non-tumorigenic cells (Supplementary Fig. 1i). PSI specifically inhibited aPKC, because loss of aPKC- ι/λ in BCC cells in combination with PSI treatment possessed no additional activity to reduce levels of *Gli1* or *Prkci* mRNA (Supplementary Fig. 1j).

To address whether the effects of aPKC- ι/λ on the HH pathway are direct, we assayed aPKC- ι/λ function in several nonpolar cell lines (Supplementary Fig. 1k, l and data not shown). These cells maintained their primary cilia or developed more after loss of aPKC- ι/λ ; however, aPKC- ι/λ removal still blocked HH activation, reducing target gene induction. We conclude that the effects of aPKC- ι/λ on HH signalling are cilia independent and are required for maximal sustained signalling.

aPKC- ι/λ is necessary for maximal HH signalling, and so we next investigated whether aPKC- ι/λ is overexpressed in BCCs. Indeed, *Prkci* expression, but not *Prkcz* expression, is specifically upregulated with *Gli1* in BCC cells (Fig. 2a). Similar results are found using freshly isolated human BCCs compared with primary human keratinocytes (Fig. 2b). Immunohistochemical staining of human BCCs and normal skin with antibodies recognizing both total and activated aPKC (P-aPKC) show higher levels in invasive and nodular tumours, with P-aPKC showing greater overexpression (Fig. 2c). Loss of aPKC- ι/λ removes both aPKC and P-aPKC staining in primary mouse dermal cells, indicating the specificity of the antibody (Supplementary Fig. 2).

Because aPKC- ι/λ and HH signalling are required for BCC cell growth, we then asked whether *Prkci* is a HH target gene. Activation of HH signalling in both polarized and non-polarized primary and immortalized cells using SHH-N ligand (the amino-terminal fragment of SHH) induces both *Gli1* and *Prkci* transcripts, but not *Prkcz* (Fig. 2d). Additionally, when we block HH signalling by treating BCC cells with cyclopamine, *Gli1* and *Prkci* transcripts, but not *Prkcz*, are specifically suppressed (Fig. 2g). Three putative GLI1-binding sites¹³ are present in the promoter region within 5 kilobases of the *Prkci* transcriptional start site in mice (Fig. 2e). Chromatin immunoprecipitation (ChIP) with BCC cells overexpressing FLAG:GLI1 enrich in regions containing the three GLI1-binding sites (Fig. 2f), indicating that *Prkci* is a direct target of GLI1. The first two GLI1-binding sites promote expression of luciferase when expressed in BCC cells, suggesting that these sites are functional (Supplementary Fig. 3). In addition, expression of *Pard6a* (aPKC- ι/λ inhibitor) is reduced whereas *Cdc42* (activator) is overexpressed in primary mouse BCC tumours¹⁴ (Fig. 2h). Because aPKC- ι/λ is typically found in an inhibited PARD6A complex, less PARD6A would result in excessive free and active aPKC- ι/λ whereas more CDC42 would activate any existing PARD6A-aPKC- ι/λ complexes. Interestingly, when HH signalling is inhibited with the SMO antagonist SANT-1, *Pard6a* transcript levels are increased and *Cdc42* levels are decreased (Fig. 2i), further supporting the idea that HH signalling promotes aPKC- ι/λ activation. We conclude that aPKC- ι/λ is part of a HH-mediated positive feedback loop leading to its overexpression in human and mouse BCCs.

To gain insight into aPKC- ι/λ 's mechanism of action, we determined whether aPKC- ι/λ -dependent genes in tumours differed from those regulated by SMO. We treated BCC cells with SANT-1 or PSI and performed 3'-end polyadenylated RNA sequencing. We found that the expression level of 5,700 SANT-1-dependent and 4,762

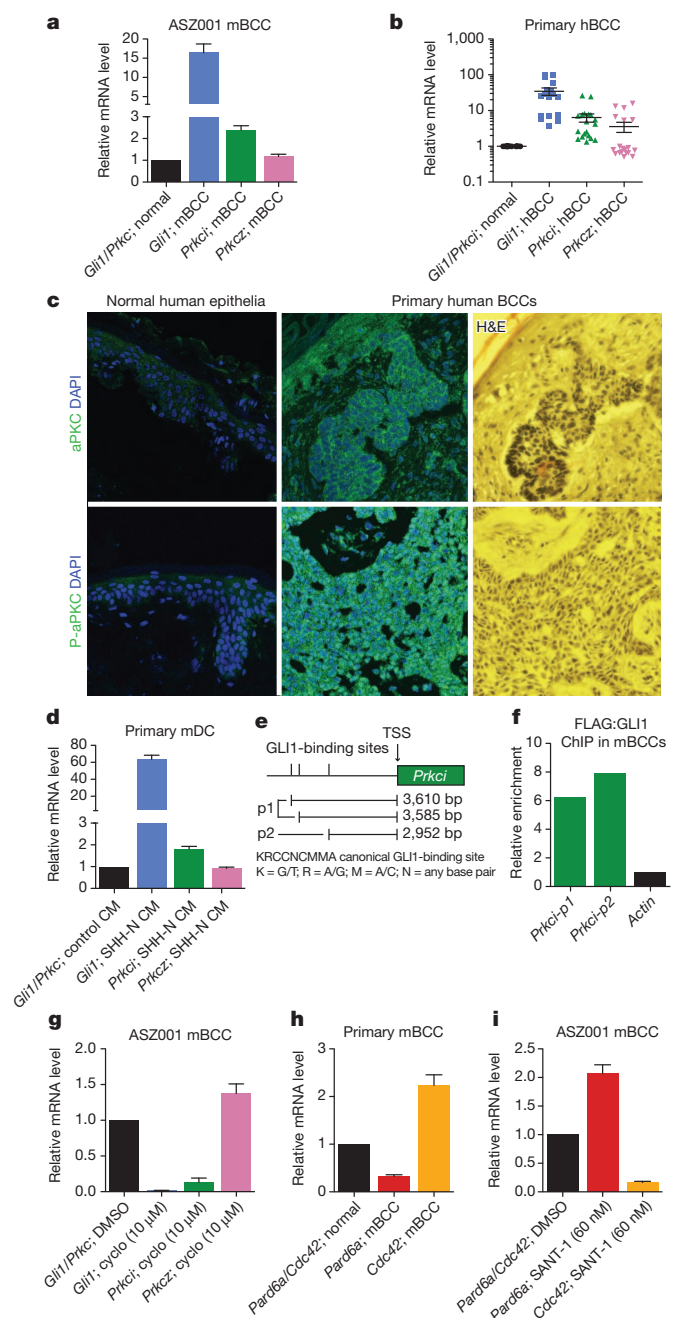


Figure 2 | aPKC- ι/λ and HH form a positive-feedback loop in BCCs.

a, b, *Gli1*, *Prkci*, and *Prkcz* mRNA levels in mouse BCC cells (**a**) ($n = 3$) and primary human BCC tumours (**b**; hBCC) ($n = 7$). **c**, Total and activated aPKC- ι/λ (P-aPKC) overexpressed in primary human BCC tumours. **d**, *Prkci* is upregulated in SHH-N-treated mouse dermal cells ($n = 3$). CM, conditioned media. **e**, GLI1-binding sites within the promoter region of *Prkci*. TSS, transcriptional start site. **f**, FLAG:GLI1 ChIP of *Prkci* promoter GLI1 sites. **g**, Cyclopamine suppresses *Prkci* expression in BCC cells ($n = 3$). **h**, *Pard6a* expression is reduced and *Cdc42* is upregulated in mouse BCC tumours ($n = 3$). **i**, SANT-1-treatment of BCC cells increases *Pard6a* and decreases *Cdc42* mRNA expression ($n = 3$). Error bars, s.e.m.

PSI-dependent transcripts changed twofold or more when compared with a control (Fig. 3a). Also, 4,325 transcripts overlapped between the inhibitor-treated data sets ($P < 1.0 \times 10^{-300}$), with most transcripts being downregulated in both sets (Fig. 3b). Gene ontology terms associated with commonly changed transcripts include cell cycle regulation, protein transport and localization, and cell division (Fig. 3c). Global transcript expression regardless of fold-change showed a strong positive correlation between drug treatments, with a Pearson

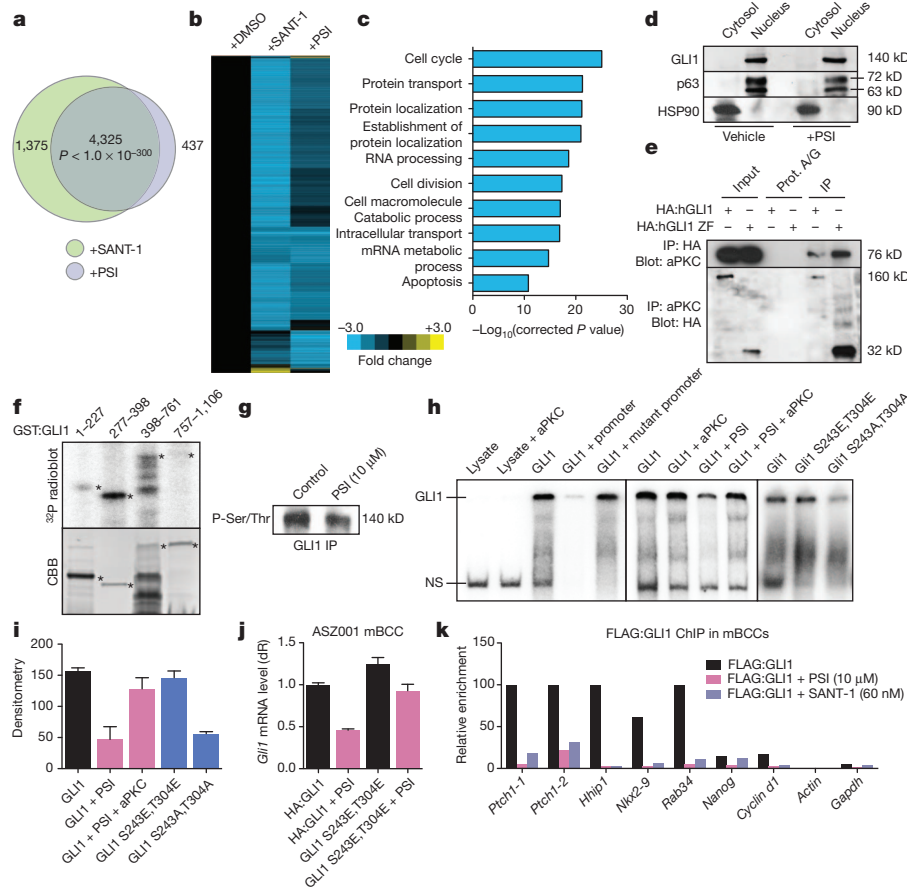


Figure 3 | aPKC-1/λ phosphorylates and activates GLI1. **a, b**, Venn diagram (**a**) and heat map (**b**) of significantly changed transcripts after SANT-1 or PSI treatment in BCC cells. **c**, Gene ontology terms of commonly altered transcripts. **d**, PSI does not affect nuclear GLI1 in BCC cells. **e**, aPKC-1/λ interacts with IVT human GLI1 or GLI1 DNA-binding domain. **f**, aPKC-1/λ phosphorylates human GLI1 DNA-binding domain. CBB, Coomassie brilliant blue. **g**, PSI reduces phosphorylated serine/threonine levels of immunoprecipitated GLI1

from BCC cells. **h**, aPKC-1/λ promotes DNA binding of IVT human GLI1 at Ser 243 and Thr 304 in an electrophoretic mobility shift assay. NS, non-specific binding. **i**, Densitometry of aPKC-1/λ rescue, and phosphomimetic versus phosphodeficient GLI1 electrophoretic mobility shift assay ($n = 3$). **j**, BCC cells expressing phosphomimetic GLI1 show reduced PSI sensitivity ($n = 3$). Error bars, s.e.m. **k**, FLAG:GLI1 ChIP showing PSI and SANT-1 inhibit GLI1 binding to target chromatin sites in mouse BCC cells.

correlation of 0.495. Comparison with previously published HH-dependent data sets from mouse medulloblastomas/granular neural precursors or developing mouse limb bud^{15,16} reveals substantial overlap (Supplementary Fig. 4a). We found that 321 of the 1,077 GLI1-binding sites found in medulloblastomas/granular neural precursors ($P = 1.36 \times 10^{-11}$) and 41 of the 396 GLI3-binding sites identified in the developing limb bud ($P = 8.92 \times 10^{-9}$) overlap with our commonly changed data set. Representative gene expression profiles among the data sets are displayed in a cluster heat map in Supplementary Fig. 4b. Validation of a subset of transcript expression levels using quantitative reverse-transcription PCR shows that the relative values from our data set closely mirror actual mRNA levels on drug treatment (Supplementary Fig. 4c, d). These results indicate that aPKC-1/λ and SMO regulate a common set of HH target genes in BCCs.

The striking overlap of transcriptional targets suggested that aPKC-1/λ might regulate GLI transcription factors. To determine where aPKC-1/λ acts, we added subthreshold concentrations of cyclopamine or PSI to BCC cells. We found that only cyclopamine outcompeted SAG-mediated activation (Supplementary Fig. 5a), indicating that aPKC-1/λ functions downstream of SMO. Moreover, aPKC-1/λ inhibition slightly increases rather than decreases GLI1 stability (Supplementary Fig. 5b), does not affect GLI2 or GLI3 processing (Supplementary Fig. 5c), and does not alter GLI1 nuclear localization (Fig. 3d and Supplementary Fig. 5d), suggesting that aPKC-1/λ affects GLI activity. Intriguingly, loss of aPKC-1/λ protein in mouse fibroblasts results in a GLI1 band with slightly smaller apparent

molecular weight (Supplementary Fig. 5e, f). By contrast, loss of MIM, despite primary cilia defects that prevent substantial activation of the HH pathway⁸, have more aPKC-1/λ protein and a GLI1 band with a slightly larger apparent molecular weight, suggesting aPKC-1/λ modifies GLI1 post-translationally.

Consistent with the notion of aPKC-1/λ-dependent alteration of GLI1 activity, aPKC-1/λ and GLI1 form a complex as recombinant HIS:aPKC-1/λ and *in vitro*-translated (IVT) human HA:GLI1 or HA:GLI1 zinc-finger co-immunoprecipitate (Fig. 3e). Purified aPKC-1/λ directly phosphorylates GLI1 *in vitro* (Fig. 3f), with the majority of the phosphorylation occurring in the zinc-finger DNA-binding region of GLI1. Immunoprecipitation of endogenous GLI1 from BCC cells shows PSI-dependent phosphorylation at serine/threonine residues, further supporting an *in vivo* role for aPKC-1/λ (Fig. 3g).

PSI-treated IVT human GLI1:V5/HIS, where endogenous aPKC-1/λ is inhibited in the reaction, significantly reduced binding to radio-labelled *GLI1* target DNA in an electrophoretic mobility assay (Fig. 3h, i). Addition of recombinant aPKC-1/λ overcame the effects of PSI to rescue GLI1-dependent DNA binding, whereas the addition of heat-inactivated aPKC-1/λ did not (Supplementary Fig. 5g), indicating that GLI1 phosphorylation by aPKC-1/λ is necessary for maximal DNA binding. The phosphorylation state of GLI1 seems to be critical because higher concentrations of aPKC-1/λ led to paradoxically decreased DNA binding (Supplementary Fig. 5g).

We performed a mutagenesis screen of the GLI1 DNA-binding domain to determine the site of aPKC-1/λ phosphorylation and

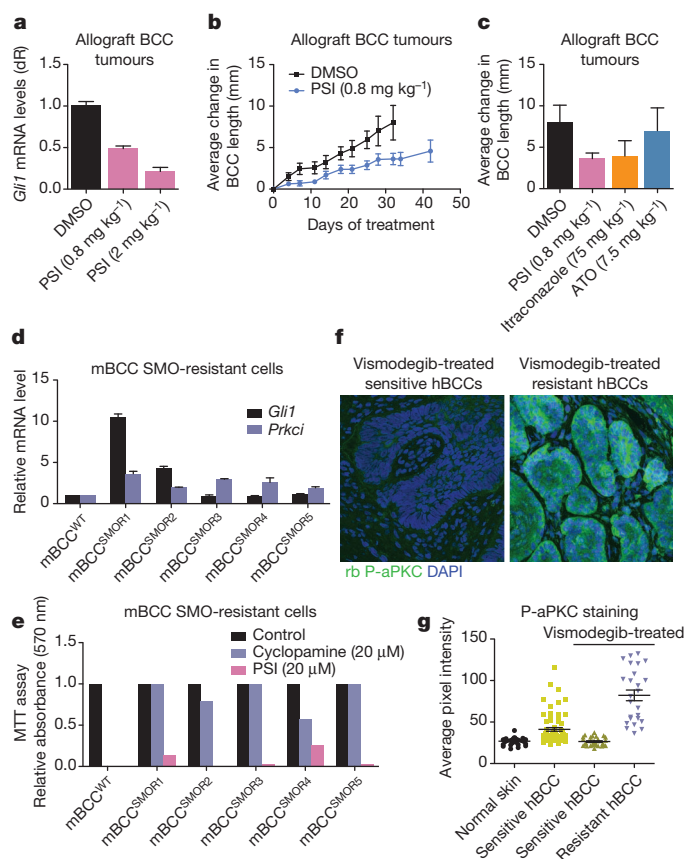


Figure 4 | Topical aPKC inhibitor suppresses primary tumour growth.

a, PSI inhibits HH signalling in allografted mouse BCC tumours from *Ptch1*^{+/-}; *K14-creER2;p53*^{lox/lox} mice ($n = 7$). **b**, Topical treatment of allografted BCC tumours slows tumour growth (DMSO, $n = 10$; PSI, $n = 9$). **c**, Intermediate levels of PSI ($n = 8$) compared with intermediate concentrations of itraconazole ($n = 8$) and arsenic trioxide ($n = 5$) after 29 days of treatment. **d**, **e**, Five independently derived SMO-resistant BCC cell lines (mBCC^{SMOR1} to mBCC^{SMOR5}) that amplify *Prkci* or both *Prkci* and *Gli1* mRNA levels (**d**) are sensitive to PSI treatment (**e**). mBCC^{WT}, SMO-sensitive BCC cell line. **f**, **g**, Vismodegib-treated resistant human BCC tumours ($n = 6$) display higher levels of active aPKC- λ than do vismodegib-treated sensitive tumours ($n = 8$), non-drug-treated tumours ($n = 17$) and normal skin ($n = 7$). Error bars, s.e.m.

found that residues Ser 243 and Thr 304 seem to mediate aPKC- λ /GLI1 effects. Phosphomimetic GLI1 (GLI1^{S243E,T304E}) bound to target DNA just as well as wild-type GLI1 did, whereas phosphodeficient GLI1 (GLI1^{S243A,T304A}), which accumulates less aPKC- λ phosphorylation (Supplementary Fig. 5h), has less DNA-binding ability (Fig. 3h, i). Moreover, GLI1^{S243E,T304E} is less sensitive to PSI in BCC cells, suggesting that these sites are functional aPKC- λ /GLI1 sites (Fig. 3j). To confirm that aPKC- λ regulates GLI1 binding *in vivo*, we performed ChIP of FLAG:GLI1 in BCC cells using GLI1 target genes^{17,18}. On all GLI1 targets assayed, PSI-treated tumour cells left GLI1 nuclear protein levels unchanged but reduced the association with chromatin (Fig. 3d, k). Non-HH target genes were left unchanged by PSI treatment. We conclude that aPKC- λ regulates HH signalling by phosphorylating and activating GLI1 to increase its affinity for DNA, illustrating a rare instance where post-translational modification of a zinc-finger domain promotes DNA binding and transcriptional activity.

To explore whether aPKC inhibitors can be used successfully as a BCC therapeutic, we topically treated allografted BCC tumours¹⁴ with PSI. This tumour model accurately describes human BCCs and has previously been used to validate HH pathway inhibitors now in clinical use¹⁹. In allografted BCCs, *Gli1* mRNA decreased as the concentration of topical PSI was increased (Fig. 4a). Also, tumour size was suppressed for intermediate concentrations of PSI, with no apparent acquired resistance

(Fig. 4b). This compares favourably with treatment with intermediate concentrations of SMO antagonist itraconazole¹⁹ or GLI2 inhibitor arsenic trioxide²⁰ (Fig. 4c). Tumours lost their classical palisade patterning on PSI treatment, and apoptosis increased (Supplementary Fig. 6). Cell proliferation was reduced along with GLI1 protein levels. Mice treated with topical or intraperitoneal PSI showed no apparent adverse effects (Supplementary Fig. 7) except a mild hair cycling phenotype (not shown) suggesting that aPKC treatment is tumour selective.

Because aPKC- λ acts downstream of SMO, we determined whether PSI could inhibit cell growth of SMO-resistant tumours. Following methods to generate resistant lines for other chemotherapeutics such as K-ras or B-raf²¹, we generated multiple independent BCC cell lines that were resistant to high levels of SANT-1. These SMO-resistant lines displayed increased expression of *Prkci* mRNA and protein, with varying levels of *Gli1* mRNA (Fig. 4d and Supplementary Fig. 8a). Other HH target genes displayed differential expression patterns that followed *Gli1* or *Prkci* mRNA levels, or were generally suppressed (Supplementary Fig. 8b). We verified SMO resistance by treating the cells with high concentrations of structurally unrelated cyclopamine and found little effect on cell proliferation (Fig. 4e). Treatment of these lines, or SANT-1-sensitive parental lines, with PSI drastically reduced cell proliferation, suggesting that active aPKC- λ has a role in SMO-inhibitor-resistant human tumours. Comparison of SMO-inhibitor-sensitive and SMO-inhibitor-resistant locally invasive human BCCs, several of which lacked *SMO* and *SUFU* mutations as well as *GLI1/2* amplification (B. Yauch, personal communication), showed elevated levels of active aPKC- λ in resistant tumours with polyclonal and monoclonal antibodies, corroborating the increase of active aPKC- λ levels as a mode of resistance (Fig. 4f, g and Supplementary Fig. 8c, d). Taken together, these data indicate that BCCs become dependent on aPKC- λ to drive HH activation and tumour growth, and that suppression of aPKC- λ activity is sufficient to prevent BCC progression in both SMO-sensitive and SMO-resistant lines. Our results highlight aPKC- λ inhibition as a viable, tumour-selective alternative to SMO inhibitors to treat HH-dependent and SMO-resistant cancers.

METHODS SUMMARY

All mouse studies were approved by and conformed to the policies and regulations of the Institutional Animal Care and Use Committees at Stanford University and the Children's Hospital Oakland Research Institute. *Ptch1*^{+/-}; *K14-creER2;p53*^{lox/lox} mice were used to develop BCC tumours. Tumours were allografted as previously described¹⁴. Nine tumours from three mice were treated topically twice daily with 0.8 mg kg⁻¹ PSI dissolved in DMSO for at least 32 days, with measurements on some tumours lasting 42 days. Ten tumours from three mice were treated with DMSO twice daily as a control. Mice were killed and tumours collected when tumour size exceeded the limit in our animal care guidelines. We measured the change in tumour size with callipers every three to four days. Pairwise comparisons between DMSO and PSI treatment were done using a two-sided unpaired *t*-test with GraphPad PRISM software.

The electrophoretic mobility shift assay was performed by incubation of 50 fmol double-stranded radio-labelled *GLI1* oligonucleotides (5'-AGCCCGGACCAC CCACGAGAA-3') in binding buffer (25 mM HEPES pH 7.5, 25 mM KCl, 2.5 mM MgCl₂, 1 mM DTT, 10% glycerol, 25 μ M poly(dI-dC) and 5 μ M ZnSO₄) with IVT GLI1:V5/HIS, HA:GLI1, HA:GLI1^{S243E,T304E} or HA:GLI1^{S243A,T304A} lysate for 10 min at 25 °C. Unlabelled *GLI1* oligonucleotides or *GLI1* mutant oligonucleotides (2 pmol) (5'-AGCCCGGAGGAGGCACGAGAA-3') were used as competition. Endogenous aPKC was inhibited in reticulocyte lysate with PSI during the translation reaction, and rescue was performed by adding recombinant HIS: aPKC- λ for 15 min before addition of radio-labelled *GLI1* oligonucleotides. Samples were resolved on 6% acrylamide gel, exposed to a phosphor screen (Molecular Dynamics) and imaged using a GE Typhoon 9410.

Full Methods and any associated references are available in the online version of the paper.

Received 1 May 2012; accepted 4 January 2013.

- Ng, J. M. Y. & Curran, T. The Hedgehog's tale: developing strategies for targeting cancer. *Nature Rev. Cancer* **11**, 493–501 (2011).

2. Yauch, R. L. *et al.* Smoothed mutation confers resistance to a Hedgehog pathway inhibitor in medulloblastoma. *Science* **326**, 572–574 (2009).
3. Buonamici, S. *et al.* Interfering with resistance to smoothed antagonists by inhibition of the PI3K pathway in medulloblastoma. *Sci. Transl. Med.* **2**, 51ra70 (2010).
4. Dijkgraaf, G. J. P. *et al.* Small molecule inhibition of GDC-0449 refractory smoothed mutants and downstream mechanisms of drug resistance. *Cancer Res.* **71**, 435–444 (2011).
5. Chang, A. L. S. & Oro, A. E. Initial assessment of tumor regrowth after vismodegib in advanced basal cell carcinoma. *Arch. Dermatol.* **148**, 1324–1325 (2012).
6. Atwood, S. X., Chang, A. L. S. & Oro, A. E. Hedgehog pathway inhibition and the race against tumor evolution. *J. Cell Biol.* **199**, 193–197 (2012).
7. St Johnston, D. & Ahringer, J. Cell polarity in eggs and epithelia: parallels and diversity. *Cell* **141**, 757–774 (2010).
8. Bershteyn, M., Atwood, S. X., Woo, W.-M., Li, M. & Oro, A. E. MIM and cortactin antagonism regulates ciliogenesis and hedgehog signaling. *Dev. Cell* **19**, 270–283 (2010).
9. Callahan, C. A. *et al.* MIM/BEG4, a sonic hedgehog-responsive gene that potentiates Gli-dependent transcription. *Genes Dev.* **18**, 2724–2729 (2004).
10. Aszterbaum, M. *et al.* Ultraviolet and ionizing radiation enhance the growth of BCCs and trichoblastomas in patched heterozygous knockout mice. *Nature Med.* **5**, 1285–1291 (1999).
11. Atwood, S. X. & Prehoda, K. E. aPKC phosphorylates Miranda to polarize fate determinants during neuroblast asymmetric cell division. *Curr. Biol.* **19**, 723–729 (2009).
12. Standaert, M. L. *et al.* Insulin activates protein kinases C- ζ and C- λ by an autophosphorylation-dependent mechanism and stimulates their translocation to GLUT4 vesicles and other membrane fractions in rat adipocytes. *J. Biol. Chem.* **274**, 25308–25316 (1999).
13. Winklmayr, M. *et al.* Non-consensus GLI binding sites in Hedgehog target gene regulation. *BMC Mol. Biol.* **11**, 2 (2010).
14. Wang, G. Y. *et al.* Establishment of murine basal cell carcinoma allografts: a potential model for preclinical drug testing and for molecular analysis. *J. Invest. Dermatol.* **131**, 2298–2305 (2011).
15. Lee, E. Y. *et al.* Hedgehog pathway-regulated gene networks in cerebellum development and tumorigenesis. *Proc. Natl Acad. Sci. USA* **107**, 9736–9741 (2010).
16. Vokes, S. A., Ji, H., Wong, W. H. & McMahon, A. P. A genome-scale analysis of the cis-regulatory circuitry underlying sonic hedgehog-mediated patterning of the mammalian limb. *Genes Dev.* **22**, 2651–2663 (2008).
17. Vokes, S. A. *et al.* Genomic characterization of Gli-activator targets in sonic hedgehog-mediated neural patterning. *Development* **134**, 1977–1989 (2007).
18. Po, A. *et al.* Hedgehog controls neural stem cells through p53-independent regulation of Nanog. *EMBO J.* **29**, 2646–2658 (2010).
19. Kim, J. *et al.* Itraconazole, a commonly used antifungal that inhibits Hedgehog pathway activity and cancer growth. *Cancer Cell* **17**, 388–399 (2010).
20. Kim, J., Lee, J. J., Kim, J., Gardner, D. & Beachy, P. A. Arsenic antagonizes the Hedgehog pathway by preventing ciliary accumulation and reducing stability of the Gli2 transcriptional effector. *Proc. Natl Acad. Sci. USA* **107**, 13432–13437 (2010).
21. Little, A. S. *et al.* Amplification of the driving oncogene, KRAS or BRAF, underpins acquired resistance to MEK1/2 inhibitors in colorectal cancer cells. *Sci. Signal.* **4**, ra17 (2011).

Supplementary Information is available in the online version of the paper.

Acknowledgements We would like to thank K. Qun for bioinformatics assistance, J. Kim for archival BCC tissue, A. Chang and S. Aasi for clinical trial operations, K. Chang for technical assistance, and H. Chang and P. Khavari for reading the manuscript. This work was supported by NIH NRSA 1F32CA14208701 (S.X.A.) and NIH grants AR052785 and AR046786 (A.E.O.).

Author Contributions S.X.A. and A.E.O. designed the experiments. S.X.A. performed the experiments. M.L. aided the biochemical and knockdown analyses. A.L. and J.Y.T. performed the allograft BCC drug treatments. J.Y.T. provided vismodegib-resistant tumour samples. S.X.A. and A.E.O. wrote the manuscript.

Author Information Reprints and permissions information is available at www.nature.com/reprints. The authors declare competing financial interests: details are available in the online version of the paper. Readers are welcome to comment on the online version of the paper. Correspondence and requests for materials should be addressed to A.E.O. (oro@stanford.edu) or S.X.A. (satwood@stanford.edu).

METHODS

Tumour immunofluorescence. Human tumours from SMO-inhibitor-sensitive and SMO-inhibitor-resistant patients were obtained from patients enrolled in clinical trials performed by the Stanford group (A.E.O. and J.Y.T.) and clinical trials NCT00833417 and NCT00957229. Patients gave consent under an approved Stanford IRB protocol (#18325). Active and total aPKC levels in human tumour sections were determined by immunofluorescence using rabbit anti-aPKC (1:250; Santa Cruz Biotechnology), rabbit anti-p-aPKC Thr 410 (1:100; Santa Cruz Biotechnology) or mouse anti-p-aPKC Thr 410 (1:100; Santa Cruz Biotechnology). Confocal images were acquired on a Leica SP2 AOBs laser scanning microscope with a HCX PL APO $\times 63$ oil-immersion objective. Average pixel intensity over five distinct areas per tumour section was determined using IMAGEJ. Images were arranged with IMAGEJ, Adobe PHOTOSHOP, and Adobe ILLUSTRATOR.

Cell culture. Primary mouse dermal cells were isolated as previously described⁸. Dermal cells were grown in Amniomax media containing supplement and antibiotics (Invitrogen). ASZ001 cells were grown in 154CF media containing 2% chelated FBS, HKGS supplement and antibiotics (Invitrogen). Keratinocytes (HPA Culture Collections) were grown in CnT-07 media containing supplement and 0.07 mM CaCl_2 (CellNTEC). Cells were serum-starved for between 24 and 48 h to induce ciliogenesis. The MTT cell proliferation assay was performed using the manufacturer's protocol (Invitrogen). Cells were transfected with FuGene6 or nucleofected using an Amaxa Human Keratinocyte Nucleofector kit according to the manufacturer's protocol.

SMO-resistant cell lines were generated by treating ASZ001 BCC cells with increasingly higher concentrations of SANT-1 in every passage for three weeks. Final resistant cell lines were grown in 60 μM SANT-1. Cyclopamine was used to inhibit HH signalling to verify SMO resistance.

Antibodies and immunofluorescence staining. Cells were fixed with either 4% paraformaldehyde or 100% methanol for 10 min. Normal horse serum (1%) and 0.1% Triton X-100 in PBS was used for blocking. Tissues were fixed with 4% paraformaldehyde and embedded in paraffin. Sections (10 μm) were cut and deparaffinized under standard conditions before staining. Tissue sections were blocked using 20% normal horse serum and 0.1% Triton X-100 in PBS. The following antibodies were used: rabbit anti-aPKC (1:500; Santa Cruz Biotechnology), rabbit anti-p-aPKC Thr 410 (1:100; Santa Cruz Biotechnology), mouse anti-p-aPKC Thr 410 (1:100; Santa Cruz Biotechnology), rabbit anti-PARD6A (1:100; Santa Cruz Biotechnology), mouse anti-PARD6A (1:100; Santa Cruz Biotechnology), mouse anti-PARD3 (1:500; Millipore), mouse anti-CDC42 (1:500; Santa Cruz Biotechnology), rabbit anti-MIM (1:1,000; ref. 8), rabbit anti- γ -tubulin (1:500; Sigma), mouse anti- γ -tubulin (1:500; Abcam), mouse anti-acetylated tubulin (1:2,000; Sigma), goat anti-GLI2 (1:500; R&D Systems), goat anti-GLI3 (1:250; R&D Systems), rat anti-HA (1:1,000; Covance), rabbit anti-KI67 (1:200; Lab Vision), mouse anti-GLI1 (1:1,000; Cell Signaling), rabbit anti-phosphoserine/threonine (1:1,000; Abcam), mouse anti-actin (1:5,000; Sigma), rabbit anti-HSP90 (1:200; Santa Cruz Biotechnology), mouse anti-p63 (1:200; Santa Cruz Biotechnology) and TUNNEL stain (Roche). Secondary antibodies were from Invitrogen. Confocal images were acquired on a Leica SP2 AOBs laser scanning microscope with a HCX PL APO $\times 63$ oil-immersion objective. Images were arranged with IMAGEJ, Adobe PHOTOSHOP, and Adobe ILLUSTRATOR.

Protein purification and binding experiments. All proteins were expressed and purified as previously described²². IVT proteins were produced using the manufacturer's protocol in rabbit reticulocyte lysate from Promega. Endogenous proteins were immunoprecipitated by using 5 μg rabbit anti-aPKC- u/λ , chicken anti-MIM, mouse anti-PARD3, rabbit anti-PARD6A, rat anti-HA, mouse anti-GLI1 or mouse anti-FLAG (Sigma) with protein A/G-conjugated beads according to the manufacturer's protocol (Santa Cruz Biotechnology). *In vivo*-phosphorylated GLI1 was detected by immunoprecipitation of GLI1 from BCC cells treated with 10 μM MG132 in the presence or absence of 10 μM PSI for 6 h. Samples were separated by SDS-polyacrylamide gel electrophoresis (PAGE) and transferred to nitrocellulose, followed by antibody incubations and visualization using chemiluminescent substrate (ThermoScientific).

Centrosomes were purified from mouse C3H 10T1/2 cells as previously described²³. Supernatant fractions were isolated by incubation of mouse BCC cells with lysis buffer (10 mM HEPES pH 7.5, 1.5 mM MgCl_2 , 10 mM KCl, 0.4% NP-40) for 2 min on ice. Nuclei were spun down and washed twice with lysis buffer before equal-volume resuspension in PBS and addition of SDS loading buffer.

Kinase assays. HIS:aPKC- u/λ (Abcam) was incubated with GST, GST:GLI1 or GST:GLI1 fragments at 30 °C for 15 min in kinase reaction buffer (20 mM Tris-HCl pH 7.5, 10 mM MgCl_2 , 1 mM DTT, 10 mM ATP) with 20 nM $[\gamma\text{-}^{32}\text{P}]\text{ATP}$. The reaction was quenched by addition of SDS loading buffer and heated at

95 °C for 10 min. The protein was resolved by SDS-PAGE, exposed to a phosphor screen (Molecular Dynamics) and imaged using a GE Typhoon 9410.

Luciferase assays. ASZ001 cells were nucleofected (Amaxa) with pGL3-Basic (Promega) containing the following GLI-binding sites or mutant sites multimerized ($\times 6$) head to tail: site 1 (GACCCCCAA); site 1 mutant (GAAACACAG); site 2 (TGCCCCCA); site 2 mutant (TGAACACCT); site 3 (TACCCCCAA); site 3 mutant (TAAACATAG); GLICS (GACCACCCA); GLICS mutant (GATAA TCCG). Nucleofected cells were grown to confluency and lysed, and luciferase expression was determined using the Dual-Luciferase Assay System (Promega) and a TD-20/20 Luminometer.

Lentiviral knockdown and drug treatments. Lentiviral pLKO.1 vector containing short hairpin RNAs (Open Biosystems) to *Prkci* (sh3:CCGTTCCACCATGA AATGGATA, sh5:CCAGACAGAAAGCAGGTGTGT), or pSicoR-puro vector containing shRNA to *Mtss1* (ref. 8) were used. Lentivirus containing empty vector pSicoR-puro was used for control knockdowns. Lentiviral infection was performed and cells assayed after three days for *Prkci* mRNA and four days for *Mtss1* mRNA. Protein knockdown was confirmed by western blot or qRT-PCR.

Drug treatments for cells were performed with myristoylated PSI (myr-SIYRRGARRWRKLY), myristoylated scramble peptide (myr-RGIRYRLRARSWK), SANT-1 (Tocris Bioscience), cyclopamine (Tocris Bioscience), SAG (EMD), Go6983 (Tocris Bioscience) and cyclohexamide (Sigma). Subconfluent ASZ001 cells were serum-starved and inhibitors were added for 48 h before MTT assay (Invitrogen) and for 24 h before cilia visualization and GLI target gene induction assay. Stability assays performed with ASZ001 pre-incubated with PSI for 1 h before 20 $\mu\text{g ml}^{-1}$ cyclohexamide addition at various time points. Mouse blood parameters were tested by treating mice topically twice daily with DMSO or 0.8 mg kg^{-1} PSI dissolved in DMSO for 3 d.

Chromatin immunoprecipitation. Protein-DNA complexes were captured by fixing ASZ001 cells expressing FLAG:GLI1 and were pre-incubated for 24 h with inhibitors, fixed for 10 min with 1% formaldehyde and quenched with 0.125 M glycine for 5 min. ChIP was performed using the manufacturer's protocol adapted from Upstate. Briefly, cells were lysed for 10 min at 4 °C in lysis buffer (50 mM HEPES pH 7.5, 140 mM NaCl, 1 mM EDTA, 10% glycerol, 0.1% NP-40, 0.2% Triton-X100, protease inhibitors (Roche)) and nuclei were pelleted and lysed for 10 min at 4 °C in nuclei lysis buffer (10 mM Tris-HCl pH 8, 100 mM NaCl, 1 mM EDTA, 0.5 mM EGTA, 0.5% N-lauroylsarcosine, protease inhibitors) to obtain DNA. DNA was sheared to a range of 100–600 base pairs (bp) in size by sonication for 25 min. ChIP-grade FLAG-antibody-conjugated magnetic beads (Sigma) were incubated with nuclei lysate overnight at 4 °C. Beads were washed in RIPA buffer and DNA was reverse crosslinked by incubation at 65 °C overnight in elution buffer (50 mM Tris-HCl pH 8, 10 mM EDTA, 1% SDS). RNA and protein were digested with RNase A (0.2 $\mu\text{g ml}^{-1}$; 37 °C for 2 h) and proteinase K (0.2 $\mu\text{g ml}^{-1}$; 55 °C for 2 h), respectively, and DNA was purified by phenol chloroform extraction using standard protocols. Relative fold enrichment was determined by adding DNA to Brilliant II SYBR Green qPCR Master Mix Kit (Agilent Technologies) containing primers to known GLI target sites listed in Supplementary Table 1. ChIP with FLAG-antibody-conjugated magnetic beads in ASZ001 without FLAG:GLI1 was used as a negative control.

3'-end RNA sequencing. The 3'-end RNA-Seq library was generated from ASZ001 cells incubated with or without inhibitors for 24 h. RNA was purified using TRIzol (Invitrogen) and poly A-RNA selected using the micro-poly(A)purist kit (Ambion). We heat-sheared 200 ng mRNA for 12 min at 85 °C and performed first-strand cDNA synthesis using Superscript III (Invitrogen) for 1 h at 50 °C. Second-strand synthesis was performed using *Escherichia coli* DNA Ligase (Invitrogen), *E. coli* DNA Polymerase I (NEB) and *E. coli* RNase H (Epicentre) for 2 h at 16 °C. We added T4 DNA Polymerase (NEB) for an additional 15 min before quenching with EDTA. We purified double-stranded cDNA with MinElute Reaction Cleanup Kit (Qiagen). Complementary DNA was poly-A-tailed using Klenow Fragment 3' to 5' exonuclease (NEB) for 30 min at 37 °C. We ligated Illumina linker using T4 DNA Ligase (Enzymatics) overnight at 25 °C. We purified 220–300-bp bands using 3% NuSieve GTG agarose (Lonza) and a MinElute Gel Extraction Kit (Qiagen). We amplified the DNA using Phusion PCR Master Mix (NEB) and a 15-cycle PCR program. We purified 220–300-bp bands using 3% NuSieve GTG agarose (Lonza) and MinElute Gel Extraction Kit. We sequenced DNA using Illumina Genome Analyzer IIx.

We aligned 36-bp raw reads with BOWTIE using the NCBI37/mm9 reference genome. Differential expression analysis was performed on the 3' exon with the CUFFLINKS suite using mouse RefSeq gene predictions as a reference transcriptome. Annotated coding transcripts were filtered for significant expression by a RPKM of 25 in at least one sample set. Transcripts that changed by two-fold or more in drug-treated samples were hierarchically clustered using the

CLUSTER program and visualized in Java TREEVIEW. Transcripts were validated using Brilliant II SYBR Green qRT-PCR Master Mix Kit (Agilent Technologies) with primers listed in Supplementary Table 1. The two-tailed *P* value between our gene sets and other gene sets was calculated using Fisher's exact test.

22. Atwood, S. X., Chabu, C., Penkert, R. R., Doe, C. Q. & Prehoda, K. E. Cdc42 acts downstream of Bazooka to regulate neuroblast polarity through Par-6 aPKC. *J. Cell Sci.* **120**, 3200–3206 (2007).
23. Meigs, T. E. & Kaplan, D. D. Isolation of centrosomes from cultured Mammalian cells. *Cold Spring Harb. Protocols*. doi:10.1101/pdb.prot5039 (2008).

A bacteriophage encodes its own CRISPR/Cas adaptive response to evade host innate immunity

Kimberley D. Seed¹, David W. Lazinski¹, Stephen B. Calderwood^{2,3} & Andrew Camilli¹

Bacteriophages (or phages) are the most abundant biological entities on earth, and are estimated to outnumber their bacterial prey by tenfold¹. The constant threat of phage predation has led to the evolution of a broad range of bacterial immunity mechanisms that in turn result in the evolution of diverse phage immune evasion strategies, leading to a dynamic co-evolutionary arms race^{2,3}. Although bacterial innate immune mechanisms against phage abound, the only documented bacterial adaptive immune system is the CRISPR/Cas (clustered regularly interspaced short palindromic repeats/CRISPR-associated proteins) system, which provides sequence-specific protection from invading nucleic acids, including phage^{4–11}. Here we show a remarkable turn of events, in which a phage-encoded CRISPR/Cas system is used to counteract a phage inhibitory chromosomal island of the bacterial host. A successful lytic infection by the phage is dependent on sequence identity between CRISPR spacers and the target chromosomal island. In the absence of such targeting, the phage-encoded CRISPR/Cas system can acquire new spacers to evolve rapidly and ensure effective targeting of the chromosomal island to restore phage replication.

Vibrio cholerae serogroup O1 is the primary causative agent of the severe diarrhoeal disease cholera, and lytic *V. cholerae* phages have been implicated in easing disease burden, particularly in the endemic region surrounding the Bay of Bengal^{12,13}. We recently described the isolation of the ICP1 (for the International Centre for Diarrhoeal Disease Research, Bangladesh cholera phage 1)-related, *V. cholerae* O1-specific virulent myoviruses that are omnipresent among cholera patient rice-water stool samples collected at the ICDDR,B from 2001 to 2011 (ref. 14 and present study). *V. cholerae* readily evolves resistance to ICP1 predation through mutations in O1 antigen biosynthetic genes outside the human host; however, this mutational escape comes at a cost as virulence necessitates maintenance of the O1 antigen¹⁵. This dynamic between predation by ICP1 and virulence of *V. cholerae* O1, specifically in the context of human infection, provides a unique opportunity for discovery of novel bacterial immunity and phage immune evasion strategies. One bacterial defensive strategy against phages is the CRISPR/Cas system. CRISPR loci consist of an array of short direct repeats separated by highly variable spacer sequences of precise length corresponding to segments of previously captured foreign DNA (protospacers)^{4,7,9}. CRISPR loci are found in ~40% and ~90% of sequenced bacterial and archaeal genomes, respectively^{8,16}. The CRISPR array is transcribed and the transcript cleaved into small CRISPR RNAs (crRNAs) that, in conjunction with the Cas proteins, execute an efficient process of immunity in which foreign nucleic acids are recognized by hybridization to crRNAs and cleaved^{4,7,8}.

We isolated eleven ICP1-related phages from stools of cholera patients at the ICDDR,B (ref. 14 and present study), five of which encode a CRISPR/Cas system located between open reading frames (ORFs) 87 and 88 of the ancestral ICP1 genome¹⁴. The GC content of this CRISPR/Cas system is the same (~37%) as the rest of the ICP1 genome. The ICP1 CRISPR/Cas system consists of two CRISPR loci (designated CR1 and CR2) and six *cas* genes (Fig. 1a) whose

organization and protein products are most homologous to Cas proteins of the type 1-F (*Yersinia pestis*) subtype system¹⁷ (Supplementary Table 1). *V. cholerae* is divided into two biotypes, classical and El Tor, the former of which is associated with earlier pandemics and has since been replaced by the El Tor biotype¹⁸. The classical strain, *V. cholerae* O395, has a CRISPR/Cas system belonging to the type I-E (*Escherichia coli*) subtype¹⁷, and to date there has not been any description of El Tor strains possessing a CRISPR/Cas system. Thus, the origin of the CRISPR/Cas system in ICP1 phage is unknown. Protospacer-adjacent motifs (PAMs) are type-specific, short conserved sequence motifs in the immediate vicinity of protospacers that are required for acquisition and targeting^{7,9,11,19}. In contrast to the GG PAM reported for the type I-F CRISPR/Cas systems in bacteria¹⁹, the protospacers targeted by the ICP1 CRISPR array have a GA PAM (Supplementary Fig. 1).

The majority of spacers in the ICP1 CRISPR show 100% identity to sequences within an 18-kilobase (kb) island found in a subset of *V. cholerae* strains that include the classical strain O395 isolated in India in 1964, El Tor strain MJ-1236 isolated in Bangladesh in 1994, and several El Tor strains collected at the ICDDR,B between 2001 and 2011 (Supplementary Table 2). The 18-kb island resembles the phage-inducible chromosomal islands (PICIs) of Gram-positive bacteria, including the prototype *Staphylococcus aureus* pathogenicity islands (SaPIs)^{20,21}. SaPIs are induced to excise, circularize and replicate

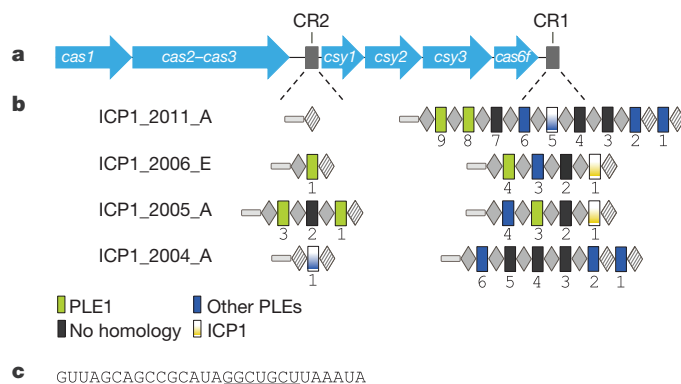


Figure 1 | Genomic organization of the ICP1 CRISPR/Cas system. **a**, The ICP1 phage CRISPR/Cas system consists of six *cas* genes and two CRISPR loci (CR1 and CR2). **b**, For each CRISPR locus, the repeat (28 bp) and spacer (32 bp) content is detailed as grey diamonds and coloured rectangles, respectively. Repeats (28 bp) that match the repeat consensus are shown in grey diamonds, and degenerate repeats are indicated in hatched grey diamonds. An AT-rich leader sequence precedes each CRISPR locus (grey rectangle). Spacers are coloured according to the percentage identity (solid represent 100% identity, gradient represents 81–97% identity). A fifth ICP1-related phage (ICP1_2003_A) has a genetically identical CRISPR/Cas system to ICP1_2004_A, and has been omitted for simplicity. **c**, The RNA sequence of the CR1 and CR2 consensus repeat with the partially palindromic sequence forming the predicted stem in the crRNA underlined.

¹Howard Hughes Medical Institute and Department of Molecular Biology and Microbiology, Tufts University School of Medicine, Boston, Massachusetts 02111, USA. ²Division of Infectious Diseases, Massachusetts General Hospital, Boston, Massachusetts 02114, USA. ³Harvard Medical School, Boston, Massachusetts 02114, USA.

following infection by certain phages. They use varied mechanisms to interfere with the phage reproduction cycle to enable their own promiscuous spread²¹, and this can protect the surrounding bacterial population from further phage predation. The organization of the *V. cholerae* 18-kb island targeted by the ICP1 CRISPR/Cas system is similar in length, base composition and organization to that observed in the SaPIs subset of PICIs, with an integrase homologue at one end and a GC content lower than that of the host species (37% compared to 47.5%). We therefore refer to the 18-kb element as the *V. cholerae* PICI-like element (PLE) (Fig. 2).

To address the functional relevance of the ICP1 CRISPR/Cas system, we focused on the interaction between the paired ICP1_2011_A phage and the *V. cholerae* O1 El Tor strain (harbouring PLE1) that were isolated from the same stool sample (for simplicity hereafter referred to as ICP1 and *V. cholerae* PLE⁺). ICP1 has two CRISPR spacers (8 and 9) (Fig. 1b) that have 100% identity to sequences within the *V. cholerae* PLE (Fig. 2 and Supplementary Table 2). Using the standard soft agar overlay method, we found that ICP1 can plaque efficiently on *V. cholerae* PLE⁺ (Fig. 3b). We used northern blot analysis to confirm that ICP1 crRNAs are transcribed and processed during *V. cholerae* infection (Supplementary Fig. 2). To test whether targeting of the PLE by the ICP1 CRISPR/Cas system affects phage fitness, we eliminated spacer 8 and 9 targeting. Spacer 8 targeting was disrupted by introducing silent mutations into its target within the PLE, generating *V. cholerae* PLE(8*) (Fig. 3a). We then infected this strain with a spontaneous ICP1 spacer 9 deletion mutant, referred to as ICP1(ΔS9). ICP1(ΔS9) was blocked for plaque formation on *V. cholerae* PLE(8*); however, it maintained wild-type plaquing efficiency on *V. cholerae* PLE⁺ (Fig. 3b). Importantly, *V. cholerae* PLE(8*) is sensitive to plaque formation by ICP1 (Fig. 3b), which still harbours one spacer (S9) targeting the PLE. These results demonstrate that ICP1 CRISPR/Cas must target the PLE for destruction in order to effectively infect and form plaques, and that a single spacer that targets the PLE is sufficient to facilitate successful phage replication. A mutant in which PLE ORFs 7–20 were deleted was susceptible to infection by ICP1(ΔS9) with wild-type plaquing efficiency (Supplementary Fig. 3). This demonstrates that an intact PLE is required to inhibit ICP1 in the absence of CRISPR targeting. These results, in conjunction with the observation that PLE1 circularizes following ICP1 infection (Supplementary Fig. 4), further support our designation of the 18-kb island as a PICI-like element.

It has been well documented in the type I-E (*E. coli*) system that CRISPR interference requires an intact PAM and a fully complementary seed region (a non-contiguous 7 base pair (bp) sequence immediately adjacent to the PAM)²². To address the sequence requirements of the ICP1 CRISPR/Cas system we constructed a series of point mutations in the spacer 8 target in *V. cholerae* PLE that span the PAM, seed region and remainder of the target sequence, and determined their effect on immunity. In accordance with previous results, we found that single mutations within the PAM or the first four positions in the seed region immediately adjacent to the PAM abolish ICP1 CRISPR/Cas immunity (Supplementary Fig. 5). Interestingly, mutations of increasing distance from the PAM showed a concordant decreasing effect on immunity. Up to five mismatches outside of the seed region of the target are known to be tolerated in the type I-E system²², and similarly we found that three and five mutations outside of the seed region were tolerated; however, eight mutations were not (Supplementary Fig. 5).



Figure 2 | Genomic organization of PLE1, a representative *V. cholerae* PLE targeted by the CRISPR/Cas system of ICP1-related phages. The integrase (*int*) is in blue, genes encoding hypothetical proteins (with numerical ORF designations) are grey. The locations of protospacers incorporated into the

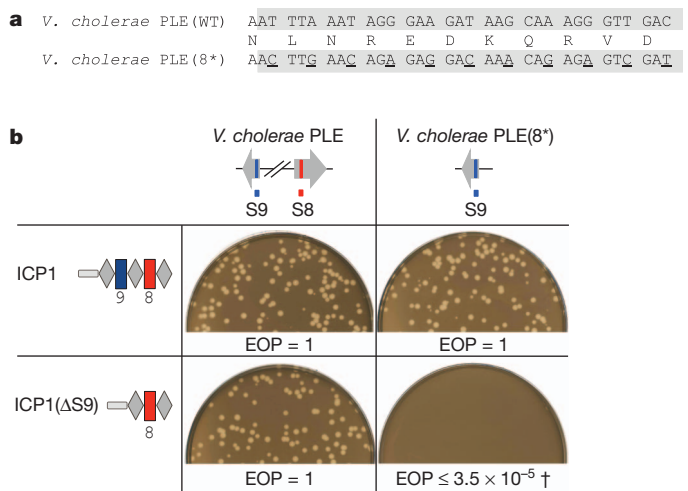


Figure 3 | Sequence-based targeting by the ICP1 CRISPR/Cas system is essential for lytic growth on *V. cholerae* PLE⁺. a, Disruption of the *V. cholerae* PLE target protospacer generating *V. cholerae* PLE(8*). The 32 bp protospacer sequence is shaded in grey. b, The sensitivity of each strain (top row) to ICP1 or ICP1(ΔS9) (left column) is shown. Identity between the spacer and targeted protospacer is indicated by the red and blue rectangles. The efficiency of plaquing (EOP, which is the plaque count on the mutant host strain divided by that on the wild-type host strain) is indicated. A dagger indicates that the EOP is 10⁻⁵ or 10⁻⁸ depending on the presence of PLE in the host strain used for propagation as discussed in the text.

In experiments where the ICP1 CRISPR/Cas system could not target the *V. cholerae* PLE and therefore plaque formation was greatly reduced, we observed phage escape mutants at frequencies that were dependent on the host strain on which the phage had been previously propagated. When ICP1(ΔS9) was grown on a PLE⁺ host before plaquing on *V. cholerae* PLE(8*), the efficiency of plaquing (EOP, which is the plaque count on the mutant host strain divided by that on the wild-type host strain) was 3.5×10^{-5} . The CRISPR loci from ten independent ICP1(ΔS9) escape mutants were sequenced, and in all cases, a new spacer was present at the leader end of the CRISPR CR1 array. Furthermore, the new spacers had 100% identity to sequences within the PLE (Fig. 2), and all newly integrated spacers target the PLE with the conserved GA dinucleotide PAM sequence (Supplementary Fig. 1b). The experimentally acquired spacers target both the coding and noncoding strands (Supplementary Table 3), although most (nine out of ten) target the coding strand. The pre-existing spacer (S8) (although mismatched in these experiments) also targets the coding strand; these data are in support of recent evidence that the DNA strand from which new protospacers are incorporated is heavily biased towards the existing protospacer orientation^{23,24}. In contrast to when phage were propagated on a PLE⁺ host before plaquing on *V. cholerae* PLE(8*), phage escape mutants were detected at a much lower frequency (EOP = 1.1×10^{-8}) when ICP1(ΔS9) was grown on a *V. cholerae* PLE⁻ host. This shows that new spacers targeting the PLE are incorporated into the CRISPR array during ICP1(ΔS9) infection of the PLE⁺ host (the immunization process), and that an immune host possessing an untargeted PLE can subsequently be used to select for new ICP1 CRISPR acquisition events that confer targeting and thus restore phage replication. These results demonstrate that the ICP1

CRISPR locus as spacers 8 and 9 (S8 and S9 of ICP1_2011_A) are indicated in green above the map. The locations of experimentally acquired protospacers are shown below the map in red.

CRISPR/Cas system is fully functional as an adaptive immune evasion system that benefits the phage.

ICP1 has evolved to effectively target the *V. cholerae* PLE with an adaptive immune evasion system that has never before been shown to function in bacterial viruses. During ICP1 infection of *V. cholerae* PLE⁺, PLE circularizes (Supplementary Fig. 4) and inhibits ICP1 through an unknown mechanism. To replicate successfully, ICP1 uses the CRISPR/Cas system to target the PLE for destruction. Because host cell death and DNA damage is inherent to lytic phage infection, CRISPR-mediated DNA cleavage of the PLE does not affect ICP1 infection. Sequencing data has been used to identify putative CRISPR arrays within a *Clostridium difficile* prophage²⁵, and more recently in metagenomic data sets of free viruses^{26,27}. However, there is currently no evidence for expression or function of these putative arrays. We show that the ICP1-encoded CRISPR/Cas system actively and autonomously functions to inhibit host immunity and thereby permit lytic infection. This finding, in conjunction with the previous observations regarding the presence of CRISPR loci in other phages^{25–27}, suggests that the use of the so-called bacterial adaptive immune system by these bacterial predators may be an underappreciated immune evasion strategy in the unfolding phage versus host co-evolutionary arms race.

METHODS

Phages (ICP1_2011_A and ICP1_2006_E) and *V. cholerae* were isolated from cholera rice-water stool samples and propagated as described^{14,15}. Genomic libraries were generated for phage and host strains as described²⁸ and sequenced using an Illumina HiSeq2000. A *V. cholerae* O1 El Tor isolate collected at the ICDDR,B in 2006, which was sequenced in this study and found to not harbour a PLE, was used as the PLE[−] host for propagation experiments. We used the CRISPRFinder program¹⁶ to identify CRISPR loci. WebLogo²⁹ was used to generate sequence logos for identification of the PAM. Point mutations were constructed using splicing by overlap extension (SOE) PCR and introduced using pCVD442-lac as previously described¹⁵. The PLE1 deletion construct (missing 8.6 kb including ORFs 7–20) was constructed using SOE PCR and introduced by natural transformation with subsequent deletion of the antibiotic-resistance marker using the FLP recombinase method as described³⁰. ICP1(ΔS9) was identified by screening for alterations in the CRISPR array by PCR following growth on *V. cholerae* PLE⁺. RNA was purified using the mirVana kit (Ambion) at the indicated times and run on 12% polyacrylamide urea gels. Northern blots were pre-hybridized in Ultrahyb-oligo (Ambion) and hybridization was carried out at 37 °C overnight using 32-nucleotide 5' end-labelled DNA probes (generated with [γ -32P]ATP and T4 polynucleotide kinase) complementary to spacers 8 and 6.

Received 9 November 2012; accepted 23 January 2013.

- Brüssow, H. & Hendrix, R. W. Phage genomics: small is beautiful. *Cell* **108**, 13–16 (2002).
- Labrie, S. J., Samson, J. E. & Moineau, S. Bacteriophage resistance mechanisms. *Nature Rev. Microbiol.* **8**, 317–327 (2010).
- Stern, A. & Sorek, R. The phage-host arms race: shaping the evolution of microbes. *Bioessays* **33**, 43–51 (2011).
- Horvath, P. & Barrangou, R. CRISPR/Cas, the immune system of bacteria and archaea. *Science* **327**, 167–170 (2010).
- Barrangou, R. *et al.* CRISPR provides acquired resistance against viruses in prokaryotes. *Science* **315**, 1709–1712 (2007).
- Marraffini, L. A. & Sontheimer, E. J. CRISPR interference limits horizontal gene transfer in staphylococci by targeting DNA. *Science* **322**, 1843–1845 (2008).
- Bhaya, D., Davison, M. & Barrangou, R. CRISPR-Cas systems in bacteria and archaea: versatile small RNAs for adaptive defense and regulation. *Annu. Rev. Genet.* **45**, 273–297 (2011).
- van der Oost, J., Jore, M. M., Westra, E. R., Lundgren, M. & Brouns, S. J. J. CRISPR-based adaptive and heritable immunity in prokaryotes. *Trends Biochem. Sci.* **34**, 401–407 (2009).

- Karginov, F. V. & Hannon, G. J. The CRISPR system: small RNA-guided defense in bacteria and archaea. *Mol. Cell* **37**, 7–19 (2010).
- Garneau, J. E. *et al.* The CRISPR/Cas bacterial immune system cleaves bacteriophage and plasmid DNA. *Nature* **468**, 67–71 (2010).
- Marraffini, L. A. & Sontheimer, E. J. CRISPR interference: RNA-directed adaptive immunity in bacteria and archaea. *Nature Rev. Genet.* **11**, 181–190 (2010).
- Faruque, S. M. *et al.* Self-limiting nature of seasonal cholera epidemics: role of host-mediated amplification of phage. *Proc. Natl Acad. Sci. USA* **102**, 6119–6124 (2005).
- Nelson, E. J., Harris, J. B., Morris, J. G., Calderwood, S. B. & Camilli, A. Cholera transmission: the host, pathogen and bacteriophage dynamic. *Nature Rev. Microbiol.* **7**, 693–702 (2009).
- Seed, K. D. *et al.* Evidence of a dominant lineage of *Vibrio cholerae*-specific lytic bacteriophages shed by cholera patients over a 10-year period in Dhaka, Bangladesh. *MBio* **2**, e00334–10 (2011).
- Seed, K. D. *et al.* Phase variable O antigen biosynthetic genes control expression of the major protective antigen and bacteriophage receptor in *Vibrio cholerae* O1. *PLoS Pathog.* **8**, e1002917 (2012).
- Grissa, I., Vergnaud, G. & Pourcel, C. The CRISPRdb database and tools to display CRISPRs and to generate dictionaries of spacers and repeats. *BMC Bioinformatics* **8**, 172 (2007).
- Makarova, K. S. *et al.* Evolution and classification of the CRISPR-Cas systems. *Nature Rev. Microbiol.* **9**, 467–477 (2011).
- Longini, I. M. *et al.* Epidemic and endemic cholera trends over a 33-year period in Bangladesh. *J. Infect. Dis.* **186**, 246–251 (2002).
- Mojica, F. J. M., Diez-Villasenor, C., Garcia-Martinez, J. & Almendros, C. Short motif sequences determine the targets of the prokaryotic CRISPR defence system. *Microbiology* **155**, 733–740 (2009).
- Novick, R. P., Christie, G. E. & Penadés, J. R. The phage-related chromosomal islands of Gram-positive bacteria. *Nature Rev. Microbiol.* **8**, 541–551 (2010).
- Ram, G. *et al.* Staphylococcal pathogenicity island interference with helper phage reproduction is a paradigm of molecular parasitism. *Proc. Natl Acad. Sci. USA* **109**, 16300–16305 (2012).
- Semenova, E. *et al.* Interference by clustered regularly interspaced short palindromic repeat (CRISPR) RNA is governed by a seed sequence. *Proc. Natl Acad. Sci. USA* **108**, 10098–10103 (2011).
- Datsenko, K. A. *et al.* Molecular memory of prior infections activates the CRISPR/Cas adaptive bacterial immunity system. *Nature Commun.* **3**, 945–947 (2012).
- Swarts, D. C., Mosterd, C., van Passel, M. W. J. & Brouns, S. J. J. CRISPR interference directs strand specific spacer acquisition. *PLoS ONE* **7**, e35888 (2012).
- Sebahia, M. *et al.* The multidrug-resistant human pathogen *Clostridium difficile* has a highly mobile, mosaic genome. *Nature Genet.* **38**, 779–786 (2006).
- Minot, S. *et al.* The human gut virome: inter-individual variation and dynamic response to diet. *Genome Res.* **21**, 1616–1625 (2011).
- Garcia-Heredia, I. *et al.* Reconstructing viral genomes from the environment using fosmid clones: the case of haloviruses. *PLoS ONE* **7**, e33802 (2012).
- Lazinski, D. W. L. & Camilli, A. Homopolymer tail-mediated ligation PCR: a streamlined and highly efficient method for DNA cloning and library construction. *Biotechniques* **54**, 25–34 (2013).
- Crooks, G. E., Hon, G., Chandonia, J. M. & Brenner, S. E. WebLogo: a sequence logo generator. *Genome Res.* **14**, 1188–1190 (2004).
- De Souza Silva, O. & Blokesch, M. Genetic manipulation of *Vibrio cholerae* by combining natural transformation with FLP recombination. *Plasmid* **64**, 186–195 (2010).

Supplementary Information is available in the online version of the paper.

Acknowledgements The authors thank the Tufts University Core Facility for sequencing and computational support. This work was supported by US National Institutes of Health grants AI055058 (A.C.), AI045746 (A.C.) and AI058935 (S.B.C.). A.C. is a Howard Hughes Medical Institute Investigator.

Author Contributions K.D.S. and D.W.L. performed experiments. K.D.S., D.W.L. and A.C. designed experiments. K.D.S. and A.C. wrote the manuscript. S.B.C. provided materials. All authors discussed the results and commented on the manuscript.

Author Information The sequences for the CRISPR/Cas system in ICP1_2011_A and ICP1_2006_E have been deposited at GenBank (accession numbers KC152959 and KC152958, respectively). The sequences for the *V. cholerae* PLEs identified in clinical isolates from the ICDDR,B have been deposited at GenBank/EMBL/DBJ under the accession numbers KC152960 (PLE1) and KC152961 (PLE2). Reprints and permissions information is available at www.nature.com/reprints. The authors declare no competing financial interests. Readers are welcome to comment on the online version of the paper. Correspondence and requests for materials should be addressed to A.C. (andrew.camilli@tufts.edu).

Replication stress links structural and numerical cancer chromosomal instability

Rebecca A. Burrell^{1*}, Sarah E. McClelland^{1*}, David Endesfelder^{1,2}, Petra Groth³, Marie-Christine Weller³, Nadeem Shaikh¹, Enric Domingo⁴, Nnennaya Kanu¹, Sally M. Dewhurst¹, Eva Gronroos¹, Su Kit Chew^{1,5}, Andrew J. Rowan¹, Arne Schenk², Michal Sheffer⁶, Michael Howell¹, Maik Kschischo², Axel Behrens¹, Thomas Helleday³, Jiri Bartek^{7,8}, Ian P. Tomlinson⁴ & Charles Swanton^{1,5}

Cancer chromosomal instability (CIN) results in an increased rate of change of chromosome number and structure and generates intratumour heterogeneity^{1,2}. CIN is observed in most solid tumours and is associated with both poor prognosis and drug resistance^{3,4}. Understanding a mechanistic basis for CIN is therefore paramount. Here we find evidence for impaired replication fork progression and increased DNA replication stress in CIN⁺ colorectal cancer (CRC) cells relative to CIN⁻ CRC cells, with structural chromosome abnormalities precipitating chromosome missegregation in mitosis. We identify three new CIN-suppressor genes (*PIGN* (also known as *MCD4*), *MEX3C* (*RKHD2*) and *ZNF516* (*KIAA0222*)) encoded on chromosome 18q that are subject to frequent copy number loss in CIN⁺ CRC. Chromosome 18q loss was temporally associated with aneuploidy onset at the adenoma–carcinoma transition. CIN-suppressor gene silencing leads to DNA replication stress, structural chromosome abnormalities and chromosome missegregation. Supplementing cells with nucleosides, to alleviate replication-associated damage⁵, reduces the frequency of chromosome segregation errors after CIN-suppressor gene silencing, and attenuates segregation errors and DNA damage in CIN⁺ cells. These data implicate a central role for replication stress in the generation of structural and numerical CIN, which may inform new therapeutic approaches to limit intratumour heterogeneity.

Structural and numerical chromosomal instability are commonly observed together in solid tumours⁶ (Supplementary Fig. 1a–c). This co-occurrence can be experimentally induced by defective mitotic checkpoint function or chromosome attachment to the mitotic spindle, or through pre-mitotic defects affecting chromosome structure, such as faulty DNA repair and replication^{6–10}. However, the mechanisms underlying CIN in cancer remain unclear.

Colorectal cancers can be broadly classified as CIN⁺/aneuploid or CIN⁻/microsatellite unstable³. CIN⁺ cells displayed an increased frequency of chromosome segregation errors compared to CIN⁻ cells¹¹ (median 38% versus 18%, $P = 0.0025$, Mann–Whitney U -test; Supplementary Fig. 2a). To address whether mitotic or pre-mitotic mechanisms are responsible for these segregation errors, we analysed high-resolution images of anaphases in a panel of CIN⁺ CRC cells. Most of the segregation errors consisted of chromosome fragments without centromeres (acentrics; Fig. 1a) and anaphase bridges (54–81%, median 70%; Fig. 1a, b), indicative of structural chromosome aberrations arising through pre-mitotic defects¹². By contrast, only 10–43% of segregation errors were lagging chromosomes with centromeres (median 20%; Fig. 1a, b), suggesting that mitotic dysfunction resulting in improper chromosome attachments⁶ cannot explain most segregation errors in CIN⁺ CRC cells (Supplementary Fig. 2b).

Furthermore, kinetochore distortion of lagging chromosomes (reflecting merotelic attachments⁶) was rare (0–12% of segregation errors, median 8%; Supplementary Fig. 2c). We did not observe differences in mitotic timing, mitotic checkpoint function, sister chromatid cohesion or supernumerary centrioles between CIN⁺ and CIN⁻ cells, and multipolar spindles were infrequent (0–18%, median 8%; Supplementary Fig. 2d–i). These data suggest that mitotic dysfunction occurs at low frequency in CIN⁺ CRC cells, and that most of the observed chromosome segregation errors result from structural chromosome aberrations. Accordingly, 22–71% (median 36%) of CIN⁺ cell metaphases had structurally abnormal chromosomes, including acentric chromosomes, dicentric chromosomes and double-stranded DNA breaks (Fig. 1b, c and Supplementary Fig. 2j).

Next we sought a putative cause for these structural chromosome alterations. Activation of the DNA-damage response has been observed in both colorectal adenomas and carcinomas^{13,14}, and is thought to reflect DNA replication stress^{13,15,16}. Pharmacological induction of replication stress in HCT-116 (CIN⁻) cells resulted in structural chromosome aberrations and segregation errors, 82% of which were bridges or acentric chromosomes (Supplementary Fig. 3a–f). Importantly, numerical chromosome changes were also induced (Supplementary Fig. 3g, h), demonstrating that replication stress can result in both structural and numerical chromosomal instability¹⁷.

DNA replication stress results in several cellular phenotypes including DNA damage in prometaphase^{10,15,16}, ultrafine anaphase DNA bridges (UFBs)¹⁶, and 53BP1-positive nuclear bodies in G1 cells^{15,18} (Fig. 1d and Supplementary Fig. 3i–m). CIN⁺ cells showed increased prometaphase DNA damage (median 74% CIN⁺ versus 34% CIN⁻ cells with ≥ 3 γ H2AX foci; $P = 0.033$, Mann–Whitney U -test; Fig. 1d, e) in the absence of increased oxidative DNA damage (Supplementary Fig. 4a–c). γ H2AX foci were not confined to telomeres (Supplementary Fig. 4d, e). CIN⁺ cells also displayed more 53BP1 nuclear bodies in G1 cells ($P = 0.028$, Mann–Whitney U -test; Fig. 1d, f). Consistent with the hypothesis that replication stress may drive chromosome segregation errors in CIN⁺ cells, UFBs were enriched in anaphases with segregation errors compared with anaphases without segregation errors ($P = 0.00018$, paired t -test; Fig. 1d, g).

To assess DNA replication directly, DNA fibre assays were performed for two CIN⁻ and four CIN⁺ cell lines to measure progression of individual replication forks, fork stalling and asymmetry between sister replication forks. CIN⁺ cells showed significantly slower fork rates than CIN⁻ cell lines (0.56–0.83 kb min⁻¹ versus 1.11–1.12 kb min⁻¹, $P < 0.05$; Fig. 1h, i and Supplementary Fig. 5a, b). Furthermore, there was evidence of increased replication fork stalling and asymmetric sister fork progression in several CIN⁺ cell lines

¹Cancer Research UK London Research Institute, 44 Lincoln's Inn Fields, London WC2A 3LY, UK. ²University of Applied Sciences Koblenz, RheinAhrCampus, Department of Mathematics and Technology, Joseph-Rovan-Allee 2, 53424 Remagen, Germany. ³Science for Life Laboratory, Division of Translational Medicine and Chemical Biology, Department of Medical Biochemistry and Biophysics, Karolinska Institutet, Box 1031, Stockholm S-171 21, Sweden. ⁴Molecular and Population Genetics and NIHR Biomedical Research Centre, The Wellcome Trust Centre for Human Genetics, Oxford OX3 7BN, UK. ⁵UCL Cancer Institute, Paul O'Gorman Building, Huntley Street, London WC1E 6BT, UK. ⁶Department of Physics of Complex Systems, Weizmann Institute of Science, Rehovot 76100, Israel. ⁷Danish Cancer Society Research Center, Strandboulevarden 49, DK-2100 Copenhagen, Denmark. ⁸Institute of Molecular and Translational Medicine, Palacky University Olomouc, CZ-775 15, Czech Republic.

*These authors contributed equally to this work.

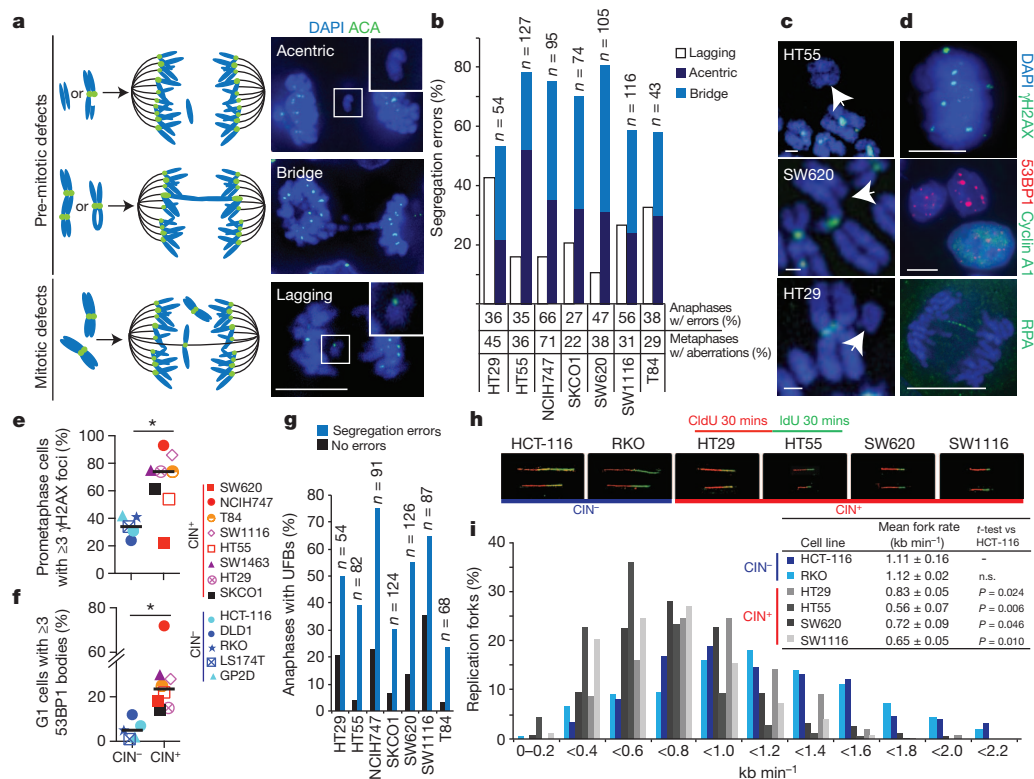


Figure 1 | Replication stress generates chromosome segregation errors in CIN⁺ cells. **a**, Schematic illustrating pre-mitotic and mitotic origins of chromosome segregation errors. Right panels denote example images in SW1116 (CIN⁺) cells stained with 4',6-diamidino-2-phenylindole (DAPI) and anti-centromere antibodies (ACAs). Scale bar, 10 μ m. **b**, Percentage of segregation errors in CIN⁺ cell lines that are lagging chromosomes, acentrics or anaphase bridges. Bridges extend fully between DNA masses; acentrics and lagging chromosomes were distinguished using ACA staining. Segregation errors not classifiable as bridges, lagging chromosomes or acentrics (<15%) are omitted for clarity. Percentage of anaphases showing segregation errors ($n > 100$ per cell line), and metaphases displaying structural aberrations ($n = 38$ –84 per cell line) are shown. **c**, Structurally abnormal chromosomes identified on metaphase chromosome spreads, hybridized to an all-centromere probe (green) and stained with DAPI. Scale bars, 1 μ m. **d**, Replication-stress-associated cellular phenotypes in NCH747 (CIN⁺) cells stained with DAPI

and antibodies as indicated; γ H2AX foci in prometaphase (top); 53BP1 bodies in G1 (cyclin A1⁻) cells (middle); anaphase UFBs, detected with antibodies for the single-stranded DNA-binding protein RPA²⁷ (bottom). Scale bars, 10 μ m. **e**, Percentage of prometaphase DNA damage in CIN⁺ versus CIN⁻ cells ($n > 100$ cells per cell line, $*P = 0.033$). **f**, Percentage of G1 53BP1 bodies in CIN⁺ versus CIN⁻ cells ($n > 250$ cells per cell line, $*P = 0.028$). **g**, Percentage of anaphase UFBs. **h**, **i**, Four CIN⁺ and two CIN⁻ cell lines were incubated sequentially with 5-chlorodeoxyuridine (CldU) and 5-iododeoxyuridine (IdU) for 30 min each. DNA fibre assays were performed and replication rates at individual replication forks were assessed. Representative fibres from each cell line are shown (**h**, original magnification, $\times 63$). **i**, Distribution of replication fork rates (CldU, $n > 300$ forks in total per cell line, $n = 3$ experiments), with mean replication fork rates (CldU, $n > 60$ forks per experiment, mean \pm s.e.m., $n = 3$ experiments) shown in the key (inset). Two-tailed t -test relative to HCT-116 cells.

(Supplementary Fig. 5c–e), consistent with impaired replication fork progression. These data indicate that increased replication stress, as demonstrated using established hallmarks and direct measurement of replication fork progression, may contribute substantially to chromosome missegregation in CIN⁺ CRC cells.

We sought a genetic basis for the increased replication stress and chromosome segregation errors in CIN⁺ cells. Examining whole-exome sequencing data in colorectal tumours from The Cancer Genome Atlas (TCGA)¹⁹, and mutation status for 64 genes in CRC cell lines (COSMIC), showed that the only gene mutated at significantly higher frequencies in CIN⁺ tumours or cell lines was *TP53*, which is also mutated in 13–33% of CIN⁻ tumours and cell lines (Supplementary Fig. 6a, b). Mutations in *TP53* are thought to be permissive for CIN rather than causative²⁰. These data suggest that although mutations in known oncogenes or tumour suppressors may contribute to replication stress in cancer cells^{14,21}, they are unlikely to account exclusively for the increased replication stress in CIN⁺ CRC cells. We therefore addressed whether further genetic aberrations may contribute to CIN.

We proposed that regions of consistent somatic copy number loss in CIN⁺ CRC might encode CIN-suppressor genes, the loss of which could contribute to the induction of chromosome missegregation. To

identify CIN-specific regions of loss, comparative genomic hybridization (CGH) data were analysed for a cohort of 26 aneuploid colorectal tumours and 20 CIN⁺ cell lines. Chromosome 18q was most frequently subject to copy number loss, observed in 88% of aneuploid tumours and 80% of CIN⁺ cell lines (Fig. 2a, b and Supplementary Table 1), consistent with published studies in CRC and other tumour types^{22–24}. Copy number losses in CIN⁺ tumours and cell lines were highly concordant ($P < 0.001$, Fisher's exact test; Supplementary Table 2). Next we examined the temporal sequence and consequences of 18q copy number loss in tumours. In a cohort of 28 adenomas (pre-invasive tumour) with carcinoma in the same specimen (Fig. 2c), 18q loss of heterozygosity (LOH; indicative of copy number loss) was observed in 21 out of 28 (75%) carcinomas, compared with 10 out of 28 (35.7%) adenomas, implicating 18q loss in the adenoma–carcinoma transition. Chromosome 18q LOH was significantly associated with aneuploidy in both adenomas and carcinomas (Fig. 2d and Supplementary Fig. 6c).

To identify candidate CIN-suppressor genes encoded within regions of recurrent copy number loss, HCT-116 cells were transfected with pools of four short interfering RNAs (siRNAs) targeting the most frequently lost genes, present at ≤ 1 copy in at least 30% of CIN⁺ cell lines (94 genes encoded on chromosome 18q; Supplementary

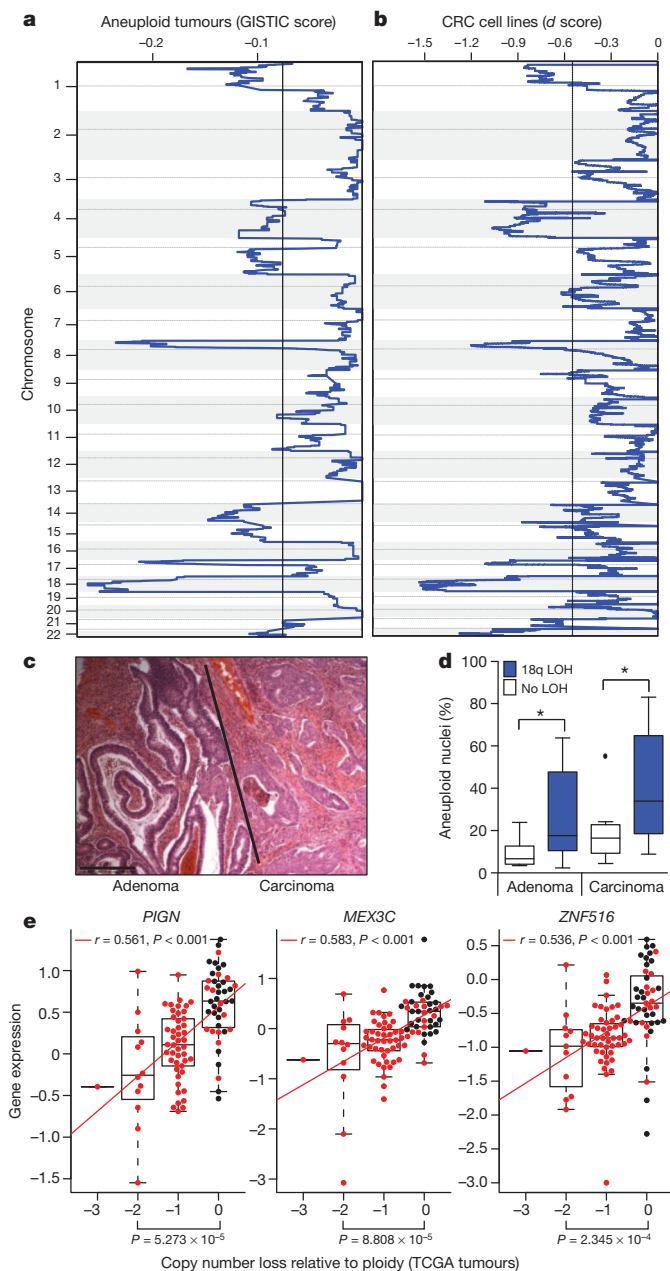


Figure 2 | Somatic copy number loss of chromosome 18q in CIN⁺ CRC. **a**, GISTIC analysis for somatic copy number loss in 26 aneuploid colorectal tumours. $Q = 0.25$ determines significance (black line). **b**, Significance analysis of microarrays (SAM)-based d scores for somatic copy number loss in 20 CIN⁺ CRC cell lines compared to 9 CIN⁻ cell lines. $Q = 0.25$ determines significance, black line. **c**, Haematoxylin and eosin-stained tumour specimen, showing adenoma with adjacent carcinoma. Scale bar, 300 μ m. **d**, Percentage of aneuploid nuclei, measured by DNA image cytometry, in paired adenomas and carcinomas ($n = 20$) with/without 18q LOH (Tukey box plot with outliers shown; * $P < 0.05$, two-tailed t -test). **e**, Spearman's rank correlation between mRNA expression and DNA copy number for PIGN, MEX3C and ZNF516 in CIN⁻ ($n = 28$, black dots) versus CIN⁺ ($n = 74$, red dots) tumours (TCGA). Tumours were defined as CIN⁺ based on a weighted genome integrity index > 0.2 (see Methods). Statistic: Mann–Whitney U -test.

Table 3). After 48 h, anaphase segregation errors were quantified (Supplementary Fig. 7a). Importantly, this approach would identify both mitotic and pre-mitotic defects. siRNA pools inducing segregation errors to ≥ 3 standard deviations above the frequency in control-transfected cells were assessed in validation assays. All sequences targeting PIGN, MEX3C and ZNF516 induced segregation errors and efficiently depleted messenger RNA levels (Supplementary Fig. 7b–d).

Additional independent siRNA sequences targeting each of the three genes also induced segregation errors (Supplementary Fig. 7e), and these genes were prioritized for further analysis, although we cannot exclude a contribution of other genes encoded on 18q to CIN. Of note, MEX3C is the only protein-coding gene located between two genes implicated in CRC carcinogenesis, DCC and SMAD4. Copy number loss of PIGN, MEX3C or ZNF516 is observed in 85% of the 20 CIN⁺ cell lines and 84% of aneuploid tumours ($n = 103$) in the independent TCGA cohort¹⁹, with loss of all three genes in 70% of CIN⁺ cell lines and 79% of aneuploid tumours (Supplementary Table 4). Importantly, reduced copy number correlated significantly with reduced mRNA expression for all three genes, both in the TCGA tumour cohort and CRC cell lines (Fig. 2e, Supplementary Fig. 8a and Supplementary Table 5).

We next ensured that off-target siRNA effects reported against the mitotic checkpoint protein MAD2 and the DNA repair protein RAD51 were not causing chromosome missegregation²⁵ (Supplementary Fig. 8b–e). Two siMEX3C sequences partially depleted MAD2 protein, and were excluded from further analysis. Furthermore, expression of exogenous green fluorescent protein (GFP)-tagged MEX3C rescued segregation errors induced after silencing endogenous MEX3C using a 3'-untranslated region (UTR)-targeted siRNA, and expression of siRNA-resistant PIGN-GFP and ZNF516-GFP reduced segregation errors induced by depletion of endogenous PIGN or ZNF516 (Supplementary Fig. 8f). Silencing each CIN suppressor also induced segregation errors in two further CIN⁻ CRC cell lines, DLD1 and RKO, and in 18q-normal CIN⁺ NCIH508 cells (Supplementary Fig. 9a–c). Induction of segregation errors was independent of oncogenic KRAS signalling in HCT-116 cells, as segregation errors were also induced after CIN-suppressor gene silencing in an isogenic KRAS^{wild-type/-} cell line (Supplementary Fig. 9d).

CIN-suppressor gene silencing (using siPIGN, siMEX3C and siZNF516 siRNAs) in HCT-116 cells primarily induced acentric chromosomes and anaphase bridges (Fig. 3a) in the absence of gross mitotic defects (data not shown), similar to observations in CIN⁺ CRC cell lines with 18q loss (Fig. 1b). This suggested a pre-mitotic origin for these chromosome segregation errors and, accordingly, we observed an increased frequency of structurally abnormal chromosomes (Fig. 3a, b and Supplementary Fig. 10a). To assess chromosome non-disjunction, HCT-116 cell lines stably expressing short hairpin RNAs (shRNAs) were constructed. Silencing each CIN-suppressor gene (using shPIGN, shMEX3C and shZNF516) increased segregation error frequency (Supplementary Fig. 10b), and single cell clones grown from each cell line displayed significantly increased intracolony deviation for chromosomes 2 and 15 (Fig. 3c, d and Supplementary Fig. 10c), indicating that CIN-suppressor gene silencing induces both structural and numerical instability.

We next examined replication stress after CIN-suppressor gene silencing. Increased prometaphase DNA damage was observed (Fig. 3e), and this increased concomitantly with, rather than after, the rise in segregation error frequency (Supplementary Fig. 10d), supporting the hypothesis that the observed DNA damage reflects a cause, rather than a consequence, of segregation errors. Silencing each CIN-suppressor gene also resulted in an increased number of 53BP1 bodies in G1 cells (Fig. 3f), which were unaffected by cytokinesis inhibition, and are therefore unlikely to reflect cytokinesis-induced chromosome damage^{7,15} (Supplementary Fig. 10e–g). Silencing PIGN and ZNF516 also significantly increased the frequency of UFBs (Fig. 3g). Consistent with loss of CIN-suppressor genes contributing to replication stress in CIN⁺ cells, transient co-expression of PIGN, MEX3C and ZNF516 resulted in a partial reduction in G1 53BP1 bodies in three CIN⁺ cell lines with 18q loss (Supplementary Fig. 11a–d). DNA fibre assays revealed a shift in distribution towards reduced replication fork speeds after silencing each of the CIN-suppressor genes in HCT-116 cells, with reduced average fork rates after silencing PIGN and ZNF516 (Fig. 3h, i and Supplementary Fig. 12a, b). Furthermore, we observed

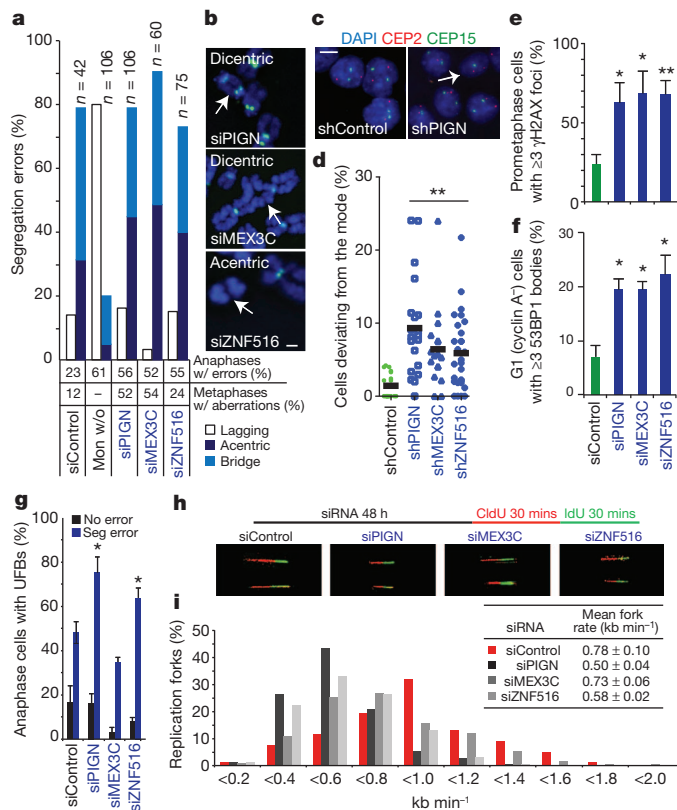


Figure 3 | Candidate suppressors of replication stress and CIN encoded on chromosome 18q. **a**, **b**, CIN-suppressor genes were silenced in HCT-116 (CIN⁺) cells using siRNAs for 48 h. siControl denotes a non-targeting siRNA control. **a**, Percentage of segregation errors accounted for by lagging chromosomes, acentrics and anaphase bridges. Other segregation errors (<15%) are omitted for clarity. For comparison, segregation errors arising via improper chromosome attachments were induced by monastrol (mon) treatment (100 μ M, 1 h, 75-min release). Percentages of anaphases displaying segregation errors and metaphases displaying ≥ 1 structurally abnormal chromosome ($n > 100$) are shown. **b**, Examples of structurally abnormal chromosomes as indicated. Scale bar, 1 μ m. **c**, **d**, Cell lines stably expressing shRNAs as indicated were seeded at low density on glass slides to allow colony formation. Slides were fixed and hybridized to DNA probes for centromeres 2 and 15. **c**, Example images of control and shPIGN cells. Arrow indicates cell with loss of chromosome 15. Scale bar, 10 μ m. **d**, Percentage deviation from the modal centromere copy number per colony (mean of two probes (CEP2 and CEP15)). Lines are median values; ** $P < 0.01$, Dunn's multiple comparison test. **e**–**g**, HCT-116 cells were scored for replication-stress-associated phenotypes after siRNA-mediated CIN-suppressor gene silencing: percentage of prometaphases with ≥ 3 γ H2AX foci ($n > 100$ per experiment) (**e**); percentage of G1 cells with ≥ 3 53BP1 bodies ($n > 150$ per experiment) (**f**); percentage of anaphases with UFBs ($n = 100$ per experiment) (**g**). Data in **e**–**g** are mean \pm s.e.m., $n = 3$; * $P < 0.05$, ** $P < 0.01$, two-tailed t -test. **h**, **i**, DNA fibre assays were performed after siRNA transfection as indicated. Representative fibre images for siRNA transfections are indicated as shown (**h**, original magnification, $\times 63$). **i**, Distribution of replication fork rates ($n > 200$ forks in total per siRNA transfection, $n = 2$ experiments), with mean fork rates ($n > 70$ forks per experiment, mean \pm s.d., $n = 2$ experiments) shown in the key (inset).

increased sister fork asymmetry after silencing each of the three genes (Supplementary Fig. 12c), consistent with impaired replication fork progression.

These data suggest that segregation errors resulting from CIN-suppressor gene silencing are driven by replication stress. To test this hypothesis further, HCT-116 cells transfected with siRNAs against CIN-suppressor genes were supplemented with nucleosides, previously shown to reduce replication-induced DNA damage⁵. Nucleosides significantly reduced the induction of segregation errors after silencing of *PIGN* (62% to 32%), *MEX3C* (57% to 36%) and *ZNF516* (43%

to 34%), whereas control segregation errors were unaffected (Fig. 4a). We then tested whether nucleoside supplementation could attenuate chromosome missegregation in CIN⁺ cell lines with 18q loss. Nucleoside supplementation significantly reduced segregation error frequency by 45–55% and attenuated prometaphase DNA damage by 28–43% in four CIN⁺ cell lines (Fig. 4b, c and Supplementary Fig. 13a), indicating suppression of replication-induced DNA damage and subsequent chromosome missegregation. The extent of the nucleoside-mediated reduction in segregation errors indicates that *de novo* generation of structural chromosome aberrations is responsible for a large proportion of chromosome missegregation events in CIN⁺ cells. By contrast, nucleoside supplementation did not affect the segregation error frequency in four CIN[−] cell lines or 18q-normal CIN[−] NCIH508 cells (Supplementary Fig. 13b, c). Nucleoside supplementation did not affect proliferation, cell cycle distribution, or cellular ATP levels⁵ (Supplementary Fig. 14a–f).

Our findings implicate replication stress as a major driver of chromosomal instability in CRC. In addition to impaired replication fork progression, CIN⁺ cells exhibit replication-stress-associated DNA damage and structurally abnormal chromosomes that missegregate during mitosis, linking structural and numerical instability. Supplementing CIN⁺ cells with nucleosides reduced both DNA damage and segregation errors, supporting a direct role for replication stress in driving CIN. Given the complex nature of replication stress and CIN, it is likely that there are several genetic aberrations contributing to these phenotypes within an individual tumour. Here, we suggest a putative genetic mechanism that may contribute to CIN in CRC, through the recurrent loss of a region on chromosome 18q, encoding three newly identified suppressors of replication stress and chromosome missegregation. The loss of chromosome 18q in many solid tumour types suggests the potential contribution of this locus to CIN in tumours beyond CRC. Furthermore, reports of DNA replication stress across several tumour types suggest replication stress may be a common route to CIN and intratumour heterogeneity^{13,26}. Efforts to target or restrain replication stress may therefore provide a rational approach to limit tumour diversity, genome evolution and adaptation.

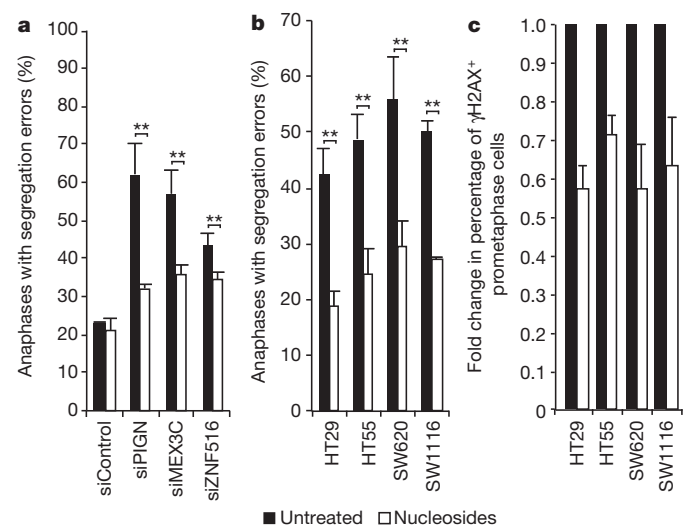


Figure 4 | Nucleoside supplementation reduces segregation error frequency and prometaphase DNA damage. **a**, Percentage of HCT-116 anaphases with segregation errors, with/without 48 h nucleoside supplementation 24 h after siRNA transfection ($n = 30$). **b**, Percentage of anaphases with segregation errors with/without 48 h nucleoside supplementation in CIN⁺ cell lines ($n = 30$). **c**, Fold change in the percentage of prometaphases exhibiting ≥ 3 γ H2AX foci with/without 48 h nucleoside supplementation in CIN⁺ cell lines ($n \geq 100$ cells per condition per cell line). Data are mean \pm s.e.m., $n = 3$ experiments; ** $P < 0.01$, two-tailed t -test. Unnormalized data are shown in Supplementary Fig. 13a.

METHODS SUMMARY

Cells were maintained at 37 °C at 5% CO₂. FISH was performed as described¹¹. The all-centromere probe was used as per manufacturer's instructions. Image acquisition was performed using a Deltavision microscope in a temperature and CO₂-controlled chamber. siRNA transfections were at 40 nM, using Lipofectamine RNAi-max (Invitrogen). Bioinformatics analysis was performed using R.

Full Methods and any associated references are available in the online version of the paper.

Received 13 April 2012; accepted 24 January 2013.

- Gerlinger, M. *et al.* Intratumor heterogeneity and branched evolution revealed by multiregion sequencing. *N. Engl. J. Med.* **366**, 883–892 (2012).
- Ding, L. *et al.* Clonal evolution in relapsed acute myeloid leukaemia revealed by whole-genome sequencing. *Nature* **481**, 506–510 (2012).
- Lengauer, C., Kinzler, K. W. & Vogelstein, B. Genetic instabilities in human cancers. *Nature* **396**, 643–649 (1998).
- McGranahan, N., Burrell, R. A., Endesfelder, D., Novelli, M. R. & Swanton, C. Cancer chromosomal instability: therapeutic and diagnostic challenges. *EMBO Rep.* **13**, 528–538 (2012).
- Bester, A. C. *et al.* Nucleotide deficiency promotes genomic instability in early stages of cancer development. *Cell* **145**, 435–446 (2011).
- Thompson, S. L. & Compton, D. A. Chromosomes and cancer cells. *Chromosome Res.* **19**, 433–444 (2011).
- Janssen, A., van der Burg, M., Szuhai, K., Kops, G. J. & Medema, R. H. Chromosome segregation errors as a cause of DNA damage and structural chromosome aberrations. *Science* **333**, 1895–1898 (2011).
- Crasta, K. *et al.* DNA breaks and chromosome pulverization from errors in mitosis. *Nature* **482**, 53–58 (2012).
- Pampalona, J., Soler, D., Genesca, A. & Tusell, L. Whole chromosome loss is promoted by telomere dysfunction in primary cells. *Genes Chromosom. Cancer* **49**, 368–378 (2010).
- Ichijima, Y. *et al.* DNA lesions induced by replication stress trigger mitotic aberration and tetraploidy development. *PLoS ONE* **5**, e8821 (2010).
- Thompson, S. L. & Compton, D. A. Examining the link between chromosomal instability and aneuploidy in human cells. *J. Cell Biol.* **180**, 665–672 (2008).
- Gisselsson, D. Classification of chromosome segregation errors in cancer. *Chromosoma* **117**, 511–519 (2008).
- Bartkova, J. *et al.* DNA damage response as a candidate anti-cancer barrier in early human tumorigenesis. *Nature* **434**, 864–870 (2005).
- Tort, F. *et al.* Retinoblastoma pathway defects show differential ability to activate the constitutive DNA damage response in human tumorigenesis. *Cancer Res* **66**, 10258–10263 (2006).
- Lukas, C. *et al.* 53BP1 nuclear bodies form around DNA lesions generated by mitotic transmission of chromosomes under replication stress. *Nature Cell Biol.* **13**, 243–253 (2011).
- Chan, K. L., Palmal-Pallag, T., Ying, S. & Hickson, I. D. Replication stress induces sister-chromatid bridging at fragile site loci in mitosis. *Nature Cell Biol.* **11**, 753–760 (2009).
- Kawabata, T. *et al.* Stalled fork rescue via dormant replication origins in unchallenged S phase promotes proper chromosome segregation and tumor suppression. *Mol. Cell* **41**, 543–553 (2011).
- Harrigan, J. A. *et al.* Replication stress induces 53BP1-containing OPT domains in G1 cells. *J. Cell Biol.* **193**, 97–108 (2011).
- Cancer Genome Atlas Research Network. Comprehensive molecular characterization of human colon and rectal cancer. *Nature* **487**, 330–337 (2012).
- Bunz, F. *et al.* Targeted inactivation of p53 in human cells does not result in aneuploidy. *Cancer Res.* **62**, 1129–1133 (2002).
- Halazonetis, T. D., Gorgoulis, V. G. & Bartek, J. An oncogene-induced DNA damage model for cancer development. *Science* **319**, 1352–1355 (2008).
- Rowan, A. *et al.* Refining molecular analysis in the pathways of colorectal carcinogenesis. *Clin. Gastroenterol. Hepatol.* **3**, 1115–1123 (2005).
- Pasello, G. *et al.* DNA copy number alterations correlate with survival of esophageal adenocarcinoma patients. *Mod. Pathol.* **22**, 58–65 (2009).
- Yatsuoka, T. *et al.* Association of poor prognosis with loss of 12q, 17p, and 18q, and concordant loss of 6q/17p and 12q/18q in human pancreatic ductal adenocarcinoma. *Am. J. Gastroenterol.* **95**, 2080–2085 (2000).
- Sigoillot, F. D. *et al.* A bioinformatics method identifies prominent off-targeted transcripts in RNAi screens. *Nature Methods* **9**, 363–366 (2012).
- Dereli-Oz, A., Versini, G. & Halazonetis, T. D. Studies of genomic copy number changes in human cancers reveal signatures of DNA replication stress. *Mol. Oncol.* **5**, 308–314 (2011).
- Chan, K. L. & Hickson, I. D. On the origins of ultra-fine anaphase bridges. *Cell Cycle* **8**, 3065–3066 (2009).

Supplementary Information is available in the online version of the paper.

Acknowledgements We thank A. Straube for reagents. C.S. is a senior Medical Research Council clinical research fellow and is funded by Cancer Research UK, the Medical Research Council, EU FP7 (projects PREDICT and RESPONSIFY), Prostate Cancer Foundation, and the Breast Cancer Research Foundation. We thank A. Futreal and The Wellcome Trust Sanger Centre and The Cancer Genome Atlas Research Network for providing genomics data. I.P.T. is supported by the Oxford Biomedical Research Centre and Cancer Research UK. J.B. is funded by the Danish Cancer Society, the Lundbeck Foundation, and the European Commission (FP7 projects DDResponse, Biomedreg and Infla-Care). T.H. is funded by the Swedish Cancer Society, the Swedish Research Council and the Torsten and Ragnar Söderberg Foundation.

Author Contributions C.S., R.A.B., S.E.M., J.B. and T.H. devised experiments. R.A.B. and S.E.M. performed most cell biological experiments with help from N.S., S.K.C., E.G., S.M.D., A.J.R. and N.K. D.E., A.S. and M.S. performed bioinformatics analysis supervised by M.K. P.G., M.-C.W. and T.H. performed and analysed the DNA fibre assays. E.D. and I.P.T. provided the adenoma-in-carcinoma cohort and CGH for aneuploid tumours. M.H. and A.B. provided experimental advice. C.S. supervised all aspects of the project. C.S., R.A.B., S.E.M., I.P.T. and J.B. wrote the paper. All authors discussed results and approved the manuscript.

Author Information Reprints and permissions information is available at www.nature.com/reprints. The authors declare no competing financial interests. Readers are welcome to comment on the online version of the paper. Correspondence and requests for materials should be addressed to C.S. (charles.swanton@cancer.org.uk).

METHODS

Cell lines. Cells were maintained at 37 °C with 5% CO₂ in DMEM with L-glutamine (Gibco) or RPMI 1640 media (NCIH747 cells; Gibco), supplemented with 10% FBS, and 1/10,000 units of penicillin–streptomycin (Sigma). Cell-line CIN status was defined as described previously²⁸.

Cell treatments. All compounds were from Sigma. Nocodazole: 50 or 100 ng ml⁻¹; aphidicolin: 0.2 µM, 24 h; monastrol wash-out: 100 µM, 1 or 16 h, washed three times in fresh medium before 75 min recovery; blebbistatin: 100 µM, 4 h. The nucleosides adenosine, cytidine, guanosine and uridine were freshly prepared for each experiment, filter sterilized, and used at 0.3 or 30 µM. H₂O₂: 350 µM, 4 h, before 16 h recovery.

Metaphase spreads and clonal FISH preparation. Metaphase spreads: cells were collected after 1-h treatment with 10 mM colcemid (Gibco), and swelled with KCl (0.4%, 37 °C, 7 min) before fixation in 3:1 methanol:acetic acid. Cells were dropped onto glass slides and aged for ~2 weeks. All-human centromere probe (Poseidon) was used according to the manufacturer's instructions.

Clonal FISH: 500 cells were expanded into colonies of 30–60 cells on glass slides before KCl treatment and fixation in 3:1 methanol:acetic acid. Slides were denatured (70 °C in 2× sodium citrate (SSC)/75% formamide, 2 min, quenched in ice-cold 70% ethanol) and dehydrated through an ethanol series. Probes (CEP2 (D2Z1 Spectrum orange), CEP15 (D15Z1 Spectrum green; Abbott Molecular Probes)) were denatured (90 °C, 6 min) and hybridized to slides (16 h, 37 °C), and then washed (50% formamide/2× SSC and 2× SSC at 42 °C, followed by 4× SSC and PBS washes at room temperature). Slides were dehydrated and mounted in Vectashield hardset plus DAPI mounting medium (H-1500).

Immunofluorescence. Cells grown on coverslips were fixed in: 10% Triton X-100, 1 M PIPES, 0.5 M EGTA, 1 M MgCl₂ and 4% formaldehyde. Mouse primary antibodies: α-tubulin (1:1,000; Sigma T6074), NDC80 (1:800; Abcam Ab3613), centrin3 (1:1,000; Abcam Ab54531), cyclin A1 (1:350; Santa Cruz sc-56299), phospho-histone H2A.X Ser 139 (1:500; Millipore 05-636), and RPA (1:500; Neomarkers MS-691-P0). Rabbit primary antibodies: 53BP1 (1:500; Santa Cruz sc-22760), β-tubulin (1:1,000, Abcam), and human ACAs (1:250; Antibodies Incorporated). Secondary antibodies (1:500; Molecular Probes): goat anti-mouse conjugated to AlexaFluor 488 (A11017), goat anti-rabbit AF594 (A11012), and goat anti-human AF647 (A21445). DNA was stained with DAPI (Roche) and coverslips mounted in Vectashield (Vector H-1000). Preparation and immunostaining of metaphase spreads was performed as described previously²⁹. Most images were acquired using an Olympus DeltaVision RT microscope (Applied Precision, LLC) equipped with a Coolsnap HQ camera. Three-dimensional image stacks were acquired in 0.2-µm steps, using an Olympus ×100 or ×60 1.4 numerical aperture UPlanSApo oil immersion objective. Deconvolution of image stacks and quantitative measurements was performed with SoftWorx Explorer (Applied Precision, LLC).

DNA fibre assays. Cells were plated (with/without siRNA transfection) 48 h before sequential pulse-labelling with CldU and IdU (Sigma Aldrich, 30 min each) and collection for DNA fibre assays as described previously³⁰.

RNA interference. siRNA transfections were performed at 40 nM by reverse transfection with Lipofectamine RNAiMax (Invitrogen). See Supplementary Table 6 for sequences used. The screen was performed in 12-well plates (0.5 × 10⁵ HCT-116 cells per well on coverslips) using siGENOME SMARTpools (Dharmacon) with one control well per plate (Dharmacon control no.2). After 48 h, cells were fixed and stained for α-tubulin. Thirty anaphases per siRNA pool were scored manually for segregation errors.

DNA transfections and GFP-tagged construct mutagenesis. H2B-mRFP cells: cells were transfected with pH2B-mRFP (gift from A. Straube) using Eugene 6.0 (Promega), and selected in 1 mg ml⁻¹ G418 before flow-sorting for mRFP expression. Cells were maintained in 500 µg ml⁻¹ G418.

shRNA cell-line synthesis: HCT-116 cells were transfected with shRNA plasmids (Open Biosystems, see Supplementary Table 7) using Eugene 6.0 (Promega) and selected in 0.5 µM puromycin for 2–3 weeks. Three colonies per shRNA were amplified, RNA was extracted and silencing assessed by quantitative PCR (qPCR). Colonies with efficient silencing were selected. Cell lines were maintained in 0.5 µM puromycin.

PIGN/MEX3C/ZNF516–GFP transfections: for siRNA rescue experiment in Supplementary Fig. 8f, 1 µg (siRNA-insensitive PIGNins–GFP and MEX3C–GFP) or 0.5 µg (ZNF516ins–GFP) DNA was either co-transfected with siRNA using Lipofectamine RNAiMax for 48 h (MEX3C) or transfected 24 h after siRNA transfection using Lipofectamine 2000 (Invitrogen) for 24 h (PIGN and ZNF516). For co-transfection into CIN⁺ cell lines, 2 µg total DNA was transfected using Lipofectamine LTX plus (Invitrogen), according to the manufacturer's instructions. PIGN–GFP and MEX3C–GFP were from GeneCopoeia, ZNF516–GFP was from Origene.

siRNA-insensitive mutagenesis: the Quikchange XL site-directed mutagenesis kit (Stratagene) was used to create three base mismatches in siRNA target sequences for PIGN oligo 3 and ZNF516 oligo 3 in PIGN–GFP and ZNF516–GFP, respectively. Mutagenesis was confirmed by sequencing.

RNA extraction and reverse transcriptase qPCR. RNA was extracted using the Qiagen RNeasy kit. Reverse transcription was performed using the first-strand cDNA synthesis kit (Amersham). qPCR was performed in 96-well plates using pre-designed TaqMan probe/primers on a ABI 7900HT system (Applied Biosystems). All reactions were performed in duplicate. The relative amount of mRNA was calculated using the comparative C_t method after normalization to GAPDH expression.

Western blotting. Cellular protein extracts were separated on NuPAGE 4–12% Bis-Tris gels (Invitrogen) then transferred to polyvinylidene fluoride membrane (Millipore). Membranes were incubated with antibodies: MAD2 (mouse 1:1,000; BD-Biosciences 610678), RAD51 (mouse 1:1,000; Abcam ab213), GFP (mouse 1:1,000; Santa Cruz sc-9996), and Turbo–GFP (rabbit 1:1,000; Evrogen) in 5% milk in TBS, and detected with a horseradish peroxidase (HRP)-conjugated secondary antibody (1:10,000; Dako) and chemiluminescence (ECL, Amersham Biosciences). Loading was quantified with HRP-conjugated anti-β-actin (1:100,000; Sigma).

Time-lapse microscopy. H2B-mRFP-labelled cells were grown in 8-well chamber slides (LabTek). Fourteen-micrometre z-stacks (seven images) were acquired using an Olympus ×40 1.3 numerical aperture UPlanSApo oil immersion objective every 3 min for 6 h using a DeltaVision microscope in a temperature and CO₂-controlled chamber. Analysis was performed using SoftWorx Explorer.

Flow cytometry. Mitotic index: cells were fixed in 70% ethanol and stained with a mouse anti-MPM2 antibody (3:500, overnight at 4 °C; Millipore 05-368) and then a goat anti-mouse AF647 (Molecular Probes; A21463) and DAPI.

8-oxo-guanine: cells (with/without H₂O₂ treatment) were fixed in 4% formaldehyde, DNA denatured in 2 M HCl for 20 min, and stained with mouse anti-8-oxoguanine (1:200; Abcam ab62623). Data were processed using FlowJo software.

Immunohistochemistry. Paraffin-embedded cell pellets (with/without H₂O₂ treatment), were sectioned at 4 µm, de-waxed in xylene, then rehydrated through ethanol series to water. Endogenous peroxidase was blocked (1.6% H₂O₂, 10 min), followed by incubation with 10% normal horse serum (30 min). Sections were incubated with mouse anti-8-oxoguanine (1:1,000, 1 h), washed three times in PBS, then incubated with biotinylated horse anti-mouse antibodies (1:400, 35 min; Vector Labs). After washing, peroxidase substrate (DAB) was added (2 min), slides were washed in water and counterstained with haematoxylin. Slides were washed, dehydrated and mounted in DPX-type mountant.

Proliferation assays. Plates were imaged using an IncuCyte long-term in-situ cell imaging system, within an incubator. Phase-contrast images were acquired every 2 h for 72 h and the percentage of cell monolayer confluence was determined automatically. Outlying wells were excluded, and growth curves constructed. Growth rates were calculated by measuring the gradient of the linear growth phase. **ATP measurement.** After nucleoside supplementation, cells were treated with Cell Titer Glo reagent (Promega). Control measurements were taken from wells containing media only with/without nucleosides. ATP levels were normalized to the biomass per well (*in vitro* toxicology assay kit sulforhodamine B solution, Sigma).

SNP 6.0 array processing. Cell lines: Affymetrix single nucleotide polymorphism (SNP) 6.0 data were obtained for 20 CIN⁺ and 9 CIN[−] cell lines (Wellcome Trust Sanger Institute). Integer copy numbers were estimated for each SNP probe using the PICNIC algorithm³¹.

TCGA: Affymetrix SNP 6.0 data were downloaded for 365 CRC samples and logR ratios and allelic differences were estimated by the Affymetrix Genotyping Console. Samples that failed the Affymetrix quality control parameters were excluded. All tumours with <60% tumour nuclei (based on pathological estimates of adjacent sections) were excluded. To estimate copy number, the GAP algorithm was used³². Ploidy was estimated by calculating the weighted median copy number across all copy number segments, with weights equal to the segment length. Copy number segments of loss and gain were defined relative to the ploidy status of each sample by subtracting the ploidy estimate from the estimated copy number of the segment.

Karyotypic complexity scores. The structural complexity score was defined as the sum of all structurally aberrant regions. Regions of intrachromosomal gain and loss were defined relative to the modal copy number of the chromosome, and each region counted as one structural aberration. To avoid overestimation, aberrant regions <1 megabase were excluded. The numerical complexity score was the sum of all whole chromosome gains and losses (chromosomes with >75% of SNP copy number values higher or lower than the ploidy of the sample were counted as whole chromosome gains or losses, respectively). Several copy number events affecting the same chromosome were scored separately (for example, −2 copies =

2 chromosome losses). The structural and numerical complexity scores were divided by 1.5 for triploid cell lines, and by 2 for tetraploid cell lines, to account for the increased likelihood of karyotypic abnormalities in polyploid genomes.

Weighted genome instability index: because FACS-based DNA index measures were not available for the TCGA tumours, and information about the microsatellite instability status was unavailable for a sufficient number of tumours, an alternative means of classification was required. The genome instability index (GII)³³ is the percentage of SNPs across the genome present at an aberrant copy number, relative to the baseline ploidy of the sample. We adapted the GII to account for variation in chromosome size, so that large chromosomes do not have a greater effect on the score than small chromosomes: the percentage of aberrant SNPs for each chromosome was calculated separately, and the mean percentage aberration was then calculated across all 22 chromosomes. To define a threshold for CIN⁻ versus CIN⁺, the weighted GII was calculated for the cell lines. A threshold of 0.2 accurately distinguished CIN⁺ from CIN⁻, as previously defined²⁸. The same threshold was then applied to the TCGA cohort of tumours.

Sequencing data (TCGA). Preprocessed level 2 somatic mutation data was obtained from the TCGA¹⁹ for 101 colorectal tumours for which SNP 6.0 copy number data was also available. All genes with ≤ 5 somatic mutations were excluded from the analysis. Colorectal tumours were classified as CIN⁺ using weighted GII > 0.2 . Somatic mutation data for the 29 colorectal cancer cell lines were obtained from the COSMIC database (<http://cancer.sanger.ac.uk/cancergenome/projects/cosmic/>). The association of CIN status with somatic mutation status of *TP53*, *APC*, *SMAD4* and *KRAS* was tested with one-sided Fisher's exact tests, and the *P* values were adjusted for multiple testing with the Benjamini and Hochberg method³⁴.

Defining somatic copy number losses in CIN⁺ versus CIN⁻ tumours and cell lines. Aneuploid tumours: bacterial artificial chromosome (BAC) array-CGH data were obtained for 26 aneuploid tumour samples, and segmented by circular binary segmentation (R package DNACopy). The genomic identification of significant targets in cancer (GISTIC) algorithm³⁵ was used to identify regions of consistent gain and loss, with thresholds of 0.1 or -0.1 for gain or loss, respectively, and a *Q* value threshold of 0.25. Aneuploidy was defined by flow cytometry (DNA index > 1.2).

Cell lines: minimum consistent regions of genomic alteration across all cell lines were assessed for DNA copy number. Each region in each cell line was normalized to the ploidy baseline of the cell line to give X_{norm} and was then defined as either lost (copy number $<$ ploidy baseline) or not lost (copy number \geq ploidy baseline) and set to 0. Each region was assessed for gain in the same manner. To test for statistical significance between CIN⁺ and CIN⁻ cell lines, a *d* score for each lost region was computed by calculating the mean normalized copy number X_{norm} across CIN⁺ ($\text{mean}(X_{\text{norm},C})$) and CIN⁻ ($\text{mean}(X_{\text{norm},M})$) cell lines, thereby accounting for both amplitude and frequency of genomic aberrations. SAM (R package siggenes) was then performed with a modified two-sample *t*-statistic:

$$d(i) = \frac{\text{mean}(X_{\text{norm},C}(i)) - \text{mean}(X_{\text{norm},M}(i))}{s(i) + s_0}$$

The parameter $s(i)$ defines the region-specific standard deviation³⁶. In contrast to a standard two-sample *t*-statistic, SAM includes an additional parameter s_0 , which decreases the influence of high sample variance. This was empirically set to 0.5, resulting in a balanced weighting of frequency and amplitude. To detect significant regions, we randomly permuted ($N = 10,000$) SNP probes for each sample separately. To save computation time, we randomly drew copy numbers for each sample, setting the probability for a given copy number to the percentage of SNP probes showing this copy number level across the genome. For each tested region, *P* values were estimated by counting the percentage of permutation *d* scores greater or equal than the observed *d* score. To adjust for multiple testing, *Q* values were estimated with the R-package qvalue and genes with $Q < 0.25$ were called significant. To ensure selection of genes consistently altered across CIN⁺ cell lines, genomic changes not seen in $\geq 50\%$ of cell lines were excluded from

further analysis. Genes were then mapped to regions using the R package BioMart³⁷. All genes present at ≤ 1 copies in $\geq 30\%$ of CIN⁺ cell lines, and no more than 1 CIN⁻ cell line, were selected for functional investigation.

Carcinoma-in-adenoma samples. Twenty archival formaldehyde-fixed and paraffin-embedded tumours showing adjacent but discrete colorectal carcinoma and adenoma were identified. Samples and records were used in accordance with UK research ethics approval (MREC06/Q1702/99). Haematoxylin and eosin slides of the samples were reviewed, regions marked as normal (if present)/adenoma/carcinoma, and used as a guide to take tissue from each region from unstained slides by needle microdissection. DNA was extracted with standard proteinase K digestion, and purified (DNeasy kit, Qiagen). Ploidy analysis was performed using automated image-based cytometry (Fairfield Imaging) as previously described^{38,39}.

LOH analysis: SNP arrays: the Illumina Sentrix Beadarray human linkage mapping panel version IVb was used according to the Goldengate genotyping assay instructions (Illumina). DNA was amplified, fragmented and hybridized to the Beadchip, followed by single-base extension. Beadchips were stained, dried and scanned using a Beadarray reader (Illumina). Image data were visualized using Genomestudio (Illumina). All samples had call rates above 0.97. Adenomas and carcinomas were marked as having LOH or no LOH in 18q according to the absence or presence of heterozygous alleles respectively.

LOH analysis using microsatellites: standard PCR conditions were used with the forward primer fluorescently labelled with the fluorescent dyes HEX or FAM. At each marker, LOH was considered present when a peak area in the adenoma or the carcinoma was reduced to 50% of the other allele, relative to the normal paired DNA. Up to five microsatellites in 18q21 (D18S46, D18S1110, D18S35, D18S69 and D18S1407) were analysed. All PCRs were performed twice and all samples analysed with SNP arrays had concordant results.

Gene expression analysis. TCGA: Agilent 244K custom gene expression (G4502A-07-3) data were downloaded for 154 CRC samples and print-tip normalized with the R-package marray. Duplicated probes were averaged.

Cell lines: Affymetrix HT-HGU133A microarray data for 20 CIN⁺ and 9 CIN⁻ cell lines were obtained from the Wellcome Trust Sanger Institute. The data were RMA-normalized with the R-package affy. Spearman's rank correlation coefficient was used for the correlation of copy number and expression data.

28. Lee, A. J. *et al.* Chromosomal instability confers intrinsic multidrug resistance. *Cancer Res.* **71**, 1858–1870 (2011).
29. Cesare, A. J. *et al.* Spontaneous occurrence of telomeric DNA damage response in the absence of chromosome fusions. *Nature Struct. Mol. Biol.* **16**, 1244–1251 (2009).
30. Groth, P. *et al.* Methylated DNA causes a physical block to replication forks independently of damage signalling, *O*⁶-methylguanine or DNA single-strand breaks and results in DNA damage. *J. Mol. Biol.* **402**, 70–82 (2010).
31. Greenman, C. D. *et al.* PICNIC: an algorithm to predict absolute allelic copy number variation with microarray cancer data. *Biostatistics* **11**, 164–175 (2010).
32. Popova, T. *et al.* Genome Alteration Print (GAP): a tool to visualize and mine complex cancer genomic profiles obtained by SNP arrays. *Genome Biol.* **10**, R128 (2009).
33. Chin, S. F. *et al.* High-resolution aCGH and expression profiling identifies a novel genomic subtype of ER negative breast cancer. *Genome Biol.* **8**, R215 (2007).
34. Benjamini, Y. & Hochberg, Y. Controlling the false discovery rate: a practical and powerful approach to multiple testing. *J. Stat. Soc.* **57**, 289–300 (1995).
35. Beroukhi, R. *et al.* Assessing the significance of chromosomal aberrations in cancer: methodology and application to glioma. *Proc Natl Acad Sci USA* **104**, 20007–20012 (2007).
36. Storey, J. D. & Siegmund, D. Approximate *P*-values for local sequence alignments: numerical studies. *J. Comput. Biol.* **8**, 549–556 (2001).
37. Durinck, S. *et al.* BioMart and Bioconductor: a powerful link between biological databases and microarray data analysis. *Bioinformatics* **21**, 3439–3440 (2005).
38. Thirlwell, C. *et al.* Clonality assessment and clonal ordering of individual neoplastic crypts shows polyclonality of colorectal adenomas. *Gastroenterology* **138**, 1441–1454 (2010).
39. Leedham, S. J. *et al.* Clonality, founder mutations, and field cancerization in human ulcerative colitis-associated neoplasia. *Gastroenterology* **136**, 542–550 (2009).

Activating RNAs associate with Mediator to enhance chromatin architecture and transcription

Fan Lai¹, Ulf A. Orom², Matteo Cesarini¹, Malte Beringer³, Dylan J. Taatjes⁴, Gerd A. Blobel⁵ & Ramin Shiekhattar¹

Recent advances in genomic research have revealed the existence of a large number of transcripts devoid of protein-coding potential in multiple organisms^{1–8}. Although the functional role for long non-coding RNAs (lncRNAs) has been best defined in epigenetic phenomena such as X-chromosome inactivation and imprinting, different classes of lncRNAs may have varied biological functions^{8–13}. We and others have identified a class of lncRNAs, termed ncRNA-activating (ncRNA-a), that function to activate their neighbouring genes using a *cis*-mediated mechanism^{5,14–16}. To define the precise mode by which such enhancer-like RNAs function, we depleted factors with known roles in transcriptional activation and assessed their role in RNA-dependent activation. Here we report that depletion of the components of the co-activator complex, Mediator, specifically and potently diminished the ncRNA-induced activation of transcription in a heterologous reporter assay using human HEK293 cells. *In vivo*, Mediator is recruited to ncRNA-a target genes and regulates their expression. We show that ncRNA-a interact with Mediator to regulate its chromatin localization and kinase activity towards histone H3 serine 10. The Mediator complex harbouring disease-causing MED12 mutations^{17,18} displays diminished ability to associate with activating ncRNAs. Chromosome conformation capture confirmed the presence of DNA looping between the ncRNA-a loci and its targets. Importantly, depletion of Mediator subunits or ncRNA-a reduced the chromatin looping between the two loci. Our results identify the human Mediator complex as the transducer of activating ncRNAs and highlight the importance of Mediator and activating ncRNA association in human disease.

To define the transcriptional complex(es) that orchestrate the responsiveness of activating lncRNAs, we used HEK293 stable cell lines expressing the heterologous TK promoter driving luciferase expression fused to ncRNA-a7 (also called *LINC00651*) controlled by its own natural promoter and depleted factors known to be involved in transcriptional activation (Supplementary Fig. 1a) and examined the responsiveness of cell lines harbouring the constructs expressing ncRNA-a7 or control constructs devoid of lncRNAs. Interestingly, only depletion of the Mediator subunit MED12 displayed a differential effect on the transcription of the reporter construct containing ncRNA-a7 (Fig. 1c). Depletion of other factors was either ineffective in changing transcriptional output (CDK9, CCNT1, NIPBL or WDR5) or reduced the transcriptional levels for both constructs (GTF2B, p300, SMC1) (Fig. 1c).

Mediator contains a complex and modular subunit composition^{19,20}. We depleted different components of Mediator corresponding to the

head, middle or the tail modules and assessed their effect on the responsiveness of the cell lines harbouring the constructs driven by ncRNA-a7 or the control construct. Overall, depletion of other subunits of the Mediator complex also reduced the ncRNA-a7-induced activation, although there was also a small reduction in transcription of the control plasmid with depletion of some of the subunits (Fig. 1d and

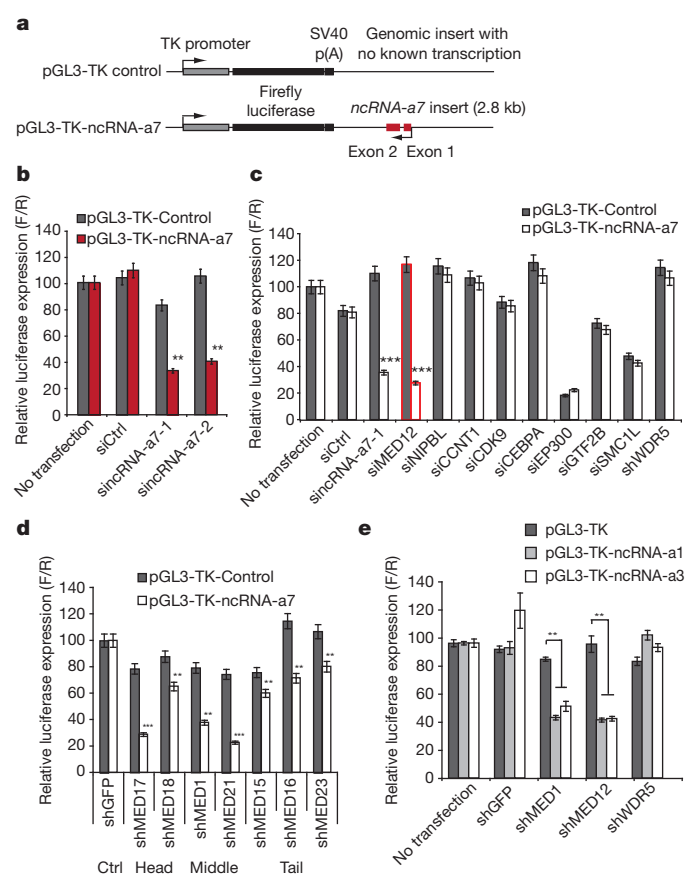


Figure 1 | Mediator confers the ncRNA-a-dependent activation of a heterologous reporter. **a**, Schematic representation of genomic control insert (top) or ncRNA-a7 insert (bottom) in luciferase reporter vector driven by a TK promoter. **b**, Depletion of ncRNA-a7 reduces the luciferase activity in the ncRNA-a7 luciferase reporter cell lines. **c**, Depletion of the transcription factors or enhancers in the control or ncRNA-a7 reporter cell lines. The red bar indicates reduced transcription using siRNA against MED12, comparable with siRNA against ncRNA-a7. **d**, Depletion of different Mediator subunits (head, middle and tail) using the ncRNA-a7 reporter cell lines. **e**, Depletion of the Mediator subunits in ncRNA-a1 or ncRNA-a3 luciferase reporter cell lines. All data shown are mean \pm s.e.m. of three independent experiments. ** $P < 0.01$, *** $P < 0.001$ by two-tailed Student's *t*-test. F/R, firefly luciferase/*Renilla* luciferase.

¹The Wistar Institute, 3601 Spruce Street, Philadelphia, Pennsylvania 19104, USA. ²Max Planck Institute for Molecular Genetics, Ihnestr., 14195 Berlin, Germany. ³Center de Regulació Genòmica i UPF, Barcelona 08003, Spain. ⁴Department of Chemistry and Biochemistry, University of Colorado, 215 UCB, Boulder, Colorado 80309, USA. ⁵Division of Hematology, The Children's Hospital of Philadelphia, Philadelphia, Pennsylvania 19104, USA.

Supplementary Fig. 1b). Similar to its effects on ncRNA-a7, depletion of the Mediator subunits decreased the RNA-induced activation of two other ncRNA-a, which were previously shown to regulate *ECM1* and *TAL1* genes (Fig. 1e). Taken together, these results identify the Mediator complex as a transducer of ncRNA-a function.

We next depleted the Mediator subunits and assessed their effect on ncRNA-a targets *in vivo*. We previously found that ncRNA-a7 and ncRNA-a3 regulate *SNAI1* and *TAL1* genes, respectively⁵. Moreover, using gene expression arrays, we had observed a profound decrease in *AURKA* transcription when ncRNA-a7 was depleted⁵. We confirmed these results by depleting ncRNA-a7 and ncRNA-a3, which led to a decrease in *SNAI1*, *AURKA* and *TAL1* transcript levels using real-time PCR (Fig. 2a, b). We next depleted two different subunits of the Mediator complex, MED1 and MED12, and assessed the *SNAI1*, *AURKA* and *TAL1* transcript levels (Supplementary Fig. 1b). Importantly, depletion of Mediator subunits decreased transcription of all three targets similar to that shown with depletion of ncRNA-a (Fig. 2a, b, the affected genes are depicted by a black bar). Interestingly, depletion of Mediator subunits did not affect the transcript levels of genes that are not regulated by ncRNA-a (*UBE2V1*, *CSTF1*, *STIL*, depicted by a white bar in Fig. 2a, b). However, whereas ncRNA-a7 transcription was not affected after Mediator depletion, there was a decrease in ncRNA-a3 levels (Fig. 2a, b).

To ensure that such transcriptional effects after Mediator depletion were direct, we performed chromatin immunoprecipitation (ChIP) using antibodies against the MED12 and MED1 subunits of Mediator. This analysis revealed that the Mediator complex occupied the promoters of ncRNA-a3, ncRNA-a7 and their targets (Fig. 2c, d). Moreover, we found RNA polymerase II (RNAPII) at these promoters, consistent with Mediator occupancy (Fig. 2c, d). Importantly, depletion of ncRNA-a7 or ncRNA-a3 decreased the occupancy of Mediator and RNAPII at their target genes without affecting the occupancy

at genes not regulated by ncRNA-a (Fig. 2c, d). These results indicate that the Mediator complex occupies the promoters of genes regulated by ncRNA-a, and depletion of ncRNA decreases the occupancy of Mediator at these sites.

The Mediator complex, via its CDK8 module, displays kinase activity towards histone H3 serine 10 (H3S10), a histone modification with strong ties to transcriptional activation^{21,22}. We next assessed whether ncRNA-a regulate Mediator kinase activity towards histone H3. Addition of ncRNA-a7 or ncRNA-a3 led to a significant stimulation of the Mediator kinase activity towards histone H3, whereas the addition of primary let7b ncRNA or ncRNA HOTAIR had no effect (Fig. 2e, f and Supplementary Fig. 2a). Such stimulation of Mediator kinase activity by ncRNA-a was specific towards histone H3 as the substrate. We did not observe any stimulation when GST-CTD (corresponding to the C-terminal domain of RPB1) or cyclin H was used as substrates (Supplementary Fig. 2b, c). Moreover, consistent with a role for ncRNA-a in stimulation of histone H3 phosphorylation, depletion of ncRNA-a7 or ncRNA-a3 led to a specific decrease in H3S10 levels at *SNAI1*, *AURKA* and *TAL1* (Supplementary Fig. 2d and e).

We next asked whether ncRNA-a could associate with the Mediator complex. We isolated Mediator using stable cell lines expressing Flag-epitope-tagged MED12 and examined its interaction with *in-vitro*-transcribed ncRNA-a7. An eluate from a stable Flag-GFP cell line was used as a control (Fig. 3a). Whereas the control primary let7 transcript (pri-let7) or the ncRNA HOTAIR (a 429-nucleotide RNA with a similar base composition as ncRNA-a7) did not specifically interact with the Mediator complex, we detected a robust and specific association between ncRNA-a7 and the Mediator complex (Fig. 3a). Notably, Mediator also associated with ncRNA-a1 and ncRNA-a3, two other ncRNA-a that were shown to activate transcription of their neighbouring genes⁵ (Fig. 3b).

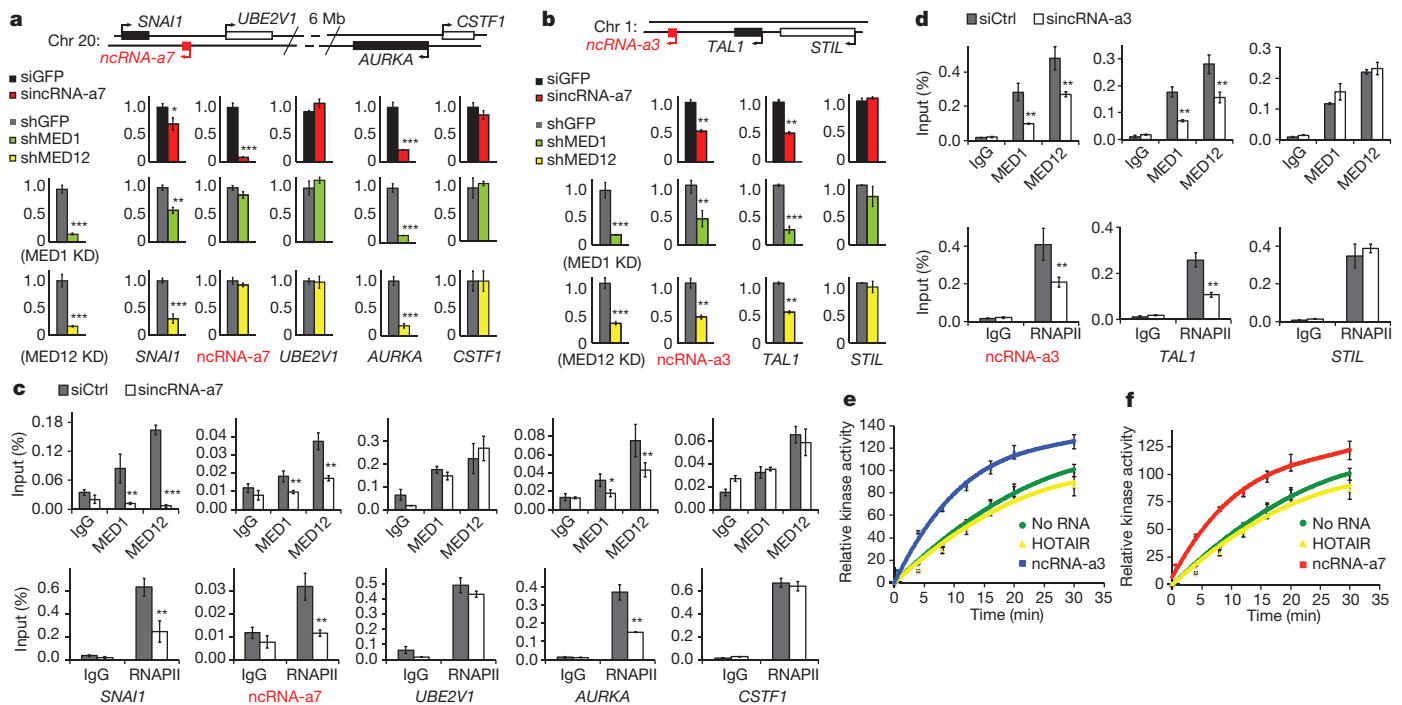


Figure 2 | Functional association of Mediator and activating ncRNAs. **a**, Knockdown of ncRNA-a7 or Mediator subunits decreases expression of *SNAI1* and *AURKA*. Depletion of ncRNA-a7 diminished *SNAI1* and *AURKA* expression as detected by real-time PCR (top row, red bars). Similarly, knockdown (KD) of MED1 (green bars) or MED12 (yellow bars) reduced expression of *SNAI1* or *AURKA*. **b**, Knockdown of ncRNA-a3 or Mediator subunits decreased *TAL1* expression. Expression of *TAL1* or control *STIL* after knockdown of ncRNA-a3 (red bars), MED1 (green bars) or MED12 (yellow bars) is shown. **c**, **d**, Knockdown of ncRNA-a7 (**c**) or ncRNA-a3 (**d**) reduces the

genomic occupancy of MED1, MED12 (top row) or RNAPII (bottom row) on *SNAI1*, *AURKA* (**c**) or *TAL1* (**d**) in A549 cells. **e**, **f**, Activating ncRNAs specifically stimulate Mediator kinase activity towards histone H3.1 substrate *in vitro*. Quantification of kinase assay after addition of ncRNA-a7 (**e**) or ncRNA-a3 (**f**) is shown. Error bars represent \pm s.e.m. ($n = 3$), $P < 0.01$ by two-tailed Student's *t*-test. The mean \pm s.e.m. for all results represents three independent experiments. * $P < 0.05$, ** $P < 0.01$, *** $P < 0.001$ by two-tailed Student's *t*-test.

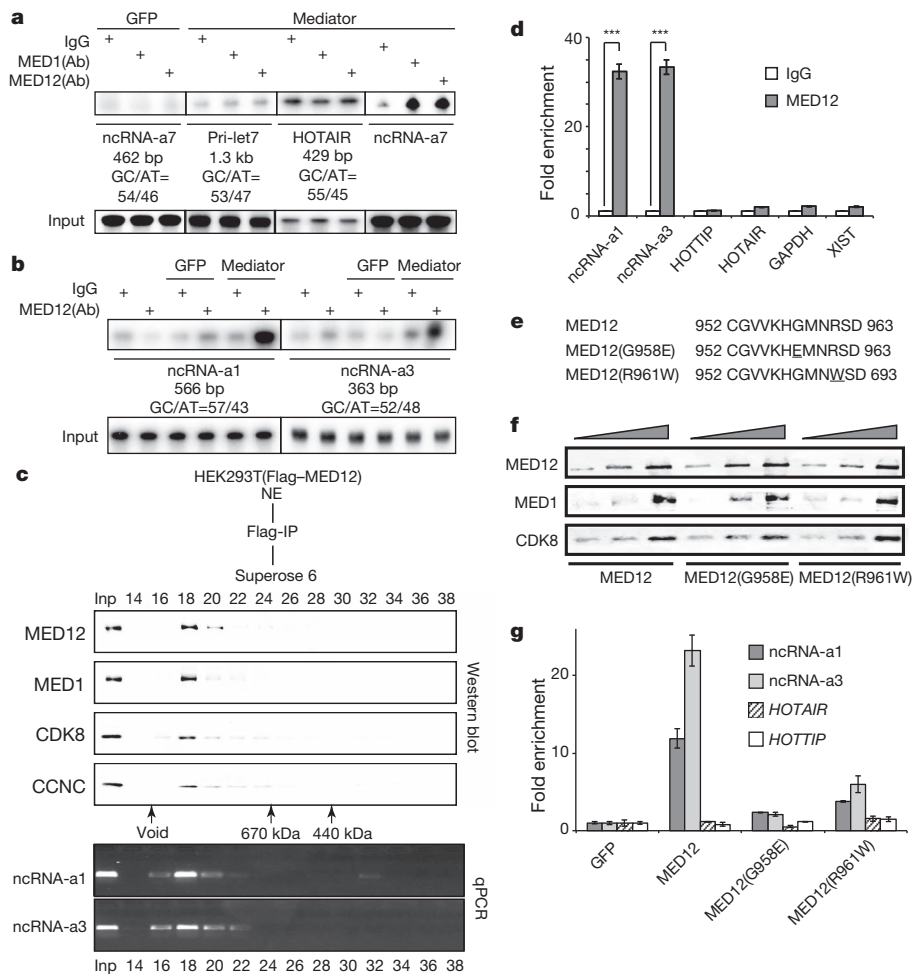


Figure 3 | Interaction of Mediator and activating ncRNAs is disrupted by FG syndrome mutations of MED12. **a, b,** ncRNA-a associate with the Mediator complex *in vitro*. RNA immune precipitation (RIP) was performed using protein A dynabeads coupled with IgG, MED1 or MED12 antibodies. Identical results were obtained in three independent experiments. **c,** Purification of Mediator protein complex and associated RNAs. The purified Flag-MED12 affinity elution was subjected to Superose 6 size-exclusion chromatography and the Mediator subunits were detected by western blot. The Superose 6 fractions (14–38) are shown on top and molecular mass markers (kilodaltons) are at the bottom. The RNAs in each fraction were extracted followed by RT–PCR using specific primers. **d,** Ultraviolet crosslink followed by RIP using HEK293T whole-cell lysates. The associated RNAs were analysed by RT–qPCR with individual specific RNA primers. The mean \pm s.e.m. are from

To assess the association of endogenous ncRNA-a and Mediator, the Flag-MED12 affinity-purified Mediator was fractionated by gel filtration and column fractions were subjected to western blot analysis and polymerase chain reaction with reverse transcription (RT-PCR) to detect the associated ncRNA-a (Fig. 3c). Whereas the HEK293 nuclear extract contained similar levels of ncRNA-a1, ncRNA-a3, HOTAIR and HOTTIP (HEK293 cells do not express ncRNA-a7; Supplementary Fig. 3a), we could only detect ncRNA-a1 and ncRNA-a3 in association with the affinity-purified Mediator (Fig. 3c). Indeed, ncRNA-a1 and ncRNA-a3 displayed a co-elution with components of the Mediator complex on gel filtration, further supporting their association with Mediator (Fig. 3c). Next, we performed RNA immunoprecipitation following ultraviolet crosslinking (UV-RIP) with anti-MED12 antibodies or IgG, as control. Activating ncRNA-a1 and ncRNA-a3 were significantly enriched in the MED12 UV-RIP, whereas other abundant control messenger RNAs or non-coding RNAs such as *GAPDH*, *HOTAIR*, *HOTTIP* and *XIST* were not (Fig. 3d). Two mutations in MED12 proteins have been linked to

three independent experiments. *** $P < 0.001$ by two-tailed Student's *t*-test. **e**, Protein sequences of MED12 mutants causing FG syndrome. Part of the protein sequence of MED12 exon 21 is shown (top row). The mutated sites indicate the G958E mutation (underlined) and the R961W mutation (underlined). **f**, HEK293T cells were transfected with Flag-MED12 or mutant constructs. After ultraviolet crosslinking, total cell extracts were immunoprecipitated and analysed by western blotting. **g**, After UV-RIP of wild-type and mutant MED12 samples shown in **f**, RT-qPCR was performed using transcript-specific primers from the lncRNAs shown. The data are representative of three independent experiments. The two-tailed Student's *t*-test indicated a $P < 0.001$ for ncRNA-a1 and ncRNA-a3, whereas there was no significant difference for *HOTAIR* and *HOTTIP*.

the development of the human genetic disorder Opitz–Kaveggia syndrome (also known as FG syndrome), causing physical anomalies and developmental delays^{17,18} (Fig. 3e). Notably, whereas such mutations in MED12 do not affect its association with other Mediator subunits, they significantly diminish its association with ncRNA-a1 and ncRNA-a3 as measured by UV-RIP (Fig. 3f, g).

We next asked whether we could detect long-range chromatin looping between the *ncRNA-a7* locus and its targets, *SNAIL1* and *AURKA* and whether ncRNA-a7 and the Mediator complex have a role in such an association. We performed chromosome conformation capture (3C) to assess the association of ncRNA-a7 with *AURKA* as well as *SNAIL1*. We also performed a similar analysis between ncRNA-a3 and the *TAL1* gene. We used anchoring points near the 3' untranslated region of ncRNA-a7 or ncRNA-a3 to measure the extent of chromatin looping between the *ncRNA-a7* or *ncRNA-a3* locus and their targets as shown in Fig. 4a, d and Supplementary Fig. 3b, c. This analysis revealed a strong association between the *ncRNA-a7* locus and the region encompassing the promoter region of *SNAIL1* (Fig. 4b, upper panel).

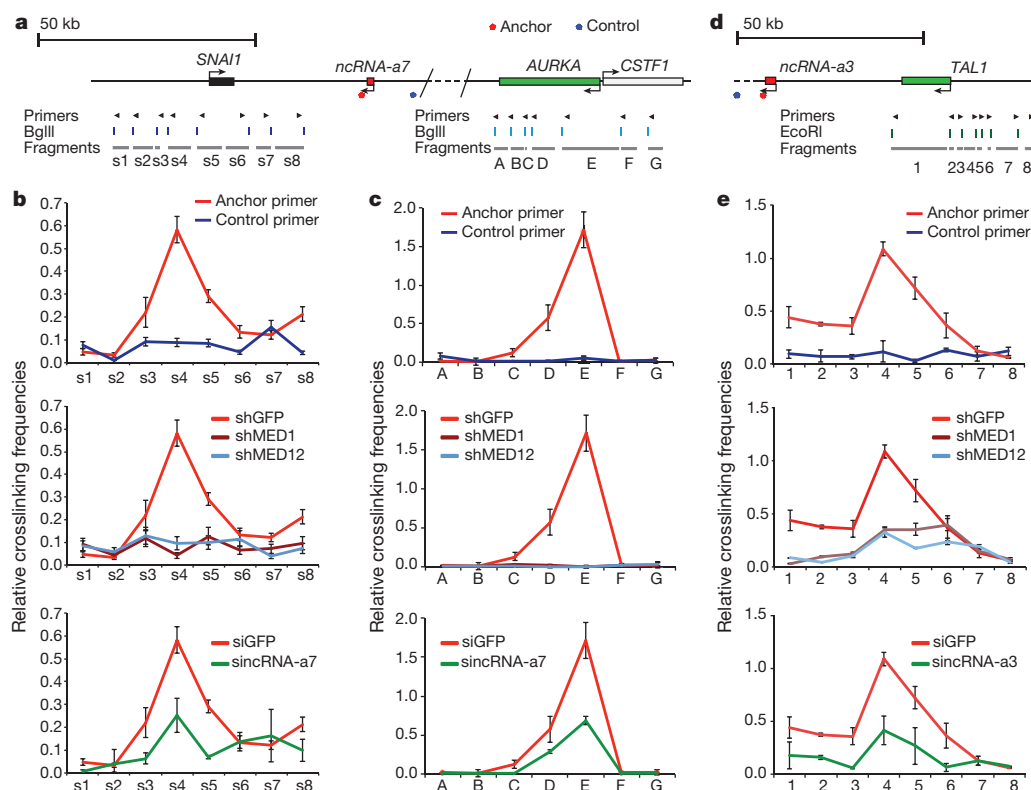


Figure 4 | Mediator complex and ncRNA-a promote chromatin looping.

The schematic diagrams represent the genomic locus between the *ncRNA-a7*, *SNAIL1* and *AURKA* loci (a), and the *ncRNA-a3* and *TAL1* loci (d). The top arrows show the position of primers, the digestion sites are shown in the middle, and the s1–s8, A–G or 1–8 fragments are presented below. The looping events between ncRNAs and their targets were detected between *ncRNA-a7* and *SNAIL1* (b), *ncRNA-a7* and *AURKA* (c) and *ncRNA-a3* and *TAL1* (e) using chromosome conformation capture (3C). Depletion of MED1 or MED12

abolished the loop interaction (b, c, e; middle panels). Knockdown of *ncRNA-a7* or *ncRNA-a3* reduced the chromosomal looping events (b, c, e; lower panels). The interaction frequency between the anchoring points and distal fragments was determined by real-time PCR and normalized to BAC templates and control anchors. Each error bar represents \pm s.e.m. from three independent experiments, $P < 0.01$ by two-tailed Student's *t*-test. Representative gel images of the 3C experiments for *AURKA* are presented in Supplementary Fig. 3.

Moreover, *ncRNA-a7* also displayed an interaction with regions near the 5' end of the *AURKA* gene that extended into the body of the gene (Fig. 4c, upper panel). There was no detectable association when a control anchor was placed in the genomic region between *ncRNA-a7* and *AURKA* (Fig. 4b, c).

Next we depleted the Mediator subunits MED1 or MED12 and assessed their potential role in mediating the chromosomal looping between *ncRNA-a7*, *SNAIL1* and *AURKA*. Depletion of either MED1 or MED12 completely abrogated the chromosomal looping between *ncRNA-a7* and *SNAIL1* (Fig. 4b, middle panel). A similar result was obtained after depletion of MED1 or MED12 at the *AURKA* locus (Fig. 4c, middle panel). Importantly, depletion of *ncRNA-a7* had a comparable effect, reducing the chromosomal looping between *ncRNA-a7* and both *SNAIL1* and *AURKA* loci (Fig. 4b, c, lower panels). Because depletion of *ncRNA-a7* using siRNAs resulted in a partial decrease of *ncRNA-a7* concentration (about 60% depletion, Supplementary Fig. 1), the residual *ncRNA-a7* may be sufficient to promote smaller levels of DNA looping seen after *ncRNA-a7* depletion.

We also performed a similar analysis measuring the extent of DNA looping between *ncRNA-a3* and that of the *TAL1* locus. Similar to results obtained with *ncRNA-a7*, we detected a specific and robust DNA looping between *ncRNA-a3* and *TAL1* (Fig. 4e). Finally, depletion of Mediator subunits MED1 and MED12 or *ncRNA-a3* nearly abolished the DNA looping between *ncRNA-a3* and *TAL1* (Fig. 4e, middle and lower panels). Notably, Mediator and *ncRNA-a* association with their target genes extend beyond the transcription start sites to include the more distal sites. This may reflect the engagement of proximal regulatory elements in *ncRNA-a* and Mediator chromatin looping (Fig. 4b, e). These results suggest a mechanism of action for

ncRNA-a and Mediator that may involve additional chromatin contacts beyond that which has been observed for distal regulatory elements and transcriptional start sites.

We propose a new mechanism of action for a class of lncRNAs termed *ncRNA-activating* (*ncRNA-a*) involved in long-range transcriptional activation through their association with the Mediator complex (Supplementary Fig. 4). It is noteworthy that such Mediator–*ncRNA-a*-dependent chromatin loops extend beyond the transcription start sites of the target promoters, which may reflect the inclusion of promoter proximal regulatory elements in such associations. Future studies could also assess whether such *ncRNA-a*–Mediator chromatin loops augment, or function exclusively of, Mediator–Cohesin complexes²³.

Recently, experiments in zebrafish uncovered a fundamental role for lncRNAs in developmental control²⁴. Moreover, recent reports have linked a number of lncRNAs to human diseases such as cancer and neurological disorders^{11,25–27}. Importantly, our studies indicated that Mediator complexes containing disease-causing mutant MED12 proteins corresponding to FG syndrome fail to associate with *ncRNA-a*. These results underscore the significance of Mediator–*ncRNA-a* association and suggest the loss of such Mediator–*ncRNA-a* interactions as a possible contributing factor in such developmental disorders.

METHODS SUMMARY

Depletion experiments using siRNA/DNA transfection and ncRNA luciferase assays. pGL3-TK-*ncRNA-a* and pGL3-TK-control constructs were generated as described previously. On-TargetPlus siRNAs and non-targeting control siRNA were purchased from Dharmacon. The modified siDNA oligonucleotides were purchased from Integrated DNA Technologies. siRNA/DNA transfections were

performed with Lipofectamine RNAiMAX (Life Technologies) according to the manufacturer's instructions, using 50 nM siRNA/DNAs in a final volume of 2 ml of culture medium without antibiotics. Cells were collected 48–72 h after two rounds of transfection.

Chromatin immunoprecipitation analysis was performed using 1×10^7 to 3×10^7 A549 or MCF7 cells were collected for each independent immunoprecipitation. After chemically crosslinking, cells were fixed in 1% formaldehyde $1 \times$ PBS with 10% serum for 15 min at room temperature. After immunoprecipitation, bound chromatin was eluted at 65 °C for 10 min in 60 μ l fresh elution buffer twice (TE, 1% SDS) and 80 μ l of elution buffer was added to the final volume of 200 μ l. Crosslinking samples were reversed overnight at 65 °C. After proteinase K treatment (0.5 mg ml⁻¹), DNA was purified using a QIAquick PCR purification kit (Qiagen).

Protein affinity purification and RNA immunoprecipitation. The affinity-purified mediator complex and the GFP protein control were generated from the Flag-tagged MED12 or GFP HEK293T stable cell lines. RNA probes, internally labelled with [α -³²P]CTP, were transcribed using T7 or Sp6 RNA polymerase (Riboprobe System, Promega). RNA immunoprecipitations were performed using Dynabeads Protein A (Invitrogen) according to the manufacturer's recommendations. Transiently transfected HEK293T cells were UV-crosslinked at 254 nm (200 mJ cm⁻²) in 10 ml ice-cold PBS and collected by scraping. Cells were incubated in lysis solution (0.1% SDS, 0.5% NP40, 0.5% sodium deoxycholate, 400 U ml⁻¹ RNase inhibitor (Roche)), and protease inhibitor at 4 °C for 25 min with rotation, followed by DNase treatment (30 U of DNase, 15 min at 37 °C).

Full Methods and any associated references are available in the online version of the paper.

Received 29 March; accepted 31 December 2012.

Published online 17 February 2013.

1. Birney, E. *et al.* Identification and analysis of functional elements in 1% of the human genome by the ENCODE pilot project. *Nature* **447**, 799–816 (2007).
2. Bertone, P. *et al.* Global identification of human transcribed sequences with genome tiling arrays. *Science* **306**, 2242–2246 (2004).
3. The FANTOM Consortium. The transcriptional landscape of the mammalian genome. *Science* **309**, 1559–1563 (2005).
4. Okazaki, Y. *et al.* Analysis of the mouse transcriptome based on functional annotation of 60,770 full-length cDNAs. *Nature* **420**, 563–573 (2002).
5. Ørom, U. A. *et al.* Long noncoding RNAs with enhancer-like function in human cells. *Cell* **143**, 46–58 (2010).
6. Guttman, M. *et al.* Chromatin signature reveals over a thousand highly conserved large non-coding RNAs in mammals. *Nature* **458**, 223–227 (2009).
7. Kapranov, P. *et al.* RNA maps reveal new RNA classes and a possible function for pervasive transcription. *Science* **316**, 1484–1488 (2007).
8. Wang, K. C. & Chang, H. Y. Molecular mechanisms of long noncoding RNAs. *Mol. Cell* **43**, 904–914 (2011).
9. Lee, J. T. The X as model for RNA's niche in epigenomic regulation. *Cold Spring Harb. Perspect. Biol.* **2**, a003749 (2010).
10. Rinn, J. L. *et al.* Functional demarcation of active and silent chromatin domains in human HOX loci by noncoding RNAs. *Cell* **129**, 1311–1323 (2007).
11. Gupta, R. A. *et al.* Long non-coding RNA HOTAIR reprograms chromatin state to promote cancer metastasis. *Nature* **464**, 1071–1076 (2010).
12. Yap, K. L. *et al.* Molecular interplay of the noncoding RNA ANRIL and methylated histone H3 lysine 27 by polycomb CBX7 in transcriptional silencing of INK4a. *Mol. Cell* **38**, 662–674 (2010).
13. Zhao, J. *et al.* Genome-wide identification of polycomb-associated RNAs by RIP-seq. *Mol. Cell* **40**, 939–953 (2010).
14. Kim, T. K. *et al.* Widespread transcription at neuronal activity-regulated enhancers. *Nature* **465**, 182–187 (2010).
15. De Santa, F. *et al.* A large fraction of extragenic RNA pol II transcription sites overlap enhancers. *PLoS Biol.* **8**, e1000384 (2010).
16. Wang, K. C. *et al.* A long noncoding RNA maintains active chromatin to coordinate homeotic gene expression. *Nature* **472**, 120–124 (2011).
17. Risheg, H. *et al.* A recurrent mutation in MED12 leading to R961W causes Opitz-Kaveggia syndrome. *Nature Genet.* **39**, 451–453 (2007).
18. Rump, P. *et al.* A novel mutation in MED12 causes FG syndrome (Opitz-Kaveggia syndrome). *Clin. Genet.* **79**, 183–188 (2011).
19. Malik, S. & Roeder, R. G. The metazoan Mediator co-activator complex as an integrative hub for transcriptional regulation. *Nature Rev. Genet.* **11**, 761–772 (2010).
20. Taatjes, D. J. The human Mediator complex: a versatile, genome-wide regulator of transcription. *Trends Biochem. Sci.* **35**, 315–322 (2010).
21. Knuesel, M. T., Meyer, K. D., Donner, A. J., Espinosa, J. M. & Taatjes, D. J. The human CDK8 subcomplex is a histone kinase that requires Med12 for activity and can function independently of mediator. *Mol. Cell Biol.* **29**, 650–661 (2009).
22. Nowak, S. J. & Corces, V. G. Phosphorylation of histone H3: a balancing act between chromosome condensation and transcriptional activation. *Trends Genet.* **20**, 214–220 (2004).
23. Kagey, M. H. *et al.* Mediator and cohesin connect gene expression and chromatin architecture. *Nature* **467**, 430–435 (2010).
24. Ulitsky, I., Shkumatava, A., Jan, C. H., Sive, H. & Bartel, D. P. Conserved function of lincRNAs in vertebrate embryonic development despite rapid sequence evolution. *Cell* **147**, 1537–1550 (2011).
25. Yu, W. *et al.* Epigenetic silencing of tumour suppressor gene p15 by its antisense RNA. *Nature* **451**, 202–206 (2008).
26. Sopher, B. L. *et al.* CTCF regulates ataxin-7 expression through promotion of a convergently transcribed, antisense noncoding RNA. *Neuron* **70**, 1071–1084 (2011).
27. Cebianca, D. S. *et al.* A long ncRNA links copy number variation to a polycomb/trithorax epigenetic switch in FSHD muscular dystrophy. *Cell* **149**, 819–831 (2012).

Supplementary Information is available in the online version of the paper.

Acknowledgements We thank Shiekhathar laboratory members for support and discussions. We thank W. Dang (Biolab laboratory) and I. Tempere for suggestions and technical help on 3C experiments. R.S. was partially supported by a cancer core grant from NIH (P30 CA 010815). D.J.T. was supported by a grant from the NCI (R01 CA127364). G.A.B. was supported by 5R37DK058044.

Author Contributions R.S., F.L. and U.A.O. conceived and designed the overall project with help from G.A.B., M.B., D.J.T. and M.C. F.L. and U.A.O. performed the RNAi screens; F.L. received advice from G.A.B. to execute the 3C experiments. F.L. and M.C. performed the ChIP experiments for Mediator. F.L. performed all experiments regarding the ncRNA association with Mediator and the kinase assays. F.L., M.C. and R.S. analysed the data and wrote the paper.

Author Information Reprints and permissions information is available at www.nature.com/reprints. The authors declare no competing financial interests. Readers are welcome to comment on the online version of the paper. Correspondence and requests for materials should be addressed to R.S. (shiekhathar@wistar.org).

METHODS

siRNA/DNA transfection and ncRNA luciferase assays. pGL3-TK-ncRNA-a and pGL3-TK-control constructs were generated as described previously. Firefly luciferase constructs, pRL-CMV and a selectable marker for puromycin resistance were co-transfected in HEK293T cells. Transfected cells were grown in the presence of $2.5 \mu\text{g ml}^{-1}$ puromycin (Sigma) for selection. Individual colonies were isolated and screened for luciferase expression. Luciferase assays were performed in 96-well white plates using Dual-Glo luciferase assay system (Promega) according to the manufacturer's protocol.

On-TargetPlus siRNAs and non-targeting control siRNA were purchased from Dharmacon. The modified siDNA oligonucleotides were purchased from Integrated DNA Technologies. siRNA or siDNA transfections were performed with Lipofectamine RNAiMAX (Life Technologies) according to the manufacturer's instructions, using 50 nM siRNA/DNAs in a final volume of 2 ml of culture medium without antibiotics. Cells were collected 48–72 h after two rounds of transfection.

Corresponding ncRNA-a HEK293T cell lines growing in 12-well dishes were transfected with corresponding siRNA oligonucleotides, using Metafectene Pro (Biontex Laboratories). Twenty-four hours after transfection, the cells were lysed in 200 μl passive lysis buffer (Promega), and firefly and Renilla luciferase activities were measured on 30 μl lysate using the Dual-Luciferase reporter assay kit (Promega). Individual experiments were realized in triplicate, and the ratios presented are the averages of three independent experiments.

siRNA sequences. siControl1: ON-TARGET non-targeting siRNA 1 (D-001810-01); siControl2: ON-TARGET Non-targeting siRNA 2 (D-001810-02); siGFP: GFP Duplex I (P-002048-01); sincRNA-a3-1: 5'-CUAUGGAAUUUAGCCCA AUU-3'; sincRNA-a3-2: 5'-GCAAGAUCACGGUGCGUCAUU-3'; sincRNA-a7-1: 5'-CCGAUUUGAGAGAGUGAGAUU-3'; sincRNA-a7-2: 5'-GAAGGGA ACAGUGCUAAAUU-3'; siMED12: 5'-UCACUACUACUACUGUUAU-3'; siNIPBL: 5'-GGGAAUAUGAAGAGCGUGAUU-3'; siCCNT1: 5'-GAACAA ACGUCCUGUGAUUU-3'; siCDK9: 5'-UGACGUCCAUGUUCGAGUAUU-3'; siCEBPA: 5'-ACAAGAACAGCAACGAGUAUU-3'; siEP300: 5'-GGACUA CCCUAACAAGUAUU-3'; siGTF2B: 5'-ACAAUCAGACAGUCCUAU-3'; siSMC1L: 5'-CAUCAAAAGCUCGUACUUCU-3'.

siDNA sequences. siGFP: 5'-T*C*A*A*C*C*T*T*T*C*A*A*C*C*C*T*T*C*T*C*C* A*C*T-3'; sincRNA-a1: 5'-C*C*T*G*C*C*C*T*T*T*C*T*T*C*T*T*C*C*T*G* T*A-3'; sincRNA-a3: 5'-G*C*T*C*C*T*T*C*G*G*T*A*A*C*T*T*C*T*C*A* T*T-3'; sincRNA-a7-1: 5'-G*T*T*T*C*C*T*T*T*T*C*T*G*A*A*C*G*C*C*T*G* G*T*A-3'; sincRNA-a7-2: 5'-C*A*T*T*C*T*T*T*C*T*C*G*T*T*C*T*T*G* C*C*A*A-C-3'. Asterisks indicate nucleoside phosphorothioates.

shRNA infections. pLKO.1 lentiviral vector containing short hairpin RNAs (shRNAs) or shRNA targeting GFP control was obtained from Open Biosystems. The TRC shRNA constructs were purchased from Open Biosystems using Lentiviral packaging system. Twenty-four hours after infection, selection with $2.5 \mu\text{g ml}^{-1}$ puromycin was performed for 48 h.

shRNA list. shGFP: RHS4459; MED12 (TRCN0000018576): 5'-CGGGT ACTTCATACTTTGG-3'; MED17 (TRCN0000019245): 5'-CCGAGCTTGC AGTTATCTATT-3'; MED18 (TRCN0000053164): 5'-GCCAGAACTGGG AGACAAGAA-3'; MED1 (TRCN0000019800): 5'-GCCGAGTTCTCTTA TCCTAA-3'; MED21 (TRCN0000013429): 5'-CCATTGGAGTATTGCA GCAAT-3'; MED15 (TRCN0000018969): 5'-GCTCAGAACCAACCATCAC-3'; MED16 (TRCN0000022139): 5'-CGACATTGACAAGGTCATGAT-3'; MED23 (TRCN0000019196): 5'-CGCAGTTATACAGCTTCTCT-3'; WDR5 (TRCN00000118050): 5'-CCAACCTATTGTCTCAGGAT-3'.

Antibodies and recombinant proteins. Antibodies and recombinant proteins used were: Pol II (SC-899, Santa Cruz), MED1 (A300-793A, Bethyl labs), MED12 (A300-774A, Bethyl labs), histone H3Ser10p (05-598, Millipore), CDK8 (SC-1521, Santa Cruz), CCNC (cyclin C, SC-1061, Santa Cruz), human rHistone H3.1 (M2503S, NEB), and human rCCNH (pka-364, ProspeC protein specialists).

RNA purification, cDNA synthesis and quantitative PCR. Cells were collected and re-suspended in TRIzol (Invitrogen) and RNA extracted according to the manufacturer's protocol. cDNA synthesis was done using random primers with Fermentas RevertAid first-strand cDNA synthesis kit. Quantitative PCR was done using IQ SYBR green super-mixes and CFX96 Touch Real-Time PCR detection system (Bio-rad). For all quantitative PCR reactions *GAPDH* was measured for an internal control and used to normalize the data. qPCR primer sequences are listed here: ncRNA-a1-qfor: 5'-GCAAGCGGAGACTTGTCTTT-3'; ncRNA-a1-qrev: 5'-GGCTGGTCTTGAACCTCTGA-3'; ncRNA-a3-qfor: 5'-TTAAGCCCAAG GAATGGAGA-3'; ncRNA-a3-qrev: 5'-AGCGGTGTGGAATAAATAGG-3'; ncRNA-a7-q1for: 5'-ATCCTGGTGGAAAAGGCATC-3'; ncRNA-a7-q1rev: 5'-GCCTGGGAAAAGCTACTTCA-3'; ncRNA-a7-q2for: 5'-CCGTTGGCTCCA CAAACCT-3'; ncRNA-a7-q2rev: 5'-CAGTGACAGTAGCAGGCATCCT-3'; MED17-qfor: 5'-CCGACGGATAGACTTACG-3'; MED17-qrev: 5'-ATTGT

TCCTCACTGAGTCCCA-3'; MED18-qfor: 5'-GGGCACCATTAAACATGAT GGA-3'; MED18-qrev: 5'-TGGTCAAGGAAGTCTCAGGT-3'; MED1-qfor: 5'-CTGGAACGGCTCCATGCAA-3'; MED1-qrev: 5'-CTTCTCCATGACTTG ACGCAC-3'; MED21-qfor: 5'-TTGCACGAACAGCAAAAGACA-3'; MED21-qrev: 5'-TGGCGCTTTGTATCTTCTCCAG-3'; MED15-qfor: 5'-ATGGACG TTTCCGGGCAAG-3'; MED15-qrev: 5'-GCATCCTCGATTTGACTGACCA-3'; MED16-qfor: 5'-TGCTGGACATGAACACACTG-3'; MED16-qrev: 5'-AGG GAACCTGGTTGGGA-3'; MED23-qfor: 5'-GGGCCTTCAGACAGTTTTG G-3'; MED23-qrev: 5'-AGCTGTGTCTTTTCCCACTCA-3'; MED12-qfor: 5'-CTCCCGATGTTTACCCTCAG-3'; MED12-qrev: 5'-ATGCTCATCCCCAGA GACAG-3'; NIPBL-qfor: 5'-CGGCCCGGATTATAGTCTCT-3'; NIPBL-qrev: 5'-TCAGGTGCCAGCTGTCTATTA-3'; CCNT1-qfor: 5'-GCCAATCTGCTTC AGGACA-3'; CCNT1-qrev: 5'-GGGAAGCTGTGTGAAGGACTGA-3'; CDK9-qfor: 5'-ATACGAGAAGCTCGCCAAGA-3'; CDK9-qrev: 5'-CCTTCTCGT TTTCCATCAGC-3'; CEBPA-qfor: 5'-CAGAGGGACCGGAGTTATGA-3'; CEBPA-qrev: 5'-TTCACATTGCACAAGGCACT-3'; EP300-qfor: 5'-GGGAGG ACAAACAGGATTGA-3'; EP300-qrev: 5'-CCAATCTGCTGTCCAGGATT-3'; GTF2B-qfor: 5'-TTCCTGCTTTTCGGTGTGTCT-3'; GTF2B-qrev: 5'-TGGATG GTTTGGACATGTGA-3'; SMC1L1-qfor: 5'-TCGGACCATTTTCAGAGGTTT-3'; SMC1L1-qrev: 5'-GGTCTTTACCCGCAGGTG-3'; WDR5-qfor: 5'-AAT TCAGCCCGAATGGAGAGT-3'; WDR5-qrev: 5'-GGATATTTCCAGCTTGT GACC-3'; CSTF1-qfor: 5'-ACAGAACCAAGGTGGCTTGA-3'; CSTF1-qrev: 5'-ACACAGACTGAGGCTTGATTTC-3'; AURKA-qfor: 5'-TTCAGGACCTG TTAAGGCTACA-3'; AURKA-qrev: 5'-ATTTGAAGGACACAAGACCCG-3'; TAL1-qfor: 5'-CAGCCTAGTGGCTTGTCTCT-3'; TAL1-qrev: 5'-GGAGC CTGAAATTTGAATGGA-3'; HOTAIR-qfor: 5'-GGTAGAAAAAGCAACC ACGAAGC-3'; HOTAIR-qrev: 5'-ACATAAACCTCTGTCTGTGAGTGCC-3'; HOTTIP-qfor: 5'-CCTAAAGCCAGCTTCTTTG-3'; HOTTIP-qrev: TGCAG GCTGGAGATCCTACT-3'; STIL-qfor: 5'-CCCAACGCCAACTGGAGATTT-3'; STIL-qrev: 5'-AGTCGGATGGTCTTCTCAGTC-3'; SNAI1-qfor: 5'-TCGG AAGCCTAACTACAGCGA-3'; SNAI1-qrev: 5'-AGATGAGCATTGGCAGCG AG-3'; UBE2V1-qfor: 5'-AAGCAAGAGCGACGCAAGAT-3'; UBE2V1-qrev: 5'-CGGAAATTCGAGGGAGCTT-3'.

Chromatin immunoprecipitation. Briefly, 1×10^7 to 3×10^7 A549 or MCF7 cells were collected for each independent immunoprecipitation. After chemically crosslinking, cells were fixed in 1% formaldehyde, $1 \times$ PBS with 10% serum for 15 min at room temperature. After quenching with 0.25 M glycine, rinsing twice with cold $1 \times$ PBS, cells were lysed for 15 min in cold Chip buffer (150 mM NaCl, 1% Triton X-100, 5 mM EDTA; 10 mM Tris-HCl, pH 7.5, 0.5 mM DTT) with protease inhibitors on ice for 10 min. DNA was sonicated to between 200- and 350-bp DNA fragments on a Diagenode Bioruptor according to manufacturer's protocol. The solubilized chromatin was cleared and diluted with lysis buffer (without SDS to bring down SDS concentration to 0.1–0.15%). 1 ml of the chromatin solution was incubated overnight with 2–6 μg of antibody using protein A Dyna Beads at 4°C . The beads were washed twice with Mixed Micelle wash buffer (0.2% SDS, 1% Triton X-100, 5.2% w/v sucrose, 5 mM EDTA, 20 mM Tris-HCl, pH 8, 150 mM NaCl), 2 times with high-salt buffer (1% Triton X-100, 1 mM EDTA, 50 mM HEPES, pH 8, 0.1% w/v deoxycholate, 500 mM NaCl), 2 times with LiCl buffer (250 mM LiCl, 0.5% NP-40, 0.5% deoxycholate, 1 mM EDTA, 10 mM Tris-HCl, pH 8), and one time with cold TE buffer (10 mM Tris-HCl, pH 7.6, 1 mM EDTA). Bound chromatin was eluted at 65°C for 10 min in 60 μl fresh elution buffer twice (TE, 1% SDS) and brought to 200 μl . Crosslinking samples were reversed overnight at 65°C . After proteinase K treatment (0.5 mg ml^{-1}), DNA was purified using a QIAquick PCR purification kit (Qiagen). ChIP primers sequences are listed here: AURKChip-for: 5'-CGAATCCTGCCAATCTACC-3'; AURKChip-rev: 5'-GATGGCGAGAAAAGCAAGAG-3'; ncRNAa7Chip-for: 5'-GGATAACCAAAAGCGTAGGAAA-3'; ncRNAa7Chip-rev: 5'-CGGTC TCTAACACAACACAGCTC-3'; CSTF1-Chip-for: 5'-TCCATTTTTCAGGAG AGAGC-3'; CSTF1-Chip-rev: 5'-CCAGTCGTTTCTGTGGTTTTC-3'; TAL1-Chip-for: 5'-TCCTTCCCCCTTTTCTTCTAC-3'; TAL1-Chip-rev: 5'-TGAACGC ACTCTACAATCC-3'; ncRNA-a3-Cfor: 5'-ATGAGAGCCTCGGAAGTTGA-3'; ncRNA-a3-Crev: 5'-CCTTGCAATCCACAGGAAGT-3'; STIL-Chip-for: 5'-AATGTTACCCACCAACCTTCC-3'; STIL-Chip-rev: 5'-CTACCCTGCAAAAC AGACCTCA-3'; UBE2V1-Chip-for: 5'-TGCTTTTGGGGAGAATGAAG-3'; UBE2V1-Chip-rev: 5'-TCCTCGAACAGGAGACTGGT-3'.

Protein affinity purification and RNA immunoprecipitation. The affinity-purified Mediator complex and the GFP protein control were generated from the Flag-tagged MED12 or GFP HEK293T stable cell lines.

RNA probes, internally labelled with [α - ^{32}P]CTP, were transcribed using T7 or Sp6 RNA polymerase (Riboprobe System, Promega).

RNA immunoprecipitations were performed using Dynabeads Protein A (Invitrogen) according to manufacturer's recommendations. 2 μg antibody was incubated with each sample, and the purified protein complex or the control

protein together with labelled RNA probes were incubated with the beads at 4 °C. The immunoprecipitated RNAs were extracted by TRIzol (Invitrogen) and resolved on the 6% Novex TBE-Urea gels (Invitrogen).

For ultraviolet crosslinking experiments, the method is modified from that of ref. 28. Transiently transfected HEK293T cells were UV-crosslinked at 254 nm (200 mJ cm⁻²) in 10 ml ice-cold PBS and collected by scraping. Cells were incubated in lysis solution (0.1% SDS, 0.5% NP40, 0.5% sodium deoxycholate, 400 U ml⁻¹ RNase Inhibitor (Roche)) and protease inhibitor at 4 °C for 25 min with rotation, followed by DNase treatment (30 U of DNase, 15 min at 37 °C).

In vitro transcription of ncRNA-a. *In vitro* transcription followed the protocol provided by the Riboprobe *in vitro* transcription systems (Promega); the designed oligonucleotides are listed here: ncRNA-a1-T7FOR: 5'-TAATACGACTCAC TATAGGGGcgcctctctcagcctccag-3'; ncRNA-a1-sp6REV: 5'-ATTTAGGTGA CACTATAGAAccaagtgtctgtgtaataggc-3'; ncRNA-a3-T7FOR: 5'-TAATACGA CTCACTATAGGGgaagtgtgcttcaggcgcggctctt-3'; ncRNA-a3-sp6REV: 5'-ATTT AGGTGACACTATAGAAAaccagcctcagcgtgtggaata-3'; ncRNA-a7-T7FOR: 5'-TAATACGACTCACTATAGGGGctgtggcagagcggagaa-3'; ncRNA-a7-SP6REV: 5'-ATTTAGGTGACACTATAGAAaccagccttagactgtgaaattttattg-3'; HOTAIR-T7FOR: 5'-TAATACGACTCACTATAGGGAGGCCCAAGAGTCTGATG TT-3'; HOTAIR-SP6REV: 5'-ATTTAGGTGACACTATAGAACTCAGGTT TTTCCAGCGTTCTC-3'. Uppercase letters indicate either the T7 or SP6 polymerase binding site, whereas lowercase letters indicate specific sequences for each ncRNA.

Kinase assays. Kinase reactions were carried out with 10–50 ng of purified Mediator protein complex and 500 ng human histone H3.1 recombinant (New England Biolabs) substrates in kinase buffer (25 mM Tris pH 8.0, 100 mM KCl, 100 μM ATP, 10 mM MgCl₂, 2 mM DTT) with the addition of 2.5 μCi [γ -³²P]ATP at 24 °C. Samples were resolved on a 4–12% SDS–polyacrylamide gel (Invitrogen) followed by transfer to PVDF membrane (Millipore) and autoradiography.

Chromosome conformation capture (3C). 3C assays followed the protocol from ref. 29, with minor modifications. A549 or MCF7 cells were filtered through a 70 μm filter to obtain a single-cell preparation. 1 × 10⁷ cells were then fixed in 1% formaldehyde for 30 min at room temperature, followed by 15 min crosslinking. The reaction was quenched with 0.25 M glycine and cells were collected by centrifugation at 240g at 4 °C. The pellet was re-suspended in 0.5 ml cold lysis buffer (10 mM Tris-HCl, pH 7.5; 10 mM NaCl; 5 mM MgCl₂; 0.1 mM EGTA) with freshly added protease inhibitors (Roche) and was lysed on ice for 15 min. Cells were Dounce homogenized on ice with pestle B using 15–20 strokes. The nuclei were collected by centrifugation at 500g for 10 min at 4 °C and were re-suspended in 0.5 ml of 1.2 × restriction enzyme buffer (NEB), including 0.3% SDS and were incubated for 1 h at 37 °C while shaking at 1,200 r.p.m. Two per cent (final concentration) Triton X-100 was added to the nuclei and then the samples were incubated for 1 h at 37 °C while shaking. 400 U restriction enzyme was added to the nuclei and the samples were incubated at 37 °C overnight while shaking. 10 μl of the samples were collected before and after the enzyme reaction to evaluate digestion efficiency. The reaction was stopped by addition of 1.6% SDS (final concentration) and incubation at 65 °C for 30 min while shaking at 1,200 r.p.m. The sample was then diluted 10-fold with 1.15 × ligation buffer (NEB) with added 1% Triton X-100 and was incubated for 1 h at 37 °C while shaking at 900 r.p.m. 100 U T4 DNA ligase (NEB) were added to the sample and the reaction was carried at 16 °C for 4 h followed by 30 min at room temperature. 300 μg of Proteinase K were added to the sample and the reaction was carried at 65 °C overnight for

de-crosslink. RNA was removed by adding 300 μg of RNase and incubating the sample for 1 h at 37 °C. DNA was purified by twice phenol-chloroform extraction and ethanol precipitation. Purified DNA was then analysed by conventional or quantitative PCR. As a control for ligation products the BAC clones were digested with 10 U of restriction enzyme overnight and then incubated with 10 U T4 DNA-ligase at 16 °C overnight. The DNA was extracted by phenol-chloroform and precipitated with ethanol. Purified DNA was then analysed by conventional or quantitative PCR. For real-time PCR, the ΔCt method was applied for analysing data, using the BAC clone Ct values as control. Ct values were normalized for each primer pair by setting the Ct value of 100 ng of BAC-clone control random ligation matrix DNA at a value of 1. Primer sequences for PCR are listed here: Backg-Control-AURKA-for: 5'-CGTATGAGCTGGCAATAGCA-3'; Backg-Control-AURKA-rev: 5'-GGAGGCATGAGAGCTTGTC-3'; Backg-Control-A7-for: 5'-ACTGGCTGAGGTTTGTGGAG-3'; Backg-Control-A7-rev: 5'-GGCCGA TTTGAGAGAGTGAG-3'; Backg-Control-SNAI1-for: 5'-CAAGAGGGGAA GGAGAGGAG-3'; Backg-Control-SNAI1-rev: 5'-TCCTAAGTCCCCAGTC TCCA-3'; ncRNA-a7 anchor primer: 5'-CTAGGTCAGGCCCAAGAGA-3'; ncRNA-a7 anchor control: 5'-ACAGAATAACCCATCCCTTTTCC-3'; A7-anchorDigTest-for: 5'-GCTTAACCCAGTGCAAGTC-3'; A7-anchorDigTest-rev: 5'-AGTTTGGAGGCTGGGAATCT-3'; AURKA-N5DigTest-for: 5'-CCT GATTCTCACCTCTTGG-3'; AURKA-N5DigTest-rev: 5'-GAGGCCCAT TCCTTAACAT-3'; SNAI1-N2DigTest-for: 5'-GGGAAAATGAGAGCAAAC TCC-3'; SNAI1-N2DigTest-rev: 5'-AAGGCCAATGTGACAGAGATG-3'; A3-DigEcoRI-for: 5'-CACTTACAGGAACAGAGGACTCA-3'; A3-DigEcoRI-rev: 5'-CAACTTCTAGATCAGCGCCTTC-3'; 3C AURKA-BglII-A: 5'-GGGACAT AAATGGGAGACTGG-3'; 3C AURKA-BglII-B: 5'-TGGGAGGAACCTCTC ACCTCT-3'; 3C AURKA-BglII-C: 5'-TGGCTCTTTGGTCTTGTCTCT-3'; 3C AURKA-BglII-D: 5'-GTTTGGGCCGTTTCTTATTG-3'; 3C AURKA-BglII-E: 5'-CAGACCTGATTCTCACCTCTTG-3'; 3C AURKA-BglII-F: 5'-CACCAA CTTTCTTCTCCACCAA-3'; 3C AURKA-BglII-G: 5'-CCACAGGCACTACT GTTACCAA-3'; 3C BglII-E-R1: 5'-CCAGGGAGGACACAGCATAA-3'; 3C BglII-E-R2: 5'-TGGTGTCTGGGTTGAAGTAACA-3'; 3C BglII-E-R3: 5'-TC GGCACCTGGTAAACTAGC-3'; ncRNA-a3 anchor primer: 5'-CAACTCTA GATCAGCGCTTC-3'; ncRNA-a3 anchor control: 5'-GTCTCTTCTTTGAT TGGAGTGG-3'; TAL1-1: 5'-GGGAATGGCAGAAGACAGAA-3'; TAL1-2: 5'-GTGTGGGTTTGTGTTTACCTC-3'; TAL1-3: 5'-CTCCATTTTGGCCTCTG TCTCT-3'; TAL1-4: 5'-ATCTTTTCCGTGTAGCTCTTCTCT-3'; TAL1-5: 5'-TGGGTTTGATTGCTCAGTACC-3'; TAL1-6: 5'-TCAATTTTGCCTGCCAT ACA-3'; TAL1-7: 5'-TTAAAAGGGCAGGGAGTTAAAAG-3'; TAL1-8: 5'-CAGATAGCCAGGAAGCAAGG-3'; SNAI1-1: 5'-GCTTTGGTCTCTGAAC TCCTG-3'; SNAI1-2: 5'-AACAACTCACATTAATAAAATATCCAGA-3'; SNAI1-3: 5'-CTACAGTCGTGTGCCACCAA-3'; SNAI1-4: 5'-ATTGGCAAGA AGGGGAAAAT-3'; SNAI1-5: 5'-TCCAACATCCCAGACCTTTC-3'; SNAI1-6: 5'-GACCATGAGAAAGCCAGAGG-3'; SNAI1-7: 5'-AAGCTCCAGTGGCAT GTGAT-3'; SNAI1-8: 5'-TGGAGTCTGGTGTGTTCTG-3'. BAC clone ID: RP-11-664B18, RP-11-1067D15, RP11-7421I (Empire Genomics).

28. Jeon, Y. & Lee, J. T. YY1 tethers Xist RNA to the inactive X nucleation center. *Cell* **146**, 119–133 (2011).
29. Hagège, H. *et al.* Quantitative analysis of chromosome conformation capture assays (3C-qPCR). *Nature Protocols* **2**, 1722–1733 (2007).

A two-step mechanism for TRF2-mediated chromosome-end protection

Keiji Okamoto¹, Cristina Bartocci¹, Iliana Ouzounov¹, Jolene K. Diedrich², John R. Yates III² & Eros Lazzerini Denchi¹

Mammalian telomeres repress DNA-damage activation at natural chromosome ends by recruiting specific inhibitors of the DNA-damage machinery that form a protective complex termed shelterin. Within this complex, TRF2 (also known as TERF2) has a crucial role in end protection through the suppression of ATM activation and the formation of end-to-end chromosome fusions^{1,2}. Here we address the molecular properties of TRF2 that are both necessary and sufficient to protect chromosome ends in mouse embryonic fibroblasts. Our data support a two-step mechanism for TRF2-mediated end protection. First, the dimerization domain of TRF2 is required to inhibit ATM activation, the key initial step involved in the activation of a DNA-damage response (DDR). Next, TRF2 independently suppresses the propagation of DNA-damage signalling downstream of ATM activation. This novel modulation of the DDR at telomeres occurs at the level of the E3 ubiquitin ligase RNF168 (ref. 3). Inhibition of RNF168 at telomeres involves the deubiquitinating enzyme BRCC3 and the ubiquitin ligase UBR5, and is sufficient to suppress chromosome end-to-end fusions. This two-step mechanism for TRF2-mediated end protection helps to explain the apparent paradox of frequent localization of DDR proteins at functional telomeres without concurrent induction of detrimental DNA-repair activities.

In mammalian cells, protection of chromosome ends requires TRF2 (ref. 4). When telomeres become critically short, insufficient recruitment of TRF2 leads to telomere de-protection and initiation of a DDR at chromosome termini. Indeed, TRF2-depleted telomeres elicit the same response as critically short telomeres, such as the recruitment of DDR factors (for example, MDC1, RNF8 and 53BP1 (also known as TP53BP1))^{2,5,6}, activation of a cell cycle checkpoint and subsequent repair activities resulting in end-to-end chromosome fusions^{1,7}. Among the telomere-binding proteins, TRF2 is unique in its ability to suppress the ATM-dependent DDR pathway and the non-homologous end-joining pathway^{2,8}.

To define the unique molecular properties of TRF2 that are involved in end protection, we performed a domain-swapping approach between TRF2 and the structurally similar but functionally divergent telomere-binding protein TRF1 (ref. 9; also known as TERF1). TRF2 and TRF1 are both composed of four domains: a carboxy-terminal MYB domain required for binding to double-stranded telomeric DNA (TTAGGG), a flexible hinge domain involved in protein–protein interaction, a TRFH domain required for homodimerization⁹ and a divergent amino-terminal domain (Fig. 1a). The N-terminal domain of TRF2 is rich in basic residues (basic domain), whereas the TRF1 N-terminal domain is composed of acidic residues (acidic domain) (Fig. 1a). We generated a set of chimaeric telomere repeat factors (TRF^c) in which TRF2 domains were replaced by the analogous TRF1 domains. The resulting constructs were tested for their ability to complement for the loss of endogenous TRF2 using TRF2 conditional (*Trf2^{flxed/flxed}*) mouse embryonic fibroblasts (MEFs). To ensure synchronous and complete TRF2 depletion we used *Trf2^{flxed/flxed}* cells carrying an inducible Cre recombinase (*Rosa26-CreERT2*) that can be

activated by 4-hydroxytamoxifen (Supplementary Fig. 1). All TRF^c constructs analysed showed the expected telomere localization in the presence or absence of endogenous TRF2 (Supplementary Fig. 2a–d). Importantly, ectopic TRF1 expression cannot complement for the loss of TRF2, as frequent DNA-damage foci at telomeres—termed telomere-induced foci (TIF)—and chromosome end-to-end fusions still appear (Fig. 1b–d). Conversely, a TRF2 construct that lacks the N-terminal basic domain (TRF2^{ΔB}) is able to suppress TIF formation and end-to-end chromosome fusions (Fig. 1b–d). Similarly, a TRF2 construct in which the DNA-binding domain was replaced with the TRF1 MYB domain (TRF^{cM}) can complement for loss of TRF2 (Fig. 1b–d). These data show that, *in vivo*, the specific ability of TRF2 to protect chromosome ends cannot be explained by a specificity of its DNA-binding domain, or by its unique N-terminal basic domain. By contrast, both the TRFH domain and the hinge domain of TRF2 are required to prevent the initial steps in the DDR pathway, as assessed by γ H2AX localization at telomeres in cells expressing a construct containing either the TRFH domain (TRF^{cT}) or the hinge domain (TRF^{cH}) of TRF1 (Fig. 1b, c). Interestingly, we found that localization of TRF^{cT} at telomeres is sufficient to inhibit the recruitment of key mediators of the DDR pathway downstream of γ H2AX, such as 53BP1 (Fig. 1c and Supplementary Figs 3a–c and 8). In agreement with this observation, TRF^{cT} can also prevent chromosome fusions (Fig. 1d, Supplementary Fig. 7 and Supplementary

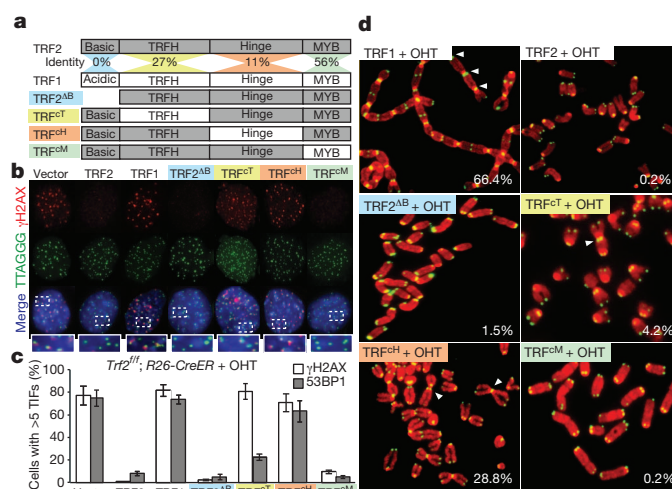


Figure 1 | Critical role for the TRFH domain and the hinge domain of TRF2 in end protection. **a**, Schematic representation of the TRF^c constructs. **b**, The indicated MEFs were treated with 4-hydroxytamoxifen (+OHT) and stained for γ H2AX, telomere DNA and 4',6-diamidino-2-phenylindole (DAPI) (blue). **c**, Quantification of cells with five or more 53BP1 (or γ H2AX) foci at telomeres. Error bars denote \pm standard deviation (s.d.) derived from three experiments. **d**, Metaphase spreads of MEFs treated as in **c** were stained for telomere DNA (green) and DAPI (red). Percentages of chromosome fusions are indicated. *fff*, floxed/floxed; *R26*, *Rosa26*.

¹Laboratory of Chromosome Biology and Genomic Stability, Department of Molecular and Experimental Medicine, The Scripps Research Institute, La Jolla, California 92037, USA. ²Department of Chemical Physiology and Cell Biology, The Scripps Research Institute, La Jolla, California 92037, USA.

Table 1), a process that requires 53BP1 recruitment^{10,11}. We rejected the hypothesis that TRF^{CT} has a dominant-negative effect because its expression in TRF2-proficient cells does not result in DNA-damage induction (Supplementary Fig. 5). By contrast, in cells expressing TRF^{CH}, both γ H2AX and 53BP1 localize to telomeres (Fig. 1b, c and Supplementary Fig. 3a–c). Interestingly, despite levels of TIFs that are comparable to those observed in TRF2-deficient (*Trf2*^{−/−}) cells, telomeres are partially protected from chromosome fusions (Fig. 1d, Supplementary Fig. 7 and Supplementary Table 1). In agreement with that observed in *Trf2*^{−/−} cells², we found that the DDR initiated at TRF^{CT}- or TRF^{CH}-bound telomeres is ATM dependent (Supplementary Fig. 6). Our finding suggests that the TRFH domain is required to prevent the initial step of the DDR response, but that other portions of TRF2 can independently suppress propagation of this signal to downstream effectors.

Next, we addressed the question of which step in the DDR response is inhibited by TRF2 by testing the localization of MDC1, RNF8 and RNF168 DNA-damage factors that are downstream of γ H2AX and upstream of 53BP1 (ref. 12). Upon TRF2 depletion, γ H2AX, MDC1 and RNF8 localize to telomeres in cells expressing TRF^{CT}, confirming that the TRF2 TRFH domain is required to prevent the initial steps in the DDR pathway (Fig. 2a, b, d). Similarly, we did not detect defects in SUMO1 accumulation at telomeres (data not shown). By contrast, the ubiquitin ligase RNF168 does not localize to TRF^{CT}-bound telomeres (Fig. 2c, d). We exclude the possibility that this is due to a general inhibition of RNF168 activity in these cells as they readily form RNF168 irradiation-induced foci (Supplementary Fig. 9). Recruitment of RNF168 at sites of damage is required for efficient 53BP1 recruitment^{3,13}, which in turn promotes chromosome fusions¹¹.

To identify the critical region of TRF2 involved in the suppression of RNF168 recruitment, we focused on the hinge domain, given the high

frequency of 53BP1 TIFs observed in cells expressing TRF^{CH} (Fig. 1d). The main function attributed to this domain until now has been the interaction with RAP1 and TIN2 (also known as TERF2IP and TIN2, respectively), two members of the shelterin complex that have been implicated in end protection^{14–16}. We excluded a role for RAP1 in inhibiting RNF168 recruitment as deletion of the RAP1-interaction motif (amino acids 286–299)¹⁷ in the context of the TRF^{CT} construct did not result in 53BP1 localization to telomeres (Fig. 3a, b and Supplementary Fig. 11b). Similarly, deletion of the TIN2-interaction motif (amino acids 352–367)¹⁸ resulted only in a minor induction of 53BP1 accumulation, thus excluding a critical role for this interaction in the suppression of RNF168 at telomeres (Fig. 3a, b and Supplementary Fig. 11b). This implicated the C-terminal portion of the hinge domain (amino acids 407–431), a region that by sequence alignment shows a high degree of conservation between species (Supplementary Fig. 10). Deletion of this region—which we have termed the inhibitor of DDR (iDDR) region—in the context of the TRF^{CT} construct resulted in levels of 53BP1 that are comparable to those observed in *Trf2*^{−/−} cells (Fig. 3a, b and Supplementary Fig. 11). To further validate this finding and to test whether this region is also sufficient to prevent DDR activation, we expressed the iDDR region in the context of TRF1 (Fig. 3a). Notably, the resulting TRF1^{iDDR} protein can complement the phenotypes associated with TRF2 loss, with significant inhibition of 53BP1 and RNF168 localization and chromosome fusions (Fig. 3b, c and Supplementary Figs 11b, f and 12). By contrast, expression of TRF1^{iDDR} could not fully complement loss of TRF2 with regards to γ H2AX localization at telomeres (Fig. 3b and Supplementary Fig. 11c), a result that is in agreement with our data indicating a critical role for the TRFH domain of TRF2 in suppressing the initial activation of the DDR.

We then addressed the mechanism for the iDDR-dependent inhibition of RNF168 recruitment to dysfunctional telomeres. RNF168 is a ubiquitin ligase that is recruited to damaged chromatin by ubiquitin chains generated by the RNF8–UBE13 (also known as UBE2N) complex^{3,13}. Ubiquitinated proteins can be detected at dysfunctional telomeres with an antibody raised against conjugated ubiquitin (FK2; Supplementary Fig. 13e). By contrast, we did not detect conjugated ubiquitin at TRF^{CT}-bound telomeres (Supplementary Fig. 13e), suggesting a defective ubiquitin-mediated signalling in this context. Two mechanisms can explain this phenotype: inhibition of RNF8 activity, or

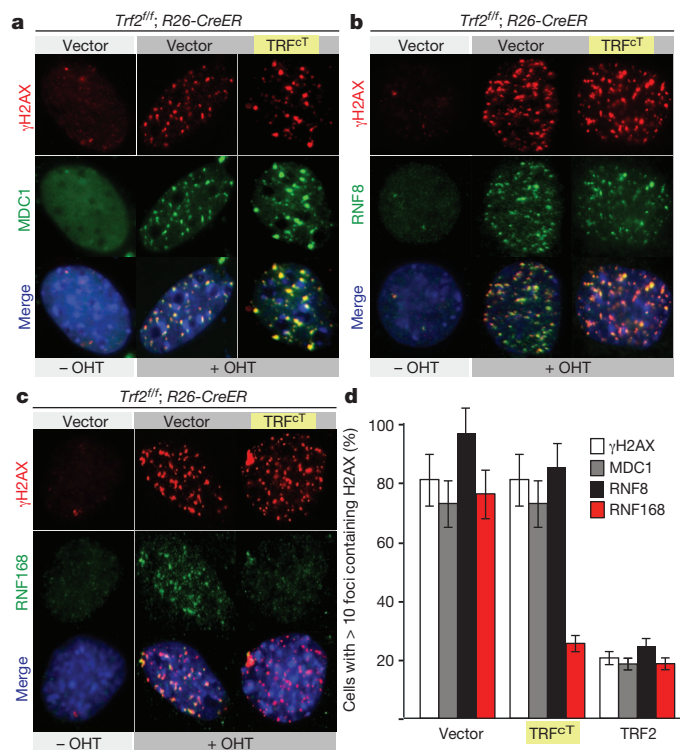


Figure 2 | Inhibition of RNF168 recruitment at chromosome ends.

a, b, MEFs infected with the indicated constructs and expressing MDC1–green fluorescent protein (GFP) (**a**) or RNF8–GFP (**b**) were treated with OHT and stained for γ H2AX, GFP and DAPI (blue). **c,** MEFs infected with the indicated constructs were stained for γ H2AX, RNF168 and DAPI (blue). **d,** Quantification of data presented in panels **a** to **c**. Median values and \pm s.d. are derived from three independent experiments.

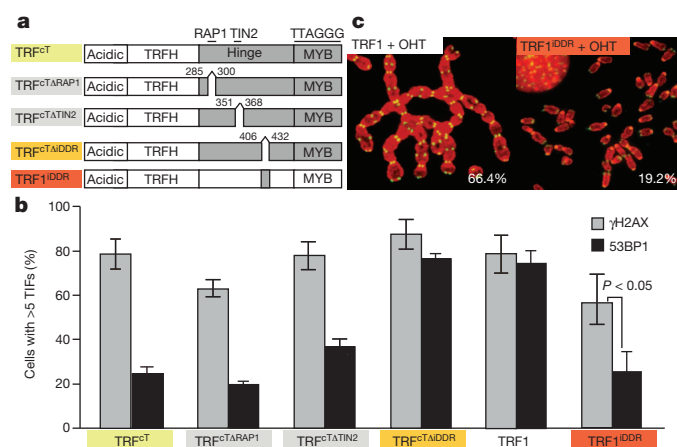


Figure 3 | The C-terminal portion of the hinge domain of TRF2 is necessary and sufficient to prevent 53BP1 localization at telomeres.

a, Schematic representation of the TRF^{CT} constructs used to define the role of the hinge domain in end protection. **b,** Quantification of cells that show five or more 53BP1 (or γ H2AX) foci colocalizing at telomeres. Error bars denote \pm s.d. derived from three experiments. Cells expressing the indicated constructs were treated with OHT to deplete endogenous TRF2. **c,** Metaphase spreads of MEFs infected with either TRF1 or TRF1^{iDDR} and treated with OHT were stained for telomere DNA (green) and DAPI (red). Percentages of chromosomes with fusions are indicated.

recruitment of deubiquitinating enzymes (DUBs). Because RNF8 is localized at telomeres in cells expressing TRF^{CT} (Fig. 2b), we focused on the two DUB enzymes that have been shown to counteract the action of RNF8-UBC13 at sites of DNA damage: OTUB1 and BRCC3 (refs 19, 20). We reasoned that if either of these DUBs has a role in TRF2-mediated end protection, reducing their levels should result in 53BP1 recruitment to telomeres in cells expressing TRF^{CT}. Efficient (>90%) short hairpin RNA (shRNA)-mediated depletion of *Otub1* did not result in 53BP1 foci formation (Supplementary Fig. 13a, b). By contrast, two independent shRNA constructs directed against *Brcc3* (with knockdown efficiencies of 95% and 98%; Supplementary Fig. 13c, d) resulted in the accumulation of 53BP1 and ubiquitin chains at telomeres in cells expressing TRF^{CT} (Fig. 4a and Supplementary Fig. 13e). Moreover, BRCC3 depletion in these cells resulted in levels of end-to-end chromosome fusions that are comparable to that observed in *Trf2*^{-/-} cells (Supplementary Fig. 14). This latter result further corroborates the previous observation suggesting a critical role for 53BP1 localization for efficient DNA-repair events.

To verify whether BRCC3-mediated suppression of the DDR is associated with the iDDR region of TRF2, we tested whether *Trf2*^{-/-} cells expressing TRF1^{iDDR} require BRCC3 expression to ensure end protection. Indeed, shRNA-mediated downregulation of *Brcc3* in these cells abolishes the protective role of TRF1^{iDDR}, resulting in levels of 53BP1 localization and chromosome fusions that are comparable to the ones observed in *Trf2*^{-/-} cells (Fig. 4a–c).

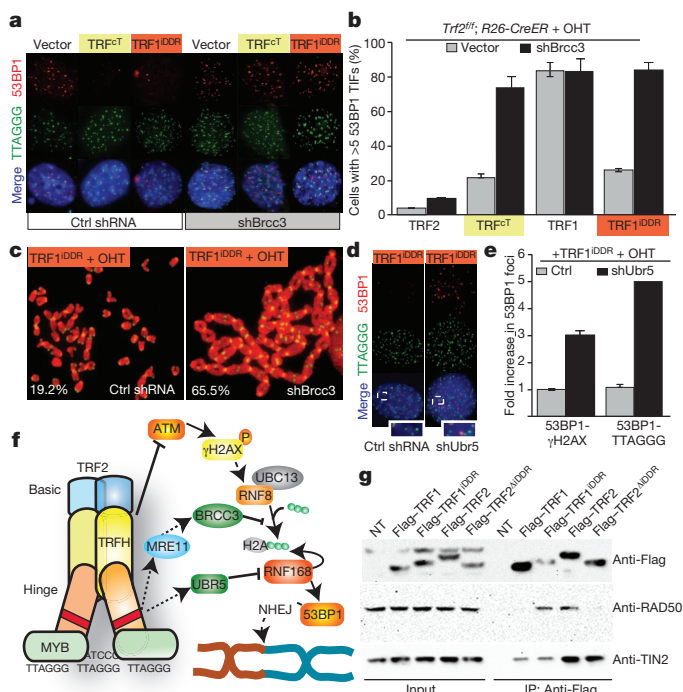


Figure 4 | Mechanism of TRF2-mediated inhibition of RNF168. **a**, Cells were infected with *Brcc3* (shBrcc3) or control (ctrl) shRNA, treated with OHT and stained for 53BP1 and telomere DNA. **b**, Quantification of staining in **a**. **c**, Metaphases of TRF1^{iDDR}-expressing cells treated as described in **a** were stained for telomere DNA (green) and DAPI (red). Percentages of chromosome fusions are indicated. **d**, TRF1^{iDDR}-expressing MEFs infected with *Ubr5* (shUbr5) shRNA or a control shRNA were treated as described in **a**. **e**, Quantification of cells with 53BP1 colocalizing with γH2AX (or telomere DNA (TTAGGG)). Data are normalized to the control samples. **f**, Schematic of the proposed model for TRF2-mediated chromosome-end protection. Dashed lines indicate that additional factors may be involved. NHEJ, non-homologous end joining. **g**, HEK293 cells were transfected with the indicated constructs. Cell extracts were immunoprecipitated (IP) with anti-Flag resin and immunoblotted as indicated. NT, not treated.

To identify proteins that can be recruited at telomeres by the iDDR region of TRF2, Flag-tagged TRF1^{iDDR} was immunoprecipitated and analysed by mass spectrometry (Supplementary Fig. 17 and Supplementary Table 3). As a negative control, we used Flag-TRF1. The members of the MRE11 complex (MRE11 (also known as MRE11A), NBS1 (also known as NBN) and RAD50) and the ubiquitin ligase UBR5 were identified in TRF1^{iDDR} immunoprecipitates but not in TRF1 immunoprecipitates in three independent experiments (Supplementary Fig. 17). We confirmed that the iDDR region of TRF2 is required and sufficient to interact with RAD50 (Fig. 4g). Interestingly, the MRE11 complex has been shown to interact directly with BRCA1 (refs 21, 22). We therefore proposed that members of the MRE11 complex could recruit BRCC3. Indeed, we found that NBS1 interacts with BRCC3 in co-immunoprecipitation experiments and can thus provide a physical link between TRF2 and BRCC3 (Supplementary Fig. 17f). On the basis of these data we propose a model in which TRF2, by its established interaction with the MRE11 complex²³, is able to recruit the BRCC3 enzyme at telomeres, which in turn can suppress RNF168 recruitment. However, we cannot rule out that additional unknown mechanisms may be involved in BRCC3 recruitment to telomeres. In addition, we found that the ubiquitin ligase UBR5 is required to mediate the iDDR-mediated end protection observed in *Trf2*^{-/-} cells expressing TRF1^{iDDR} (Fig. 4d, e and Supplementary Fig. 18). Recent reports have shown that UBR5 targets RNF168 for degradation²⁴. We therefore propose a model in which RNF168 recruitment at telomeres is opposed by the action of BRCC3 and UBR5 (Fig. 4f).

In summary, we found that two distinct regions within TRF2 are required to prevent activation of the DDR pathway at chromosome ends (Fig. 4f). Our data indicate that the TRFH domain of TRF2 can prevent activation of the ATM pathway independently from other regions of TRF2. Together with previous observations, this suggests that this region might be involved in t-loop formation, a structural conformation of chromosome ends that has been proposed to hide the ends of chromosomes from the DNA-damage machinery²⁵. In addition, we have identified a new function for TRF2 downstream of ATM activation and dependent on a portion of the hinge domain, here termed iDDR. TRF2 can sever the DNA-damage signalling cascade at the level of RNF168, preventing 53BP1 localization and, consequently, chromosome fusions. This finding provides a model to explain the apparent paradox of frequent localization of DNA-damage proteins at functional telomeres^{23,26}. Interestingly, in *Schizosaccharomyces pombe*, inhibition of Crb2 (the orthologue of mammalian 53BP1) recruitment at telomeres involves modulation of the methylation status of histone H4 (ref. 27). Our data indicate that, in mammalian cells, a similar effect is achieved by inhibiting ubiquitin-dependent signalling at chromosome ends. This new end-protection role for TRF2 is mediated by the BRCA1 complex through its associated DUB enzyme BRCC3 and by the ubiquitin ligase UBR5. In support of a critical role for the BRCA1 complex in chromosome end protection and in agreement with previous reports^{28,29}, we show that inhibition of BRCA1, RAP80 (also known as UIMC1) or BRCC3 results in partial loss of end protection (Supplementary Fig. 16). The identification of BRCC3 as a critical factor involved in TRF2-dependent telomere protection suggests that an important physiological function of the BRCA1 complex is to maintain genomic stability by aiding telomere-associated proteins in maintaining telomere integrity.

METHODS SUMMARY

MEFs. MEFs were generated as described¹, immortalized with Simian virus 40 large T antigen and treated with 4-hydroxytamoxifen (0.6 μM) to induce Cre-mediated recombination.

Constructs. TRF^{CT} constructs were generated by PCR amplification (primers used are listed in Supplementary Table 2). pLDT-GFP-RNF8, pLDT-GFP-RNF168 and GFP-MDC1 were a gift from M. D. Weitzman. pOZ-FH-BRCC3 was obtained

from Addgene. pcDNA-MYC-MRE11 and pcDNA-MYC-NBS1 were a gift from X. Wu.

Antibodies. The following antibodies were used: MYC (9B11, Cell Signaling), CHK2 (BD Biosciences), hRAD50 (Novus, NB100-154SS), hUBR5 (Santa Cruz, sc-9562), Flag (Sigma, F7425), HA (Covance, 16B12), γ H2AX (Millipore, JWB301), 53BP1 (Novus, NB 100-304), GFP (Invitrogen, A6455), BRCA1 (a gift from X. Yu), RNF168 (a gift from D. Durocher) and FK2 (Millipore, 04-263).

Purification of protein interacting with the iDDR region. HEK293 cells transfected with Flag-tagged TRF1 or Flag-tagged TRF1^{iDDR} were lysed, immunopurified using Flag resin, and samples analysed by nanoflow liquid chromatography mass spectrometry.

Full Methods and any associated references are available in the online version of the paper.

Received 27 March; accepted 21 December 2012.

Published online 6 February 2013.

- Celli, G. B. & de Lange, T. DNA processing is not required for ATM-mediated telomere damage response after TRF2 deletion. *Nature Cell Biol.* **7**, 712–718 (2005).
- Denchi, E. L. & de Lange, T. Protection of telomeres through independent control of ATM and ATR by TRF2 and POT1. *Nature* **448**, 1068–1071 (2007).
- Stewart, G. S. *et al.* The RIDDLE syndrome protein mediates a ubiquitin-dependent signaling cascade at sites of DNA damage. *Cell* **136**, 420–434 (2009).
- de Lange, T. Protection of mammalian telomeres. *Oncogene* **21**, 532–540 (2002).
- di Fagagna, F. D. *et al.* A DNA damage checkpoint response in telomere-initiated senescence. *Nature* **426**, 194–198 (2003).
- Takai, H., Smogorzewska, A. & de Lange, T. DNA damage foci at dysfunctional telomeres. *Curr. Biol.* **13**, 1549–1556 (2003).
- van Steensel, B., Smogorzewska, A. & de Lange, T. TRF2 protects human telomeres from end-to-end fusions. *Cell* **92**, 401–413 (1998).
- Smogorzewska, A., Karlseder, J., Holtgreve-Grez, H., Jauch, A. & de Lange, T. DNA ligase IV-dependent NHEJ of deprotected mammalian telomeres in G1 and G2. *Curr. Biol.* **12**, 1635–1644 (2002).
- Broccoli, D., Smogorzewska, A., Chong, L. & de Lange, T. Human telomeres contain two distinct Myb-related proteins, TRF1 and TRF2. *Nature Genet.* **17**, 231–235 (1997).
- Difilippantonio, S. *et al.* 53BP1 facilitates long-range DNA end-joining during V(D)J recombination. *Nature* **456**, 529–533 (2008).
- Dimitrova, N., Chen, Y. C., Spector, D. L. & de Lange, T. 53BP1 promotes non-homologous end joining of telomeres by increasing chromatin mobility. *Nature* **456**, 524–528 (2008).
- Lukas, J., Lukas, C. & Bartek, J. More than just a focus: the chromatin response to DNA damage and its role in genome integrity maintenance. *Nature Cell Biol.* **13**, 1161–1169 (2011).
- Doil, C. *et al.* RNF168 binds and amplifies ubiquitin conjugates on damaged chromosomes to allow accumulation of repair proteins. *Cell* **136**, 435–446 (2009).
- Sfeir, A. *et al.* Mammalian telomeres resemble fragile sites and require TRF1 for efficient replication. *Cell* **138**, 90–103 (2009).
- Sarthy, J., Bae, N. S., Scraftford, J. & Baumann, P. Human RAP1 inhibits non-homologous end joining at telomeres. *EMBO J.* **28**, 3390–3399 (2009).
- Takai, K. K., Kibe, T., Donigian, J. R., Frescas, D. & de Lange, T. Telomere protection by TPP1/POT1 requires tethering to TIN2. *Mol. Cell* **44**, 647–659 (2011).
- Sfeir, A., Kabir, S., van Overbeek, M., Celli, G. B. & de Lange, T. Loss of Rap1 induces telomere recombination in the absence of NHEJ or a DNA damage signal. *Science* **327**, 1657–1661 (2010).
- Chen, Y. *et al.* A shared docking motif in TRF1 and TRF2 used for differential recruitment of telomeric proteins. *Science* **319**, 1092–1096 (2008).
- Nakada, S. *et al.* Non-canonical inhibition of DNA damage-dependent ubiquitination by OTUB1. *Nature* **466**, 941–946 (2010).
- Shao, G. *et al.* The Rap80-BRCC36 de-ubiquitinating enzyme complex antagonizes RNF8-Ubc13-dependent ubiquitination events at DNA double strand breaks. *Proc. Natl Acad. Sci. USA* **106**, 3166–3171 (2009).
- Wang, Y. *et al.* BASC, a super complex of BRCA1-associated proteins involved in the recognition and repair of aberrant DNA structures. *Genes Dev.* **14**, 927–939 (2000).
- Chen, L., Nievera, C. J., Lee, A. Y. & Wu, X. Cell cycle-dependent complex formation of BRCA1.CtIP.MRN is important for DNA double-strand break repair. *J. Biol. Chem.* **283**, 7713–7720 (2008).
- Zhu, X. D., Kuster, B., Mann, M., Petrini, J. H. & de Lange, T. Cell-cycle-regulated association of RAD50/MRE11/NBS1 with TRF2 and human telomeres. *Nature Genet.* **25**, 347–352 (2000).
- Gudjonsson, T. *et al.* TRIP12 and UBR5 suppress spreading of chromatin ubiquitylation at damaged chromosomes. *Cell* **150**, 697–709 (2012).
- Griffith, J. D. *et al.* Mammalian telomeres end in a large duplex loop. *Cell* **97**, 503–514 (1999).
- Verdun, R. E., Crabbe, L., Hagglblom, C. & Karlseder, J. Functional human telomeres are recognized as DNA damage in G2 of the cell cycle. *Mol. Cell* **20**, 551–561 (2005).
- Carneiro, T. *et al.* Telomeres avoid end detection by severing the checkpoint signal transduction pathway. *Nature* **467**, 228–232 (2010).
- Al-Wahiby, S. & Slijepcevic, P. Chromosomal aberrations involving telomeres in BRCA1 deficient human and mouse cell lines. *Cytogenet. Genome Res.* **109**, 491–496 (2005).
- McPherson, J. P. *et al.* A role for Brca1 in chromosome end maintenance. *Hum. Mol. Genet.* **15**, 831–838 (2006).

Supplementary Information is available in the online version of the paper.

Acknowledgements We thank T. de Lange, M. D. Weitzman, D. Durucher, X. Yu and X. Wu for providing reagents. We are grateful to A. Sfeir, T. Stracker, K. Miller and C. Attwooll for critical reading of the manuscript. This work was supported by a Pew Scholars Award (E.L.D.), the Novartis Advanced Discovery Institute (E.L.D.), National Institutes of Health AG038677 (E.L.D.), National Center for Research Resources (5P41RR011823-17) (J.R.Y.) and National Institute of General Medical Sciences (8 P41 GM103533-17) (J.R.Y.).

Author Contributions E.L.D. and K.O. conceived the experimental design. K.O., C.B., I.O. and E.L.D. performed the experiments and analysed the data. J.K.D. and J.R.Y. performed the mass spectrometry analysis. E.L.D. wrote the manuscript.

Author Information Reprints and permissions information is available at www.nature.com/reprints. The authors declare no competing financial interests. Readers are welcome to comment on the online version of the paper. Correspondence and requests for materials should be addressed to E.L.D. (edenchi@scripps.edu).

METHODS

Mice and MEFs. Rosa26-CreERT2 mice (Jackson Laboratories) and mice carrying a conditional TRF2 construct¹ were crossed to generate MEFs. MEFs were immortalized with pBabeSV40LT and treated 4-hydroxytamoxifen (0.6 μ M) to induce Cre-mediated recombination.

Constructs, plasmids and viral infections. TRF^c constructs were generated by PCR amplification using as templates pBabe-MYC-TRF1 or pBabe-MYC-TRF2 constructs (primers used are listed in Supplementary Table 2). pLDT-GFP-RNF8, pLDT-GFP-RNF168 and GFP-MDC1 were a gift from M. D. Weitzman. pOZ-FH-BRCC3 was obtained from Addgene. pcDNA-MYC-MRE11 and pcDNA-MYC-NBS1 were a gift from X. Wu.

Immunofluorescence, FISH and ChIP. Immunofluorescence, fluorescence *in situ* hybridization and chromatin immunoprecipitation (ChIP) experiments were performed as described previously². The following antibodies were used: MYC (9B11, Cell Signaling), CHK2 (BD Biosciences), hRAD50 (Novus, NB100-154SS), hUBR5 (EDD) (Santa Cruz, sc-9562), Flag (Sigma, F7425) or HA (Covance, 16B12), γ H2AX (Millipore, JBW301), 53BP1 (Novus, NB 100-304), GFP (Invitrogen, A6455), BRCA1 (a gift from X. Yu), RNF168 (a gift from D. Durocher) and FK2 (Millipore, 04-263). For immunoprecipitation the following antibodies were used: MYC (9B11, Cell Signaling) and Flag M2 affinity gel (Sigma, A2220). Quantification of immunofluorescence experiments was performed by

counting at least 200 cells per condition. Data from three independent experiments were used to calculate median value and standard deviation.

shRNA. pLKO lentiviral vectors were used to express shRNAs directed against the following targeting sequences: 5'-GCTCAGTATTTACCAAGAATT-3' (*Brcc3*), 5'-GTCCATCCAAGTGGAGTACAT-3' (*Otub1*), 5'-CCCATTTCAGTATCCTG GCTT-3' (*Rap80*) and 5'-AACCAGATGTCTGTACTAAGG-3' (*Brca1*).

Purification of protein interacting with the iDDR region. HEK293 cells were transfected with Flag-tagged TRF1 or Flag-tagged TRF1^{iDDR}. Cells were lysed (50 mM Tris-HCl, pH 7.5, 150 mM NaCl, 1 mM EDTA buffer, 0.5% Triton X-100) and immunopurified with anti-Flag agarose resin (Sigma). After washing, proteins were eluted by competition with Flag peptide (Sigma). For mass spectrometry analysis samples were denatured, reduced and alkylated before an overnight digestion with trypsin. Peptide mixtures were analysed by nanoflow liquid chromatography mass spectrometry using an Eksigent nanopump and LTQ Orbitrap mass spectrometer (Thermo Scientific) using a seven-step multidimensional protein identification technology (MudPIT) separation. Tandem mass spectrometry spectra were collected in a data-dependent fashion and resulting spectra were extracted using RawXtract. Protein identification was done with Integrated Proteomics Pipeline (IP2) by searching against the UniProt Human database and filtering to 1% false positive at the spectrum level using DTASelect. Immunoprecipitation between Flag-tagged TRF proteins and RAD50 were performed on nuclear extracts.

CORRIGENDUM

doi:10.1038/nature11903

Corrigendum: Comprehensive genomic characterization defines human glioblastoma genes and core pathways

The Cancer Genome Atlas Research Network

Nature **455**, 1061–1068 (2008); doi:10.1038/nature07385

In this Article, we reported somatic mutations in the human ERBB2 gene in 7 of 91 cases analysed by capillary DNA sequencing and validated by mass spectrometric genotyping. Further analysis of these cases has revealed that the mutations were present only in the whole-genome amplified tumour DNA used for the study but not in the unamplified tumour DNA (see ref. 1 for more details). The reported mutations are likely to be artefacts of whole-genome amplification, because the ERBB2 mutations in our Article were not validated in unamplified DNA. The validity of recurrent mutations in other genes besides ERBB2 that were reported to be significantly mutated in our Article (namely TP53, PTEN, NF1, EGFR, RB1, PIK3R1 and PIK3CA) has been confirmed by The Cancer Genome Atlas Research Network using unamplified DNA (ref. 2).

1. Greulich, H, et al. Functional analysis of receptor tyrosine kinase mutations in lung cancer identifies oncogenic extracellular domain mutations of ERBB2. *Proc. Natl Acad. Sci. USA* **109**, 14476–14481 (2012).
2. The Cancer Genome Atlas Research Network. The somatic genomic landscape of glioblastoma. *Cell* (submitted).

CORRIGENDUM

doi:10.1038/nature11976

Corrigendum: Mesoangioblast stem cells ameliorate muscle function in dystrophic dogs

Maurilio Sampaolesi, Stephane Blot, Giuseppe D'Antona, Nicolas Granger, Rossana Tonlorenzi, Anna Innocenzi, Paolo Mognol, Jean-Lauren Thibaud, Beatriz G. Galvez, Ines Barthélémy, Laura Perani, Sara Mantero, Maria Guttinger, Orietta Pansarasa, Chiara Rinaldi, M. Gabriella Cusella De Angelis, Yvan Torrente, Claudio Bordignon, Roberto Bottinelli & Giulio Cossu

Nature **444**, 574–579 (2006); doi:10.1038/nature05282

In Fig. 4b of this Article, the gel for the loading control MyHC for the dog Vaccin was an unintentional duplication of the loading control for the dog Vampire (which is correct). The correct gel is shown below in Fig. 1. The error does not affect any of our results. Figure 4 has been corrected in the original Article's HTML and PDF online.

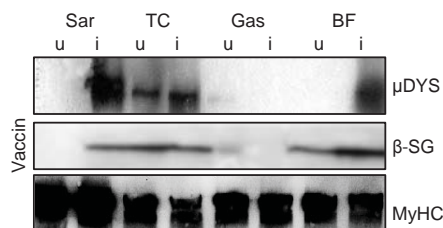


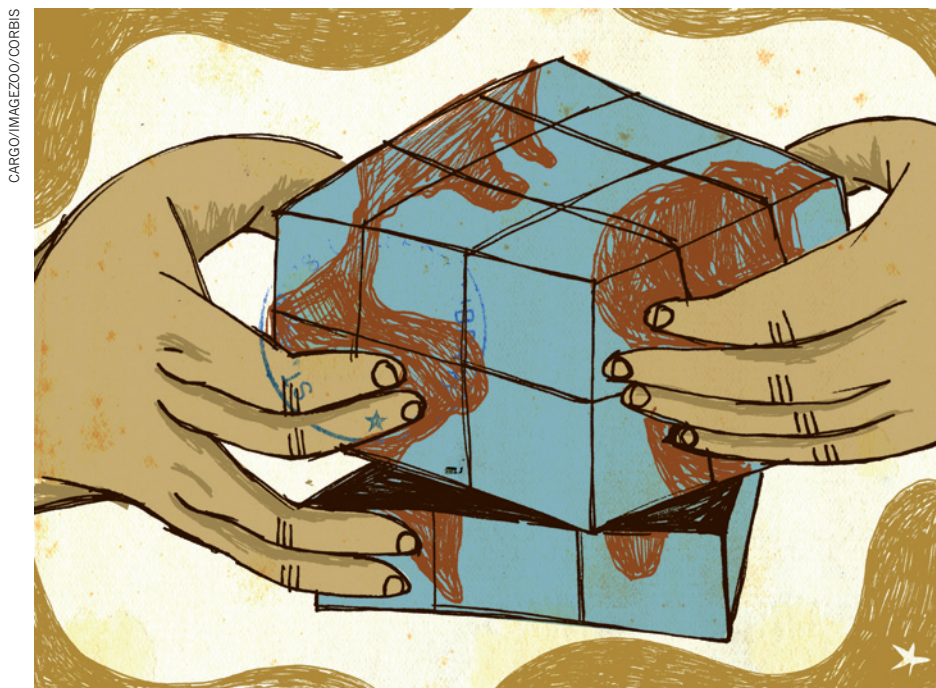
Figure 1 | This is the corrected lower-right panel of Fig. 4b of the original article.

CAREERS

RECRUITMENT Survey reveals that many drug-makers plan to hire **p.509**

UNIVERSITIES Institutions ditch European Commission ranking scheme **p.509**

NATUREJOBS For the latest career listings and advice www.naturejobs.com



SUSTAINABILITY

Environmental puzzle solvers

Sustainability training is on the rise, and institutions are working out how best to translate it into marketable skills.

BY AMANDA MASCARELLI

Just hours after defending his PhD dissertation, Thaddeus Miller was celebrating over drinks with his wife and adviser when he got a call. Portland State University in Oregon was offering him an interview for an assistant-professor position. The university's Nohad A. Toulan School of Urban Studies and Planning was "looking for someone who thinks about urban sustainability not just in terms of research but in terms of practice", says Miller. He got the job.

Miller, an environmental social scientist, was one of the first PhD graduates from the School of Sustainability at Arizona State University

(ASU) in Tempe. Established in 2007, the ASU PhD programme was one of the first in the world devoted to sustainability — using interdisciplinary approaches from fields such as Earth and environmental science, conservation biology, engineering, economics and urban planning to maintain ecosystems, the environment and natural resources. But in the past few years, colleges and schools focused on the subject have sprung up (see "The many ways to get sustainable"). In principle, sustainability training helps engineers and scientists not only to produce better materials, but also to understand the social impacts of their work.

The approach to teaching sustainability varies from institution to institution. And the

very concept has met with some scepticism. "There's definitely some risk in doing these types of programmes, both broadly for the programme and also for the individual," says Miller, who endorses the approach but notes that some employers are circumspect about the value of a sustainability degree. Among academics too, he says, there is still some cynicism. Is 'sustainability' merely a buzzword, or can it be a legitimate foundational concept for graduate education?

Programmes that are not grounded in traditional core disciplines make some people wary. But in principle, sustainability allows the pursuit of innovative approaches to environmental and societal challenges. Students attracted to sustainability programmes are often those who relish jumping between disciplines and enjoy considering how science can inform decision-making.

NEW APPROACHES

Some schools are weaving sustainability thinking into the fabric of their institutions, beginning at the undergraduate level. Others offer graduate programmes that remain largely disciplinary, yet encourage their students to cross disciplinary boundaries through extra-curricular projects. Yet others, including the ASU School of Sustainability, are still evolving.

These programmes all face a similar conundrum: how to make the interdisciplinary approach not only substantive, but also practical for early-career scientists. "We need to train ourselves at being effective at being broad," says Charles Redman, an urban ecologist and the founding director of the ASU school. "Broad is not shallow. We need excellence in bringing things together and doing interdisciplinary collaborative work."

To that end, the School of Sustainability has proposed eschewing specific subjects in favour of core competencies such as working in teams, systems thinking (which includes understanding feedbacks, cascades and unintended consequences) and understanding how values affect policy and decision-making.

The school offers two-year master of arts and master of science degrees, a PhD and an undergraduate major and minor. It will also launch a master's degree in sustainable solutions with a business focus later this year. One graduate worked with local government, non-governmental organizations and others to help the city of San Juan in Puerto Rico to adopt more sustainable practices; a current PhD candidate is working on high-school teaching strategies ►

► that encourage sustainable thinking.

Some programmes that promote sustainability have augmented, rather than abandoned, their disciplinary approaches. For example, the University of Washington in Seattle runs a graduate certificate in Environmental Management that complements the research of students doing other graduate degrees. The students form multidisciplinary teams to tackle real-world problems presented by local, federal or tribal governments under a timeline and with specific 'deliverables' such as providing cost estimates for reducing a city's carbon footprint.

Even though disciplinary boundaries are observed, some departmental barriers have been broken down. In 2008, the University of Washington brought together its marine, Earth and atmospheric departments under the umbrella of the College of the Environment to encourage cross-communication, says Lisa Graumlich, dean of the new college. "We now have a much easier way for a graduate student interested in climate change to assemble the coursework, the mentors and the professional

opportunities that bring together the dynamics of the Earth system — how the atmosphere interacts with the ocean, and how that has feedbacks with the biosphere," she says.

The Institute for Advanced Sustainability Studies in Potsdam, Germany, takes a similar approach. "The PhD itself generally stays relatively disciplinary but [the students] are in an environment where they can bring an interdisciplinary twist to it," says atmospheric scientist Mark Lawrence, a scientific director at the institute. About half of the organization's 100 scientists focus on sustainability related to climate and atmospheric science.

Crossing disciplinary boundaries is acceptable at some German universities but frowned on at others, says Lawrence. And students sometimes shy away from pursuing interdisciplinary tracks out of concern that such qualifications might not carry enough weight on their CVs, he says. "We have the challenge of developing the incentive structures and recognition so that people understand the value of interdisciplinary research."

Fledgling programmes are attempting to

ENVIRONMENTAL OPTIONS

The many ways to get sustainable

Sustainability is taught using a variety of approaches. Here are a few of them.

- The Education for Sustainability Programme at London South Bank University offers postgraduate courses focused on communicating and raising awareness about sustainability. They are held online and are open to students across the globe (see www.efsccommunity.t83.net).
- The Patel College of Global Sustainability at the University of South Florida in Tampa last year launched a sustainable-tourism track for its master's degrees, owing to demand from firms such as the Walt Disney Company, Royal Caribbean and Hilton Hotels and Resorts, says Kalanithy Vairavamoorthy, dean of the college. Sustainable tourism is meant to promote environmental and cultural awareness, he adds.
- Colorado State University in Fort Collins launched its School of Global Environmental Sustainability in 2008, and offers an undergraduate minor starting with a class called Foundations of Environmental Sustainability. The school is piloting a graduate-level course and planning a graduate curriculum.
- The Golisano Institute for Sustainability at the Rochester Institute of Technology in New York opened in 2008 and offers master's and PhD programmes in sustainability and architecture. A 7,800-square-metre, four-storey main building that opened

last month includes eight laboratories for sustainability-technology instruction.

- The Monash Sustainability Institute at Monash University in Melbourne, Australia, launched its PhD programme in 2009 and graduated its first PhD student in 2012. The institute is also designing a master's degree in sustainability.
- The College of the Environment at the University of Washington in Seattle offers more than ten graduate degrees for master's and PhD students as well as graduate-certificate programmes that cut across disciplines but focus on environmental issues.
- In January, the University of Michigan in Ann Arbor launched its Dow Sustainability Fellows Program, which will provide 40 master's and professional-degree students with US\$20,000 each for a year to do an interdisciplinary sustainability project.
- Portland State University in Oregon offers graduate certificates in sustainability and urban design, as well as certificates with a sustainability bent in transportation, hydrology and property development.
- A smattering of US liberal arts colleges are also approaching sustainability training. For example, Green Mountain College in Poultney, Vermont, offers multiple online graduate programmes including a master's of science in environmental studies, a master's of science in sustainable food systems and a master's of business administration in sustainable business. **A.M.**

establish graduate concentrations or sustainability degrees that have the rigour demanded by potential employers. To ensure that its graduates walk away with useful skills, the Patel College of Global Sustainability at the University of South Florida in Tampa undertook a six-month consultation with other colleges and relevant stakeholders — ranging from the Tampa Bay Regional Planning Council to Tampa Electric, the Sierra Club — an environmental organization based in San Francisco, California — and the International Ecotourism Society in Washington DC.

The discussions allowed the college to get down to the “nuts and bolts” of the expectations and requirements that employers have for students with a sustainability degree, says Kalanithy Vairavamoorthy, dean of the college. Desirable skills include systems thinking, strategic planning and return on investment for sustainable practices — which entails evaluating environmental performance (for example, gauging water and energy use and pollution loads), economic performance (such as efficiency gains) and social performance (including gains in green jobs). The college’s master of arts degree offers three concentrations: water, sustainable tourism and entrepreneurship, with courses covering topics such as sustainable business practices, environmental management and communicating the value of sustainability.

SUSTAINABLE CAREER PATHS

Although unconventional, sustainability training has job potential. University of Washington graduates, for example, have been offered employment in local government, national agencies and universities. They might advise on smart-grid electrical technology and energy-use issues, or work in fisheries assessment or on clean-water issues, says Julia Parrish, associate dean for academic affairs and diversity at the College of the Environment. “They can point to a specific product they’ve done in graduate school,” says Parrish. “It lands them jobs and internships. It’s a fabulous way for students to gain that breadth and real-world sustainability and environmental-science experience while still becoming experts in their disciplines.”

Parrish says college directors were careful not to limit their graduates by establishing jack-of-all-trades degrees. “When we talked to employers, whether they’re top-tier universities, federal labs or large environmental non-governmental organizations,” she says, “they said ‘we want disciplinary experts with cross-cutting skills in communication, problem-solving and leadership.’”

James Thorson, now a population ecologist with the US National Oceanic and Atmospheric Administration’s National Marine Fisheries Service in Seattle, did a PhD in aquatic and fisheries studies at the college. Alongside his degree, he also conducted a

team-oriented project with a real-world business bent: he worked with the Washington Restaurant Association in Olympia to develop standards and guidelines for restaurant sustainability. Thorson focused on energy-efficient lighting, which pushed him out of his area of expertise and into one with varied stakeholders. He learned about everything from environmental auditing and certification programmes to project management. Later, he used these skills in an outcomes assessment for the Marine Stewardship Council, an international

“Broad is not shallow. We need excellence in bringing things together.”

organization based in London that establishes standards for sustainable fishing. Making the transition from research to team-based projects is a big jump, he says. “It requires a ton of skills that graduate students don’t learn when working individually.”

Tischa Munoz-Erickson, a research social scientist with the US Forest Service in Flagstaff, Arizona, who last year graduated from ASU with a PhD, says that she and many of her fellow students worried about the number and type of positions they would find upon graduating. But she has seen plenty of demand. “There’s such a need for people with this range of skills,” she says, citing problems such as climate change and water management, which require a knack for collaborating with multiple stakeholders and an expertise in a variety of subjects.

As a PhD student, Munoz-Erickson worked on urban sustainability with the Forest Service and San Juan Urban Long Term Research Area, an interdisciplinary network of scientists in Puerto Rico. She landed her current job shortly after she graduated. The ASU School of Sustainability, she says, taught her how to speak fluently to people in various social- and natural-science disciplines; showed her the limitations of science in informing policy; and prepared her to talk to ecologists, economists and geographers. “When fleshing out what makes a city sustainable or vulnerable, natural and social scientists realized that they had different meanings for these terms and that they valued things about the city differently,” says Munoz-Erickson. As part of her PhD project, she helped to facilitate collaborative meetings to develop a common vocabulary.

“With interdisciplinarity, I find it’s not so much that you’re knowledgeable about all these disciplines,” she says. “It’s about learning the way other disciplines think and their assumptions and methodologies. By looking at your problem from all these different perspectives, it enriches the way you do your own work.” ■

Amanda Mascarelli is a freelance writer based in Denver, Colorado.

RECRUITMENT

Biomedical hiring

Many biopharmaceutical companies plan to hire scientists in the next three years, according to a report published on 4 February by the PwC Health Research Institute in Washington DC, part of London-based professional-services firm PwC. *New Chemistry: Getting the Biopharmaceutical Talent Formula Right*, which is based on surveys of company executives and recruiters, finds that 72% of drug-makers plan to boost their research capacity in the next 12 months by hiring scientists, creating partnerships or improving infrastructure. The results of the survey suggest that jobs will grow by about 30% among US medical scientists, biochemists and biophysicists by 2020. Responding companies want recruits who can develop and manage external partnerships, and who know about regulatory science, bioinformatics and outcomes research. Early-career scientists looking for opportunities need to “think about the entire value chain that leads to the development of a drug or medical device”, says Christopher Khoury, a senior manager at the Health Research Institute and lead author of the report.

UNIVERSITIES

Ranking–system doubts

Members of the League of European Research Universities (LERU) do not plan to support the U-Multirank university ranking system launched last month by the European Union (see *Nature* **494**, 273; 2013). LERU, which is based in Leuven, Belgium, and represents 21 universities across the continent, objects to what it calls a lack of reliable and objectively verifiable data in U-Multirank, problems in comparing institutions between countries, the temptation for universities to change policies or practices to improve their rankings and the burden on universities to collect data, says Kurt Deketelaere, secretary-general of the league. He says that such problems plague all existing university ranking systems, and notes that LERU pulled out of a U-Multirank advisory group in 2010 because its concerns were not addressed. “Since then, we have not seen any evidence of a substantive change of course which could lead us to revisit that decision,” says Deketelaere. Individual member universities can still participate in the programme if they choose, he says, but he notes that none has opted to join so far.

TUMBLEWEEDS AND INDELICATE QUESTIONS

A matter of honour.

BY JOHN P. MURPHY

I was very careful to pay no attention to the gnarly, four-eyed alien head peering over my shoulder. Instead, I wiped down the bar and put the glasses into the sink — the work needs to get done, after all, and I sure wasn't slacking.

The only two customers left after the rush sat and watched me. I figured I wasn't going to be able to weasel out of answering their question, but I wasn't inclined to hurry myself, either. Besides, this bet of theirs was the first time they'd stopped arguing all night — I was enjoying the peace.

"C'mon, Sal," said the lady in the mechanic's overalls. "You're stalling."

"I ain't stalling," I protested. "I'm just trying to get my work done so's I can get out of here on time." I should have told her to buy something, but her being more drunk wouldn't help matters.

"It's a simple question," the mechanic said. "Did you kill that tumbleweed yourself or not?" She was talking about old Harry — the big hairy head with all the fangs that sat nestled in with the bottles up on the top shelf.

She'd been the one to bet I'd killed it. The other one, dressed like a lawyer, pretty much called me chicken. They wouldn't like the answer; they'd just argue more. But I figured that refusing wouldn't satisfy honour on the subject, and they'd just go back to bickering anyway.

"Well, sure you think it's a simple question," I said, giving old Harry a big theatrical wink, "but that ain't so."

The other customer shook her head. She sounded like a lawyer, too. "I hardly think that if Sal had killed a sentient being, she'd have proof of it sitting out for everyone to see."

"We-ell," I said. "I don't know about that. Silver City might be a happening town now with the new spaceport and all, but it used to be a bit of a wild place. Could be maybe I did shoot the old bastard, and just got, whatchacallit, grand-mothered in."

"I knew it!" The mechanic grinned and slapped the bar.



"I didn't say that I did. And I didn't say that I didn't," I added before the lawyer chimed in. "I'm just saying, that doesn't prove nothing."

I sighed. "Arrright. I got old Harry about 20 years ago, back when you had to take them deathtrap shuttles down from orbit. I wanted some adventure, so I hooked up with a crew looking to survey the Dense."

The lawyer scowled. "That's reserved hunting ground."

"Well, if we'd knowed that the place already had tenants, let alone that they was decent folks, we might've called it off. But we didn't know that, so we didn't do that. The Dense ain't much place for humans, but we hiked for a good week along the river. It got dark. It got humid. And we got eaten alive by those furry little bugs."

"One night, out of nowhere comes these huge hairy aliens looked like pencil-necked trolls with big old swords. Me and Suki was on guard when they came roaring out of the tendrillbushes, and we got scared and started shooting. Suki took a sword to the neck, sorry to say, but not before we each dropped one of them."

"Did their heads pop off?" The mechanic interrupted.

"Oh, sure, right away," I said.

The lawyer frowned, so I explained, "Tumbleweeds can live just fine with their

heads off. Times get lean, they wade into the ocean, then they pop their tops and their noggins float away to grow a new body somewhere nicer. Sometimes when they get hurt real bad they do it too."

"That why they call them tumbleweeds," the mechanic said, "or coconut trolls."

"Anyway, things calmed down and we got to talking instead of fighting, and found out it was all a misunderstanding. Apologies all round, and we tended the wounded. One of the tumbleweeds pulled through — nice fella, comes in sometimes to shoot the shit — but the other, Harry, wasn't so lucky."

"We buried Suki according to her custom, but we had a problem with Harry. Harry's clan's death customs had rules, and we needed to know who killed him to figure out what to do with him. If I'd killed him, I was supposed to eat the ugly bugger. Otherwise, we was supposed to burn him so's Suki's ghost could eat him."

"But we lost track of their heads in the fight, see? We didn't know whether I killed Harry or winged his buddy."

The lawyer looked smug all of a sudden. "There's a loophole."

I gave her the stink eye, interrupting someone in the middle of her story like that, but she hardly noticed. "That's right, there's a loophole: when Suki and I've both croaked they can safely burn him and let us sort it out up there. So there the poor guy stays until I kick the bucket."

All three of us gave that ugly puss a good long stare.

"So!" I broke the silence. "Neither of you's right, but just so's there's no hard feelings, next round's on the house."

They finished their drinks in companionable silence and paid their tabs. If they left together, I wasn't paying no mind, just washing dishes.

"You're so full of shit, Sal," Harry snickered as he climbed off his shelf.

I just gave him a peck on the cheek and told him to hush. ■

John P. Murphy is an engineer and writer living in New Hampshire. He is a member of the SFWA, IEEE and Codex

➔ NATURE.COM

Follow Futures:

🐦 @NatureFutures

🌐 go.nature.com/mtoodm